

# **PET imaging to monitor NET-1 and GD2 expression in neuroblastoma**

A thesis presented for the degree of Doctor of Philosophy



**By**

**Stephen M. Turnock**

**Primary Supervisor:**

**Dr. Gabriela Kramer-Marek**

**Preclinical Molecular Imaging Team**

**Radiotherapy and Imaging**

**The Institute of Cancer Research**

**University of London**

**Declaration**

I, Stephen M. Turnock, confirm that the work presented in this thesis is my own. Information and work carried out by other sources has been indicated throughout the thesis.

### Acknowledgements

I would first like to thank the ICR for funding my PhD and providing a wonderful place to learn over the last 4 years.

Gabriela, I am extremely indebted that you chose me to study with you. I have learnt more than I could have imagined. From my interview with the blue suit and me nearly missing my flight back to France, I have enjoyed so much working in this team. I hope that, although difficult, the grant will allow us to continue on these projects together.

To all members of the Preclinical Molecular Imaging Team, past and present, I would like to thank you for helping me on this journey. Daniela, you taught me one invaluable bit of advice, that, it does not matter how one drives their car, as long as you keep your mind on the road you will get to your destination. Tom, you have been a joyous predecessor to follow and you have helped me in so many ways! Justyna and Julia, we will be going all over the world in our futures and I am sure to work with you again! Without PET Radiochemistry too, Graham and Dave, this project would not have made it, so I thank you greatly for this!

Chiara, I cannot thank you enough for your help over the last 4 years. You have not only been a great friend but a critical eye on the work I have carried out and presented in this thesis. I hope to continue working with you and hanging out. I will miss lunches with you and everyone else.

I'd like to thank all staff in the CCI for welcoming me in to the labs. The people have changed a lot, but there has been so many memories with you all. Lisa, you're the best lab manager there could be. I am very grateful for all the work you have done over my time here. Big Box, Carol, thank you as well for all your support and kindness to me and all students in ICR. Harriet, my running buddy, I blame you for getting me in to running and I hope to organise a race with you soon.

To all fellow staff of the ICR and RMH, it has been a great place to work, which is truly down to everyone's kindness and willing to help others here. A particular shout out goes to all the BSU staff, who have pursued the highest quality of *in vivo* research here and helped my project in many ways. Thank you to all my fellow students as well. I think our small community is extremely special and I'm glad we had a lot of memories in the pHbar together! I haven't named anyone because I wouldn't know where to stop to thank you all!

I also couldn't have completed my studies without my friends and famillama. Thank you all for giving me the support when I needed, for checking in with me and for offering many words of wisdom. I look forward to celebrating in style! Thank you to both my mum and my dad for supporting me through my education and getting me here. You've never put a limit on any of us kids and we've all gone far. Beccy, Max and Amy, (although I don't necessarily want to limit it to just you three, I also don't want to write a thesis to list everyone) you get a special mention for so many things and I love you all. To Tim (*raise a glass... cheers*), thank you for being there. I love you three.

## Abstract

Within neuroblastoma (NB), approximately 50 % of patients are considered high-risk, presenting widespread distant metastasis and, frequently, *MYCN* amplification. NB is further characterised by the selective presence of the noradrenaline transporter (NET-1) and the GD2 disialoganglioside in a majority of cases. Targeted therapies against both NET-1 and GD2 have improved patient survival, however, many patients eventually relapse from disease.

mIBG (*meta*-iodobenzylguanidine) is a noradrenaline analogue used for diagnosis and treatment of NB, yet despite 90 % of patients presenting NET-1 expressing tumours and being characterised as ‘mIBG avid’, less than 50 % respond to targeted <sup>131</sup>I-mIBG radiotherapy. This may be, in part, due to the limitations of spatial resolution and image quantification of single photon emission computed tomography (SPECT) acquisitions performed with <sup>123</sup>I-mIBG. To address these deficiencies I have investigated the use of a fluorinated noradrenaline analogue, <sup>18</sup>F-mFBG, for use with positron emission tomography (PET) imaging. Of note, a first-in-human study using <sup>18</sup>F-mFBG has demonstrated clear benefits of using this tracer compared to <sup>123</sup>I-mIBG, yet the tracer has not been fully translated to clinical practice due to a complicated radio-synthesis.

The ability of pharmacological intervention to modulate NET-1 expression in NB has been highlighted with preclinical and clinical studies using the histone deacetylase (HDAC) inhibitor, vorinostat. I wanted to build on this work by investigating compounds that may increase NET-1 expression whilst simultaneously targeting other pathways critical in patients with high-risk disease, in particular the PI3k/Akt/mTOR pathway. I hypothesised that drugs targeting mTORC1/2 can increase NET-1 expression in NB models, to which I investigated the use of <sup>18</sup>F-mFBG as a tool to quantify these changes *in vitro* and *in vivo*.

GD2 expression is also thought to be ubiquitously expressed in NB and GD2-targeted immunotherapy (Dinutuximab/Dinutuximab-Beta) has provided promising improvements in the event free survival of patients compared to historical ‘standard therapies’. However, NB tumours with positive, but low, GD2 expression are likely to relapse. Current methods to investigate tumour GD2 expression are invasive (tumour biopsies) and only provide a snapshot of the disease. In an attempt to better understand the efficacy and pitfalls of GD2 immunotherapy, I have developed an <sup>89</sup>Zr-labelled GD2 antibody that could provide a means of measuring the tumour GD2 expression level *in situ*.

**Publications arising from the work documented in this thesis:**

1. **Turnock S.**, Turton DR., Martins CD., Chesler L., Wilson TC., Gouverneur V., Smith G., Kramer-Marek G.:  $^{18}\text{F}$ -*meta*-fluorobenzylguanidine ( $^{18}\text{F}$ -mFBG) to monitor changes in norepinephrine transporter expression in response to therapeutic intervention in neuroblastoma models. *Sci Rep.* 2020 Dec 1;10(1):20918. doi: 10.1038/s41598-020-77788-3.

**Conference proceedings arising from the work documented in this thesis:**

1. Short-talk: EANM 2017, Vienna, Austria.  
**Turnock S.**, Turton DR., ... Kramer-Marek G.: Potential of PET imaging to monitor upregulation of NET-1 transporter.  
*Awarded: University of London Scholarship fund.*
2. Poster: Preclinical Nuclear Imaging Symposium 2018, London, UK.  
**Turnock S.**, Turton DR., ... Kramer-Marek G.:  $^{18}\text{F}$ -mFBG monitors changes in NET-1 expression with AZD2014 treatment.
3. Oral presentation and Poster: EMIM 2019, Glasgow, UK.  
**Turnock S.**, Turton DR., ... Kramer-Marek G.:  $^{18}\text{F}$ -mFBG-based imaging to guide  $^{131}\text{I}$ -mIBG delivery to neuroblastoma *in vitro* and *in vivo*.  
*Awarded: Best oral presentation in the study group session.*
4. Oral presentation: EMIM 2020, Virtual.  
**Turnock S.**, Da Pieve C., Smith G., Kramer-Marek G.:  $^{89}\text{Zr}$ -DFO-Dinutuximab-Beta to assess differential expression of surface GD2 in neuroblastoma.  
*Awarded: Korner Travelling Fellowship fund.*

## List of abbreviations

---

### Units

<b>A</b>	Amperes
<b>Bq</b>	Becquerels
<b>Ci</b>	Curie
<b>Da</b>	Daltons
<b>eV</b>	Electron volts
<b>g</b>	Grams
<b>h</b>	Hours
<b>L</b>	Litres
<b>m</b>	metres
<b>M</b>	Molar
<b>min</b>	Minutes
<b>mol</b>	Moles
<b>s</b>	seconds

### Abbreviations

<b>2D</b>	2-dimensional
<b>3D</b>	3-dimensional
<b>4EBP1</b>	Eukaryotic translation initiation factor 4E-binding protein 1
<b>ADCC</b>	Antibody-dependent cell-mediated cytotoxicity
<b>AKA</b>	Also known as
<b>Akt</b>	Protein kinase B
<b>ALK</b>	Anaplastic lymphoma kinase
<b>ANOVA</b>	Analysis of variance
<b>ATP</b>	Adenosine triphosphate
<b>BAT</b>	Brown adipose tissue
<b>BCA</b>	Bicinchoninic acid
<b>BET</b>	Bromodomain and extra-terminal motif
<b>bHLH</b>	Basic helix-loop-helix
<b>BID</b>	bis in die
<b>BSA</b>	Bovine serum albumin
<b>BuMel</b>	Busulfan and Melphalan Hydrochloride
<b>CAR-T</b>	Chimeric antigen receptor T cells
<b>CDC</b>	Complement derived cytotoxicity
<b>CDK1</b>	Cyclin-dependent kinase 1
<b>CEM</b>	Carboplatin, Etoposide Phosphate and Melphalan Hydrochloride
<b>CHO</b>	Chinese hamster ovary
<b>CI</b>	Confidence interval
<b>c-MET</b>	Tyrosine-protein kinase Met
<b>CNS</b>	Central nervous system
<b>CPM</b>	Counts per minute

## List of abbreviations

---

<b>CT</b>	Computed tomography
<b>DAB</b>	Diaminobenzidine
<b>DAPI</b>	4',6-diamidino-2-phenylindole
<b>DFO</b>	Desferrioxamine
<b>DMEM</b>	Dulbecco's Modified Eagle Media
<b>DMF</b>	Dimethylformamide
<b>DMI</b>	Desipramine
<b>DMSO</b>	Dimethyl sulfoxide
<b>DNA</b>	Deoxyribonucleic acid
<b>dNTP</b>	Deoxyribonucleotide triphosphate
<b>DOPA</b>	Dihydroxyphenylalanine
<b>DOTA</b>	Dodecane tetraacetic acid
<b>DOTATATE</b>	DOTA-0-Tyr3-Octreotate
<b>DOTATOC</b>	DOTA-0-Phe1-Tyr3-Octreotide
<b>DTT</b>	Dithiothreitol
<b>EBR</b>	External beam radiation
<b>EC</b>	Electron capture
<b>EDTA</b>	Ethylenediaminetetraacetic acid
<b>EFS</b>	Event-free survival
<b>EGFR</b>	Epidermal growth factor receptor
<b>EMA</b>	European Medicines Agency
<b>ER</b>	Endoplasmic reticulum
<b>ERK</b>	Mitogen-activated protein kinase
<b>ESI</b>	Electro spray ionisation
<b>FACS</b>	Flow assisted cell sorting
<b>FBP</b>	Filtered back projection
<b>FBS</b>	Foetal bovine serum
<b>FC</b>	Flow cytometry
<b>FDA</b>	Food and Drug Administration
<b>FDG</b>	Fluorodeoxyglucose
<b>FITC</b>	Fluorescein isothiocyanate
<b>FMO</b>	Fluorescence minus one
<b>FOV</b>	Field of view
<b>GAPDH</b>	Glyceraldehyde 3-phosphate dehydrogenase
<b>GD2</b>	Ganglioside G2
<b>GE</b>	General Electric
<b>GI</b>	Gastrointestinal
<b>GI<sub>50</sub></b>	Grown inhibition 50 %
<b>GLUT-1</b>	Glucose transporter-1
<b>GM-CSF</b>	Granulocyte-macrophage colony-stimulating factor
<b>GM-CSF</b>	Granulocyte-macrophage colony-stimulating factor
<b>GMP</b>	Good manufacturing practice
<b>GN</b>	Ganglioneuroma
<b>GNB</b>	Ganglioneuroblastoma
<b>GPCR</b>	G-protein coupled receptor

## List of abbreviations

---

<b>GSK3<math>\beta</math></b>	Glycogen synthase kinase 3 beta
<b>H2AX</b>	H2A histone family member X
<b>HACA</b>	Human anti-chimeric antibodies
<b>HAHA</b>	Human anti-human antibodies
<b>HAMA</b>	Human anti-mouse antibodies
<b>HCC</b>	Hepatocellular carcinoma
<b>HCl</b>	Hydrochloric acid
<b>HDAC</b>	Histone deacetylase
<b>HEPES</b>	4-(2-hydroxyethyl)-1-piperazineethanesulfonic acid)
<b>HIER</b>	Heat-induced epitope revival
<b>HPLC</b>	High Performance Liquid Chromatography
<b>HR</b>	High-risk
<b>HRP</b>	Horseradish peroxidase
<b>HVA</b>	Homovanillic acid
<b>ICC</b>	Immunocytochemistry
<b>ID</b>	Injected dose
<b>IDRF</b>	Image define risk factor
<b>IGF-1</b>	Insulin-like growth factor
<b>IgG</b>	Immunoglobulin
<b>IHC</b>	Immunohistochemistry
<b>IL-2</b>	Interleukin-2
<b>INRG</b>	The International Neuroblastoma Risk Group
<b>INRGSS</b>	The International Neuroblastoma Risk Group staging system
<b>INSS</b>	International Neuroblastoma Staging System
<b>LAT</b>	Large neutral amino acid transporter
<b>LET</b>	Linear energy transfer
<b>LOH</b>	Loss of heterozygosity
<b>LOR</b>	Line of response
<b>LSO</b>	Lutetium oxyorthosilicate
<b>LYSO</b>	Lutetium yttrium oxyorthosilicate
<b>mAb</b>	Monoclonal antibody
<b>mABG</b>	<i>meta</i> -astatobenzylguanadine
<b>MAPK</b>	Mitogen-activated protein kinase
<b>MAX</b>	Myc-associated factor X
<b>MDM2</b>	Murine double minute 2
<b>MDP</b>	Methyldiphosphonate
<b>MDSC</b>	Myeloid-derived suppressor cell
<b>MEK</b>	Mitogen-activated protein kinase kinase
<b>mFBG</b>	<i>meta</i> -fluorobenzylguanadine
<b>MFI</b>	Median fluorescence intensity
<b>MI</b>	Molecular imaging
<b>mIBG</b>	<i>meta</i> -iodobenzylguanadine
<b>MIP</b>	Maximum intensity projection
<b>MLEM</b>	Maximum-Likelihood Expectation-Maximization
<b>MOPS</b>	3-morpholinopropane-1-sulfonic acid

## List of abbreviations

---

<b>MR</b>	Magnetic resonance
<b>MRD</b>	Minimal residual disease
<b>MRI</b>	Magnetic resonance imaging
<b>MS</b>	Mass spectrometry
<b>mTOR</b>	Mammalian target of rapamycin
<b>mTORC</b>	Mammalian target of rapamycin complex
<b>MWCO</b>	Molecular weight cut-off
<b>MYCN</b>	V-Myc Avian Myelocytomatosis Viral Oncogene Neuroblastoma Derived Homologue
<b>N</b>	Neutron
<b>NA</b>	Non-amplified
<b>Na</b>	Not applicable
<b>NB</b>	Neuroblastoma
<b>NCA</b>	No-carrier added
<b>NCT</b>	National clinical trial number
<b>NE</b>	Norepinephrine
<b>NET-1</b>	Norepinephrine transporter
<b>NGS</b>	Normal goat serum
<b>NHS</b>	N-Hydroxysuccinimide
<b>NIH</b>	National Institute of Health
<b>NK</b>	Natural Killer cell
<b>NMR</b>	Nuclear magnetic resonance
<b>OECD</b>	Organisation for Economic Co-operation and Development
<b>OS</b>	Overall survival
<b>OSCC</b>	Oral squamous cell carcinoma
<b>OSEM</b>	Ordered Subset Expectation Maximization
<b>p.i.</b>	Post-injection
<b>PAGE</b>	Polyacrylamide Gel Electrophoresis
<b>PARP</b>	Poly (ADP-ribose) polymerase
<b>PBS</b>	Phosphate buffered saline
<b>PCR</b>	Polymerase chain reaction
<b>PDK</b>	Phosphoinositide-dependent kinase-1
<b>PE</b>	Phycoerythrin
<b>PEG</b>	Polyethylene glycol
<b>PET</b>	Positron emission tomography
<b>PFA</b>	Paraformaldehyde
<b>PI</b>	Propidium iodide
<b>PI3k</b>	Phosphoinositide 3-kinases
<b>PIP2</b>	Phosphatidylinositol 4,5-bisphosphate
<b>PIP3</b>	Phosphatidylinositol 3,4,5-trisphosphate
<b>PKC</b>	Protein kinase C
<b>PSMA</b>	Prostate specific membrane antigen
<b>RA</b>	Retinoic acid
<b>RBC</b>	Red blood cell
<b>RCP</b>	Radiochemical purity

## List of abbreviations

---

<b>RF</b>	Radio frequency
<b>RIPA</b>	Radioimmunoprecipitation assay
<b>RNA</b>	Ribonucleic acid
<b>RP-HPLC</b>	Reversed-phase HPLC
<b>RPLP0</b>	60S acidic ribosomal protein P0
<b>rpm</b>	Rotations per minute
<b>RPMI</b>	Roswell Park Memorial Institute
<b>RT</b>	Room temperature
<b>RTK</b>	Receptor tyrosine kinase
<b>S6</b>	Ribosomal protein S6 kinase beta-1
<b>SD</b>	Standard deviation
<b>SDS</b>	Sodium dodecyl sulfate
<b>SEM</b>	Standard error of the mean
<b>SG</b>	Silica gel
<b>SIOPEN</b>	The International Society of Paediatric Oncology - Europa Neuroblastoma
<b>SLC6A2</b>	Solute carrier family 6 member 2
<b>SNR</b>	Signal-to-noise ratio
<b>SPE</b>	Solid phase extraction
<b>SPECT</b>	Single photon emission computed tomography
<b>SSTR</b>	Somatostatin receptor
<b>STR</b>	Short tandem repeat
<b>SUV</b>	Standard uptake value
<b>TBST</b>	Tris-buffered saline plus Tween-20
<b>TLC</b>	Thin-layer chromatography
<b>TMD</b>	Transmembrane domain
<b>UF</b>	Ultra-filtered
<b>UK</b>	United Kingdom
<b>USA</b>	United States of America
<b>UV</b>	Ultraviolet
<b>VMA</b>	Vanillylmandelic acid
<b>VOI</b>	Volume of interest
<b>WB</b>	Western blot
<b>Z</b>	Proton

---

**Table of contents**

<b>Chapter 1 - Introduction</b> .....	1
1.1. Neuroblastoma .....	1
1.2. Clinical staging .....	2
1.3. Neuroblastoma risk groups .....	4
1.4. Current therapeutic strategies for NB .....	5
1.4.1. Low–intermediate risk .....	5
1.4.2. High-risk disease .....	6
1.4.3. Recurrent and refractory disease .....	8
1.5. Molecular characteristics of NB .....	8
1.5.1. The <i>MYCN</i> oncogene and MYCN protein .....	8
1.5.1.1. Targeting MYCN .....	11
1.5.1.2. PI3k/Akt/mTOR pathway and MYCN .....	12
1.5.2. Noradrenaline and the noradrenaline transporter .....	14
1.5.2.1. NET-1 targeted therapy .....	16
1.5.3. GD2 .....	18
1.5.3.1. GD2-targeted immunotherapy .....	21
1.6. Imaging neuroblastoma .....	24
1.6.1. Anatomical imaging .....	24
1.6.2. Nuclear imaging .....	26
1.6.2.1. Radiation and radioactive decay .....	26
1.6.2.1.1. Alpha decay .....	28
1.6.2.1.2. Beta decay .....	30
1.6.2.1.3. Gamma emission .....	32
1.6.2.2. Nuclear imaging modalities .....	33
1.6.2.3. Characteristics of PET radionuclides .....	37
1.6.2.4. PET quantification .....	41
1.6.3. Nuclear imaging agents currently used in NB .....	42
1.6.4. Nuclear imaging agents under investigation in NB .....	46
<b>Chapter 2 - Research aims</b> .....	50
<b>Chapter 3 - Materials and methods</b> .....	51
3.1. Cell culture .....	51
3.2. Chapter 4 .....	52
3.2.1. Cell culture .....	52

## Table of contents

---

3.2.2.	Western blot .....	52
3.2.2.1.	Cell lysis .....	52
3.2.2.2.	Tissue lysis.....	53
3.2.2.3.	Electrophoresis.....	53
3.2.2.4.	Membrane transfer.....	54
3.2.2.5.	Blocking and antibody probing.....	55
3.2.2.6.	Chemiluminescence imaging.....	55
3.2.2.7.	Image analysis.....	56
3.2.3.	Preparation of imaging agents.....	56
3.2.4.	Specificity of binding.....	58
3.2.5.	Animal studies.....	58
3.2.5.1.	Tumour establishment.....	58
3.2.5.2.	<i>In vivo</i> administration of imaging and radiotherapeutic agents.....	59
3.2.6.	Small animal imaging .....	59
3.2.6.1.	PET imaging .....	59
3.2.6.2.	CT imaging .....	60
3.2.6.3.	SPECT imaging .....	60
3.2.6.4.	MRI.....	61
3.2.6.5.	Cerenkov luminescence imaging.....	61
3.2.7.	PET quantification .....	61
3.2.8.	Organ biodistribution .....	62
3.2.9.	Autoradiography .....	62
3.2.10.	Statistics.....	62
3.3.	Chapter 5 .....	63
3.3.1.	Cell viability.....	63
3.3.2.	Cell cycle analysis.....	63
3.3.3.	Western blot .....	64
3.3.4.	Quantitative real-time PCR.....	65
3.3.5.	<sup>18</sup> F-mFBG and <sup>123</sup> I-mIBG cell uptake after AZD2014 treatment.....	66
3.3.6.	<i>In vivo</i> AZD2014 treatment studies .....	66
3.3.7.	PET imaging and biodistribution after AZD2014 treatment.....	66
3.3.8.	Autoradiography .....	66
3.3.9.	Immunohistochemistry.....	67
3.3.10.	Statistics.....	68

## Table of contents

---

3.4.	Chapter 6 .....	69
3.4.1.	Cell lines .....	69
3.4.2.	Antibodies .....	69
3.4.3.	IRDye700DX-ch14.18(CHO) conjugation .....	69
3.4.4.	Flow cytometry .....	70
3.4.5.	Immunocytochemistry.....	71
3.4.6.	Immunofluorescence .....	71
3.4.7.	DFO-ch14.18(CHO) and DFO-IgG1 conjugation .....	72
3.4.8.	<sup>89</sup> Zr radiolabelling .....	73
3.4.9.	<i>In vitro</i> serum stability of <sup>89</sup> Zr-DFO-ch14.18(CHO).....	73
3.4.10.	<sup>89</sup> Zr-DFO-ch14.18(CHO) <i>in vitro</i> binding affinity and specificity .....	74
3.4.11.	<sup>89</sup> Zr-labelled antibody animal studies.....	74
3.4.12.	PET imaging and biodistribution .....	74
3.4.13.	Autoradiography.....	75
3.4.14.	<i>Ex vivo</i> flow cytometry.....	75
3.4.15.	Statistics.....	76
<b>Chapter 4</b>	<b>- <sup>18</sup>F-mFBG PET as a tool to measure NET-1 status in NB .....</b>	<b>77</b>
4.1.	Introduction .....	77
4.2.	Results .....	80
4.2.1.	Production and analysis of <sup>18</sup> F-mFBG .....	80
4.2.2.	Characterisation of selected cell lines .....	81
4.2.3.	<sup>18</sup> F-mFBG and <sup>123</sup> I-mIBG uptake .....	82
4.2.4.	Dynamic PET imaging.....	84
4.2.5.	<sup>18</sup> F-mFBG <i>in vivo</i> distribution .....	88
4.2.6.	<sup>123</sup> I-mIBG <i>in vivo</i> distribution.....	89
4.2.7.	<sup>18</sup> F-mFBG PET/CT static imaging.....	91
4.2.8.	<sup>18</sup> F-mFBG PET quantification .....	92
4.2.9.	<i>Ex vivo</i> tumour analysis .....	94
4.2.10.	<sup>18</sup> F-mFBG PET/CT imaging of kidney capsule NB model.....	96
4.2.11.	<sup>123</sup> I-mIBG and <sup>131</sup> I-mIBG SPECT/CT imaging.....	97
4.3.	Discussion .....	100
4.3.1.	<sup>18</sup> F-mFBG production .....	101
4.3.2.	Correlation of NET-1 expression to <sup>18</sup> F-mFBG and <sup>123</sup> I-mIBG uptake <i>in vitro</i> .....	101

## Table of contents

---

4.3.3.	$^{18}\text{F}$ -mFBG dynamic PET imaging and time-activity curves .....	103
4.3.4.	<i>In vivo</i> $^{18}\text{F}$ -mFBG and $^{123}\text{I}$ -mIBG biodistribution.....	104
4.3.5.	$^{18}\text{F}$ -mFBG PET/CT imaging and quantification .....	106
4.3.6.	$^{123}\text{I}$ -mIBG and $^{131}\text{I}$ -mIBG SPECT/CT imaging.....	108
4.4.	Conclusions and future considerations.....	110
<b>Chapter 5</b>	<b>- <math>^{18}\text{F}</math>-mFBG PET to monitor changes in NET-1 expression in NB .....</b>	<b>113</b>
5.1.	Introduction.....	113
5.2.	Results.....	117
5.2.1.	AZD2014 cell viability in <i>MYCN</i> amplified and non-amplified NB cell lines.....	117
5.2.2.	AZD2014-induced mTORC1/2 inhibition and enhanced NET-1 expression in <i>MYCN</i> amplified cell lines .....	119
5.2.3.	$^{18}\text{F}$ -mFBG and $^{123}\text{I}$ -mIBG uptake in AZD2014 treated cells .....	125
5.2.4.	AZD2014 <i>in vivo</i> toxicity and NB tumour growth .....	128
5.2.5.	PET imaging and tumour uptake quantification after AZD2014 treatment .. .....	132
5.2.6.	$^{18}\text{F}$ -mFBG biodistribution studies after AZD2014 treatment .....	138
5.2.7.	<i>Ex vivo</i> tumour analysis after AZD2014 treatment.....	143
5.2.7.1.	Autoradiography .....	144
5.2.7.2.	Western blot.....	144
5.2.7.3.	Immunohistochemistry .....	148
5.2.7.4.	Quantitative-rtPCR .....	150
5.3.	Discussion .....	152
5.3.1.	AZD2014-induced mTORC1/2 inhibition in NB cells.....	153
5.3.2.	$^{18}\text{F}$ -mFBG as a tool to measure changes in NET-1 function following AZD2014 treatment <i>in vitro</i> .....	156
5.3.3.	Monitoring <i>in vivo</i> effects of AZD2014 treatment with $^{18}\text{F}$ -mFBG .....	158
5.3.4.	<i>Ex vivo</i> NB tumour analysis after AZD2014 treatment .....	162
5.3.5.	Correlation between NET-1 protein expression and $^{18}\text{F}$ -mFBG tumour uptake .....	166
5.4.	Conclusions and future directions.....	169
<b>Chapter 6</b>	<b>- <math>^{89}\text{Zr}</math>-labelled Dinutuximab-Beta for imaging GD2 positive NB .....</b>	<b>171</b>
6.1.	Introduction.....	171
6.2.	Results.....	175
6.2.1.	Characterisation of NB GD2 expression <i>in vitro</i> .....	175

## Table of contents

---

6.2.2.	Immunofluorescence of NB tumour samples.....	178
6.2.3.	<sup>89</sup> Zr labelling of ch14.18(CHO) and stability of the radioconjugate .....	179
6.2.4.	<sup>89</sup> Zr-DFO-ch14.18(CHO) cell specificity of binding assay .....	181
6.2.5.	PET imaging of <sup>89</sup> Zr-DFO-ch14.18(CHO)/IgG1 .....	183
6.2.6.	<sup>89</sup> Zr-DFO-ch14.18(CHO)/IgG1 biodistribution.....	189
6.2.7.	<i>Ex vivo</i> analysis .....	194
6.3.	Discussion .....	197
6.3.1.	Characterisation of GD2 expression in NB cell lines .....	198
6.3.2.	<sup>89</sup> Zr-DFO-ch14.18(CHO) <i>in vitro</i> characterisation.....	201
6.3.3.	<sup>89</sup> Zr-DFO-ch14.18(CHO)/IgG1 PET imaging .....	203
6.3.4.	<sup>89</sup> Zr-DFO-ch14.18(CHO)/IgG1 biodistribution.....	206
6.3.5.	<i>Ex vivo</i> analysis in the NB tumour and mouse spleen.....	209
6.4.	Conclusions and future work .....	211
<b>Chapter 7</b>	<b>- General Conclusions.....</b>	<b>212</b>
7.1.	<sup>18</sup> F-mFBG PET as a tool to measure NET-1 status in NB.....	212
7.2.	<sup>18</sup> F-mFBG PET to monitor changes in NET-1 expression in NB.....	212
7.3.	<sup>89</sup> Zr-labelled Dinutuximab-Beta to measure GD2 expression in NB.....	213
<b>Chapter 8</b>	<b>- References .....</b>	<b>215</b>

---

**List of figures**

<b>Figure 1.1</b>	Neural crest cell migration and differentiation to the trunk .....	2
<b>Figure 1.2</b>	Summary of treatment strategies for high-risk neuroblastoma.....	7
<b>Figure 1.3</b>	Schematic of <i>MYCN</i> transcription and activity.....	10
<b>Figure 1.4</b>	Simplified PI3k/Akt and mTOR pathway .....	13
<b>Figure 1.5</b>	Schematic representation of NET-1 transporter .....	15
<b>Figure 1.6</b>	Structure of noradrenaline and mIBG.....	17
<b>Figure 1.7</b>	Structure of the ganglioside GD2. ....	19
<b>Figure 1.8</b>	Simplified a- and b-series ganglioside biosynthesis pathway .....	20
<b>Figure 1.9</b>	The electromagnetic spectrum. ....	27
<b>Figure 1.10</b>	Nuclear stability and types of radioactive decay .....	28
<b>Figure 1.11</b>	Schematic of scintigraphy and SPECT acquisition .....	35
<b>Figure 1.12</b>	Schematic of positron emission and PET acquisition.....	36
<b>Figure 1.13</b>	Decay schema for $^{18}\text{F}$ and $^{124}\text{I}$ .....	40
<b>Figure 1.14</b>	CURIE and SIOPEN semi-quantitative scoring systems. ....	44
<b>Figure 3.1</b>	WB stacking order .....	54
<b>Figure 4.1</b>	Schematic representation of the Trasis AllinOne cassette.....	80
<b>Figure 4.2</b>	Schematic of $^{18}\text{F}$ -mFBG radiosynthesis and HPLC traces .....	81
<b>Figure 4.3</b>	Western Blot of NET-1 protein expression in selected NB cell lines .....	82
<b>Figure 4.4</b>	$^{18}\text{F}$ -mFBG and $^{123}\text{I}$ -mIBG uptake in NB cell lines .....	83
<b>Figure 4.5</b>	Time-activity curves in SK-N-BE(2)C NB xenografts .....	85
<b>Figure 4.6</b>	Time-activity curves in mouse bladder, whole body and heart.....	86
<b>Figure 4.7</b>	$^{18}\text{F}$ -mFBG biodistribution 6 h p.i. in SK-N-BE(2)C tumour xenograft.....	87
<b>Figure 4.8</b>	$^{18}\text{F}$ -mFBG biodistribution 1 and 4 h p.i. in NB xenografts. ....	89
<b>Figure 4.9</b>	$^{123}\text{I}$ -mIBG biodistribution 24 h p.i. in NB xenografts .....	90
<b>Figure 4.10</b>	$^{18}\text{F}$ -mFBG PET/CT images 1 and 4 h p.i. in NB xenografts .....	92

List of figures

---

<b>Figure 4.11</b> $^{18}\text{F}$ -mFBG PET tumour quantification in NB xenografts.....	93
<b>Figure 4.12</b> Correlation between PET quantification and biodistribution values.....	94
<b>Figure 4.13</b> Autoradiography of Kelly and SK-N-BE(2)C tumour sections.....	95
<b>Figure 4.14</b> <i>Ex vivo</i> WB analysis of Kelly and SK-N-BE(2)C xenografts .....	95
<b>Figure 4.15</b> $^{18}\text{F}$ -mFBG PET/CT images 1 and 4 h p.i. in kidney capsule xenografts....	97
<b>Figure 4.16</b> $^{123}\text{I}$ -mIBG SPECT/CT images 24 h p.i. in NB xenograft.....	98
<b>Figure 4.17</b> $^{131}\text{I}$ -mIBG SPECT/CT and Cerenkov images in SK-N-BE(2)C xenografts .....	99
<b>Figure 5.1</b> The role of the PI3k/Akt/mTOR pathway in the repression of NET-1 expression and function in HR-NB.....	116
<b>Figure 5.2</b> WB of MYCN expression in NB cells lines and cell viability after incubation with AZD2014 .....	117
<b>Figure 5.3</b> Cell viability (24 h) and cell cycle analysis of NB cells incubated with AZD2014 .....	118
<b>Figure 5.4</b> WB of Kelly and SK-N-BE(2)C cell lysates with AZD2014.....	120
<b>Figure 5.5</b> Densitometry of Kelly and SK-N-BE(2)C WB with AZD2014.....	121
<b>Figure 5.6</b> WB of Kelly and SK-N-BE(2)C cell lysates with AZD2014 (3–72 h).....	123
<b>Figure 5.7</b> Densitometry of Kelly and SK-N-BE(2)C WBs with AZD2014 (3–72 h).	125
<b>Figure 5.8</b> $^{18}\text{F}$ -mFBG uptake in NB cells treated with AZD2014 (24 h).....	126
<b>Figure 5.9</b> $^{18}\text{F}$ -mFBG and $^{123}\text{I}$ -mIBG uptake in NB cells treated with AZD2014 (72 h) .....	128
<b>Figure 5.10</b> Mouse body weight change following treatment with AZD2014 .....	129
<b>Figure 5.11</b> Relative tumour size of NB xenografts during the treatment with AZD2014 .....	131
<b>Figure 5.12</b> $^{18}\text{F}$ -mFBG PET/CT images 4 h p.i. in SK-N-BE(2)C xenografts after treatment with AZD2014 (1 d).....	133

## List of figures

---

<b>Figure 5.13</b> $^{18}\text{F}$ -mFBG PET/CT images 4 h p.i. in Kelly and SK-N-BE(2)C xenografts after treatment with AZD2014 (3 d) .....	134
<b>Figure 5.14</b> $^{18}\text{F}$ -mFBG PET/CT images 4 h p.i. in SK-N-BE(2)C xenografts after treatment with AZD2014 (7 d).....	135
<b>Figure 5.15</b> $^{18}\text{F}$ -mFBG PET tumour quantification in SK-N-BE(2)C xenografts after treatment with AZD2014 (20 mg/kg/day).....	136
<b>Figure 5.16</b> $^{18}\text{F}$ -mFBG PET tumour quantification in SK-N-BE(2)C xenografts after treatment with AZD2014 (25 mg/kg/day).....	137
<b>Figure 5.17</b> $^{18}\text{F}$ -mFBG PET tumour quantification in Kelly xenografts after treatment with AZD2014 (20 and 25 mg/kg/day).....	138
<b>Figure 5.18</b> $^{18}\text{F}$ -mFBG tumour uptake in SK-N-BE(2)C xenografts after treatment with AZD2014 .....	141
<b>Figure 5.19</b> $^{18}\text{F}$ -mFBG tumour uptake in Kelly xenografts after treatment with AZD2014 .....	142
<b>Figure 5.20</b> Correlation between tumour associated $^{18}\text{F}$ -mFBG PET and biodistribution values in NB tumours after treatment with AZD2014 .....	143
<b>Figure 5.21</b> Autoradiography of SK-N-BE(2)C tumour slices after treatment with AZD2014 (20 and 25 mg/kg/day).....	144
<b>Figure 5.22</b> WB of Kelly tumour lysates after AZD2014 treatment.....	145
<b>Figure 5.23</b> WB of SK-N-BE(2)C tumour lysates after AZD2014 treatment .....	148
<b>Figure 5.24</b> IHC staining of Kelly and SK-N-BE(2)C tumour slices after treatment with AZD2014. ....	150
<b>Figure 5.25</b> <i>SLC6A2</i> mRNA expression in Kelly and SK-N-BE(2)C tumours after treatment with AZD2014 .....	151
<b>Figure 5.26</b> Correlation between tumour NET-1 status and $^{18}\text{F}$ -mFBG PET and biodistribution values after treatment with AZD2014 .....	168

---

<b>Figure 6.1</b> FC histograms of PE-14G2A binding in NB cells with different GD2 expression levels .....	176
<b>Figure 6.2</b> FC histograms of PE, FITC or IRDye700DX labelled anti-GD2 antibodies and IgG2A-FITC non-specific control antibody in a panel NB cell lines .....	177
<b>Figure 6.3</b> IR700-ch14.18(CHO) confocal microscopy in NB cell lines.....	178
<b>Figure 6.4</b> Immunofluorescence of SK-N-AS, Kelly and SK-N-BE(2)C tumour slices with IR700-ch14.18(CHO) .....	179
<b>Figure 6.5</b> Schematic of the p-NCS-Bz-DFO conjugation to mAb and radiolabelling of DFO-mAb conjugate with $^{89}\text{Zr}$ .....	180
<b>Figure 6.6</b> Mouse serum stability of $^{89}\text{Zr}$ -DFO-ch14.18(CHO) .....	181
<b>Figure 6.7</b> $^{89}\text{Zr}$ -DFO-Antibody specificity of binding in NB cells.....	182
<b>Figure 6.8</b> $^{89}\text{Zr}$ -DFO-ch14.18(CHO) binding in Kelly-GD2 <sup>High</sup> and Kelly cells after few and multiple passages <i>in vitro</i> .....	183
<b>Figure 6.9</b> $^{89}\text{Zr}$ -DFO-ch14.18(CHO) PET/CT in SK-N-BE(2)C xenografts.....	184
<b>Figure 6.10</b> $^{89}\text{Zr}$ -DFO-ch14.18(CHO) PET/CT in SK-N-AS xenografts .....	186
<b>Figure 6.11</b> $^{89}\text{Zr}$ -DFO-IgG1 PET/CT in SK-N-AS xenografts.....	187
<b>Figure 6.12</b> $^{89}\text{Zr}$ -DFO-ch14.18(CHO) and $^{89}\text{Zr}$ -DFO-IgG1 PET quantification in NB tumours.....	188
<b>Figure 6.13</b> $^{89}\text{Zr}$ -DFO-ch14.18(CHO) daily PET quantification in SK-N-AS tumours .....	189
<b>Figure 6.14</b> $^{89}\text{Zr}$ -DFO-ch14.18(CHO) biodistribution in SK-N-BE(2)C xenografts...	190
<b>Figure 6.15</b> $^{89}\text{Zr}$ -DFO-ch14.18(CHO) biodistribution in SK-N-AS xenografts .....	192
<b>Figure 6.16</b> $^{89}\text{Zr}$ -DFO-IgG1 biodistribution in SK-N-AS xenografts.....	192
<b>Figure 6.17</b> $^{89}\text{Zr}$ -DFO-ch14.18(CHO) tumour uptake in SK-N-BE(2)C and SK-N-AS xenografts and $^{89}\text{Zr}$ -DFO-IgG1 tumour uptake in SK-N-AS xenografts.....	193

## List of figures

---

<b>Figure 6.18</b> Correlation between $^{89}\text{Zr}$ -DFO-ch14.18(CHO) PET and biodistribution values in NB tumours.....	194
<b>Figure 6.19</b> $^{89}\text{Zr}$ -DFO-ch14.18(CHO) and $^{89}\text{Zr}$ -DFO-IgG1 autoradiography in NB tumours and mouse spleen .....	195
<b>Figure 6.20</b> Flow cytometry of ex vivo spleen and NB tumour samples with IR700-ch14.18(CHO).....	196
<b>Figure 6.21</b> Correlation between $^{89}\text{Zr}$ -DFO-ch14.18(CHO) uptake values in the spleen and bone of SK-N-AS xenografts .....	208

---

## List of tables

<b>Table 1.1</b> International Neuroblastoma Risk Group Staging System.....	3
<b>Table 1.2</b> INRG risk classification .....	5
<b>Table 1.3</b> Examples of alpha emitting radionuclides .....	29
<b>Table 1.4</b> Examples of beta minus emitting radionuclides.....	31
<b>Table 1.5</b> Examples of positron emitting radionuclides.....	32
<b>Table 1.6</b> Examples of gamma-emitting radionuclides.....	33
<b>Table 1.7</b> Common PET radioisotopes.....	39
<b>Table 3.1</b> List of antibodies used for WB analysis.....	55
<b>Table 3.2</b> List of antibodies used for WB analysis.....	64
<b>Table 3.3</b> List of PCR TaqMan gene expression primers. ....	65
<b>Table 3.4</b> List of antibodies for IHC. ....	68
<b>Table 3.5</b> List of antibodies for flow cytometry .....	70
<b>Table 3.6</b> List of antibodies for immunofluorescence.....	72
<b>Table 3.7</b> List of fluorescently labelled antibodies for flow cytometry .....	76
<b>Table 4.1</b> $^{18}\text{F}$ -mFBG and $^{123}\text{I}$ -mIBG uptake in NB cell lines .....	84
<b>Table 4.2</b> Biodistribution of $^{18}\text{F}$ -mFBG 6 h p.i. in SK-N-BE(2)C xenograft.....	87
<b>Table 4.3</b> Biodistribution of $^{18}\text{F}$ -mFBG 1 and 4 h p.i. in NB xenografts.....	89
<b>Table 4.4</b> Biodistribution of $^{123}\text{I}$ -mIBG 24 h after injection in NB xenografts.....	91
<b>Table 5.1</b> Biodistribution of $^{18}\text{F}$ -mFBG in SK-N-BE(2)C tumour-bearing mice following AZD2014 treatment .....	139
<b>Table 5.2</b> Biodistribution of $^{18}\text{F}$ -mFBG in Kelly tumour-bearing mice following AZD2014 treatment .....	140
<b>Table 6.1</b> Biodistribution of $^{89}\text{Zr}$ -DFO-ch14.18(CHO) in SK-N-BE(2)C xenografts. ....	190
<b>Table 6.2</b> Biodistribution of $^{89}\text{Zr}$ -DFO-ch14.18(CHO) and $^{89}\text{Zr}$ -DFO-IgG1 in mice bearing SK-N-AS tumour xenografts.....	193



## **Chapter 1 - Introduction**

### **1.1. Neuroblastoma**

Neuroblastoma (NB) is the most common solid cancer of early childhood; with around 100 new cases per year in the UK [1-4]. NB arises from the neural crest, most probably the sympathoadrenal lineage (Figure 1.1) [5, 6]. Neural crest cells are, under normal circumstance, temporary cells that differentiate to a wide progeny of cell lineages along the sympathetic chain; in the trunk, heart and face [7, 8]. Therefore, NB primary tumour masses form at any of the widespread depositories of these cells. The principal primary sites are located at the adrenal medulla (35 %) and paraspinal sympathetic ganglia (60 %), although in more rare cases other primary sites such as the pelvis, neck and stomach have been described [9, 10]. Clinical presentation of NB is therefore varied by this early and irregular development pattern. NB mostly affect children under the age of 5, although rare cases have been recorded prenatally [11] up to and beyond 10 years of age [12, 13]. Patients may present abdominal pains, irregular bowel habits, bruising around the eyes, chest pain, wheezing, or back and bone pains, depending on location, tumour size, and degree of metastasis [14].

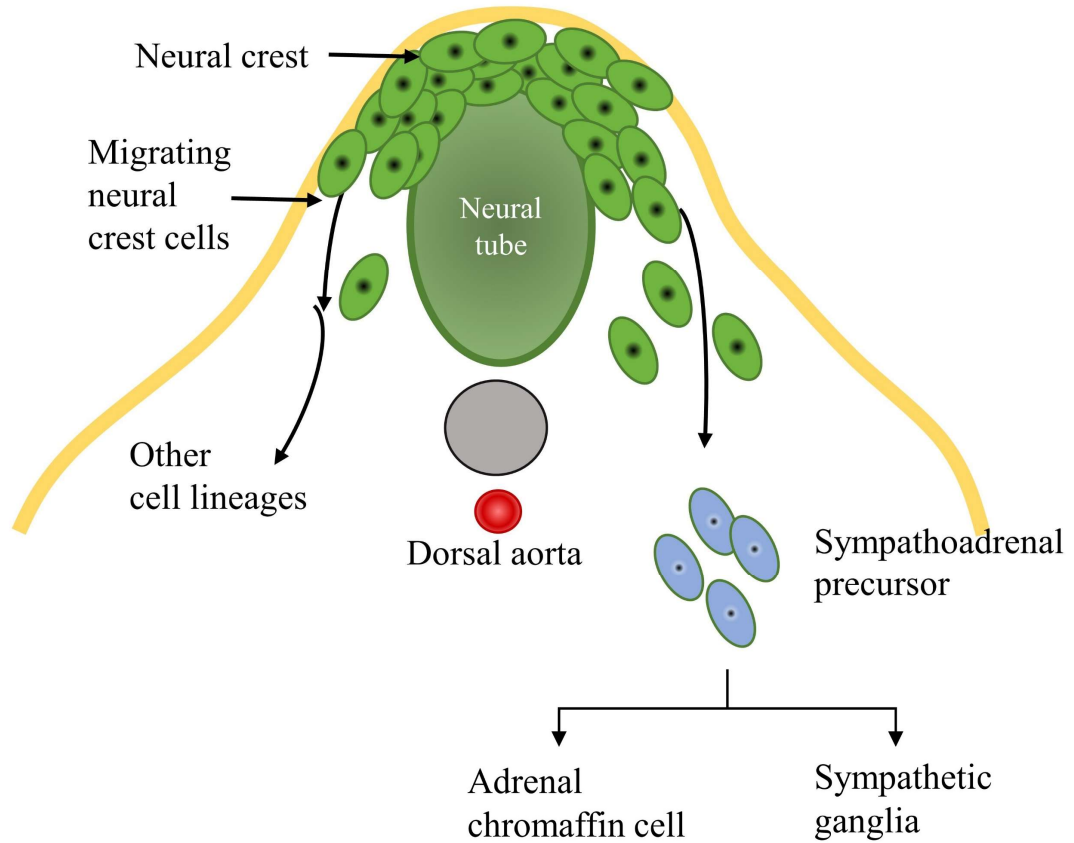


**Figure 1.1** Neural crest cell migration and differentiation to the trunk. A process of epithelial-to-mesenchymal transition allows cells of the neural crest to delaminate and migrate from the neural tube. Through a series of transcriptional and epigenetic signals, neural crest cells migrate to the dorsal aorta and differentiate into sympathoadrenal precursor cells. These further differentiate into cells of the adrenal gland and peripheral nervous system. Aberrations in cell-fate signals can lead to the development of NB along this axis. Figure adapted from Matthay *et al.* 2016 [15].

## 1.2. Clinical staging

Since the 1990's, the International Neuroblastoma Staging System (INSS) has been used to diagnose and classify NB following structural imaging and subsequent surgical intervention. Patients are stratified into stages based principally on the extent of disease dissemination, lymph node involvement and the presence of metastasis [16, 17]. The International Neuroblastoma Risk Group (INRG) Staging System (INRGSS) has been built around the INSS structure to standardise staging preoperatively based on image-

defined risk factors (IDRFs) through implementation of computed tomography (CT) or magnetic resonance imaging (MRI) (Table 1.1) [18]. The stages can be broadly defined as localised tumour with no IDRFs (L1), loco-regional tumour with IDRFs (L2), metastatic disease (M), and confined metastases in children younger than 18 months (MS). A detailed list of IDRFs can be found in the INRG Task Force Report [18]. Supplementary to CT and MRI, either iodine-123 *meta*-iodobenzylguanidine (<sup>123</sup>I-mIBG) scintigraphy or a technetium-99m-diphosphonate (<sup>99m</sup>Tc-MDP) bone scans can assess further the extent of metastasis and bone involvement of the disease; and are therefore recommended for a complete INRGSS categorisation.

Stage	Description
<b>L1</b>	Localized tumour not involving vital structures as defined by the list of image-defined risk factors and confined to one body compartment
<b>L2</b>	Locoregional tumour with presence of one or more image-defined risk factors
<b>M</b>	Distant metastatic disease (except stage MS)
<b>MS</b>	Metastatic disease in children younger than 18 months with metastases confined to skin, liver, and/or bone marrow
<p><b>NOTE. Patients with multifocal primary tumours should be staged according to the greatest extent of disease as defined in the table.</b></p>	

**Table 1.1** International Neuroblastoma Risk Group Staging System. Taken from Monclair *et al.*, 2015 [18].

### 1.3. Neuroblastoma risk groups

The INRG stage is one key indicator of risk for NB patients, which ranges from very low to high-risk disease. Second, patients who are older than 18 months are at greater risk compared to those under 18 months [19-21]. The chances of disease relapse/event-free survival (EFS) and ultimately overall survival (OS) for patients are guided by these risk groups [21]. However, crucial biological prognostic factors need to also be identified for complete risk stratification and treatment planning. Therefore, tumour biopsies and bone marrow aspirates are necessary to assess the biological features of NB. From these sample analyses, *MYCN* amplification is synonymous to a poor prognosis and high-risk disease, with the only exception being of benign or intermediary benign ganglioneuroma / ganglioneuroblastoma stage L1 or L2 disease [22, 23] where the *MYCN* status does not influence risk of the disease outcome (Table 1.2). Other genetic markers include DNA ploidy, chromosome 17q gain, and 1p and 11q loss of heterozygosity (LOH), all of which increase disease risk (Table 1.2) [20, 24-27]. Further, an undifferentiated or poorly differentiated cell population, as assessed by histology, is indicative of high-risk disease owing to the pluripotency and potential heterogeneity of NB's progenitor cell population [6, 28].

Risk of disease is reflected by the 5-year EFS of NB patients. For very low risk patients (around 28 % of cases), EFS is greater than 85 %, low risk (27 % of cases) between 75 % up to 85 %, intermediate risk (9 % of cases) from 50 % to 75 % and high-risk disease (36 % of cases) presenting lower than 50 % EFS [10, 20]. EFS is an important measure for NB risk, not only because of the good OS rates in low risk groups that reduce the power of analyses [20], but also as disease recurrence following primary care contributes to a much worse prognosis — with OS rates of only 20 % [21].

INRG Stage	Age (months)	Histologic Category	Grade of Tumor Differentiation	MYCN	11q Aberration	Ploidy	Pretreatment Risk Group	
L1/L2		GN maturing; GNB intermixed					A Very low	
L1		Any, except GN maturing or GNB intermixed		NA			B Very low	
				Amp			K High	
L2	< 18	Any, except GN maturing or GNB intermixed		NA	No		D Low	
					Yes		G Intermediate	
					No		E Low	
	≥ 18	GNB nodular; neuroblastoma	Differentiating	NA	Yes		H Intermediate	
					Poorly differentiated or undifferentiated	NA		
						Amp		N High
M	< 18			NA		Hyperdiploid	F Low	
	< 12			NA		Diploid	I Intermediate	
	12 to < 18			NA		Diploid	J Intermediate	
	< 18			Amp			O High	
	≥ 18						P High	
MS					No		C Very low	
	< 18			NA	Yes		Q High	
					Amp			R High

**Table 1.2** INRG risk classification by categorisation of INRG stage, age and biological features of NB. GN: ganglioneuroma; GNB: Ganglioneuroblastoma; NA: Non-amplified; Amp: Amplified; blank field = any. Taken from Cohn *et al.* Journal of clinical oncology 2009 [20].

#### 1.4. Current therapeutic strategies for NB

##### 1.4.1. Low–intermediate risk

Patients diagnosed with NB will undergo treatment based on their staging and diagnostic characteristics. Low or intermediate disease cases will principally start with observation (typically for patients < 18 months of age), surgery, chemotherapy and, in exceptional cases, external beam radiation (EBR) therapy. Although surgery is performed to remove the bulk of the tumour in localised primary disease (L1), some lesions are notably difficult to excise due to their localisation near delicate vital organs and structures (e.g. the aorta, vena cava, kidney, liver, and nerve tissue) and require neoadjuvant or adjuvant intervention. Chemotherapy is used either before surgery (neoadjuvant) to shrink the large bulky tumours, or postoperatively (adjuvant), where surgery cannot fully remove the tumour burden.

EBR uses high-energy x-rays (typically 6 MV) to target and kill either unresectable cancer cells or metastatic regions that surgery cannot feasibly target [29, 30]. It is also used when the response to chemotherapy is slow or unsuccessful. As a primary method in local control of disease, EBR can diminish macroscopic lesions following surgery and chemotherapy. Local failure (i.e. relapse of the tumour at the site of EBR) is less than 20 % at 5 years with 20–24 Gy EBR [29].

For patients with MS stage NB (metastatic disease but younger than 18 months), disease observation is often the first step in the treatment pipeline. No active therapies are used since, frequently, a spontaneous tumour regression can occur in this subset of patients without intervention [31]. However, the aforementioned strategies are implemented on patients who are symptomatic, have unfavourable histology or have metastasis to the liver.

### **1.4.2. High-risk disease**

Further to those strategies used in low and intermediate risk disease, patients with high-risk NB (HR-NB) will receive aggressive induction chemotherapy in the form of COJEC (vincristine, carboplatin, etoposide, cyclophosphamide, and cisplatin) [32]. Further, high-dose consolidation chemotherapy consisting of either Busulfan and Melphalan Hydrochloride (BuMel) or Carboplatin, Etoposide Phosphate and Melphalan Hydrochloride (CEM) combinations will be used [33, 34]. Both these regimens are associated with greater survival than COJEC induction chemotherapy alone, although further study is required to optimise the patient benefit between the different BuMel and CEM courses. A recent SIOPEN international phase 3 trial [NCT01704716] comparing the two regimens as to which offered the greatest patient benefit concluded that BuMel provides a better long-term EFS compared to CEM [35], leading to the continued use of BuMel over CEM in Europe. Unfortunately, all high-dose chemotherapy results in

increased off-target side effects, and in particular in the destruction of blood-forming stem-cells (i.e. myeloablation). To reduce the adverse effects, stem-cell rescue is usually carried out aiming to re-establish cell populations. The process consists on first removing the blood-forming stem-cells from the patient and then re-injecting them following the intense line therapy. This enables the use of higher chemotherapy doses, and leads to an improvement in EFS observed, with potential improvements in OS [34, 36-38].

Maintenance therapy (or post-consolidation) is used to mitigate the risk of residual cancer cells growing into a recurrent cancer site. Isotretinoin and immunotherapy using the monoclonal antibodies (mAbs) ch14.18 (Dinutuximab) or ch14.18(CHO) (Dinutuximab-Beta) are implemented in this effect, and are further discussed later. These therapies are used in line with agents aiming to restore the immune system, including interleukin-2 (IL-2) and granulocyte-macrophage colony-stimulating factor (GM-CSF). A summary of the typical therapeutic agents for induction, consolidation and post-consolidation therapies are presented in Figure 1.2.

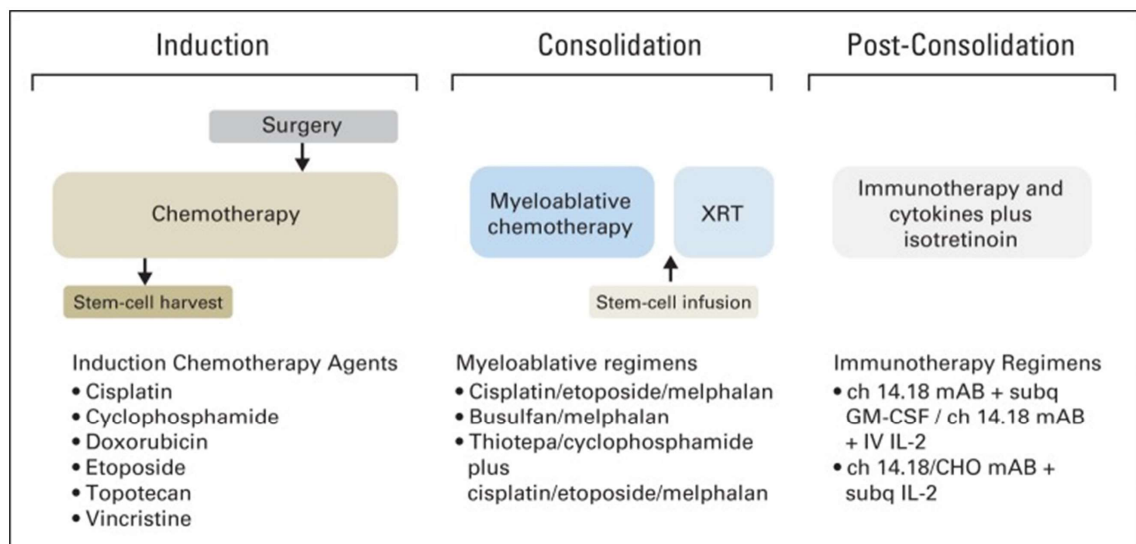


**Figure 1.2** Summary of treatment strategies for newly diagnosed HR-NB. Taken from Pinto *et al.* Journal of clinical oncology 2015 [39].

### 1.4.3. Recurrent and refractory disease

Approximately half of HR-NB patients will relapse following intense multimodal therapy. Relapse is associated with extremely poor survival and limited treatment options. Clinical trials are therefore at the forefront of recurrent and refractory NB treatment. For example, the use of virgin chemotherapy agent combinations such as irinotecan and temozolomide alongside continued Dinutuximab-Beta are studied by the BEACON trial [NCT02308527]. Targeted molecular radiotherapy with <sup>131</sup>I-mIBG in combination with chemotherapy (vincristine and irinotecan) or radiosensitizing agents such as vorinostat are the subject of the N2011-01 trial [NCT02035137]. Two paediatric MATCH Treatment Trial studies [NCT03233204 and NCT03213678] are investigating unique drugs that exploit weaknesses in the cancer such as the DNA damage repair inhibitor olaparib, or the phosphatidylinositol-3-kinase (PI3k)/mammalian target of rapamycin (mTOR) inhibitor samotolisib. Novel therapeutic strategies in NB look to focus on the unique molecular targets that are present in this disease which are discussed next in more detail.

## 1.5. Molecular characteristics of NB

### 1.5.1. The *MYCN* oncogene and MYCN protein

*MYCN* (*V-Myc* Avian Myelocytomatosis Viral Oncogene Neuroblastoma Derived Homologue) is a proto-oncogene discovered in 1983 by Schwab *et al.* [40]. Its amplification is considered one of the most robust genetic markers of high-risk in NB. Approximately 20 % of NB have *MYCN* amplification [20, 41, 42].

*MYCN* is part of the *Myc* family of regulatory and proto-oncogenic genes which includes *c-MYC* (*MYC*) and the lesser characterised *l-MYC*. *c-MYC* expression occurs in most proliferative cells and deregulation is implicated in a variety of adult cancers [43-45]. *MYCN* on the other hand is both spatially and temporally restricted, highlighting the

distinction between the two homologs. Specifically, high *c-MYC* levels are seen during cell division; whereas *MYCN* expression is found in cells undergoing differentiation [46, 47]. Further, in juvenile mice *MYCN* expression is restricted to the kidney, fore- and hind-brain, whereas expression is muted in adult mice [41, 48], supporting *MYCN*'s role primarily in organism development. During periods of rapid cellular expansion (e.g. embryogenesis), high *MYCN* activity is essential to maintain the pluripotency of the cell [49], including cells of the neural crest. Either *MYCN* or *c-MYC* homozygous knock-out is fatal in embryonal development [50, 51], whereas the development of murine models which have a constitutively active *MYCN*, through the tyrosine hydroxylase promoter (Th-*MYCN*), spontaneously produce NB-like paraspinal tumours [52, 53].

*MYCN* amplification is also linked with other genetic abnormalities associated with poor prognosis in NB including 1p LOH and 17q gain [54, 55]. Another driver of NB, anaplastic lymphoma kinase (ALK) is hyper-activated in association with *MYCN* amplification [56], further compounding the poor-prognosis of *MYCN* amplified HR-NB.

The MYC protein family is a member of the basic helix-loop-helix (bHLH) group of transcription factors and includes c-MYC, N-MYC (*MYCN*), and also L-MYC. After dimerising with the myc-associated factor X (MAX), using a conserved HLHZip domain, the \*-MYC protein binds to the canonical DNA E-box promoter motif (CAC(G/A)TG) [57] facilitating the transcription of an array of proteins associated with cell proliferation and apoptosis, metabolism and growth, cell migration, and angiogenesis (Figure 1.3) [41, 58].

The expression and stability of the *MYCN* protein is tightly regulated under normal conditions by extracellular and intracellular stimuli [59, 60]. During mitosis, ubiquitination and subsequent degradation of the protein through phosphorylation by the cyclin-dependent kinase 1 (CDK1)/Cyclin-B complex at serine-62 (S62) and by glycogen

synthase kinase 3 beta (GSK3 $\beta$ ) at threonine-58 (T58) enable the rapid turn-over of MYCN in the cell, and prevents over expansion of the cell population (Figure 1.3) [61, 62]. Conversely, growth factors such as insulin or insulin-like growth factor (IGF-1), acting through the phosphoinositide 3-kinases/protein kinase B (PI3k/Akt) signalling pathways, promote cellular expansion by limiting the degradation of MYCN through inhibition of GSK3 $\beta$  phosphorylation (Figure 1.3) [62].

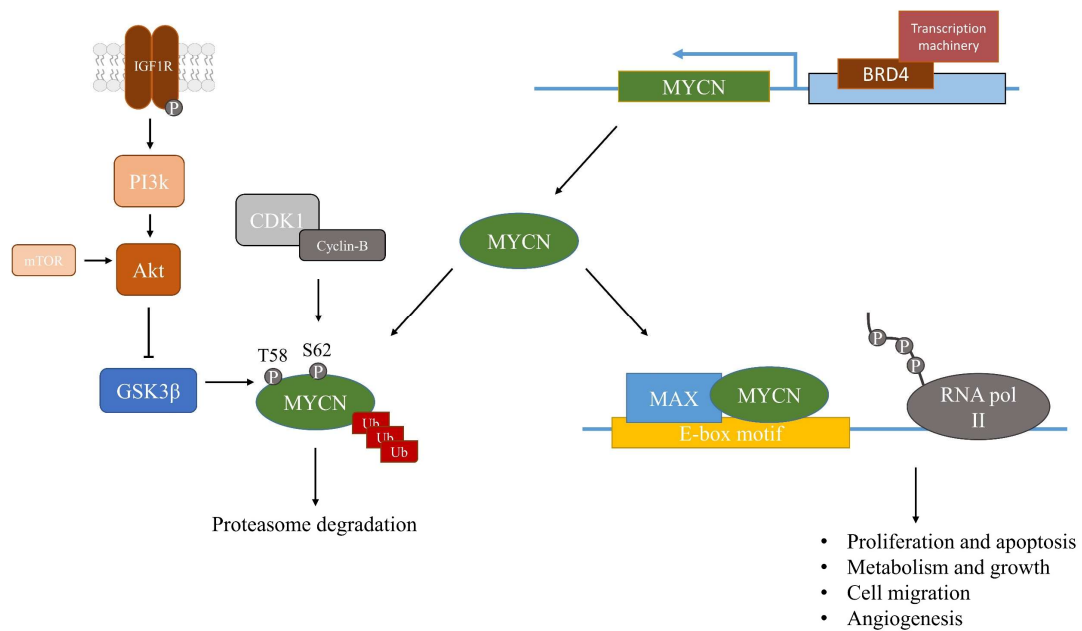


**Figure 1.3** Schematic of *MYCN* transcription and activity. MYCN dimerization with MAX and subsequent binding to the E-box motifs within the DNA structure leads to transcription of many target genes. MYCN is tightly regulated by GSK3 $\beta$  and CDK1/cyclin-B phosphorylation and subsequent degradation. Ub = ubiquitin, RNA pol II = RNA polymerase II.

An increased *MYCN* copy number (>4), and subsequent overexpression of the gene, is correlated to a rise in both MYCN protein expression and activity which has been linked to tumorigenesis and poor clinical outcome for NB patients [42, 63, 64]. Raschella *et al.* further reported that MYCN overexpression did not correlate to the expression level of its classical dimerization partner MAX, suggesting the role of MYCN as the main driver of tumorigenesis, as compared to the basal role of MAX [65]. Further, like c-MYC,

MYCN acts as a global enhancer of transcription by opening up the DNA structure through acetylation of chromatin in NB cells [66].

### 1.5.1.1. Targeting MYCN

The development of targeted agents aiming to interrupt the function of the MYCN protein has been quite challenging. Key issues are the “undruggability” of MYC proteins due to the lack of identified active sites to target as well as their essentiality for normal cellular function. Although not a target for MYCN itself, 13-cis-retinoic acid (isotretinoin; retinoic acid (RA)) has been shown to reduce MYCN expression levels in NB cells through the induction of cell differentiation and is currently the only clinically approved agent in NB that has shown to manipulate MYCN levels [67, 68].

Isotretinoin promotes NB cell differentiation and growth arrest, potentially through the downregulation of oncogenic microRNAs [68-70]. Interestingly, Guglielmi *et al.* demonstrated that RA induced differentiation was dependent on *MYCN* expression, which first increased before dropping off after cellular differentiation [70]. In initial clinical trials, isotretinoin treatment improved the 3-year EFS and was of particular efficacy for the cure of minimal residual disease in a cohort of patients [34].

Isotretinoin has also been shown to inhibit MYC-MAX heterodimerisation potentially through increased MYCN turnover or increased competition with other heterodimers of MAX (e.g. Mad1) [71]. If MYCN overexpression is uninterrupted, the MYC-MAX dimer becomes more promiscuous by binding at the lower affinity, non-canonical E-box motifs (CANNTG) and initiates transcription processes at these sites [66, 72]. The inhibition of the MYC-MAX dimer formation using small molecules is a promising area of research. Inhibitors such as 10058-F4, initially investigated to perturb c-MYC-MAX dimerization, has been shown to affect MYCN-MAX interactions to a similarly potent degree [73, 74].

Alternatively, inhibiting its transcription may help limit *MYCN*'s oncogenic activity. This could be most important in *MYCN* amplified cells, whereby 'normal' transcription leads to abnormally high protein levels. Inhibitors of the bromodomain and extra-terminal motif (BET) have been extensively studied pre-clinically [75]. Molibresib (GSK525762) is currently in clinical trials in adult solid cancer patients, and enrolment has included one patient with NB who saw a stable disease [76]. Birabresib (OTX015) [NCT01587703] and mivebresib (ABBV-075) [NCT02391480] are also under investigation in adult cancer, although all these trials have not yet demonstrated durable responses [76-78]. Preclinical developments in dual targeted agents to both BET and other drivers of *MYCN* transcription, such as ALK, may lead to more efficacious tumour responses [79].

### **1.5.1.2. PI3k/Akt/mTOR pathway and MYCN**

The PI3k/Akt and the mTOR cell signalling pathways are two interconnected networks vital for the maintenance of cell survival, cell proliferation and growth. PI3k/Akt/mTOR signalling is initiated through the activation of either receptor tyrosine kinases (RTKs), or G-protein coupled receptors (GPCRs) by hormones and growth factors. Activated RTKs/GPCRs promote the PI3k-mediated phosphorylation of phosphatidylinositol 4,5-bisphosphate (PIP2) to phosphatidylinositol 3,4,5-trisphosphate (PIP3) resulting in the activation of Akt and the consequent series of cellular growth and expansion signals (Figure 1.4). mTOR is a serine/threonine protein kinase that regulates cell growth, proliferation, survival, protein synthesis, and transcription through its complexes mTORC1 and mTORC2. The complexes work both upstream and downstream of Akt and form a series of feedback loops [80]. Akt activation of mTORC1 leads to further phosphorylation of its substrates p70 ribosomal s6 kinase-1 (S6K) and eukaryotic translation initiation factor 4E-binding protein 1 (4EBP1). Further, Akt is phosphorylated by mTORC2 at serine-473 (p-Akt<sup>S473</sup>) which stimulates further phosphorylation of

threonine-308 (p-Akt<sup>T308</sup>) by phosphoinositide-dependent kinase-1 (PDK1) and leads to full Akt activation.

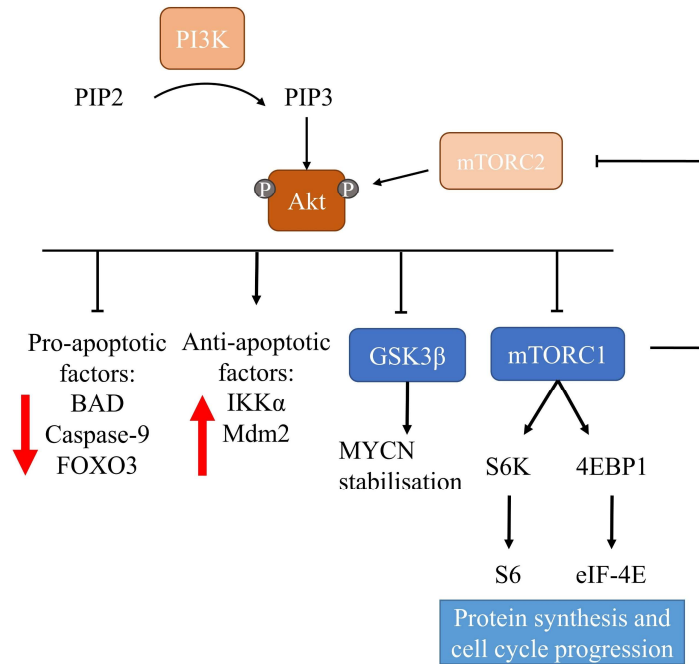


**Figure 1.4** Simplified PI3k/Akt and mTOR pathway interactions resulting in survival and proliferation of the cell.

Altered PI3k/Akt/mTOR activation is a hallmark of HR-NB [81]. The pathway plays a major role in the stabilisation of MYCN [82], and both mTOR and PI3k inhibitors reduce MYCN protein expression in NB [83, 84]. However, the efficacy of single-agent such as temsirolimus (mTOR inhibitor) or perifosine (Akt inhibitor) therapy has been limited [85-88]. There are still continued investigations into PI3k inhibitors, such as copanlisib, in paediatric cancer, including NB [NCT03458728].

Resistance mechanisms may stifle the full potential of PI3k/Akt/mTOR inhibitors. Xu *et al.* reported the use of mTOR inhibitor AZD8055 in NB preclinical studies and showed that after an initial growth arrest, an acquired resistance developed within the tumour through the activation of the mitogen-activated protein kinase kinase (MEK) mitogen-activated protein kinase (ERK) alternative signalling pathway [89]. AZD2014, the

successor to AZD8055, was initially included in the paediatric ESMART clinical trial for solid tumours [NCT02813135] [90-92], but has subsequently been pulled from this investigation owing to lack of efficacy in adult disease [93, 94]. Multifaceted treatment approaches may provide more robust responses compared to targeting individual proteins/pathways alone. mTOR inhibitors in combination with murine double minute 2 (MDM2), or PIM/PI3k/mTOR triplet inhibitors, are being investigated preclinically [95, 96]. The ongoing RIST-rNB-2011 trial [NCT01467986] is looking at the therapeutic benefit of molecular targeted drug combinations consisting of chemotherapy agents with rapamycin (mTOR inhibitor) and the pan-kinase inhibitor dasatinib.

### **1.5.2. Noradrenaline and the noradrenaline transporter**

Noradrenaline (norepinephrine; NE) is a member of the catecholamine family of neurotransmitters and hormones that also includes dopamine and adrenaline (epinephrine). NE is normally produced and secreted from noradrenergic neurons and the adrenal medulla, where it acts as a neurotransmitter and hormone, respectively. The effects of noradrenaline are, in large, stimulatory, and ready the body for increased activity. Stimulation and release of noradrenaline from the adrenal medulla causes the systemic activation of  $\alpha_1$  and  $\beta_{1/2/3}$  G-protein-coupled receptors (GPCRs) on target cells. The results are an increased heart rate, an intensification of glycogenesis and lipolysis, and arterial constriction with consequent rise in blood pressure. Signalling is self-modulated by NE activation of  $\alpha_2$  GPCRs on the presynaptic ganglia that inhibits further NE release, and reuptake of NE into the presynaptic ganglia and adrenal medulla through the noradrenaline transporter (norepinephrine transporter; NET-1).

NET-1 is principally expressed in the neuronal ganglia of sympathetic nervous system and chromaffin cells of the adrenal medulla. The transporter, encoded by the *SLC6A2* gene, is a 12 transmembrane domain (TMDs) protein with both N- and C- termini in the

cytoplasmic site, a large extracellular loop (between TM3 and TM4), and various sites for glycosylation (Figure 1.5). It is a member of a family of sodium- and chloride-dependent transporter proteins involved in neurotransmitter recycling, specifically NE [97]. NET-1 is a key protein in the maintenance and inactivation of noradrenergic signalling [98] and, upon surface expression, NET-1 transports noradrenaline into the cell via a saturable, ATP-dependent active mechanism known as Uptake-1. NE is then stored in synaptic vesicles to be degraded or recirculated depending on demand. NE (and also adrenaline) is metabolised to vanillylmandelic acid (VMA) and ultimately excreted in the urine. Highly sympathetically innervated tissues include the heart, gastrointestinal (GI) tract and, importantly in children, the brown adipose tissue (BAT) [99-102].

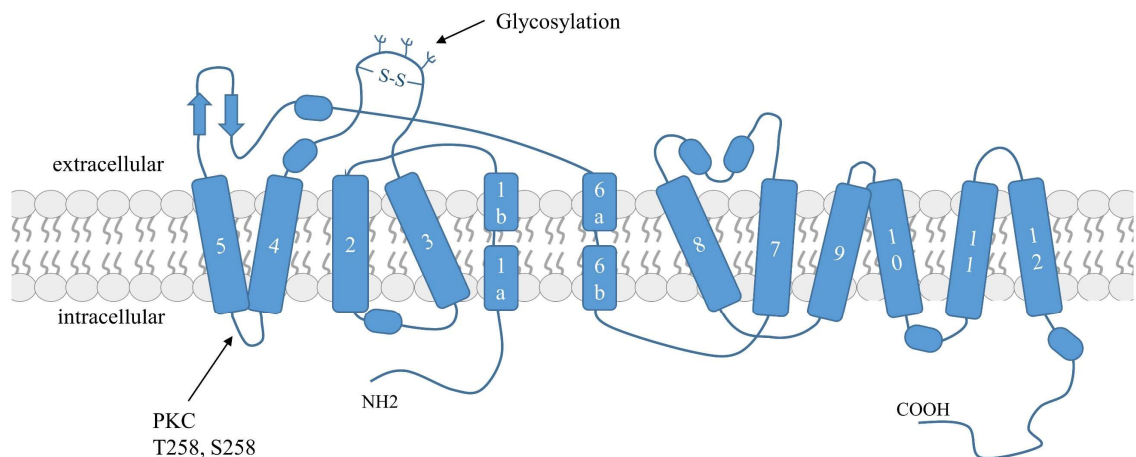


**Figure 1.5** Schematic representation of NET-1 transporter with glycosylation sites between TMD3 and TMD4, and PKC phosphorylation site indicated between TMD4 and TMD5. Figure modified from [103].

Since NB arises from the same cell lineage as the adrenal medulla, an increase in catecholamine metabolite levels in blood and urine is observed in NB patients [104, 105]. Therefore, catecholamine level testing (e.g. increased VMA/HVA ratio in urine, where HVA, or homovanillic acid, is the main metabolite of dopamine) is used to diagnose and monitor NB disease [106]. The sensitivity of this technique is limited, and a low tumour

burden may not be identified. However, Strenger *et al.* reported the potential benefits of measuring urinary catecholamine metabolites to guide treatment strategies, especially between stage 4 and 4s disease [107]. This has been exemplified in more recent clinical analysis, whereby a broader panel of catecholamine metabolites are assessed to provide a greater insight to disease stage and prognosis [108]. One limitation of measuring catecholamine secretions in the diagnosis of NB, is that this technique does not indicate the localisation and dissemination of the disease.

NET-1 is expressed in around 90 % of NBs, yet heterogeneously. The total transporter expression levels can vary due to the degree of promotor activity in the transcription of *SLC6A2* [109]. Further, the surface expression of NET-1 is dynamically regulated by the intracellular levels of sodium ions, which stabilise the transporter, by PKC activity, and on the N-linked-glycosylation of the protein itself [110, 111].

NET-1 has been a therapeutic target for NB treatment for over 30 years using the NE analogue *meta*-iodobenzylguanidine (mIBG).

### **1.5.2.1. NET-1 targeted therapy**

For many years,  $^{131}\text{I}$  (half life = 8.02 days) radiolabelled mIBG ( $^{131}\text{I}$ -mIBG) has been used in the treatment of NB. mIBG is structurally similar to NE (Figure 1.6) and is taken up by NB cells in a NET-1 expression-dependant manner [112-114]. mIBG uptake is further blocked by the NET-1 inhibitors desipramine and imipramine [115, 116], indicating the involvement of the same mechanism of uptake through the transporter as NE (Uptake 1). Upon entering the cell, mIBG is retained in the cytoplasm and mitochondria [117-119].

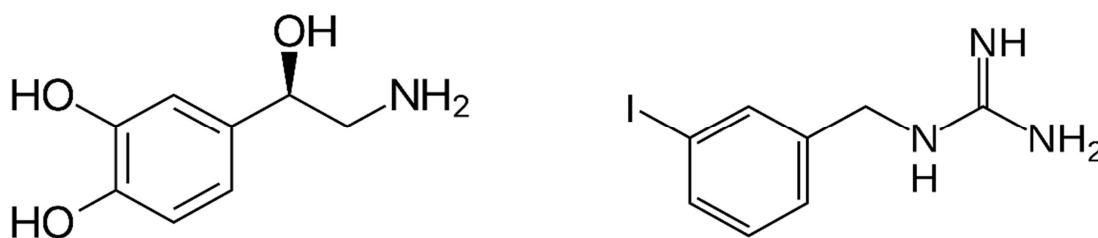


**Figure 1.6** Structure of noradrenaline (left) and mIBG (right).

Radioiodine-labelled mIBG-based therapy has been shown to reduce NB tumour growth in animal models of the disease. Historically, both iodine-125 ( $^{125}\text{I}$ ) and  $^{131}\text{I}$  have been assessed for therapeutic intervention.  $^{125}\text{I}$  (half-life = 59.49 days) decays through electron-capture and emits Auger electrons that have therapeutic potentials [120, 121]. Auger electrons have quite low energy (< 25 keV) which is deposited over short distances in tissues (0.001–20  $\mu\text{m}$ ). This extremely short range yields high linear energy transfer (LET), which makes Augers an attractive for radiation treatment of cancer [122, 123]. However, this is most effective in close proximity to nuclear DNA, rather than multicellular, heterogeneous tumours [121]. On the other hand,  $^{131}\text{I}$  emits higher energy beta particles (mean energy 182 keV; tissue range = 0.54–2.0 mm) that can impose its energy over a larger area compared with  $^{125}\text{I}$  [122, 124]. Although a lower LET is possible, the therapeutic agent  $^{131}\text{I}$ -mIBG has indeed demonstrated a superior tumour ablation in 3D models *in vitro* (i.e. spheroids) and *in vivo* compared with  $^{125}\text{I}$ -mIBG [125, 126], which has led to clinical application of  $^{131}\text{I}$ -mIBG. Alternatively labelled mIBG derivatives using the alpha emitter astatine-211 ( $^{211}\text{At}$ -mABG) has been investigated in targeting NB micro-metastasis and minimal residual disease [126-128]. Alpha and beta particle therapy is discussed in greater detail later (page 28).

$^{131}\text{I}$ -mIBG is frequently used in the relapse setting, when patients have not responded to chemotherapy, radiotherapy and/or surgery. The response rates have improved year on

year, but remain around 50 % in the most recent reports [129-132]. Clinical studies have demonstrated that higher doses of  $^{131}\text{I}$ -mIBG produce more favourable outcomes in NB patients. However, an increase in the whole body absorbed dose results in a parallel rise of haematological toxicities (e.g. thrombocytopenia), which is dose-limiting in  $^{131}\text{I}$ -mIBG therapy [133]. Efforts to improve the  $^{131}\text{I}$ -mIBG efficacy in the tumour are under clinical investigation. Radiotracer uptake into the tumour cell can be enhanced through the use of no-carrier-added (NCA)  $^{131}\text{I}$ -mIBG to increase the radioactive concentration of mIBG entering the target cell [131, 134]. The consequent higher radioactive payload to the NB cells results in amplified damage and cell death. Alternatively, combinatorial therapies using chemotherapeutic drugs (e.g. vincristine, irinotecan, vorinostat) with  $^{131}\text{I}$ -mIBG aim to amplify the benefits of the treatment with the radiotracer by either sensitising the target cells to radiation-induced DNA damage [135-137], or increasing NET-1 expression and function with associated enhanced entrance of the agent in the cell [138, 139]. Further, the use of  $^{131}\text{I}$ -mIBG during the early stages of treatment regimens of HR-NB are being assessed to reduce the prospect of disease relapse [NCT01175356] [NCT03126916] [140-142].

### **1.5.3. GD2**

GD2 is a surface ganglioside expressed exclusively on cells of neural ectoderm origin, which includes the central nervous system (CNS) and peripheral neurones, melanocytes, and NB [143-145]. Gangliosides are glycosphingolipids which are molecules formed by oligosaccharides (generally composed by common monosaccharides such as glucose or galactose) attached to a lipid tail containing the sphingolipid ceramide. For GD2, the oligosaccharide chain glucose-galactose-galactosamine (Glc-Gal-GalNAc) extends from the ceramide tail and further, two sialic acids branch off the galactose molecule (Figure



synthase) transfers a N-acetyl-galactosamine residue to the structure of GM3 and GD3 producing GM2 and GD2, respectively [146] (Figure 1.8).

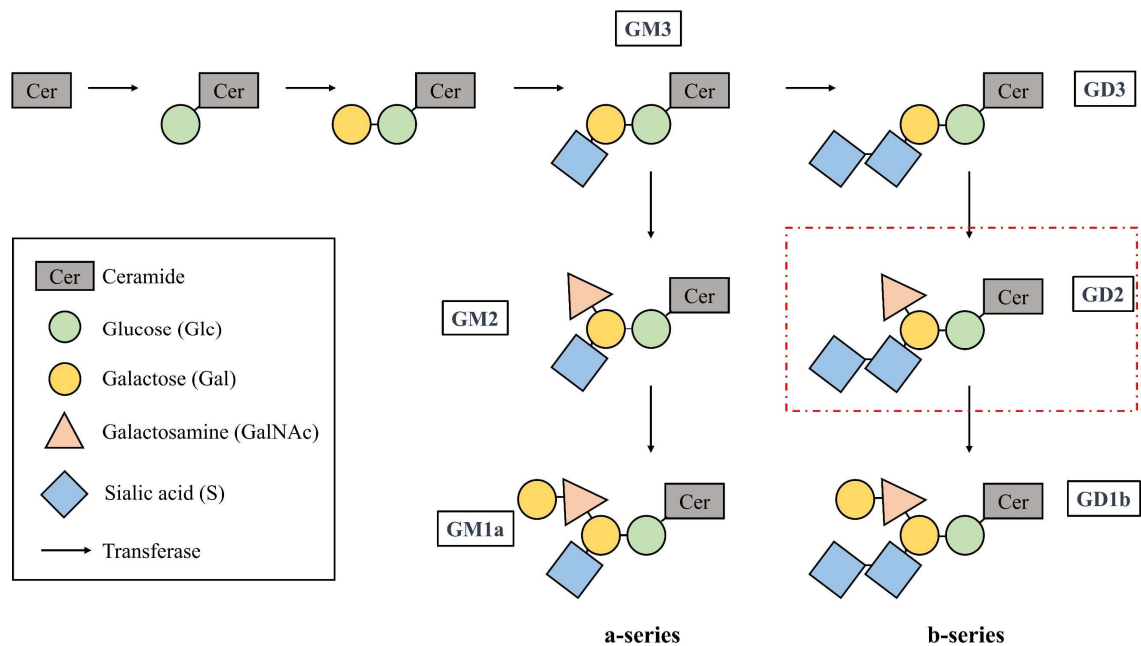


**Figure 1.8** Simplified a- and b-series ganglioside biosynthesis pathway. GD2 is highlighted in the red dotted box.

Ganglioside expression in normal tissue changes dramatically over time. During mouse brain development, the levels of simple gangliosides (GM3/GD3) are initially high. They are replaced by more complex gangliosides (GD1a/GT1b) in the adult brain [148]. Gangliosides have been found to have a role in neuronal maintenance [149, 150], and GD2 is also involved in pain signalling/transduction on peripheral neurones [151]. Further, GD3 and GD2 have been highlighted as stem cell and cancer stem cell markers [144, 152, 153].

In NB, a variety of gangliosides are expressed and high levels of the ‘b-series’ gangliosides (GD3, GD2, GD1b, GT1b, GQ1b) are reported to associate with a comparatively good prognosis [154, 155]. Of note, high levels of GM2/GD2 synthase are reported in NB cells resulting in a GD2 expression of around 5–10 million molecules per cell [145, 156]. Studies have used GD2 as a detection marker of NB in bone marrow

aspirates using either immunocytochemistry or flow cytometry analysis [157, 158]. Detection of circulating free GD2 (as a result of ganglioside shedding) has also been investigated as a measure of tumour burden in NB [159-161].

In NB, GD2 is thought to be involved in the cell interaction with the extra-cellular matrix [162], and also a potential role in immune evasion has been proposed [163, 164]. Additionally, the possible function of GD2 as a modulator and activator of RTK signalling, with consequent activation of c-MET and the PI3k/AKT pathway, has been investigated [165, 166]. GD2 has also been linked to the activation of cell death signals through apoptotic and necrotic mechanisms [167].

### **1.5.3.1. GD2-targeted immunotherapy**

Owing to its high tumour expression and restricted distribution in normal tissue, GD2 targeted immunotherapy is an important treatment option for patients with NB [168]. Classically, monoclonal antibody-based immunotherapy in clinical use is mostly targeting membrane proteins on the cell of interest [169]; anti-GD2 immunotherapy is unique in that the antigen is a carbohydrate. Despite the small size of GD2 (~1.4 kDa) and structural similarities with other gangliosides, monoclonal antibodies (mAbs) selected against GD2 have shown high affinity and extremely selective binding characteristics [170]. Importantly, GD2 immunotherapy has been pivotal in the treatment and survival of patients with NB [171].

In the late 1980s, the murine anti-GD2 mAbs m3F8 (IgG3) and 14.G2a (IgG2A) were developed [172, 173] and showed promising immune-activity through activation of antibody-dependent cell-mediated cytotoxicity (ADCC) and complement derived cytotoxicity (CDC). ADCC occurs when the bound IgG is recognised by and activates Fc $\gamma$  receptor expressing cells, initiating the release of cytotoxic granules that cause subsequent cell lysis [174-176]. Fc $\gamma$  expressing natural killer (NK) cells are thought to be

the main effectors of ADCC [177, 178]. Additionally, CDC is instigated through the recruitment of complement component 1q (C1q) by association with the bound antibody through the classical complement pathway. This process cascades to form membrane attack complexes that permeate the cell and cause cell death [176, 179].

Early promising phase I/II clinical trials using murine GD2 mAbs paved the way for the immunotherapy of NB [172, 180, 181]. However, being xenogeneic (i.e. non-human), these early mAbs triggered the production of human anti-mouse antibodies (HAMA) in the patient [180]. A HAMA response, characterised by an allergic-like reaction, not only can decrease the therapeutic efficacy of the antibody treatment but also can be life-threatening. Further, one major side-effect observed after the administration of m3F8 and 14.G2a was allodynia (pain) thought to be provoked by complement activation on the nociceptive C nerve fibres [180, 182].

The development of chimeric GD2 mAbs, whereby the murine constant region (IgG2A) is substituted with a human IgG1 one, was promoted to alleviate the previously mentioned side-effects [183] and to potentially boost ADCC [184]. The ch14.18 and ch14.18(CHO) mAbs were the first immunotherapy agents to be approved for NB by the FDA and EMA under the name of Dinutuximab and Dinutuximab-Beta, respectively. The principal difference between the two molecules is the method of production: the host cell lines used for the expression of Dinutuximab is SP2/0, while Dinutuximab-Beta is produced in Chinese Hamster Ovary (CHO) cells. This results in a different post-translational glycosylation pattern on the mAbs, and the potential dichotomy of their effector functions [185].

Of note, a reduction in pain and allergic reactions to these mAbs, compared to the murine ones, was observed; however, a residual immunogenicity against the murine portion of the chimeric antibody (HACA or human anti-chimeric antibody response) was still

detected [186, 187]. Nowadays, Dinutuximab-based consolidation therapy is considered standard of care for HR-NB [171] and includes combined granulocyte-macrophage colony-stimulating factor (GM-CSF) and interleukin-2 (IL-2) as booster cytokines [171, 188, 189]. GM-CSF aims to activate antigen processing and the production of further stimulatory cytokines, whereas IL-2 promotes T-cell and NK cell activation. However, IL-2 combinations have also demonstrated increased toxicities that may be detrimental to any EFS benefits observed in NB patients [190].

In their third generation, humanized anti-GD2 mAbs have been developed including hu3F8 and hu14.18K322A antibodies. In clinical trials, both these agents could be administered in a higher dosage compared to their murine and chimeric counterparts, which could bolster the therapeutic effect of the immunotherapy [191, 192]. Higher doses could be administered most probably as consequence of reduced mAb immunogenicity [193]. Hu14.18K322A therapy also results in less pain compared with ch14.18 treatment [194]. The K322A mutation sought to reduce CDC, which is thought to contribute to pain experienced in patients [195, 196], however analysis of complement levels in patients undergoing Hu14.18K322A treatment do not fully support this hypothesis [194]. Lower immunogenicity and pain enable the administration of higher mAb doses that may result in greater EFS and fewer relapses of disease.

Recently, therapies combining anti-GD2 mAbs with <sup>131</sup>I-mIBG [NCT02914405] [NCT03332667] are being investigated to improve outcome compared to monotherapy alone in refractory or relapsed NB. Alternatively, <sup>131</sup>I-radiolabelled anti-GD2 mAbs (i.e. <sup>131</sup>I-3F8) have been tested to specifically deliver the radioactive payload to the NB target cells, thus enhancing cell damage [197].

One major clinical interest is in adoptive immunotherapy, whereby harvested immune cells are injected into the patient. Firstly, as NK cell activation is a key driver of ADCC

and of tumour response to mAb therapy, studies are implementing adoptive transfer of haploidentical NK cells to enhance the immune response during anti-GD2 mAb therapy and subsequently increase NB cells killing [NCT03242603] [NCT02650648] [198]. Further, chimeric antigen receptor T-cell (CAR T-cell) therapy [199-201] using engineered T-cells that are targeted to the GD2 antigen are under many clinical trials including but not limited to: 2<sup>nd</sup> generation CART [NCT02761915], 3<sup>rd</sup> Generation CAR-T with IL-15+iCaspase9 [NCT03721068], and 4<sup>th</sup> Generation CAR-T [NCT02765243]. To date, however, CAR T-cell therapy has shown mixed clinical responses in NB [200, 202]. Beyond the safety of these new CAR-T cell therapy trials, both reducing CAR T-cell exhaustion [203] and the suppressive effects of regulatory T-cell [204] or myeloid-derived suppressor cell (MDSC) populations may be important to enhance the efficacy of GD2 targeted treatments [205].

### **1.6. Imaging neuroblastoma**

The standardised staging system, INRGSS, is based exclusively on clinical imaging modalities to characterise NB [18]. It firstly employs anatomical imaging techniques, such as CT and MRI, to confirm the spread and infiltration of disease and the encasement or compression of vital structures such as vasculature (aorta/vena cava) and the trachea, amongst other IDRFs. Nuclear imaging modalities are then used to further assess the extent of metastasis and bone involvement of the disease.

#### **1.6.1. Anatomical imaging**

CT imaging primarily refers to “X-ray CT” in which the radiation is delivered to the body and is attenuated by the material it passes through [206]. The degree of X-ray attenuation depends on the density of the material through which it travels. A tissue’s X-ray attenuating ability is expressed by its attenuation coefficient. The higher the attenuation coefficient (higher the tissue density), the lower the number of photons that reach the

detector when passing through tissue. Image contrast is achieved between tissues where high density materials (e.g. bone) appear white and lower density material (e.g. fat) appears black [207]. The X-ray source and mutual solid state detectors are rotated through one complete revolution around the patient to produce a series of 2D projections acquired at different angles. Appropriate reconstruction of the data produces a 3D image of the scanned object.

MRI technology relies on the differences in radio wave absorption and emission in tissues when exposed to a strong magnetic field created by the MRI magnet (0.5–3 Tesla). This is observed due to the nuclear magnetic resonance (NMR) phenomena, whereby atomic nuclei (namely  $^1\text{H}$ , but also  $^{13}\text{C}$ ,  $^{19}\text{F}$ ,  $^{31}\text{P}$ ) possess a ‘spin’ that makes them dipolar magnets [208, 209]. During imaging, the polar  $^1\text{H}$  atoms align with the external magnetic field ( $B_0$ ), then a predetermined radio frequency (RF) pulse is delivered and absorbed by the  $^1\text{H}$  atom causing them to flip along the RF axis ( $B_1$ ). After the pulse is turned off, the  $^1\text{H}$  atoms realign with  $B_0$  and their stored energy is released. This is captured by a coil surrounding the patient which transforms the radio wave into an electrical signal and ultimately into the MR image. Depending on the  $^1\text{H}$  content (analogous mostly to the amount of  $\text{H}_2\text{O}$ ) of a tissue or tissue structure, the contrast is generated.

The foremost negative aspect of CT imaging is associated to the use of ionising radiations. The energy of CT X-rays (20–150 keV) can disrupt the electron charge of nearby particles, thus ionising them and causing radiolysis (breakage of chemical bonds such as DNA breakage). Conversely, MRI does not emit ionising radiations and provides greater detail of soft tissue structure owing to a better spatial resolution than CT (10–100  $\mu\text{m}$  in MRI vs 50–200  $\mu\text{m}$  for CT), but it is more costly and the scanning times are longer than CT (in the region of 45 min for MRI vs 5 min for CT).

Nowadays, a CT scan is a necessary adjunct in EBR treatment planning to accurately map tissue electron densities and estimate attenuation coefficients for the delivered radiotherapy [210, 211]. Some methodologies are being investigated for MRI based treatment planning, though they are yet to be integrated into current clinical setups [212, 213].

Standard CT and MRI scans provide good anatomical information of the body and can highlight the sites of tumour masses. However, they cannot by themselves provide details on the molecular make-up of the tumour. Molecular imaging (MI) techniques, on the other hand, involve imaging cellular biochemical processes with a high degree of sensitivity, specificity, and signal-to-background [214]. Targeting moieties are labelled with a variety of detectable agents to visualise these processes *in vivo* [215]. Although targeted contrast agents are being investigated for use in MRI and CT, the majority of MI agents are created for nuclear imaging [216-218].

### **1.6.2. Nuclear imaging**

Nuclear imaging is a branch of MI comprising three principle techniques: Planar scintigraphy, single photon emission computed tomography (SPECT) and positron emission tomography (PET) [216]. These imaging systems all use molecules labelled with radioactive isotopes to examine organ/tissue function and structure. This so called ‘radiotracer’ is introduced into the body and the path of the probe can be traced *in situ* by scanning for the emissions of radioactive decay. Before focussing on the radiotracers used for imaging NB, the details of the physics, technologies and implementation of nuclear medicine in oncology are described in the following sections.

#### **1.6.2.1. Radiation and radioactive decay**

Radiation is generally defined as the energy emitted by unstable elements in the form of either subatomic particles or electromagnetic waves. Particle radiation is fast moving

subatomic particles that possess both energy and mass and most notably includes alpha and beta radiations. Electromagnetic radiation possess both particle-like and wave-like characteristics and its basic properties are: frequency, wavelength and energy. The electromagnetic spectrum ranges from the high frequency (short wavelength) waves including gamma and X-rays, and UV light, to the low frequency (long wavelength) infrared light, microwaves and radiowaves (Figure 1.9). The energy of a single electromagnetic photon ( $E$ ) is proportional to the photon's frequency ( $\nu$ ) and is a multiple of the Plank's constant,  $h$  ( $6.62607015 \times 10^{-34}$  J·s or  $4.1357 \times 10^{-15}$  eV·s) [219] according to the following equation:  $E = h\nu$ .

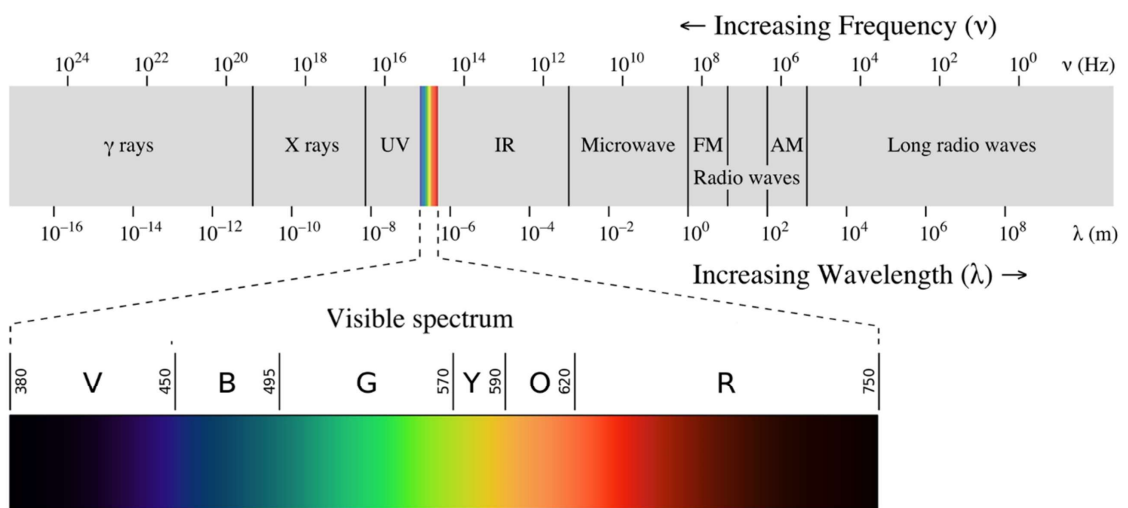


**Figure 1.9** The electromagnetic spectrum.

Radioactive decay is the physical process in which an unstable nucleus of a radioactive atom releases energy and matter to reach a more stable state. As seen in Figure 1.10, the likelihood that an element will undergo radioactive decay is dependent on its relative neutron ( $N$ ) mass and proton ( $Z$ ) mass, with stable nuclei indicated in black. The graph indicates the stability of the nuclei and the most prominent decay for a single nucleus depending on  $N/Z$  ratio. For example, the nuclei located above the black area have more neutrons (i.e. their  $N/Z$  is too large) than the nuclei in the black line, therefore they will

lose neutrons by radioactive decay to stabilise (beta decay). However, for heavier nuclei, the radioactive decay to a stable state often occurs in a complex decay chains and is a mix of alpha, beta and gamma (photon) emissions.

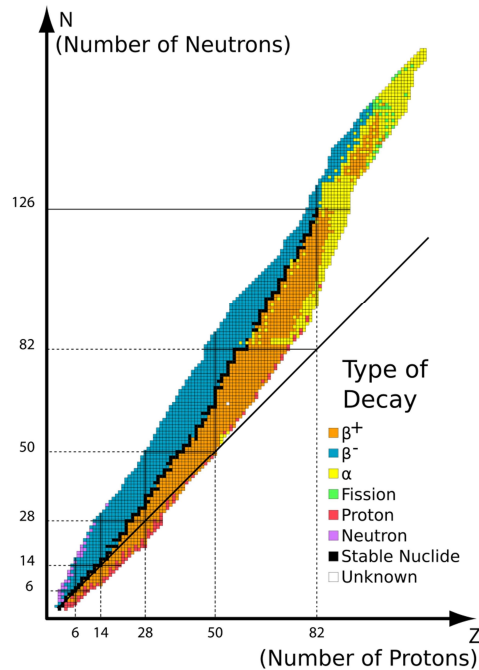


**Figure 1.10** Nuclear stability and types of radioactive decay. Stable nuclei with atomic numbers up to about 20 have an  $N/Z = 1$  (black solid line). The later deviation from the line on the band of stability is a consequence of the non-unity N-to-Z ratio required for the total stability of nuclei, meaning that more neutrons are needed to stabilise the repulsive forces from fewer protons within a nucleus (i.e.  $N > Z$ ). The band of stability can be used to determine the occurrence of alpha, beta decay, positron emission or electron capture.

#### 1.6.2.1.1. Alpha decay

Alpha decay occurs when an alpha ( $\alpha$ ) particle, consisting of two protons and two neutrons (i.e. a helium nucleus), is emitted from the radionuclide. This is a phenomenon seen primarily in heavier radionuclides (yellow nuclei in Figure 1.10) such as astatine-211 ( $^{211}\text{At}$ ) or radium-223 ( $^{223}\text{Ra}$ ). Alpha decay reduces the atomic mass of the parent nucleus by four and the atomic number ( $Z - 2$ ) by two.

The large size of the  $\alpha$ -particles means that this type of radiation travels very short distances (e.g. 10 to 18 cm in air) before depositing its energy on to matter. Alpha-particles have a very low penetration power and can be stopped by an ordinary sheet of paper or even by the outer layer of dead skin. For these reasons, this kind of particles have one of the highest ionising power (high linear energy transfer (LET)) and a great ability to damage tissue. For imaging, alpha-cameras exist but can only be used to visualise radionuclide distribution in *ex vivo* tissue slices [220], therefore alpha decay is not directly imaged in medicine but the application of the ionising power of  $\alpha$ -emitting nuclides in targeted alpha therapy (TAT) is rapidly developing [221, 222].

$^{223}\text{Ra}$  dichloride, an alpha emitting radiopharmaceutical that specifically targets bone lesions, is currently the only approved alpha therapy agent and is used for the treatment of metastatic castration-resistant prostate cancer with symptomatic bone metastases [223, 224]. Therapies based on other alpha emitters, such as  $^{211}\text{At}$  [NCT03128034], and actinium-225 ( $^{225}\text{Ac}$ ) [NCT03276572] [NCT04225910] [NCT03441048] are under clinical investigation.  $^{211}\text{At}$ -mABG (*meta*-astatobenzylguanidine) has been shown to induce short range cytotoxicity in NB, useful for the treatment of micro-metastases and in minimal residual disease (MRD) [126, 225]. However, the use of TAT in solid tumours such as NB is still yet to be realised.

Radionuclide	Half-Life	$E_{\text{mean}}$ (MeV)	$R_{\text{mean}}$ ( $\mu\text{m}$ )
Astatine-211	7.2 h	6.79	60
Radium-223	11.4 d	5.64	45
Actinium-225	10.0 d	6.83	61

**Table 1.3** Examples of alpha emitting radionuclides used in nuclear medicine.  $E$  = energy,  $R$  = range in tissue.

#### 1.6.2.1.2. Beta decay

In beta decay, the unstable nucleus emits either an electron ( $\beta^-$ ) or a positron ( $\beta^+$ ).

During the decay of a neutron-rich nuclide (blue nuclei in Figure 1.10) such as iodine-131 ( $^{131}\text{I}$ ), yttrium-90 ( $^{90}\text{Y}$ ) and lutetium-177 ( $^{177}\text{Lu}$ ), one neutron converts into a proton releasing an electron ( $\beta^-$ ) alongside an anti-neutrino ( $-\nu$ ). The daughter isotope has an unchanged atomic mass and a  $Z$  increased by one ( $Z + 1$ ) compared to the parent element. The smaller size of  $\beta^-$  compared to  $\alpha$  particles gives them a greater penetration power and they are stopped by a few millimetres of sheet aluminium.  $\beta$  particles also have much less ionizing power than  $\alpha$ , however, they still interact and damage matter and are widely used in radionuclide therapy.

$\beta^-$  emitters used as targeted radiotherapeutics include  $^{177}\text{Lu}$ -PSMA for prostate cancer [226],  $\text{Na}^{131}\text{I}$  for the treatment of hyperthyroidism and thyroid cancer [227] as well as  $^{131}\text{I}$ -mIBG for NB [228]. The energy of the  $\beta^-$  particle dictates the range and degree of damage that can be induced by the radionuclide [229]. Therefore, comparisons between different radio-conjugates such as  $^{177}\text{Lu}$ - and  $^{90}\text{Y}$ -DOTATOC (for somatostatin receptor expressing neuroendocrine tumours) are being investigated to determine the therapeutic advantages in different disease settings [230-233].

Radionuclide	Half-Life	$E_{\text{mean}}$ (MeV)	$E_{\text{max}}$ (MeV)	$R_{\text{mean}}$ (mm)	$R_{\text{max}}$ (mm)
Yttrium-90	64.1 h	0.933	2.284	2.4	11.3
Iodine-131	8.0 d	0.182	0.807	0.4	2.3
Lutetium-177	6.7 d	0.133	0.497	0.25	1.8

**Table 1.4** Examples of beta minus emitting radionuclides commonly used in nuclear medicine.  $E$  = energy,  $R$  = tissue range.

In a proton-rich nucleus (orange nuclei in Figure 1.10), such as fluorine-18 ( $^{18}\text{F}$ ), gallium-68 ( $^{68}\text{Ga}$ ), and zirconium-89 ( $^{89}\text{Zr}$ ), to reach stability, one proton converts into a neutron emitting a positron ( $\beta^+$ ) alongside a neutrino ( $\nu$ ). The daughter element has an unchanged atomic mass and a  $Z$  decreased by one ( $Z - 1$ ) compared to the parent element. Like  $\beta^-$  particles, high energy positrons are ionising, however, after losing the majority of its energy the positron can collide with an electron (electron-positron annihilation) with the consequent emission of two 511 keV photons with opposite directions. Therefore, positron emitting nuclides are used for nuclear PET imaging.

$^{18}\text{F}$ -fluoro-deoxyglucose (FDG), a radiolabelled glucose analogue, is the most common PET imaging tool in oncology owing to the over-expression of GLUT1 glucose transporters in many cancer types and its robust historical data [234, 235]. Other PET imaging agents are targeted to specific markers aiming to elucidate patient specific tumour characteristics. These include agents such as  $^{89}\text{Zr}$ -labelled antibodies like  $^{89}\text{Zr}$ -cetuximab [236] and  $^{89}\text{Zr}$ -atezolizumab [NCT04222426], or  $^{68}\text{Ga}$ -labelled peptides like  $^{68}\text{Ga}$ -DOTATOC [237] and  $^{68}\text{Ga}$ -PSMA [NCT03689582], to name but a few examples.

Radionuclide	Half-Life	$E_{\text{mean}}$ (MeV)	$E_{\text{max}}$ (MeV)	$R_{\text{mean}}$ (mm)	$R_{\text{max}}$ (mm)	% $\beta^+$ emission
Fluorine-18	109.7 min	0.250	0.634	0.6	2.4	96.7
Gallium-68	67.8 min	0.836	1.899	3.2	9.2	89.1
Zirconium-89	3.3 d	0.396	0.902	1.3	3.8	22.8

**Table 1.5** Examples of positron emitting radionuclides commonly used in nuclear medicine.  $E$  = energy,  $R$  = tissue range.

Electron capture (EC;  $\epsilon$ ) is another form of beta decay, whereby an electron from an inner orbital of the atom combines with a proton to be converted into a neutron (with the release of a neutrino). The daughter element has an unchanged atomic mass and a  $Z$  decreased by one ( $Z - 1$ ) compared to the parent element. If the daughter element is in an excited energy state, they will release gamma radiations during the transition to the stable ground state.

### 1.6.2.1.3. Gamma emission

During gamma emission ( $\gamma$ ), one or more gamma rays (or photons) of varying, yet discrete energies radiate from the unstable nucleus. Since the nucleus emits only energy to become stable, the daughter element has the same  $N$  and  $Z$  as the parent element but a lower energy status (isomeric transition). Gamma rays are short wave electromagnetic emissions with a high penetration power which enforce the use of shielding made from dense materials, such as lead or concrete, to block their path. Gamma rays are ionising; however, as they penetrate relatively unencumbered through the body, the ionising power

of photons is much weaker than alpha and beta particles. Owing to these characteristics, gamma ray emitters are widely used for diagnostic imaging purposes in nuclear medicine.

Technetium-99m ( $^{99m}\text{Tc}$ ) is the backbone of nuclear medicine, with around 80 % of its diagnostic imaging procedures using this isotope [238, 239].  $^{99m}\text{Tc}$  is the product of the beta decay of molybdenum-99 ( $^{99}\text{Mo}$ ) and undergoes isometric transition releasing 140 keV  $\gamma$ -emissions (89 % abundance). Additionally, indium-111 ( $^{111}\text{In}$ ) and iodine-123 ( $^{123}\text{I}$ ) are used for planar scintigraphy and SPECT imaging. Although primarily employed for its  $\beta^-$  emitting properties,  $^{131}\text{I}$  also produces photons that can be detected for nuclear imaging which can be advantageous in monitoring therapeutic intervention.

Radionuclide	Half-life	Principal $\gamma$ energy (keV)	% principal $\gamma$
Technetium-99m	6.0 h	140	89.1
Indium-111	67.2 h	171	90.2
		245	94.0
Iodine-123	13.2 h	159	83.3
Iodine-131	8.0 d	364	81.7

**Table 1.6** Examples of gamma-emitting radionuclides commonly used in nuclear medicine.

### 1.6.2.2. Nuclear imaging modalities

Planar scintigraphy is the most basic of the nuclear imaging techniques. It images the distribution of the gamma emitting material (e.g.  $^{99m}\text{Tc}$ ,  $^{111}\text{In}$ ) in the body using a gamma camera placed above the lying patient. A gamma camera consists of a collimator, a scintillation crystal (predominantly thallium-doped sodium iodide NaI(Tl)) and

photomultiplier tubes. These allow for the co-ordination of gamma emissions from the patient, conversion of the photon to a visible light signal, and propagation of the signal, respectively (Figure 1.11). Planar scintigraphy is relatively quick and cheap compared to other nuclear imaging techniques, but produces only two-dimensional (2D) images. As a consequence, the signal from above or below the target of interest impedes contrast and the accurate quantification of the target-associated radioactivity.

On the other hand, SPECT produces three-dimensional (3D) images through rotation of the gamma-camera around the lying patient; providing high detection sensitivity and diagnostic accuracy [240, 241]. The same radiotracers can be used for both planar scintigraphy and SPECT. The 3D SPECT images can also be co-registered with anatomical imaging techniques (i.e. CT) to gain precise disease localisation [242]. This is important for the identification of lesions that are either small or near to radiotracer-avid normal tissues/organs [243].

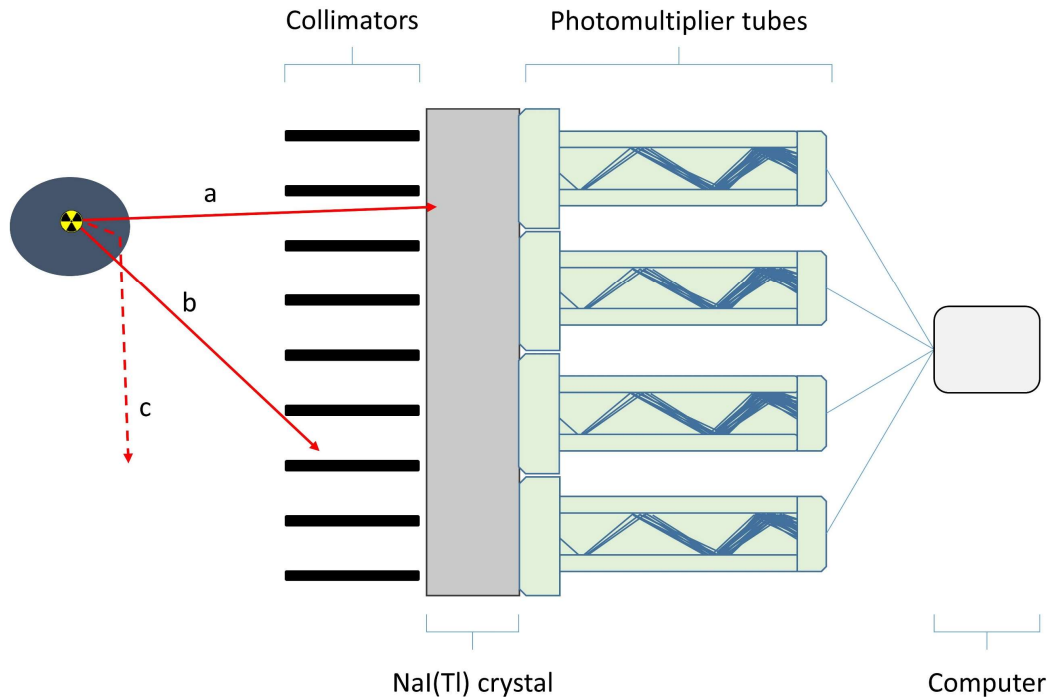


**Figure 1.11** Schematic of scintigraphy and SPECT acquisition from the decay of a gamma emitting radionuclide. Photons are released from the radioactive source whereby the collimator allows for the detection of photons that are ejected perpendicular to the camera (a) and blocks those which are ejected at too great an angle (b). The thallium-doped NaI scintillation crystal converts the photon into a light signal that is propagated through photomultiplier tubes adjoining the crystal. The light signal is ultimately converted to an electronic signal that is fed to a computer for data acquisition and reconstruction. Photons ejected from the source may also scatter (c), and would not be captured by the gamma camera.

PET imaging also produces 3D images that can be co-registered either with CT, or, more recently, MRI acquisitions [244]. During the decay of PET radionuclides (e.g.  $^{18}\text{F}$ ,  $^{68}\text{Ga}$ ), the released positron travels a certain distance before annihilating with a nearby electron (Figure 1.12-i). That distance, known as the positron range, depends on the particle kinetic energy and on the radionuclide that is decaying. The annihilation event causes the production of two photons with same energy (511 keV) and near opposite trajectories (Figure 1.12-i) which are recorded in coincidence by the solid-state scintillation detectors that surround the patient (Figure 1.12-ii). Differently from SPECT, PET scanners do not

need collimators as the co-ordination of the signal is calculated by a line of response (LOR) between the photon detection (Figure 1.12-i). Also, the relatively low density NaI(Tl) crystal used in SPECT has poor stopping power, low efficiency, for the 511 keV photons [245]. Therefore, higher density cerium-doped lutetium oxyorthosilicate (LSO) or lutetium yttrium oxyorthosilicate (LYSO) are the scintillation crystals most widely used in PET scanners [246]. Further, LSO and LYSO crystals have a shorter decay-time than NaI(Tl) (40–42 ns versus 230 ns, respectively) which reduces the ‘dead-time’ of the crystal and improves photon count rate [247]. A short decay time also shortens the detection gate and reduces artefacts and noise [246].

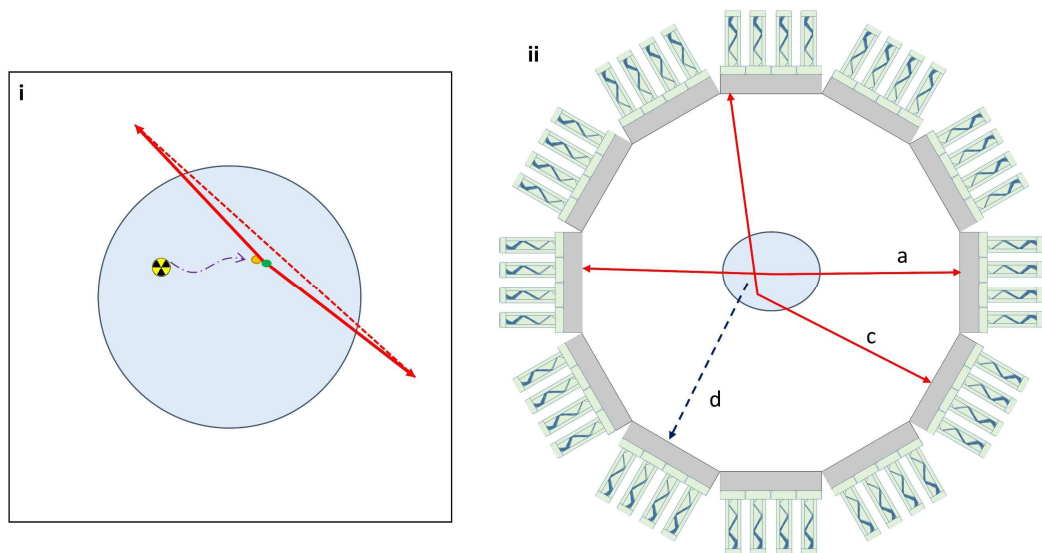


**Figure 1.12** Schematic of positron emission and PET acquisition. i) The positron travels through space (purple arrow) from its radioactive source before annihilating with a nearby electron. Upon annihilation, there is a release of two photons in near opposite direction (red arrows). A LOR (red dotted line) is generated from the slight deviation from  $180^\circ$ . ii) For PET acquisitions, solid state detectors surround the object to be imaged. The detection of events in coincidence allows for determination of the radioactive source location. A true coincidence is depicted in (a), but photon scatter (c) can occur, causing incorrect calculations of the LOR. Radionuclides can also emit prompt gammas (photons not produced by positron annihilation) that are detected by the solid state detectors (d).

The system sensitivity, indicated as photon counts per unit radioactivity (cps/MBq), of PET is nearly 100 times that of SPECT as a result of the detection of events in coincidence and the faster decay time crystals used in scintillation detectors in PET scanners [248-250]. This in turn leads to greater image resolution, lower noise, and quicker acquisition times compared to SPECT. However, the innate positron range of PET radionuclides reduces the maximum resolution possible for each radionuclide. Higher energy positrons are characterised with higher positron ranges (Table 1.7), and lower resolution. Further, the 511 keV photons are not emitted exactly 180° from one another (non-collinearity) which therefore affects the image resolution. Although SPECT does not possess this same limitation, the modernisation of SPECT infrastructure is needed to improve absolute image quality currently in the clinical setting [250, 251].

Because of the above mentioned characteristics, quantifying the amount of activity accumulated within the target of interest requires longer image acquisition and more computational input in SPECT compared to PET. Although significant advancements in SPECT quantification have been recently achieved, the standardisation of protocols is still required [252]. Further, owing to the mechanical limitations of clinical SPECT equipment, quantitation of small lesions is still difficult. For these reasons, I have focussed on the characteristics of PET radionuclides in the following sections.

### **1.6.2.3. Characteristics of PET radionuclides**

The selection criteria of positron emitting radionuclides for MI studies should be based on their chemical and physical properties (such as half-life, decay mode, positron energy) together with their production and availability.

Based on their chemical characteristics, PET radionuclides can be grouped into the following four main groups: Organic elements (e.g.  $^{11}\text{C}$ ,  $^{13}\text{N}$ ,  $^{15}\text{O}$ ); halogens (e.g.  $^{18}\text{F}$ ,  $^{124}\text{I}$ ); metals (e.g.  $^{68}\text{Ga}$ ); and transition metals (e.g.  $^{89}\text{Zr}$ ,  $^{64}\text{Cu}$ ) [253]. The choice

of radionuclide may first be precluded by the ability to perform the appropriate radiochemistry. For example, organic elements and halogens may be directly incorporated into the tracer, whereas metals and transition metals require the use of a chelator to attach the nuclide to the targeting moiety [254]. The chemistry ultimately needs to produce a high yield of the radiotracer with a high radiochemical purity (RCP), be stable during production and during the whole investigation period, and not reduce or impede the specificity of the targeting moiety [254].

One of the main physical characteristics of a radionuclide, the half-life, indicates the amount of time needed for one-half of the radioactive nuclei in the sample to decay. It is an important property to consider during the design of a radioactive probe: the physical half-life of the element should be compatible with the biological half-life of the carrier molecules. For example, radioactive elements with short physical half-life such as  $^{11}\text{C}$ ,  $^{18}\text{F}$ ,  $^{68}\text{Ga}$  are suitable for the radiolabelling of small molecules and peptides that have fast peak tissue concentrations into the target of interest (e.g.  $^{18}\text{F}$ -FDG = ~30 min to 2 h), and are equally rapidly cleared from the body. With a biological half-life of 3–20 days and slow pharmacodynamics, larger molecules such as monoclonal antibodies require long lived radioisotopes such as  $^{89}\text{Zr}$  to achieve adequate images [253]. The half-life of common radioisotopes is listed in Table 1.7.

Isotope	Half-life	Branching ( $\beta^+$ ) as %	$E_{\max}$ (MeV)	$E_{\text{mean}}$ (MeV)	$R_{\max}$ (mm)	$R_{\text{mean}}$ (mm)
$^{11}\text{C}$	20.4 min	99.8	0.960	0.386	4.2	1.2
$^{13}\text{N}$	10.0 min	99.8	1.199	0.492	5.5	1.8
$^{15}\text{O}$	2 min	99.9	1.732	0.735	8.4	3.0
$^{18}\text{F}$	110 min	96.9	0.634	0.250	2.4	0.6
$^{64}\text{Cu}$	12.7 h	17.5	0.653	0.278	2.5	0.7
$^{68}\text{Ga}$	67.8 min	87.7, 1.2	1.899, 0.821	0.836	9.2	3.5
$^{89}\text{Zr}$	78.4 h	22.7	0.902	0.396	3.8	1.3
$^{124}\text{I}$	100.2 h	11.7, 10.8	1.535, 2.138	0.975, 0.687	10.0, 7.1	4.4, 2.8

**Table 1.7** Common PET radioisotopes.  $E$  = energy,  $R$  = positron range in tissue. From [255].

Ideally, an unstable nucleus would transform into a stable daughter product after just one type of decay event. In reality, the event can be more complex. All the transitions occurring during the decay of a radionuclide can be graphically represented in a diagram called decay scheme. The decay schema for  $^{18}\text{F}$  and  $^{124}\text{I}$  are shown in Figure 1.13, whereby the vertical position displays the elements, their energy levels, and transition energy, with the arrow indicating the direction of the decay. The X-axis is indicative of the atomic (proton) number.

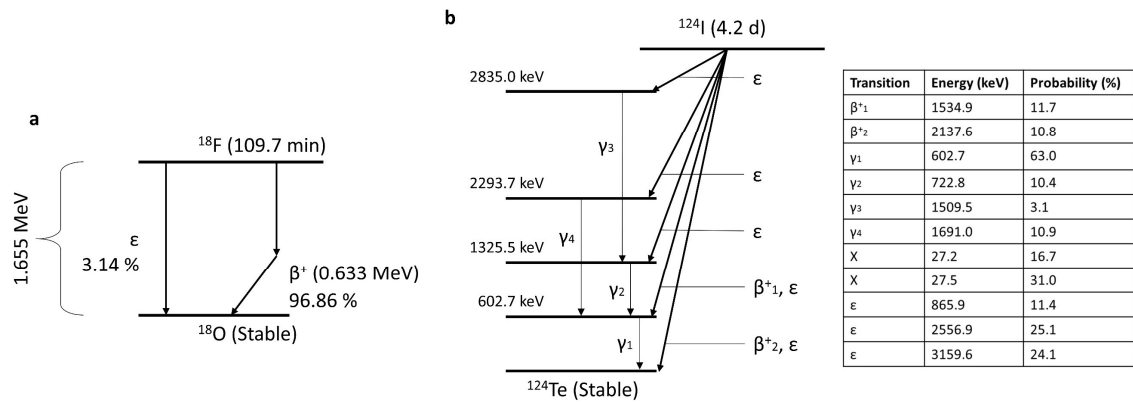


**Figure 1.13** Decay schema for **a)**  $^{18}\text{F}$  and **b)**  $^{124}\text{I}$ .

The branching fraction of a radioelement is the percentage of emissions produced from elemental decay that are of one decay mode. In the case of  $^{18}\text{F}$ , positron decay accounts for 96.9 % of the total emissions, and EC the other 3.1 %. On the other hand,  $^{124}\text{I}$  has only 22.5 % emissions from positron decay (Table in Figure 1.13). Table 1.7 shows the positron branching fraction of common PET radionuclides. It is important to have a precise determination of branching fractions because if not just one but a variety of gamma radiations are produced through different decay modes, they can decrease detection efficiency and increase the signal to noise ratio (SNR) of scans. This is a particular issue in  $^{68}\text{Ga}$  and  $^{124}\text{I}$  PET imaging, owing to the production of gammas outside the annihilation event and within a defined energy window (i.e. prompt gammas) that could lead to LOR calculation errors and reduce the quality of the image and the PET quantification [255]. Finally, if a radioelement has a high ratio of alpha or  $\beta^-$  decay alongside positron decay, an increased radiation dose to the cells, where the radioactive probe accumulates, should be expected. This is the case of  $^{64}\text{Cu}$ , whereby decay is approximately 17.4 %  $\beta^+$ , 39 %  $\beta^-$  and 43.6 % EC. On the other hand, this effect could be useful if a combined imaging and therapeutic agent is required [256].

Other important properties of PET radionuclides worth mentioning are the positron energy and range and their impact on PET images. Higher energy positrons travel further

from their atomic source before annihilation compared to low energy positrons. In these cases, since the annihilation event happens far away from the actual elemental source, the spatial resolution of the detection is reduced. This effect negatively impacts the detection of, in particular, smaller lesions [257, 258]. Positron energies and ranges are detailed in Table 1.7.

#### 1.6.2.4. PET quantification

The high sensitivity and high specificity are important factors contributing to PET imaging's unique quantitative character and the wide use of PET in clinical oncology. Over and above a qualitative image interpretation, a semi-quantitative index, i.e. the standard uptake value (SUV), is implemented to assess the radiotracer uptake in a lesion or organ of interest [259]. Using the SUV, interpatient comparisons on tumour phenotype can be performed. The SUV is simply derived from the tissue radioactivity concentration within a volume of interest (VOI) on the PET image at a defined time point ( $r$ ) which is then normalised to the decay-corrected amount of injected radiotracer ( $\alpha'$ ) and—most typically—to the patient's body weight ( $w$ ) [260].

$$\text{SUV} = r / (\alpha'/w)$$

The SUV can then be presented in a variety of ways, including but not limited to:

- $\text{SUV}_{\text{Max}}$  SUV of the most tracer-avid voxel within the VOI.
- $\text{SUV}_{\text{Mean}}$  SUV of the mean average of all the voxels within the VOI.
- $\text{SUV}_{\text{Peak}}$  SUV of the mean average voxel within a fixed-size VOI, centred on a region of high tumour uptake.
- $\text{SUV}_{50}$  SUV of the mean average voxel within a VOI including only voxels with greater than 50 % maximum value.

Each determined SUV value has advantages and disadvantages. For example,  $SUV_{Max}$  has less intra- inter-observer variability compared to the  $SUV_{Mean}$ , but is affected more by image noise. The  $SUV_{Peak}$  combines the reproducibility of the  $SUV_{Max}$ , whilst mitigating some of the affects from image noise [261]. However,  $SUV_{Peak}$  will only be representative of a portion of the tissue or tumour. The  $SUV_{50}$  is a good way to measure the metabolically active tumour region, however it can be influenced by high signal in the non-malignant tissue [262]. Moreover, all SUVs are dependent on the instrumentation and reconstruction methods used. This makes it more difficult to compare data between sites performing the scans, as each PET setup will be different [259].

### 1.6.3. Nuclear imaging agents currently used in NB

As part of the INRGSS,  $^{123}I$ -mIBG and  $^{99m}Tc$ -MDP SPECT scans are recommended to aid in the diagnosis, staging, response evaluation, and follow-up of NB patients. However, additional radioactive agents directed to different molecular processes and targets have also been investigated. The most important of both the already established and potential radioactive probes for NB imaging are described below.

Targeting the NET-1 transporter,  $^{123}I$ -mIBG is the imaging counterpart of  $^{131}I$ -mIBG, the molecular radiotherapy agent commonly used in NB (see page 16). Based on the similar *in vivo* behaviour of the two compounds,  $^{123}I$ -mIBG SPECT is generally used to identify and characterise NB disease extent and is a necessary prerequisite to the induction of a  $^{131}I$ -mIBG therapy regime in NB. Although  $^{131}I$ -mIBG was initially used for imaging purposes [263], the safer physical characteristics of the  $^{123}I$  radioisotope (i.e. lower energy photons, shorter half-life, lack of  $\beta^-$  emission) allow for much higher doses of  $^{123}I$ -mIBG to be safely administered, resulting in better image quality [264-266].

A  $^{123}I$ -mIBG planar scintigraphy scan is currently the gold standard of NB diagnosis and disease management. In order to measure the extent of disease in patients, semi-

quantitative scoring systems have been developed, of which CURIE and SIOPEN are the systems most commonly implemented [267-270]. The methodology for each scoring is based on the partition of the body into either 10 (CURIE, 9 + 1 soft tissue) or 12 anatomical regions (SIOPEN) and each segment/region is given a score (based on the number of  $^{123}\text{I}$ -mIBG-avid lesions) that represents the extent of the disease (Figure 1.14). For the CURIE system, a score between 0–3 is attributed to each section, with 0 indicating no disease, a score of 1 or 2 representing 1 or 2 distinct NB lesions, respectively, and a score of 3 denoted for >50 % lesion coverage in the segment. This leads to a maximum score of 30 by the CURIE system. Alternatively, the SIOPEN scoring system attributes a score of 0–6 in each anatomical region. For 0, 1, 2 and 3 the score represents the number of distinct lesions observed. A score of 4 indicates four or more distinct lesions covering less than 50 % of the region, whereas a score of 5 indicates diffuse disease with 50–99 % coverage. A maximum score of 6 is attributed to a region when 100 % of the volume is covered with disease according to the  $^{123}\text{I}$ -mIBG scan. The summate score result in a maximum of 72 in the SIOPEN system. Both methods have shown good prognostic value, with higher scores representative of poor clinical outcomes [267, 269, 270].

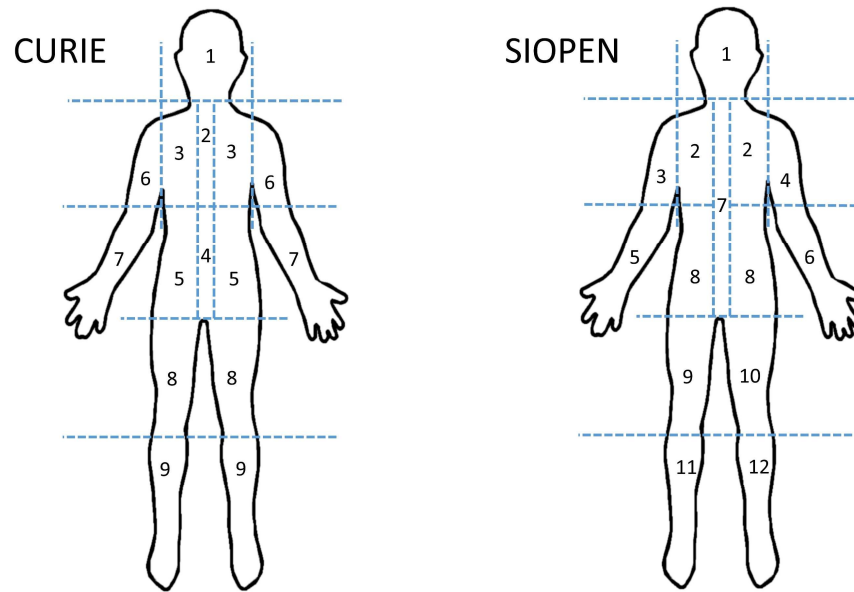


**Figure 1.14** Anatomical regions for CURIE (left) and SIOPEN (right) semi-quantitative scoring systems.

However,  $^{123}\text{I}$ -mIBG is not taken up by all NB lesions and are therefore described as ‘mIBG non-avid’ [132]. mIBG imaging is also not suitable for the detection of liver metastases owing to the heterogeneous uptake between different lobes of the normal tissue [271], therefore, alternative imaging may be necessary to have a more accurate picture of the extent of the disease.

$^{99\text{m}}\text{Tc}$ -methyl diphosphonate ( $^{99\text{m}}\text{Tc}$ -MDP), a bone-seeking agent that preferentially accumulates in bone and is usually used for the detection of skeletal metastases across the whole body using SPECT [272]. Also paediatric solid tumour malignancies, like NB, are often associated with bone metastases and increasing cases of extra osseous uptake of the bone-scan agent have been recorded in NB [273, 274].  $^{99\text{m}}\text{Tc}$ -MDP scan is clinically used to distinguish advanced stage of the disease. However,  $^{99\text{m}}\text{Tc}$ -MDP has been shown to be inferior to  $^{123}\text{I}$ -mIBG for the detection of bone lesions from the same patients [275, 276]. Nonetheless, the bone-scan can support mIBG imaging, especially for the detection of mIBG non-avid lesions [266].

As an alternative to the aforementioned radiotracers used in SPECT imaging, 2-Deoxy-2-[fluorine-18]fluoro-D-glucose or  $^{18}\text{F}$ -FDG is the most common PET radiotracer used in oncology [277]. It is a radiofluorinated analogue of glucose and targets metabolically active cells via the glucose transporter, GLUT-1 [234, 235]. Upon entering the target cell,  $^{18}\text{F}$ -FDG is converted to  $^{18}\text{F}$ -FDG-6-phosphate and then, unlike glucose, it is unable to be metabolised further, leading to its accumulation within the cell [278, 279]. Owing to the high dependency of cancer cells on glucose as an energy source, an increase in glucose metabolism (i.e. Warburg effect [280]) is generally considered as one of the main characteristics of cancer [281]. Based on that effect,  $^{18}\text{F}$ -FDG accumulates in cancer cells and therefore tumours are easily defined against normal tissue on an FDG scan. However, high  $^{18}\text{F}$ -FDG-avidity has been observed in inflammatory sites [282] and in the brain [283] leading to false-positive interpretations and specifically limiting the detection of cranial and near cranial lesions.

Of note,  $^{18}\text{F}$ -FDG PET can only evaluate the overall metabolic state of a tumour, and would grant limited benefits to patients' stratification for targeted therapy like  $^{131}\text{I}$ -mIBG. In NB, a major diagnostic utility comparative study by Sharp *et al.* showed the superiority of  $^{18}\text{F}$ -FDG PET to  $^{123}\text{I}$ -mIBG scintigraphy in detecting low and medium-risk disease, but highlighted its inferiority in high-risk disease due to lower radiotracer accumulation in bone metastases [284]. Further, Taggart *et al.* showed that there was a discordance between mIBG-avid and FDG-avid tumours following relapse of disease [285]. Therefore, although  $^{18}\text{F}$ -FDG scans showed good prognostic significance in NB, their use can only aid but cannot replace  $^{123}\text{I}$ -mIBG despite the advantages of PET imaging over SPECT [286].

#### 1.6.4. Nuclear imaging agents under investigation in NB

PET analogues of  $^{123}\text{I}$ -mIBG have been developed by substituting the gamma emitter  $^{123}\text{I}$  for the positron emitting halogens  $^{124}\text{I}$  or  $^{18}\text{F}$  [287, 288] without the loss of the NET-1 transporter targeting properties. Firstly,  $^{124}\text{I}$ -mIBG has been shown to produce superior lesion detection compared to  $^{123}\text{I}$ -mIBG in the clinic [289] resulting in an increased CURIE score in NB patients [290]. The half-life of  $^{124}\text{I}$  (4.2 d) is closer to that of the therapeutic radionuclide  $^{131}\text{I}$  (8.0 d) compared to  $^{123}\text{I}$  (13.2 h). This is particularly useful for estimating organ and tumour dosimetry for treatment planning and a clinical trial comparing  $^{124}\text{I}$ -mIBG PET/CT to conventional  $^{123}\text{I}$ -mIBG SPECT/CT in NB is ongoing [NCT02043899]. However, because the studies are quite lengthy ( $\sim 2$  days hospitalisation), patients and carers have been reluctant to consent to follow-up scans. Consequently, this resulted in very low patient enrolment, compromising the potentiality of  $^{124}\text{I}$ -mIBG PET/CT for routine clinical use [290]. Additionally,  $^{124}\text{I}$  is not a pure positron emitter, with positrons accounting for just 23 % of its decay emissions [255]. The radionuclide also emits prompt gammas within the PET energy window (see page 37) that reduces the signal-to-noise ratio and require special corrections during image reconstruction. Therefore, compared to other positron emitters like  $^{18}\text{F}$ ,  $^{124}\text{I}$  PET necessitates longer scan times and the administration of higher radiotracer activities in order to produce optimal images [255].

Secondly, like  $^{124}\text{I}$ -mIBG,  $^{18}\text{F}$ -mFBG produces superior lesion detection compared to  $^{123}\text{I}$ -mIBG [288, 291].  $^{18}\text{F}$  has a much shorter physical half-life (109.7 min) compared to both  $^{123}\text{I}$  and  $^{131}\text{I}$ , therefore PET scans are normally performed within 4 h of the radiotracer administration [292]. Interestingly,  $^{18}\text{F}$ -mFBG also has a shorter biological half-life compared to the iodinated counterparts [288], which can be attributed to a higher hydrophilicity and quicker body clearance of the radiotracer [293]. Consequently, not

being compromised by high background signals, high quality PET images can be acquired at earlier time-points. Shorter tracer injection-to-scan times also reduce patient hospitalisation and therefore contribute to improve patients' well-being. Moreover patients and carers may be more disposed to consent to follow-up scans if they are needed to monitor tumour response to therapy [294, 295]. Compared to  $^{124}\text{I}$ ,  $^{18}\text{F}$  is a near pure positron emitter (96.9 % branching fraction) and good quality images can be achieved by injecting lower amounts of radioactivity [288, 296]. For measuring  $^{18}\text{F}$ -mFBG tumour uptake, over and above the use of the SIOPEN or CURIE scoring systems, routine quantitative and semi-quantitate SUV calculations can be adopted [291], offering potential for the use of the agent to quantitatively assess disease response following intervention.

Traditional radiochemical strategies for  $^{18}\text{F}$ -mFBG have focused on electron-poor aromatics to carry out nucleophilic aromatic substitution reactions (e.g. Balz-Schieman reaction) and production of the radiotracer has been limited mostly because of its multi-step synthesis performed manually [297]. However, new radiosynthetic strategies have become recently available. In 2014, Zhang *et al.* reported an updated radiosynthesis of this agent that required 3 steps and 3 hours to end of synthesis. The pure product was achieved with a decay-corrected radiochemical yield (RCY) of roughly 11 % and a molar activity of about 18 GBq/ $\mu\text{mol}$  [138]. Further, Rotstein *et al.* reported the synthesis of  $^{18}\text{F}$ -mFBG via a spirocyclic iodonium(III) ylide (~14% RCY) [298]. The groups of Sanford and Gouverneur published approaches to the fluorination of electron-rich aromatics via copper-mediated destannylation or deborylation [299]. Ultimately, these published methods have led to greater access to  $^{18}\text{F}$ -mFBG for clinical translation.

Alternative PET imaging agents have been investigated to visualise different molecular targets expressed in NB. Firstly,  $^{18}\text{F}$ -DOPA is an analogue of

L-3,4-dihydroxyphenylalanine (L-DOPA), the precursor of catecholamines.  $^{18}\text{F}$ -DOPA is actively transported into cells through the large neutral amino acid transporter system (LAT1) that is responsible for the cell uptake of essential amino acids in key body districts such as placenta and blood brain barrier [300].  $^{18}\text{F}$ -DOPA could be considered as a promising PET alternative to  $^{123}\text{I}$ -mIBG in NB, due to its ability to follow the metabolism of catecholamines [301]. In support of this, it has been shown that  $^{18}\text{F}$ -DOPA has a good correlation with  $^{123}\text{I}$ -mIBG uptake in NB and has specific advantages for the detection of liver lesions and small lesions [302, 303]. However, this imaging agent has not been validated for the appropriate planning of therapeutic regimes involving  $^{131}\text{I}$ -mIBG and there are ongoing challenges associated with producing GMP compliant radiosynthesis methods of  $^{18}\text{F}$ -DOPA for its clinical use [304]. Nonetheless, clinical trials investigating the potential uses of  $^{18}\text{F}$ -DOPA are under investigation [NCT03042416] [NCT03541720] [NCT01943097].

Secondly, the somatostatin receptor 2 (SSTR2) has been shown to be highly expressed in a variety of human neuroendocrine tumours including NB [305-307]. SSTR2-targeting radiolabelled 1,4,7,10-tetraazacyclododecane-1,4,7,10-tetraacetic acid–octreotate analogues, such as  $^{68}\text{Ga}$ -DOTATOC and  $^{68}\text{Ga}$ -DOTATATE, have become an effective imaging option for SSTR-positive neuroendocrine tumours and are both being investigated clinically in NB [NCT04081701] [NCT03583528]. Additionally, both conjugates can be radiolabelled also with the therapeutic radioisotopes  $^{177}\text{Lu}$  or  $^{90}\text{Y}$  [230, 231], thus providing a potential “theranostic pair” for NB lesions that do not accumulate mIBG [308, 309]. A clinical trial is testing peptide receptor radionuclide therapy using  $^{90}\text{Y}$ -DOTATOC in patients with neuroendocrine and somatostatin receptor positive tumours using  $^{68}\text{Ga}$ -DOTATOC PET-CT imaging for diagnosis, staging, treatment targeting, and monitoring therapy response [NCT03273712]. Further, a lack of

correlation between SSRT2 and NET-1 receptor expression in NB [306, 310] results in differential uptake patterns of  $^{123}\text{I}$ -mIBG and  $^{68}\text{Ga}$ -DOTATATE seen in NB tumours as well as adult neuroendocrine malignancies [311-313]. Therefore, future incorporation of  $^{68}\text{Ga}$ -DOTA-TOC -TATE imaging in NB diagnosis may improve management of mIBG non-avid disease.

Finally, large biomolecules such as antibodies, can be radiolabelled for the molecular imaging of cancers. ImmunoPET, which combines the targeting specificity of monoclonal antibody (mAb) and the sensitivity of PET technique is a rapidly expanding field [314]. Many research projects and clinical trials are examining the expression of some of the most common cancer targets (e.g. HER2, EGFR, CD20) by using target specific radiolabelled mAbs [315, 316]. However, in NB currently just one pilot clinical trial for immunoPET is underway. In this regard, the safety and pharmacokinetics of a  $^{124}\text{I}$  labelled hu3F8 is being investigated [NCT02307630]. Historically, the murine version of this antibody, m3F8, labelled with  $^{124}\text{I}$ , has also been used to determine GD2 expression in NB [317], however, the high cost and the limited availability of the radioisotope has restricted the number of potential human studies. Nonetheless, imaging GD2 in NB ( $^{131}\text{I}$ -m3F8 planar scintigraphy) has shown superior lesion detection compared to  $^{131}\text{I}$ -mIBG or  $^{99\text{m}}\text{Tc}$ -MDP in highly disseminated NB [318]. Pre-clinically, a small number of investigations have therefore looked to radiolabel GD2-targeting mAbs for immunoPET in GD2 expressing cancers [319, 320]. Both the hu14.18K322A [319] and ch14.18(CHO) [320] mAbs have been successfully radiolabelled with  $^{64}\text{Cu}$  and shown to selectively target GD2 expressing tumour xenografts, including NB, *in vivo*. However, ~38 % of emissions from  $^{64}\text{Cu}$  are  $\beta^-$ , which whilst provide potentially useful therapeutic effects to the tumour, the use of this radioisotope for diagnostic and serial imaging is limited due to toxicity to healthy tissue [321, 322].

## Chapter 2 - Research aims

In light of this background, I hypothesised that the development of NB target-specific PET agents can aid in the clinical decision making during treatment of HR-NB patients.

To investigate this hypothesis two main research aims were set out:

1. To assess the ability of the fluorinated noradrenaline analogue  $^{18}\text{F}$ -mFBG as a tool to quantify actual tumour NET-1 expression.
  - a. To assess whether  $^{18}\text{F}$ -mFBG PET is a suitable alternative to  $^{123}\text{I}$ -mIBG to measure NET-1 expression in NB cells and *in vivo* models, and
  - b. To assess the potential of  $^{18}\text{F}$ -mFBG to quantify changes in NET-1 expression in response to pharmacological intervention using a dual mTORC1/2 inhibitor.
  
2. To develop and characterise a  $^{89}\text{Zr}$  radiolabelled ch14.18(CHO) (Dinutuximab-Beta) mAb in order to visualise and delineate GD2 positive NB tumour cells *in vivo*.

## Chapter 3 - Materials and methods

### 3.1. Cell culture

Cells were cultured in appropriate media, either Dulbecco's Modified Eagle Media (DMEM; Gibco, Life Technologies, UK) or RPMI 1640 (Gibco, Life Technologies, UK), supplemented with 10 % heat-inactivated foetal bovine serum (FBS, Gibco, Life Technologies, UK). Adherent cells were maintained as a monolayer at 37 °C in a humidified atmosphere containing 5 % CO<sub>2</sub> and were manipulated in a laminar flow Class II hood. To minimise stress conditions, cells were passaged (split) 1–2 times per week according to cellular confluence. Media was removed from cultures, and the adherent cells were washed with Dulbecco's PBS (Gibco, Life Technologies, UK) to remove any residual media. Cells were then incubated with Trypsin- ethylenediaminetetraacetic acid (EDTA) (Gibco, Life Technologies, UK), a serine protease, at 37 °C to disrupt the C-terminal lysine/arginine-mediated cell-to-cell and cell-to-flask interactions and obtain a single-cell suspension. An excess of media containing 10 % FBS was added to the suspension to inhibit and neutralise Trypsin-EDTA activity. Cells were spun in a centrifuge at 1200 rpm (Model: Eppendorf 5810R) and re-suspended in fresh media for further use.

The authenticity of all cell lines was confirmed by short tandem repeat (STR) DNA profiling analysis (Eurofins Medigenomix, Germany) and compared to those published online (<https://www.dsmz.de/services/services-human-and-animal-cell-lines/online-str-analysis.html>). Cell lines were routinely tested for mycoplasma contamination using a PCR detection kit (Surrey Diagnostics Ltd UK).

For cryogenic preservation of cell stocks, cryogenic vials containing aliquots of approximately  $1 \times 10^6$  cells in 1 mL storage solution (600  $\mu$ L FBS, 300  $\mu$ L Medium, 100  $\mu$ L dimethyl sulfoxide (DMSO)) were first moved to a –80 °C freezer in a cryo-box

containing isopropanol (Sigma-Aldrich, UK) before transferring to long-term liquid nitrogen storage ( $-192\text{ }^{\circ}\text{C}$ ) at least 24 h later.

### **3.2. Chapter 4**

#### **3.2.1. Cell culture**

SK-N-SH, SK-N-BE(2)C, Kelly and NBL5 human NB cell lines were kindly provided by Professor Louis Chesler, Paediatric Solid Tumour Biology and Therapeutics group, The Institute of Cancer Research, UK. SK-N-SH and SK-N-BE(2)C cell lines were cultured in DMEM, and NBL5 and Kelly in RPMI 1640 (see page 51).

#### **3.2.2. Western blot**

Materials and equipment for Western blot (WB) were obtained from Thermo Fisher Scientific UK unless otherwise stated.

##### **3.2.2.1. Cell lysis**

A radioimmunoprecipitation assay (RIPA) complete buffer was freshly prepared as follows: for 1 mL of solution: RIPA Lysis and Extraction Buffer (943  $\mu\text{L}$ , formulation from manufacturer: 25 mM Tris-HCl pH 7.6, 150 mM NaCl, 1 % NP-40, 1 % sodium deoxycholate, 0.1 % SDS), 1 mM EDTA (2  $\mu\text{L}$  of 0.5 M stock, pH 8), 10  $\mu\text{L}$  Halt™ Phosphatase Inhibitor Cocktail (100 $\times$ ), 40  $\mu\text{L}$  cOmplete™ Protease Inhibitor Cocktail (25 $\times$ , ROCHE, Switzerland) and 0.05 M NaF (5  $\mu\text{L}$  of 1 M stock,). Cells were washed with PBS and subsequently incubated in an appropriate volume of RIPA complete ( $4\text{ }^{\circ}\text{C}$ , 20 min). Cell lysates were collected in to a 1.5 mL micro centrifuge tube (Eppendorf, UK) and further homogenised using a sonicator (5 secs; Sonic Dismembrator Model 100, Fisher Scientific, UK). Samples were centrifuged (Model: Eppendorf 5424R) at 10,000 rpm,  $4\text{ }^{\circ}\text{C}$  for 10 min before being stored at  $-20\text{ }^{\circ}\text{C}$  for further use.

### 3.2.2.2. Tissue lysis

Tissues samples were snap-frozen in liquid nitrogen and stored on dry ice prior processing. Approximately 15 mg of sample were isolated from each tissue and placed in a MK28-R re-inforced metal homogenising tube (Precellys, VWR, USA) before adding the Tissue Extraction Reagent I (10 mL/g of tissue; Invitrogen, UK; Composition: 50 mM Tris (pH 7.4) 250 mM NaCl, 5 mM EDTA, 2 mM Na<sub>3</sub>VO<sub>4</sub>, 1 mM NaF, 20 mM Na<sub>4</sub>P<sub>2</sub>O<sub>7</sub>, 0.02 % NaN<sub>3</sub> and proprietary detergent) with cOmplete™ Protease Inhibitor Cocktail (25×, ROCHE, Switzerland). The tissue samples were then homogenised using the Precellys®24 Homogenizer system (Bertin Instruments, VWR, USA) (6500 rpm / 3 × 20 s). The suspension was transferred to a 1.5 mL micro centrifuge tube and centrifuged (Model: Eppendorf 5424R) at 10,000 rpm , 4 °C for 10 min before being stored at –20 °C for further use.

### 3.2.2.3. Electrophoresis

The total protein was quantified using the bicinchoninic acid (BCA) protein kit assay (Pierce, UK). The suitable amount of NuPAGE™ LDS Sample Buffer (4×) (Composition: 106 mM Tris-HCl, 141 mM Tris Base, 2 % LDS, 10 % Glycerol, 0.51 mM EDTA, 0.22 mM SERVA Blue G250, and 0.175 mM Phenol Red) and NuPAGE™ Sample Reducing Agent (10×) (Composition: 500 mM dithiothreitol (DTT)) and UF water were added to the lysate and the samples were denatured at 70 °C for 10 min. Samples were loaded into NuPAGE™ 4–12 % Bis-Tris Protein Gels (Formulation: Bis-Tris-HCl buffer pH 6.4, Acrylamide, Bis-acrylamide, APS, ultrapure water) and placed into an XCell SureLock™ Mini-Cell with running buffer. The running buffer was prepared by diluting NuPAGE™ MOPS SDS Running Buffer (20×) (Formulation: 50 mM 3-(N-morpholino)propanesulfonic acid (MOPS), 50 mM Tris Base, 0.1 % SDS, 1 mM EDTA, pH 7.7) in distilled H<sub>2</sub>O (dH<sub>2</sub>O) to obtain a 1× solution. Novex™ Sharp

Pre-stained Protein Standard (3.5 to 260 kDa size range; in 65 mM Tris pH 6.5, 30 % glycerol, 2 % SDS, and 2.5 mM EDTA) was used as the molecular weight marker. The gels were run for ~90 min at 185 V using a PowerPac™ HC High-Current Power Supply (Bio-Rad, USA).

#### 3.2.2.4. Membrane transfer

A wet transfer was performed using an XCell II Blot Module. A suitable volume of NuPAGE™ Transfer Buffer (20×) (Composition: 25 mM Bicine, 25 mM Bis-Tris, 1 mM EDTA pH 7.2) was diluted with 10 % methanol in dH<sub>2</sub>O to obtain a final 1× solution. Nitrocellulose membrane (Amersham Protran 0.45 NC) (GE Healthcare, USA) and blotting paper (Whatman™ 3 mm chromatography paper, GE Healthcare, USA) were cut to the size of the gel. The membrane, blotting paper and sponges were soaked in transfer buffer. The transfer cassette was stacked as shown in Figure 3.1, in the direction of the current.

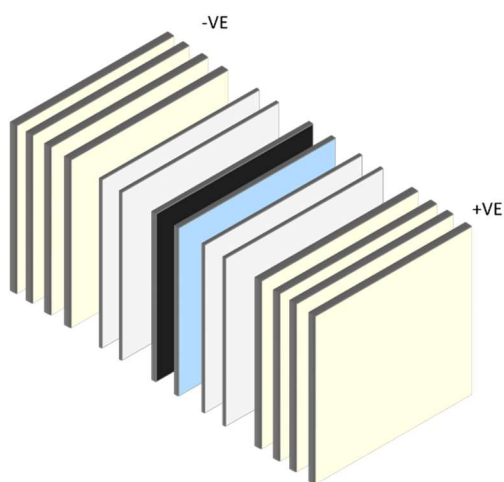


**Figure 3.1** WB stacking order. Layering of sponge (yellow), blotting paper (grey), gel (black), nitrocellulose membrane (blue) in the transfer box in the direction of current.

The cassette was tightly sealed and filled up with transfer buffer and placed in the tank that was filled with chilled H<sub>2</sub>O. The transfer was run for 2.5 h at a constant current (350 mA) using a PowerPac™ HC High-Current Power Supply (Bio-Rad, USA).

### 3.2.2.5. Blocking and antibody probing

The membranes were removed from the cassette and washed with Tris-buffered saline plus Tween-20 (TBST; 0.5 %; Sigma-Aldrich, USA) before being placed in a blocking solution of 5 % milk TBST or 5 % BSA TBST for 1 h. The suitable primary antibody was diluted in the appropriate blocking solution according to the manufacturer's protocol and incubated with the membrane overnight (4 °C). The next day, the membranes were washed thrice with TBST and incubated with the relevant horseradish peroxidase (HRP) conjugated secondary antibody (1 h at RT). Following the incubation the membranes were again washed thrice with TBST.

Antibody	Species	Catalogue no.	Supplier	Dilution	Molecular Weight (kDa)
NET-1	Mouse	NET-17	mAbTechnologies	1:1000	50–80
MYCN	Mouse	OP13	Merck Millipore	1:1000	62
GAPDH	Rabbit	5174	Cell Signalling	1:1000	37
$\beta$ -actin	Rabbit	4967	Cell Signalling	1:1000	42
Anti-Rabbit IgG HRP linked	Goat	7074	Cell Signalling	1:1000	Na
Anti-Mouse IgG HRP linked	Goat	7076	Cell Signalling	1:1000	Na

**Table 3.1** List of antibodies used for WB analysis.

### 3.2.2.6. Chemiluminescence imaging

The membranes were processed using Pierce™ Fast Western Kit, SuperSignal™ West Pico following the manufacturer's instructions. SuperSignal™ West Femto Maximum Sensitivity Substrate was additionally used for proteins with low expression levels. Membranes were incubated for 5 min and then imaged using a ChemiDoc XRS+ (Bio-

Rad, USA), with an image being taken every 2 seconds to ensure that the optimum exposure time was captured (ImageLab, Bio-rad, USA).

### 3.2.2.7. Image analysis

Images were prepared and analysed using ImageJ software (NIH, USA). Protein band density was measured and normalised to the loading control ( $\beta$ -actin or GAPDH) for each gel run. During treatment studies, band density was compared to control cells/tumours performed on the same membrane and no comparison was drawn between bands from other membranes.

### 3.2.3. Preparation of imaging agents

$^{123}\text{I}$ -mIBG was purchased from GE Healthcare (AdreView, UK).

The synthesis of  $^{18}\text{F}$ -mFBG was performed by Mr David Turton of the PET Radiochemistry team, The Institute of Cancer Research, UK. A description of the process is outlined for completion.

$^{18}\text{F}$  fluoride was produced on a GE PETrace cyclotron by 16 MeV irradiation of an enriched [ $^{18}\text{O}$ ]H<sub>2</sub>O target, and supplied by Alliance Medical UK.  $^{18}\text{F}$ -fluoride (~16 GBq) in water was delivered to a Trasis AllInOne (AiO) module and loaded on a Sep-Pak Accell Plus QMA Plus Light cartridge (46 mg sorbent, Waters, UK). The  $^{18}\text{F}$  fluoride was eluted using a 1 mL solution of Krypofix 222 (2.5 mg, Sigma-Aldrich, UK) in aqueous potassium carbonate (0.1 mL, 5 mg/mL, Sigma-Aldrich, UK) and acetonitrile (0.9 mL, Thermo Fisher Scientific, UK). The eluted solution was dried at 125 °C under a stream of nitrogen with gradually increasing applied vacuum. A reaction mixture consisting of tetrakis pyridine copper triflate (5 mg, 7.4  $\mu\text{mol}$ ), Sigma-Aldrich, Gillingham, UK) and the precursor: (tert-butyl-N-[(1Z)-{bis[(tert-butoxy)carbonyl]amino}]{[(tert-butoxy)carbonyl]}{[3-(tetramethyl-1,3,2-dioxaborolan-2-yl)phenyl]methyl})amino)methylidene

]carbamate) (10 mg, 14.8  $\mu\text{mol}$ ); provided by Professor Veronique Gouverneur, Department of Chemistry, Oxford University, UK) in anhydrous dimethylformamide (DMF) (0.5 mL, Sigma-Aldrich, Gillingham, UK) was added to the dry  $^{18}\text{F}$ -fluoride and heated for 20 min at 120  $^{\circ}\text{C}$ . A water flush was used to remove unreacted  $^{18}\text{F}$  from the reaction mixture by solid phase extraction (SPE) using an Oasis Plus short HLB cartridge (225 mg sorbent; Waters, UK). The crude product was eluted with acetone (2 mL, Sigma-Aldrich, UK), and subsequently dried under a nitrogen flow. The product was deprotected using hydriodic acid (57 %, 400  $\mu\text{L}$ ; Sigma-Aldrich, UK) at 125  $^{\circ}\text{C}$  for 10 min. The crude product was then dissolved in water (9 mL) and purified by semi-preparative high Performance Liquid Chromatography (HPLC) on a Luna C18 column (7.8  $\times$  250 mm, 10  $\mu\text{m}$ , Phenomenex, UK), with isocratic elution of 10 % ethanol/90 % of 0.1 % aqueous phosphoric acid ( $\text{H}_3\text{PO}_4$ , Sigma-Aldrich, UK) at a flow rate of 3 mL/min. The column output was monitored for radioactivity and UV absorption at 254 nm. The purified product was collected into a vial containing water (20 mL) and then concentrated by weak cation exchange SPE (Strata X CW resin, 30 mg sorbent; Phenomenex, UK). The product was eluted using 0.1 % aqueous  $\text{H}_3\text{PO}_4$  and ethanol (1:4 v/v), dried under a nitrogen flow, and then dissolved in the desired volume of water. The chemical and radiochemical purity, and the molar activity were determined by RP-HPLC analysis using an Agilent Infinity 1260 quaternary pump system equipped with a 1260 variable wavelength UV detector (Agilent Technologies, UK) fitted with a Luna 5  $\mu\text{m}$  C18 column (150  $\times$  4.6 mm; Phenomenex, UK). An isocratic elution with 95 % of 0.1 % aqueous  $\text{H}_3\text{PO}_4$  and 5 % acetonitrile as mobile phase was used at a flow rate of 1 mL/min. Elution profiles were recorded using Laura software (Lablogic, UK). The UV absorbance was recorded at 254 nm. The radioactivity of the eluate was monitored using a NaI radiodetector (Lablogic, UK). A stock solution of mFBG was used as reference for the determination of the product molar activity.

### 3.2.4. Specificity of binding

To evaluate the specificity of tracer uptake, approximately  $3.0 \times 10^5$  adherent cells were incubated with either  $^{18}\text{F}$ -mFBG (150 kBq) or  $^{123}\text{I}$ -mIBG (5 kBq) for 1 h, 37 °C, in the presence or absence of the specific NET-1 inhibitor desipramine (D3900, 50  $\mu\text{M}$ , Sigma Aldrich, UK). Subsequently, cells were washed with PBS, trypsinised and the cell-associated radioactivity was measured using a  $\gamma$ -counter (2480 WIZARD<sup>2</sup>, PerkinElmer, UK). For each cell line, the cell-associated radioactivity was normalised to the number of cells and then each group was presented as a percentage of the signal acquired for SK-N-BE(2)C cells (mean of  $n = 3$  independent experiments performed in triplicate  $\pm$  SEM).

### 3.2.5. Animal studies

All studies were conducted in compliance with licenses issued under the UK Animals (Scientific Procedures) Act 1986 and approved by the institutional ethical review according to the United Kingdom National Cancer Research Institute Guidelines for Animal Welfare in Cancer Research [323]. Female Nu(NCr)-Foxn1<sup>nu</sup> mice (5–7 weeks) obtained from the in-house breeding colony were used in the studies.

#### 3.2.5.1. Tumour establishment

For cell injections, mice were anaesthetised with gaseous isoflurane (1.5–2.0 % v/v in air). Subcutaneous xenografts were generated by injection of either Kelly ( $5 \times 10^6 / 80 \mu\text{L}$  PBS/Matrigel (30 % v/v; BD Matrigel<sup>TM</sup> Matrix, BD Bioscience, USA)) or SK-N-BE(2)C ( $1 \times 10^6 / 80 \mu\text{L}$  PBS/Matrigel) into the lower flank. To monitor tumour growth, upon appearance of a tumour mass, calliper measurements were taken 3 times per week and an approximate tumour volume was calculated based on the formula: Volume =  $\frac{1}{2}(\text{width}^2 \times \text{length})$ .

With the aid of Ms Barbara Martins da Costa, Paediatric Solid Tumour Biology and Therapeutics group, The Institute of Cancer Research, UK, kidney capsule xenografts

were generated as follows: a 1 cm incision to the left flank was made, the kidney was externalised and either Kelly ( $2 \times 10^5 / 30 \mu\text{l}$  PBS) or SK-N-BE(2)C ( $2 \times 10^5 / 30 \mu\text{l}$  PBS) cells were injected. After the cell injection, the kidney was put back into the peritoneal cavity and the peritoneal wall sutured. A metal clip was put in place to close the skin and removed 48 h later. Mice were monitored and body weight measured 3 times a week. To monitor the tumour growth, mice were scanned using a M3™ Compact MRI system and software (Aspect imaging, Israel) twice per week.

### **3.2.5.2. *In vivo* administration of imaging and radiotherapeutic agents**

When the tumours measured approximately  $100\text{--}200 \text{ mm}^3$ , anaesthesia was induced in the mice using 3% isoflurane delivered in oxygen (1 L/min). The mice were injected intravenously via the tail vein with  $^{18}\text{F}$ -mFBG ( $\sim 7.5 \text{ MBq}$ ),  $^{123}\text{I}$ -mIBG ( $\sim 20 \text{ MBq}$ ) or  $^{131}\text{I}$ -mIBG ( $\sim 20 \text{ MBq}$ ) in a total volume of  $100 \mu\text{L}$  in sterile saline.

### **3.2.6. Small animal imaging**

For all imaging experiments, anaesthesia was induced in the mice using 3% isoflurane delivered in oxygen (1 L/min). Core body temperatures were maintained using a thermoregulated heating pad throughout each study period.

#### **3.2.6.1. PET imaging**

PET studies were conducted using an Albira trimodal PET/SPECT/CT imaging system with Albira monitor software package (V5.8, Bruker, USA). For  $^{18}\text{F}$ -radiotracer imaging, whole body PET static images were acquired with a  $511 \text{ keV} \pm 153.3 \text{ keV}$  energy window for 10 min. For dynamic PET imaging, serial, static PET scans were acquired sequentially from the time of injection as follows:  $30 \times 10 \text{ s}$ ,  $20 \times 30 \text{ s}$ ,  $8 \times 300 \text{ s}$ ,  $11 \times 600 \text{ s}$ , (2.5 h total). Mice were allowed to recover completely from anaesthesia before a second dynamic scan consisting of serial  $15 \times 600 \text{ s}$  static PET acquisitions (2.5 h total).

The image data were normalised to correct for PET non-uniformity, dead-time count losses, positron branching ratio, attenuation, and physical decay to the time of injection. No partial-volume averaging corrections were applied. All static PET images were reconstructed using the Albira monitor software package using a Maximum-Likelihood Expectation-Maximization (MLEM) algorithm (12 iterations) with a voxel size of  $0.5 \times 0.5 \times 0.5 \text{ mm}^3$ . Dynamic PET images were further reconstructed 20, 24 and 30 iterations of the MLEM algorithm.

### **3.2.6.2. CT imaging**

CT studies were conducted using an Albira trimodal PET/SPECT/CT imaging system with Albira monitor software package (V5.8, Bruker, USA). Whole body CT scans were performed at a voltage of 45 kV, current of 400  $\mu\text{A}$  and 250 projections (1 s per projection). The CT images were reconstructed using a filtered back projection (FBP) algorithm with a voxel size of  $0.5 \times 0.5 \times 0.5 \text{ mm}^3$ .

### **3.2.6.3. SPECT imaging**

SPECT studies were conducted using an Albira trimodal PET/SPECT/CT imaging system with Albira monitor software package (V5.8, Bruker, USA).  $^{123}\text{I}$ -mIBG SPECT imaging was performed 24 h p.i. for 30 min (60 s per projection) using single-pinhole low-energy collimators and a 50 mm FOV. A  $159 \pm 128 \text{ keV}$  energy window was used and images reconstructed with an Ordered Subset Expectation Maximization (OSEM) algorithm, 2 iterations.  $^{131}\text{I}$ -mIBG SPECT imaging was performed 24 h, 48 h and 6 d p.i of the compound for 30 min (60 s per projection) using a single-pinhole high-energy collimators and a 50 mm FOV. A  $364 \pm 72 \text{ keV}$  energy window was applied and images reconstructed with an OSEM algorithm, 2 iterations.

#### **3.2.6.4. MRI**

<sup>1</sup>H MRI was performed by Dr. Yann Jamin, Magnetic Resonance team, The Institute of Cancer Research, UK, on a horizontal bore Bruker Biospec 70/20 (Ettlingen, Germany) controlled by Paravision 6 using a 40 mm volume coil. Respiratory rate was monitored using physiological monitoring equipment (SA Instruments, Stony Brook, NY, USA). T2-weighted images were acquired in the axial plane using a rapid acquisition with relaxation enhancement (RARE) sequence over a 3 cm × 3 cm field of view (repetition time (TR) = 4500 ms, effective echo time (TE<sub>eff</sub>) = 36 ms, 2 averages, RARE factor = 8, in-plane resolution 234 μm × 234 μm, 20 1 mm thick contiguous slices) and used for identification, localisation and assessment of tumours.

#### **3.2.6.5. Cerenkov luminescence imaging**

Cerenkov images were acquired 24 h, 48 h and 6 d post administration of <sup>131</sup>I-mIBG using an IVIS/Spectrum/CT imaging system (PerkinElmer, USA) fitted with an iKon camera (product code: IS1443N6678, Andor, Oxford Instruments, UK). Images were captured with a 300 s exposure using an open emission filter. Images were visualised and prepared using the Living Image® Software (Version: 4.5.2; Perkin Elmer, USA).

#### **3.2.7. PET quantification**

Images were analysed using the PMOD software package (PMOD Technologies Ltd, Switzerland). A volume of interest (VOI) was drawn around the tumour using CT anatomical images and an automatic isocontour was applied to the hottest 50 % of voxels within the region. The mean (PET<sub>50</sub>) and hottest 50 voxel (PET<sub>HotAv</sub>) counts from the VOI were extracted and converted into percentage of injected dose per gram of tissue (%ID/g) using a calibration factor (MBq/g/counts) calculated by scanning an <sup>18</sup>F source of known activity and volume. 1 cm<sup>3</sup> on PET acquisitions were assumed to equal 1 g (n ≥ 3 mice ± SD).

### 3.2.8. Organ biodistribution

Following the final imaging acquisition (i.e. 1 or 4 h p.i. for  $^{18}\text{F}$ -mFBG) and 24 h p.i. for  $^{123}\text{I}$ -mIBG) the mice were sacrificed, and the tumour and major organs were excised, weighed and their associated radioactivity was measured using a  $\gamma$ -counter (2480 WIZARD<sup>2</sup>, PerkinElmer, UK). The results were expressed as % ID/g ( $n = >3$  mice  $\pm$  SD).

### 3.2.9. Autoradiography

Dissected tumours were set in an optimal-cutting-temperature compound (Tissue-Tek<sup>TM</sup>, USA) and snap-frozen in liquid nitrogen vapour. The tumours were then sectioned to a thickness of 10  $\mu\text{m}$  using a cytomicrotome (Thermo Fisher Scientific, UK) and mounted on slides. Slides were exposed to an X-ray film for 4 h which was scanned using a Typhoon FLA 7000 phosphorimager (GE Healthcare Life Sciences, UK), pixel size 25  $\mu\text{m}$ . Images were processed using ImageJ (NIH, USA).

### 3.2.10. Statistics

Unless otherwise stated *in vitro* experiments are displayed as the mean  $\pm$  SEM of three independent experiments each performed in triplicate and *in vivo* experiments as mean  $\pm$  SD. Statistical significance was determined using Prism software (GraphPad Software v8.0, USA). Statistically significant differences between groups were assumed if  $p \leq 0.05$ . No data were excluded from the analysis, including all outliers. When presented, the  $p$  values were calculated by unpaired two-tailed Student's  $t$  tests with Holm-sidak correction, a one-way ANOVA with Tukey post-hoc correction or a two-way ANOVA with Sidak's multiple comparisons post-hoc correction.

### **3.3. Chapter 5**

#### **3.3.1. Cell viability**

SK-N-BE(2)C cells ( $6 \times 10^4$ ), or Kelly, NBL5 and SK-N-SH cells ( $8 \times 10^4$ ) were seeded overnight in 96 well culture plates. Fresh media (100  $\mu$ L) containing AZD2014 (0–1  $\mu$ M) was added to the cells and incubated for 72 h. Cell Titer Glo® (Promega, USA) was then added directly into the wells (1:1 media:Cell Titer Glo®), and mixed. After 10 min, an aliquot of the mix (100  $\mu$ L) was transferred to an opaque white 96 well plate and subsequently luminescence was read using an Omega LUMIstar® microplate reader (BMG Labtech, Germany). The generated luminescent signal, (proportional to the amount of ATP present) was recorded and data were presented as the mean of  $n = 3$  independent experiments (performed in triplicate)  $\pm$  SEM.

#### **3.3.2. Cell cycle analysis**

SK-N-BE(2)C or Kelly cells ( $5 \times 10^5$ ) were seeded overnight in 6 well culture plates. Fresh media (1.5 mL) containing AZD2014 (0, 200 or 500 nM) was added to the cells and incubated for 24 h. After incubation, cells were washed with PBS and collected using trypsin into 1.5 mL microcentrifuge tubes (Eppendorf, UK). The cells were spun in a microcentrifuge (Model: Eppendorf 5424R; 1500 rpm; 3 min) and the cell pellet resuspended in PBS. The suspension was then pipetted 'drop-wise' into 5 mL 70 % ice cold ethanol and subsequently stored at  $-20$  °C until further use. When ready to use, the cells were centrifuged (Model: Eppendorf 5810R) and washed twice with PBS. Cells were incubated in a solution of 40 ng/mL RNase and 100 ng/mL propidium-iodide (PI) at 37 °C for 15 min. After incubation cells were stored on ice and flow cytometry performed on a BD™ LSRII flow cytometer (BD Biosciences, USA). The data were processed using FlowJo software (V10, BD Bioscience, USA), and data analysed using GraphPad Prism software (v.8, La Jolla, CA, USA).

**3.3.3. Western blot**

Cells were seeded overnight in 6 well plates and subsequently treated with AZD2014 (0–500 nM) in fresh media for 3–72 h. Seeding densities were determined to ensure samples did not reach confluence. Cell lysates and tissue homogenates were processed, and WBs performed as described above (see page 52). The antibodies used are listed in Table 3.2.

Antibody	Species	Catalogue no.	Supplier	Dilution	Molecular Weight (kDa)
NET-1	Mouse	NET-17	mAbTechnologies	1:1000	50–80
MYCN	Mouse	OP13	Merck Millipore	1:1000	62
p-Akt <sup>S473</sup>	Rabbit	9271	Cell Signalling	1:1000	60
Akt	Rabbit	9272	Cell Signalling	1:1000	60
p-S6 <sup>S240/244</sup>	Rabbit	2215	Cell Signalling	1:1000	32
S6	Mouse	2317	Cell Signalling	1:500	32
p-4EBP1 <sup>T37/46</sup>	Rabbit	2855	Cell Signalling	1:1000	10–20
4EBP1	Rabbit	9644	Cell Signalling	1:1000	10–20
β-actin	Rabbit	4967	Cell Signalling	1:1000	42
Anti-Rabbit IgG HRP linked	Goat	7074	Cell Signalling	1:1000	Na
Anti-Mouse IgG HRP linked	Goat	7076	Cell Signalling	1:1000	Na

**Table 3.2** List of antibodies used for WB protein analysis.

### 3.3.4. Quantitative real-time PCR

Material and equipment were obtained from ThermoFisher Scientific, UK unless otherwise stated.

SK-N-BE(2)C and Kelly tumour RNA was extracted from samples (~20 mg) using an RNeasy Mini Kit (Qiagen, UK) according to the manufacturer's instruction. RNA was eluted in RNase free water and the final concentration (ng/ $\mu$ L) was measured using UV-vis (260 nm) spectroscopy using a Nanodrop 2000. A 260/280 ratio around 2.0 indicated pure RNA in the sample mix. 2  $\mu$ g of sample RNA was then converted to cDNA using a High-Capacity cDNA Reverse Transcription Kit according to the manufacturer's instruction and using a thermocycler (Biorad, UK) on the following cycle: 25 °C for 10 min, 37 °C for 2 h, 85 °C for 5 min, 4 °C > 5 min.

For quantitative real-time PCR (qRT-PCR), 100 ng of cDNA was added to 10  $\mu$ L PCR Mastermix (Constituents: Taq DNA polymerase (0.05 U/ $\mu$ L), reaction buffer, 4 mM MgCl<sub>2</sub>, and 0.4 mM of each deoxyribonucleotide triphosphate (dNTP)), 1  $\mu$ L of each TaqMAN Assay labelled primer (Table 3.3), and brought to a final volume of 20  $\mu$ L with RNase- and DNase- free water in a Applied Biosystems™ 96-well PCR plate. The plate was sealed with clear plastic and the PCR ran using a StepOne Real-time PCR machine using the inbuilt 40-min fast PCR cycle. Data were analysed using Applied Biosystems™ StepOne software v2.3.

Gene	Colour	Assay ID	Lot
SLC6A2	FAM	Hs00426573_m1	1459244
RPLP0	VIC	Hs99999902_m1	1510076

**Table 3.3** List of PCR TaqMan gene expression primers.

### **3.3.5. $^{18}\text{F}$ -mFBG and $^{123}\text{I}$ -mIBG cell uptake after AZD2014 treatment**

SK-N-BE(2)C cells and Kelly cells were seeded overnight in 12 well plates and subsequently treated with AZD2014 (0–500 nM) in fresh media for 24 or 72 h.  $^{18}\text{F}$ -mFBG and  $^{123}\text{I}$ -mIBG cell specific uptake was characterised as previously described (see page 58). Uptake was normalised to cell viability as performed by Cell Titer Glo® (see page 63) in cells treated in parallel, and subsequently measured as a percentage of uptake for untreated cells in each cell line.

### **3.3.6. *In vivo* AZD2014 treatment studies**

Subcutaneous xenograft models were generated as described above (see page 58). For treatment studies, AZD2014 stock solution in DMSO was diluted in PEG400 to a final concentration of 2 mg/mL (10 % DMSO maximum). When SK-N-BE(2)C or Kelly tumours measured 50–100 mm<sup>3</sup>, mice were treated daily, for a total of either 1, 3 or 7 days, by oral gavage with AZD2014 (20 or 25 mg/kg/day) or vehicle control. Tumour size (by calliper measurements (see page 58)) and body weight were recorded daily during treatment. Mice were monitored for changes in body weight or appearance that could denote signs of treatment toxicity. A 10 % reduction in body weight in a single 24 h period, or a 20 % reduction overall, resulted in the mouse being sacrificed and the end of any further experimental procedure.

### **3.3.7. PET imaging and biodistribution after AZD2014 treatment**

24 h following the final treatment dose, mice were injected with  $^{18}\text{F}$ -mFBG (~7.5 MBq) and PET images were acquired 1 and 4 h p.i. (see page 59). After the final imaging session, mice were sacrificed, and tissues taken for biodistribution. The processes were performed as described before (see page 62).

### **3.3.8. Autoradiography**

Autoradiography was performed following the procedure previously described (see page 62).

### **3.3.9. Immunohistochemistry**

Tumours were placed in formalin (10 % v/v) for 24 h and moved to 70 % ethanol before paraffin-embedding. Samples were sectioned into 5 µm slices for histological and immunohistochemistry analysis. Sections were placed in xylene (20 min) to be cleared of wax, and the tissues were rehydrated in stepwise dilutions of ethanol (10 min each; 100–70 %) and dH<sub>2</sub>O (20 min). For haematoxylin and eosin (H&E) staining, slides were first stained in Gills III haematoxylin (1 min; Pioneer Research Chemicals, UK), differentiated (2 s; 0.5 % hydrochloric acid in 70 % ethanol) and blued in tap water (10 min). Samples were counterstained with an aqueous eosin Y solution (1 min; Pioneer Research Chemicals, UK) before being rapidly dehydrated in ethanol (70–100 %) and slides were mounted with a coverslip fixed with mounting medium (Pertex, Pioneer Research Chemicals, UK). For antibody staining, tumour sections underwent heat induced epitope revival (HIER) with citric acid based antigen unmasking solution (H3300, Vector Laboratories, UK) in a pressure cooker (4 min). Slides were then cooled, and sections blocked for non-specific staining (1 h, RT; 2.5 % normal goat serum (NGS) in PBS). The relevant primary antibody, in Dako antibody diluent (Cat: S3302; Agilent, USA; composition: 0.05 mol/L Tris-HCl buffer containing 0.1 % Tween, stabilizing proteins to reduce background, and 0.015 mol/L sodium azide), was then substituted on to the tissue section and incubated overnight at 4 °C. The following day, the slides were washed in TBST and endogenous peroxidases were blocked using a 2 % H<sub>2</sub>O<sub>2</sub> solution in methanol (10 min) before incubation with the secondary HRP-conjugated antibody (1 h, RT). For chromogen development, slides were incubated with the diaminobenzidine (DAB)-peroxidase substrate kit (4 min; Impact DAB, SK-4105, Vector Laboratories). Samples were counterstained with Gills III haematoxylin as previously described, dehydrated in ethanol, cleared in xylene and mounted with a coverslip. Whole section digital images were captured on a Nanozoomer XR (Hamamatsu Photonics, Japan) and

processed using NDP.view2 software. The primary and secondary antibodies are listed in Table 3.4.

Antibody	Species	Catalogue no.	Supplier	Dilution
<b>p-S6<sup>S240/244</sup></b>	Rabbit	2215	Cell Signalling	1:2000
<b>S6</b>	Mouse	2317	Cell Signalling	1:100
<b>p-4EBP1<sup>T37/46</sup></b>	Rabbit	2855	Cell Signalling	1:1000
<b>4EBP1</b>	Rabbit	9644	Cell Signalling	1:1000
<b>Ki67</b>	Rabbit	9027	Cell Signalling	1:200
<b>Anti-Rabbit IgG HRP linked</b>	Goat	7074	Cell Signalling	1:500
<b>Anti-Mouse IgG HRP linked</b>	Goat	7076	Cell Signalling	1:500

**Table 3.4** List of antibodies for IHC.

### 3.3.10. Statistics

Unless otherwise stated *in vitro* experiments are displayed as the mean  $\pm$  SEM of three independent experiments each performed in triplicate and *in vivo* experiments as mean  $\pm$  SD. Statistical significance was determined using Prism software (GraphPad Software v8.0, USA). Statistically significant differences between groups were assumed if  $p \leq 0.05$ . No data were excluded from the analysis, including all outliers. When presented, the p values were calculated by unpaired two-tailed Student's t tests with Holm-sidak correction, a one-way ANOVA with Tukey post-hoc correction or a two-way ANOVA with Tukey's multiple comparisons post-hoc correction.

### **3.4. Chapter 6**

#### **3.4.1. Cell lines**

SK-N-BE(2)C, Kelly and SK-N-AS human NB cell lines were provided by Professor Louis Chesler, Paediatric Solid Tumour Biology and Therapeutics group, The Institute of Cancer Research, UK. The SK-N-AS cell line was maintained in DMEM supplemented with 10 % FBS media, and all other cells were cultured as specified above (see page 51).

#### **3.4.2. Antibodies**

The anti-GD2 antibody, ch14.18(CHO) (Dinutuximab-Beta), was purchased from Creative Biolabs (Creative Biolabs, USA). Cat: TAB-731. Lot: CB181116.

The Ultra-LEAF™ purified human IgG1  $\kappa$  isotype control (clone: QA16A12) was purchased from BioLegend (BioLegend, UK). Cat: 403502. Lot: B273389.

#### **3.4.3. IRDye700DX-ch14.18(CHO) conjugation**

Conjugation of the IRDye700DX to ch14.18(CHO) was performed by Dr Chiara Da Pieve, PET Radiochemistry team, The Institute of Cancer Research, UK, and the labelled antibody herein is referred to as IR700-ch14.18(CHO). Firstly, centrifugal ultrafiltration using an Amicon® filter (Merck, USA) was used to exchange the antibody buffer with 50 mM borate, pH 8.4 according to the manufacturer's instruction. The antibody was recovered from the filter in a volume of ~150  $\mu$ L. The concentration, and consequently the amount of antibody, was measured by UV-vis (NanoDrop™ 2000, Thermofisher Scientific, USA) at the wavelength of 280nm. IRDye® 700DX NHS Ester (LI-COR Biosciences, USA) in DMSO (5 mM) was added to the antibody solution in a 10 molar excess. The solution was incubated for 5 h, RT, before being stored overnight at 4 °C. The product was purified by gel filtration using a Zeba™ Spin Desalting Column (0.5 mL, Thermofisher Scientific, USA) with a 40 kDa molecular weight cut-off (MWCO) and pre-equilibrated following the manufacturer's instruction. The final mAb

concentration and the mAb-to-IR700 ratio were determined by UV-vis at the wavelengths of 280 and 689 nm, respectively (NanoDrop™ 2000).

#### 3.4.4. Flow cytometry

Approximately  $3 \times 10^5$  cells were collected, washed in PBS and transferred into a 1.5 mL microcentrifuge tube. Cells were incubated in a thermomixer with an appropriate amount of fluorescently labelled antibody (Table 3.5), in cell staining buffer (Cat 420201, Biolegend, USA) (4 °C, 20 min, 500 rpm). After incubation, cells were washed with cold cell staining buffer, centrifuged (1500 rpm, 3 min), and the cell pellet resuspended in 300  $\mu$ L of PBS with DAPI (4',6-diamidino-2-phenylindole) for data acquisition. Flow cytometry studies were performed using a BD™ LSRII flow cytometer (BD Biosciences, USA). For each sample a minimum of 10,000 events were recorded, and the population corresponding to live (DAPI negative) single cells was gated and analysed. Three independent experiments were performed, and each point was normalised to the median fluorescence intensity acquired  $\pm$  SD. The data were processed using FlowJo software (V10, BD Bioscience, USA), and data analysed using GraphPad Prism software (v.8, La Jolla, CA, USA).

Antibody	Colour	Catalogue no.	Supplier	Dilution
<b>GD2:14G2a</b>	FITC	357313	Biolegend	1:20
<b>GD2:14G2a</b>	PE	357303	Biolegend	1:20
<b>GD2:ch14.18(CHO)</b>	IRdye700DX	Na	In house	1:50
<b>IgG2a, kappa</b>	FITC	400210	Biolegend	1:20

**Table 3.5** List of antibodies for flow cytometry. FITC = fluorescein, PE = R-phycoerythrin.

#### **3.4.5. Immunocytochemistry**

Cells were seeded 24 h before analysis on confocal glass bottom dishes (MatTek, USA). Cells were incubated in the nuclear staining buffer at 37 °C for 20 min (composition: PBS, 5 µg/mL Hoechst®33342, 1 % FBS) before incubating with the IR700-ch14.18(CHO) antibody (2 mg/µL) in staining buffer at 4 °C for 1 h. Cells were washed thrice with PBS before images were captured using a Zeiss LSM700 confocal microscope (Carl Zeiss Inc, Germany) equipped with a 63X Plan-Apochromat oil immersion objective and a 10X Plan NeoFluar air objective. Images were analysed using the Zen 3.0 (Blue edition) software (Zeiss, Germany).

#### **3.4.6. Immunofluorescence**

Tissue sections were processed in the same method as for autoradiography, with sections cut to 5 µm thickness (see page 62). Slides were stored at -20 °C until ready to use. Tissue sections were fixed in 2 % paraformaldehyde (PFA) for 30 min before being placed in blocking solution of PBS + 1 % FBS + 0.1 % Triton X (1 h, RT). Anti-GD2 IR700-ch14.18(CHO) (see page 69) (Table 3.6) was diluted in blocking solution and pipetted on tissue sections and incubated for 1 h, RT. Sections were washed in PBS and counterstained with Hoechst®33342 (5 µg/mL) before a coverslip was fixed in place using fluorescent mounting media (Dako S3023). Microscope scanning was performed using a Zeiss LSM700 confocal microscope (Carl Zeiss Inc, Germany) and Zeiss Axio Scan.Z1 with Hamamatsu Orca Flash. Digital images were processed using Zeiss 3.0 (Blue edition) software.

Antibody	Colour	Catalogue no.	Supplier	Dilution
GD2:ch14.18(CHO)	IRdye700DX	Na	In house	1:300

**Table 3.6** List of antibodies for immunofluorescence. FITC = fluorescein.

### 3.4.7. DFO-ch14.18(CHO) and DFO-IgG1 conjugation

Conjugation of DFO to ch14.18(CHO) was performed by Dr Chiara Da Pieve, PET Radiochemistry team, The Institute of Cancer Research, UK. Firstly, centrifugal ultrafiltration with an Amicon® filter was used to concentrate and exchange the antibody buffer with 0.1 M carbonate buffer; pH 9.0 according to the manufacturer's instruction. The antibody was recovered from the filter in a volume of ~100 µL. The concentration and amount of antibody conjugate was measured by the UV-vis absorbance value at 280 nm and dividing by 1.4. To a solution of the antibody in carbonate buffer, EDTA (50 mM stock; 50 µL/10 mg protein; Sigma-Aldrich, UK) was added to mop up free metal ions in the solution. A solution of p-isothiocyanatobenzyl-desferrioxamine (p-NCS-Bz-DFO; Chematech, France) in DMSO (10 mM) (Sigma-Aldrich, UK) was then added in a 5 molar excess, and the samples incubated in a thermos shaker (RT, 4 h, Grant Bio, Camlab, UK). The antibody conjugate was purified using a Zeba™ Spin Desalting Column (0.5 mL, 40 kDa MWCO) pre-equilibrated in 0.5M HEPES buffer (4-(2-hydroxyethyl)-1-piperazineethanesulfonic acid) (Sigma-Aldrich, UK), following the manufacturer's instruction. The final concentration was measured by UV-vis at 280 nm. The mAb-to-DFO ratio was estimated by mass spectrometry by Mr Meirion Richards (Structural Chemistry Group, Cancer Therapeutics, The Institute of Cancer Research, UK) performed on a 6520 Series qToF mass spectrometer fitted with a dual electro spray ionisation (ESI) source (Agilent, USA).

#### 3.4.8. <sup>89</sup>Zr radiolabelling

Radiolabelling was performed by Dr Chiara Da Pieve, PET Radiochemistry team, The Institute of Cancer Research, UK. Firstly, <sup>89</sup>Zr in 1M oxalic acid (BV Cyclotron VU, NL) was neutralised with Na<sub>2</sub>CO<sub>3</sub> (2 M; 4.5 μL/10 μL <sup>89</sup>Zr. Sigma-Aldrich, UK) and 0.5 M HEPES (25 μL / 10 μL <sup>89</sup>Zr). The neutralised <sup>89</sup>Zr solution was added to a solution of DFO-ch14.18(CHO) or DFO-IgG1 in 0.5M HEPES (~0.20 MBq/μg). The solution was incubated for 1 h, RT. A suitable volume of 0.1 M EDTA (Sigma-Aldrich, UK) was added to chelate free <sup>89</sup>Zr<sup>4+</sup> ions (1:20 EDTA:Reaction Mix) and the solution was incubated for 15 min. The product was purified using Zeba™ Spin Desalting Column according to the manufacturer's instruction.

The incorporation of <sup>89</sup>Zr and the radiochemical purity (RCP) of the purified radioconjugates were determined by instant thin layer chromatography (ITLC) using silica gel-impregnated strips (ITLC-SG; Agilent Technologies, UK) using 0.1 M ammonium acetate 25 mM EDTA (pH 5.5) as the mobile phase. Strips were visualised and quantified using the phosphor technology module of a Typhoon FLA 7000 scanner. The radioconjugate appears at the origin ( $R_f = 0.0-0.1$ ) while <sup>89</sup>Zr-EDTA is running with the solvent front ( $R_f = 0.9-1.0$ ).

#### 3.4.9. *In vitro* serum stability of <sup>89</sup>Zr-DFO-ch14.18(CHO)

The stability of <sup>89</sup>Zr-DFO-ch14.18(CHO) with respect to loss of radioactivity from the radiolabelled antibody was assessed by incubating the radioconjugate (~2.8 MBq) in mouse serum (500 μL, Sigma-Aldrich, UK) in a thermo shaker at 37 °C (300 rpm). Samples were taken at 0, 1, 3 and 7 days and analysed by ITLC-SG. <sup>89</sup>Zr-oxalate solution (~2.8 MBq) incubated in mouse serum (500 μL) was processed in the same way and used as control.

#### **3.4.10. $^{89}\text{Zr}$ -DFO-ch14.18(CHO) *in vitro* binding affinity and specificity**

To evaluate  $^{89}\text{Zr}$ -DFO-ch14.18(CHO) specificity of binding, approximately  $3.0 \times 10^5$  adherent cells were incubated with a 5 nM solution of the radioconjugate for 1 h, on ice. Subsequently cells were carefully washed with  $2 \times$  PBS, trypsinised, collected and the cell-associated radioactivity was measured using a  $\gamma$ -counter (2480 WIZARD<sup>2</sup>, PerkinElmer, UK). Cells were counted from a control well, and cell-associated activity presented as counts per minute (CPM)/cell. For the blocking studies, the cells were incubated with unlabelled ch14.18(CHO) antibody (50-fold molar excess) for 15 min prior to the addition of  $^{89}\text{Zr}$ -DFO-ch14.18(CHO). Cell binding of the non-specific  $^{89}\text{Zr}$ -DFO-IgG1 was used as a further control.

#### **3.4.11. $^{89}\text{Zr}$ -labelled antibody animal studies**

Subcutaneous SK-N-BE(2)C tumour xenografts were generated as previously described (see page 58). For SK-N-AS xenografts,  $5 \times 10^6$  cells / 80  $\mu\text{L}$  PBS/Matrigel (30 % v/v; BD Matrigel<sup>TM</sup> Matrix, BD Bioscience, USA) were injected to the right flank. When tumour xenografts measured 100–200  $\text{mm}^3$ , mice were anaesthetised with isoflurane/O<sub>2</sub> mixture (1.5–2.0 % v/v) and injected intravenously via the tail vein with either  $^{89}\text{Zr}$ -DFO-ch14.18(CHO) (10  $\mu\text{g}$ ;  $\sim 1.8$  MBq) or  $^{89}\text{Zr}$ -DFO-IgG (10  $\mu\text{g}$   $\sim 1.3$  MBq) in a total volume of 100  $\mu\text{L}$  in sterile saline.

#### **3.4.12. PET imaging and biodistribution**

Static PET/CT images were acquired every 24 h p.i. for up to 96 h, using an Albira PET/SPECT/CT system. Imaging was performed as described above (see page 59) but for 15 min instead of 10 due to the lower branching ratio of  $^{89}\text{Zr}$  compared to  $^{18}\text{F}$ . After the final PET scan, mice were sacrificed, and tumours and major organs taken for biodistribution studies (see page 62) and further *ex vivo* analysis (see below).

#### **3.4.13. Autoradiography**

Autoradiography of tumour and spleen was performed as outlined above (see page 62). Sections were exposed to the X-ray film for 24 h before processing using the Typhoon FLA 7000 phosphorimager (GE Healthcare Life Sciences, UK).

#### **3.4.14. *Ex vivo* flow cytometry**

Mouse spleen and NB tumour xenografts were excised and placed in fresh filtered red blood cell (RBC) lysis buffer (0.15 M NH<sub>4</sub>Cl, 1 mM NaHCO<sub>3</sub>, 0.1 mM EDTA dissolved in sterile irrigation water; pH 7.2-7.4 with 1 M HCl) on ice. Tissues were manually macerated with a scalpel and sterile frosted glass slides and the dissociated tissue placed in a centrifuge tube. An excess (10 mL) of media was added and the mix was spun at 1300 rpm in a centrifuge (Model: Eppendorf 5810R). The supernatant was discarded, and the pellet resuspended in fresh media (3 mL). A 70 µm cell strainer was used to remove multicellular masses (Corning; UK). Cells were counted and approximately  $1 \times 10^6$  cells were taken for each sample. Cells were incubated in a thermomixer with an appropriate amount of fluorescently labelled antibody (Table 3.7), in cell staining buffer (Cat 420201, Biolegend, USA) (4 °C, 20 min, 500 rpm). Fluorescence minus one (FMO) samples were included to calculate compensation requirements. After incubation, cells were washed with cold cell staining buffer, centrifuged (1500 rpm, 3 min), and the cell pellet resuspended in 300 µL of PBS for data acquisition. Flow cytometry studies were performed using a BD™ LSR II flow cytometer (BD Biosciences, USA). For each sample a minimum of  $1 \times 10^5$  events were recorded. NB cells were determined by CD9<sup>+</sup> and CD45<sup>-</sup> gating. Three independent tissues were performed for each sample, and each point was normalised to the median fluorescence intensity acquired  $\pm$  SD. The data were processed using FlowJo software (V10, BD Bioscience, USA), and data analysed using GraphPad Prism software (v.8, La Jolla, CA, USA).

Antibody	Colour	Catalogue no.	Supplier	Dilution
CD9	PE	312105	Biolegend	1:100
CD45	BV510	659482	BD biosciences	1:100
GD2:ch14.18(CHO)	IRDye700DX	Na	In house	1:50

**Table 3.7** List of fluorescently labelled antibodies for flow cytometry of fresh tumour and spleen samples. PE = R-phycoerythrin.

#### 3.4.15. Statistics

Unless otherwise stated *in vitro* experiments are displayed as the mean  $\pm$  SEM of three independent experiments each performed in triplicate and *in vivo* experiments as mean  $\pm$  SD. Statistical significance was determined using Prism software (GraphPad Software v8.0, USA). Statistically significant differences between groups were assumed if  $p \leq 0.05$ . No data were excluded from the analysis, including all outliers. When presented, the p values were calculated by unpaired two-tailed Student's t tests with Holm-sidak correction, a one-way ANOVA with Tukey post-hoc correction or a two-way ANOVA with Tukey's multiple comparisons post-hoc correction.

## Chapter 4 - <sup>18</sup>F-mFBG PET as a tool to measure NET-1 status in NB

### 4.1. Introduction

Neuroblastoma (NB) is characterised by the presence of surface noradrenaline transporters (NET-1) stemming from its sympathoadrenal lineage. Owing to its specific targeting of NET-1 expressing cells, the noradrenaline analogue, *meta*-iodobenzylguanadine, radiolabelled with <sup>131</sup>I (<sup>131</sup>I-mIBG; half-life = 8.02 days) has been used clinically in the detection and treatment of refractory and recurrent NB over the last 30 years [228]. Due to the unfavourable dosimetry profile and decay characteristics of <sup>131</sup>I, <sup>123</sup>I labelled mIBG (<sup>123</sup>I-mIBG; half-life = 13 h) was introduced as a more suitable and effective imaging alternative using 2D planar scintigraphy and 3D single photon emission computed tomography (SPECT) [243]. Consequently, <sup>123</sup>I-mIBG imaging is currently a necessary adjunct for the INRGSS and patient stratification for <sup>131</sup>I-mIBG radionuclide therapy.

Around 90 % of NB tumours are characterised as ‘mIBG avid’ by <sup>123</sup>I-mIBG planar imaging with CURIE/SIOPEN scoring systems [132] and would benefit from targeted molecular therapy. However, despite significant improvements in <sup>131</sup>I-mIBG regimen delivery, only around 50 % of patients respond to current interventions [129-132, 324]. Although CURIE and SIOPEN methods have provided a robust and reproducible means to quantify NB disease dissemination, they do not critically evaluate levels of NET-1 expression in individual tumour lesions and therefore may over-simplify tumour phenotypes. This diminishes the prognostic value of the scoring systems.

<sup>123</sup>I-mIBG imaging, although very useful, shows some limitations linked to the detection sensitivity intrinsic to the scintigraphy and SPECT imaging modality. Conversely, PET allows for 2–3 times greater photon detections during an imaging session resulting in greater image contrast and consequent visualisation of lesions even with low-radioactive

probe uptake. The PET analogues of mIBG, <sup>124</sup>I-mIBG (half-life = 4.2 d) and <sup>18</sup>F-mFBG (half-life = 109.8 min) have both demonstrated superior lesion detection over <sup>123</sup>I-mIBG in the clinic and they are currently being investigated in clinical trials [NCT02348749] [NCT04258592] [NCT02043899] [288-290]. At present, <sup>124</sup>I PET is also under investigation to estimate <sup>131</sup>I dosimetry on account of the chemical, and half-life similarities of the two isotopes. <sup>124</sup>I is not a pure positron emitter, however, with a low positron branching fraction (~23 %) [255]. Furthermore, <sup>124</sup>I emits prompt gammas with energies within the PET energy window, which complicates the signal quantification analysis. On The Other Hand, <sup>18</sup>F is a near pure positron emitter (96.9 % β<sup>+</sup> emissions), and standard quantitative and semi-quantitative methods are habitually used for <sup>18</sup>F-FDG scans allowing for a convenient implementation of the <sup>18</sup>F based radiotracers in clinical studies. Further, owing to a shorter half-life, after <sup>18</sup>F-mFBG administration patients can be conveniently imaged within a few hours rather than the 1–2 days recommended for <sup>124</sup>I-mIBG. The high positron branching fraction of <sup>18</sup>F also serves to reduce the necessary activity delivered for clear PET imaging and can therefore reduce radiation exposure to both the patient and carers—important when regarding patient wellbeing [288]. A short <sup>18</sup>F-mFBG imaging period (i.e. a few hours p.i. of the radiotracer) may also allow for subsequent follow up scans to monitor tumour response during therapy without undue inconvenience [294, 295].

Until recently, the use of <sup>18</sup>F-mFBG has been limited mostly because of its multi-step synthesis, which initially had to be performed manually. In 2014, Zhang *et al.* improved the original procedure and achieved the pure product with a decay-corrected radiochemical yield (RCY) of roughly 11 % and a molar activity of about 18 GBq/μmol [138]. Since then, newer, simplified radiosynthetic approaches have been developed and applied to the production of <sup>18</sup>F-mFBG for clinical use [298, 299, 325, 326].

On this background, I investigated NET-1 expression in several models of NB using <sup>18</sup>F-mFBG PET. I compared the *in vitro* specificity of <sup>18</sup>F-mFBG (produced following a fully-automated cassette-based radiosynthesis developed by the PET Radiochemistry group) with <sup>123</sup>I-mIBG and further studied the pharmacokinetics of both radiotracers *in vivo* using biodistribution analysis and PET or SPECT imaging, respectively. I quantified <sup>18</sup>F-mFBG tumour uptake as a measure of tumour NET-1 expression level. Finally, distribution of <sup>131</sup>I-mIBG was also assessed by SPECT and Cerenkov luminescence imaging in the NET-1 expressing SK-N-BE(2)C NB xenograft model. Cerenkov luminescence imaging allows for an alternative, 2D representation, of <sup>131</sup>I-mIBG distribution. This phenomenon is attributed to the movement of high energy  $\beta$  particles through a dielectric medium faster than the speed of light in that same medium. The particles interact with charged molecules that subsequently release their energy through photons which can then be imaged [327-329].

## 4.2. Results

### 4.2.1. Production and analysis of $^{18}\text{F}$ -mFBG

The automated radiosynthesis and subsequent quality control analysis of  $^{18}\text{F}$ -mFBG were developed and carried out by Mr David Turton, PET Radiochemistry team, The Institute of Cancer Research, UK. Although detailed descriptions of the radioactive agent and its preparation are outside the scope of this thesis, some basic elements will be reported. The schematic representation of the Trasis AllinOne cassette used for the production of  $^{18}\text{F}$ -mFBG is seen in Figure 4.1. and the production methodology in Chapter 3 (see page 54).

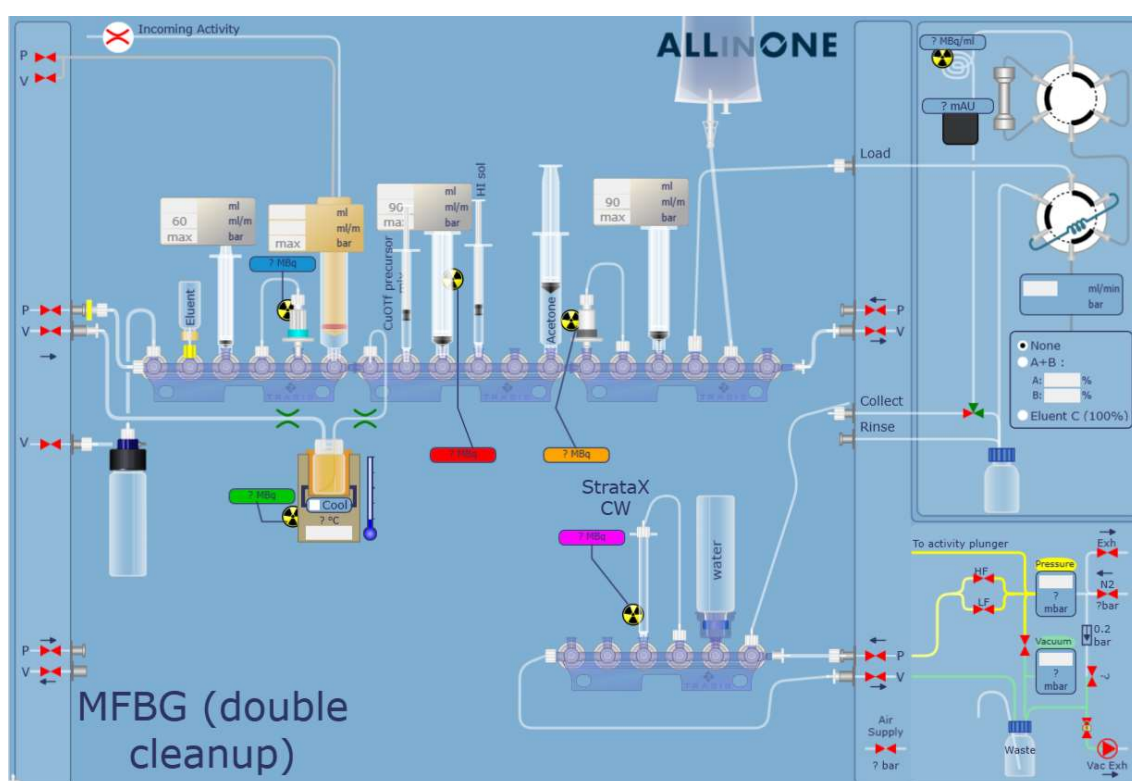


**Figure 4.1** Schematic representation of the Trasis AllinOne cassette set up used for the synthesis of  $^{18}\text{F}$ -mFBG.

The two-step automated  $^{18}\text{F}$ -mFBG radiosynthesis (Figure 4.2-A) yielded the final product with a decay corrected  $6.0 \pm 1.4$  % RCY and molar activity of  $59.0 \pm 35.9$  GBq/ $\mu\text{mol}$  ( $n = 10$ ) at end of synthesis in an overall production time of 110 min. The purified product was achieved with a RCP >98 %, verified by RP-HPLC (Figure 4.2-B).

A  $1.30 \pm 0.54$  MBq/ $\mu\text{L}$  solution of the final product was obtained in volumes of  $\sim 100$   $\mu\text{L}$ , which allowed for the biological investigation of the radioactive agent.

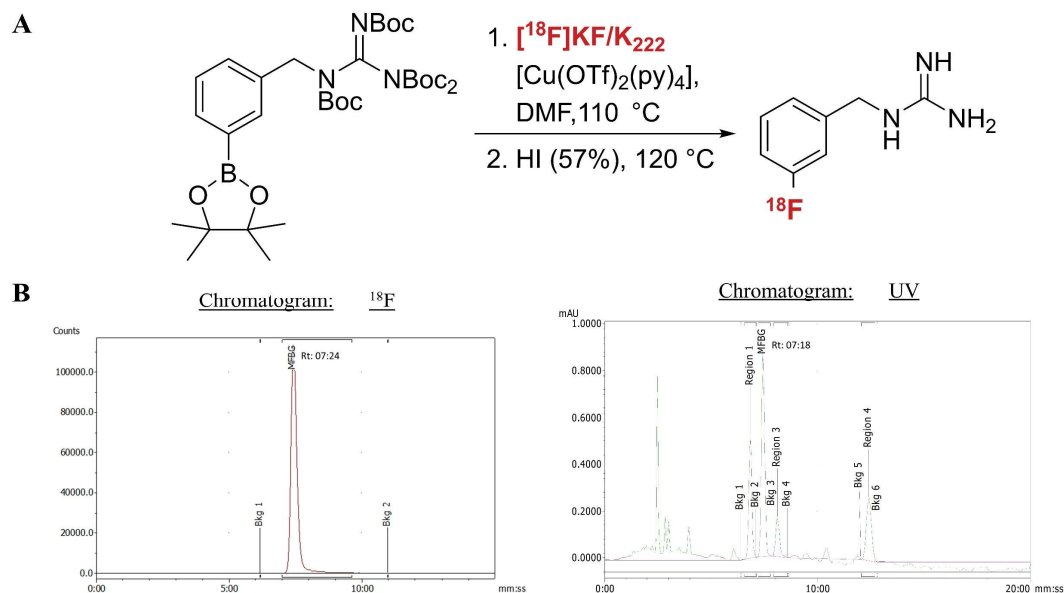


**Figure 4.2** A) Schematic of the two-steps radiosynthesis of  $^{18}\text{F}$ -mFBG. B) Representative HPLC traces of purified  $^{18}\text{F}$ -mFBG. Retention times (Rt) are indicated as minute:seconds (min:s). The product elutes at 7:24 min:s in the radiochromatogram (left) and 7.18 min:s in the UV chromatogram (right).

#### 4.2.2. Characterisation of selected cell lines

Owing to the expression of NET-1 as the essential route of radiolabelled mIBG or mFBG uptake, the protein levels were initially assessed in a panel of NB cell lines by WB to have a selection of cells with NET-1 intensities ranging from low to high for further experiments. Figure 4.3-A indicates that the Kelly cell line had undetectable levels of NET-1 protein by WB, whereas the SK-N-BE(2)C cell line overexpressed the transporter and SK-N-SH and NBL5 cells has intermediate expression. When the band density was measured and normalised to GAPDH expression, SK-N-BE(2)C cells had a significantly higher NET-1 expression to all other cell lines. No difference in protein expression was observed between SK-N-SH and NBL5 cell lines (Figure 4.3-B).

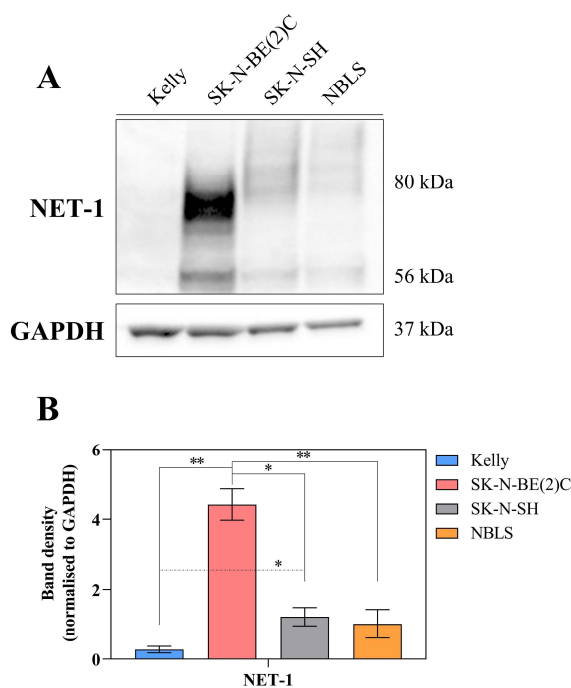


**Figure 4.3** **A)** WB of total NET-1 protein expression in selected NB cell lines. GAPDH was used as the loading control. **B)** Quantification of WB band density. Data are presented as mean  $\pm$  SD of independent blots (n = 4). \* p < 0.05, \*\* p < 0.01; one-way ANOVA with Tukey post-hoc test.

#### 4.2.3. <sup>18</sup>F-mFBG and <sup>123</sup>I-mIBG uptake

The selected NB cell lines were incubated with a solution of either <sup>18</sup>F-mFBG (150 kBq/well) or <sup>123</sup>I-mIBG (5 kBq/well) for 1 h at 37 °C. For both radiotracers, the greatest cell associated radioactivity was observed in SK-N-BE(2)C, to which the other cell lines were then compared (Figure 4.4). The uptake of both <sup>123</sup>I-mIBG and <sup>18</sup>F-mFBG was higher in NBL5 cells compared with SK-N-SH. Radiotracer uptake in Kelly cells was the lowest measured in the cell lines selected (Figure 4.4). Pre-incubation of the cells with desipramine, a selective noradrenaline reuptake inhibitor, successfully reduced the radiotracers' uptake in all cell lines. (Figure 4.4; Table 4.1). <sup>18</sup>F-mFBG uptake paralleled that of <sup>123</sup>I-mIBG and these data correlated with a goodness of fit ( $r^2$ ) of 0.98, and the slope of the line was 0.98 (Figure 4.4-C).

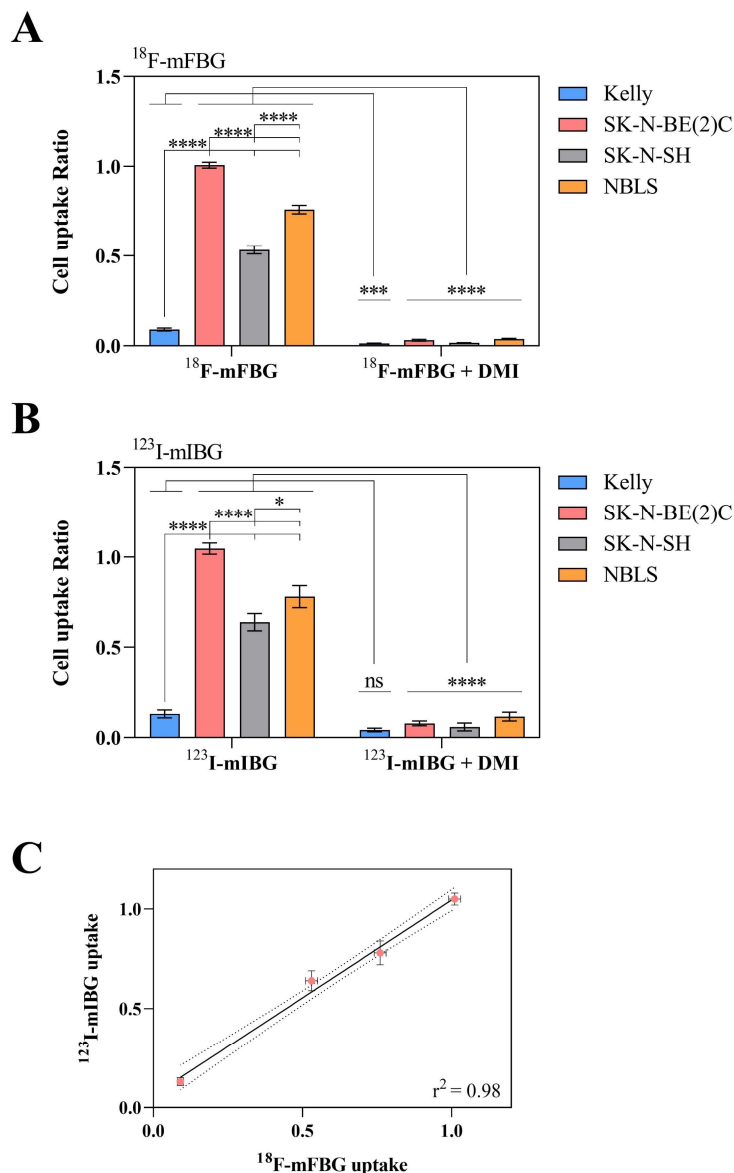


**Figure 4.4** A) <sup>18</sup>F-mFBG and B) <sup>123</sup>I-mIBG uptake in NB cell lines (1 h at 37 °C), with and without 50 μM desipramine (DMI; 15 min pre-incubation). C) Correlation between <sup>18</sup>F-mFBG and <sup>123</sup>I-mIBG uptake ( $r^2 = 0.98$ ). Data are displayed as mean ± SEM. N = 3 independent experiments performed in triplicate. Dotted line represents 95 % confidence interval (CI). \*  $p < 0.05$ , \*\*\*  $p < 0.001$ , \*\*\*\*  $p < 0.0001$ ; two-way ANOVA with Sidak post-hoc test.

Radiotracer uptake (mean $\pm$ SEM)				
	Kelly	SK-N-BE(2)C	SK-N-SH	NBLS
$^{18}\text{F}$ -mFBG	0.09 $\pm$ 0.01	1.01 $\pm$ 0.02	0.53 $\pm$ 0.02	0.76 $\pm$ 0.02
$^{18}\text{F}$ -mFBG + DMI	0.01 $\pm$ 0.00	0.03 $\pm$ 0.00	0.02 $\pm$ 0.00	0.04 $\pm$ 0.00
$^{123}\text{I}$ -mIBG	0.13 $\pm$ 0.02	1.05 $\pm$ 0.03	0.64 $\pm$ 0.05	0.78 $\pm$ 0.06
$^{123}\text{I}$ -mIBG + DMI	0.04 $\pm$ 0.01	0.08 $\pm$ 0.01	0.06 $\pm$ 0.02	0.12 $\pm$ 0.02

**Table 4.1**  $^{18}\text{F}$ -mFBG and  $^{123}\text{I}$ -mIBG uptake in NB cell lines after 1 h incubation at 37 °C, with and without 50  $\mu\text{M}$  desipramine (DMI; 15 min pre-incubation). Data are presented as mean  $\pm$  SEM. N = 3 independent experiments performed in triplicate.

#### 4.2.4. Dynamic PET imaging

In order to first investigate the pharmacokinetics of  $^{18}\text{F}$ -mFBG *in vivo*, I performed dynamic PET scans in mouse NB tumour xenografts using the NET-1 expressing SK-N-BE(2)C cell line. Tumour-bearing mice were injected with  $^{18}\text{F}$ -mFBG ( $\sim 8$  MBq, 100  $\mu\text{L}$ ) and concomitantly underwent a dynamic PET/CT scan (2  $\times$  3 h scans with a 40 min interval subject to the requirements of the Home Office project licence). Subsequently, tumour uptake was assessed over the 6 h scan by manual drawing of a VOI around the tumour region.

During the first PET scan, in all instances the  $^{18}\text{F}$ -mFBG tumour uptake increased rapidly up to 60 min p.i. and at a slower rate thereafter. The signal from the tumour plateaued at around 100 min p.i. (Figure 4.5). When only 12 iterations of the MLEM algorithm were applied to the reconstruction of both scan 1 and 2, there was an inconsistency in signal acquired from before and after the break in scanning. Data were further reconstructed with 20, 24 and 30 MLEM iterations and using just 20 iterations, the discrepancy between the two scans was reduced. More iterations only slightly reduced this difference further (Figure 4.5). For the duration of the second scan, the tumour signal remained stable in two of the three mice (M2 and M3, Figure 4.5), and dropped slightly in the other one (M1, Figure 4.5).

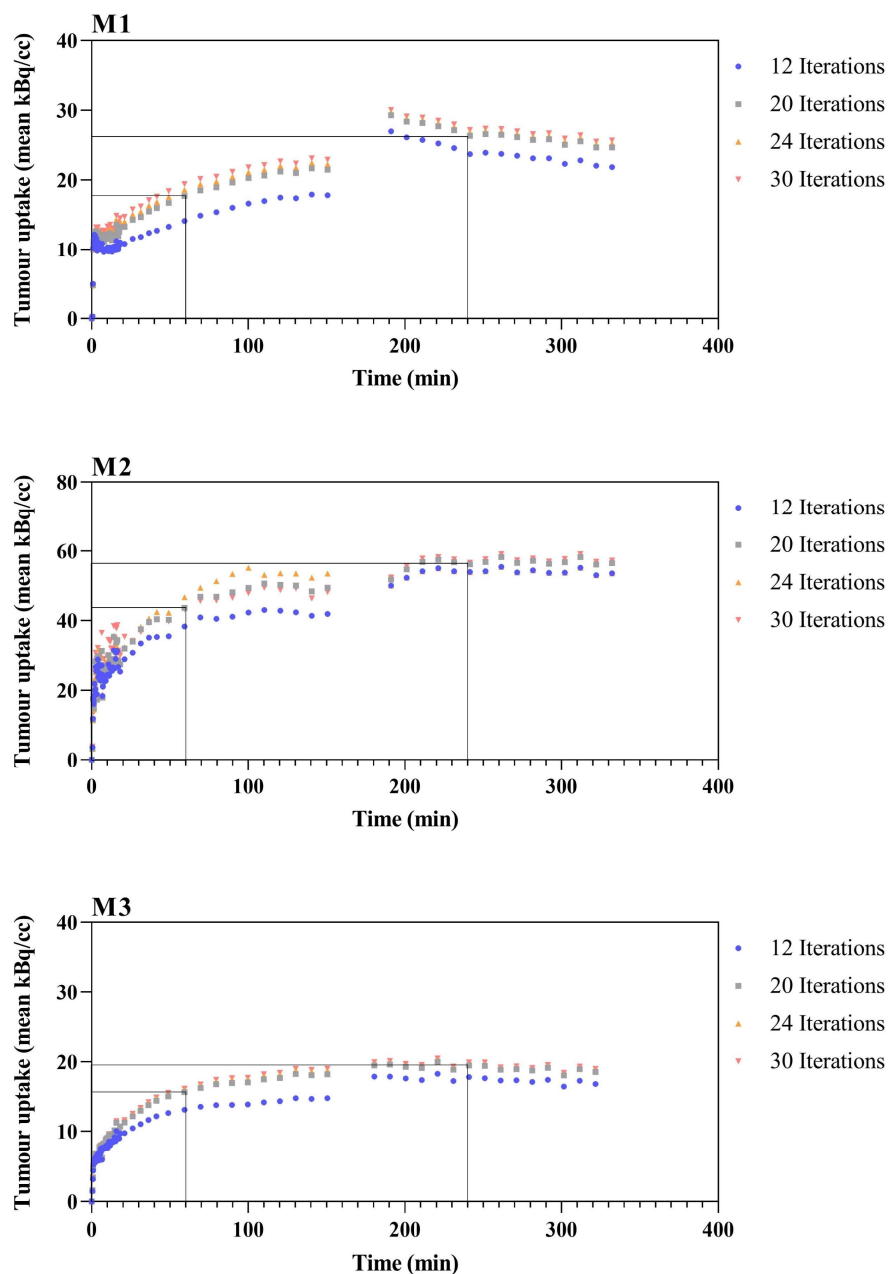


**Figure 4.5** Time-activity concentration curves in SK-N-BE(2)C NB xenografts following injection of  $^{18}\text{F}$ -mFBG ( $\sim 8$  MBq) in individual mice. A VOI was manually drawn around the whole tumour volume and mean activity recorded within (kBq/cc). PET scans were reconstructed with 12, 20, 24 and 30 MLEM iterations. Black lines indicate tumour uptake values at 60 and 240 min.

The signal jump between the first and second scan, most pronounced when reconstructing with 12 MLEM iterations, was most likely attributed to the proximity of the tumour to the bladder and affected by the filling status of the organ (i.e. filling, full, or void). Being

one of the main organs involved in the tracer clearance, the bladder showed a rapid accumulation of radioactivity during the first scan and was naturally voided before the second scan took place leading to over 80 % reduction in the  $^{18}\text{F}$ -mFBG signal from the organ (Figure 4.6). This was further captured as a consequential fall in the signal from the whole body which dropped by a maximum of 72.1 % in M1 and 45.9 % in M3 between the first and second scan in the mice. The  $^{18}\text{F}$ -mFBG signal from the heart was also captured using PET and showed the immediate radiotracer distribution in the blood pool after i.v. injection, followed by an initial fast clearance from the organ up to  $\sim 30$  min p.i. and a subsequently slower tissue clearance after this time (Figure 4.6).

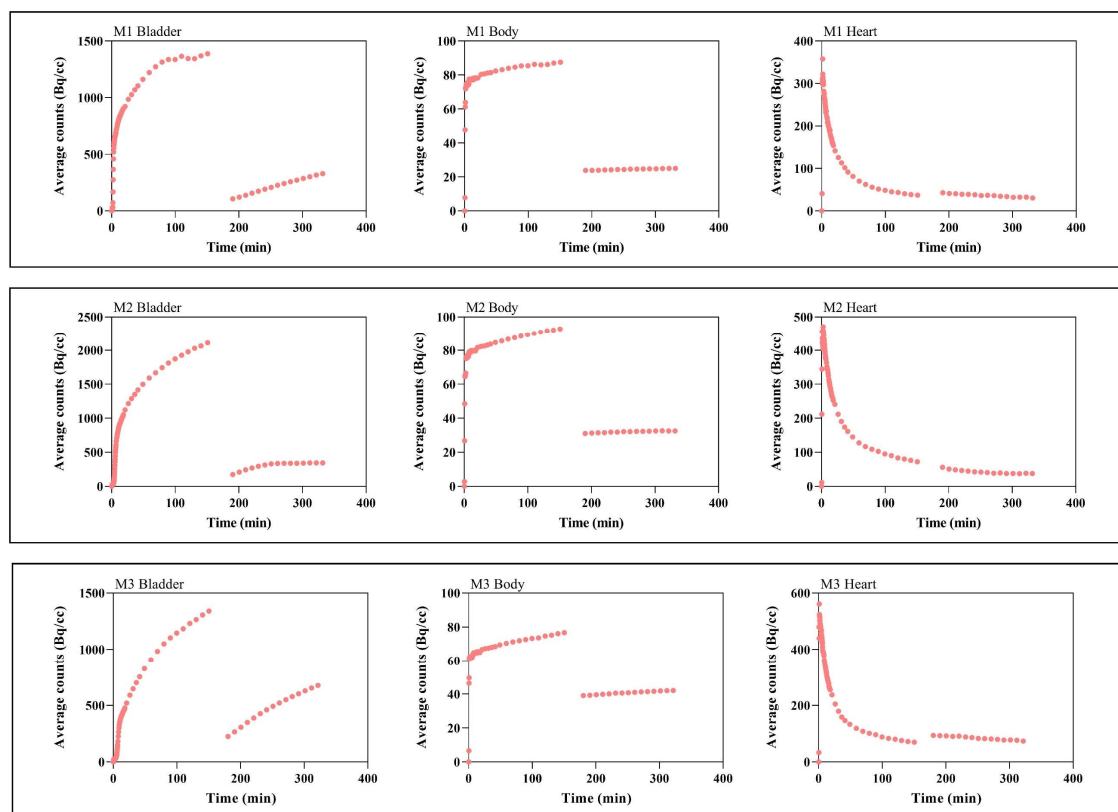


**Figure 4.6** Time-activity concentration curves in mouse bladder, whole body and heart following injection of  $^{18}\text{F}$ -mFBG ( $\sim 8$  MBq) in individual mice. A VOI was manually drawn around the organ/body of interest and mean activity recorded within (Bq/cc). PET scans were reconstructed with 20 MLEM iterations.

Biodistribution studies were performed following the second scan to consolidate PET imaging of the tumour and major organs (Figure 4.7). The highest radiotracer uptake was in the heart ( $2.88 \pm 1.31$  %ID/g), brown adipose tissue (BAT;  $4.79 \pm 3.07$  %ID/g) and small intestines ( $4.54 \pm 0.91$  %ID/g) (Table 4.2). The tumour uptake ( $1.77 \pm 0.82$  %ID/g) was higher than both muscle and blood background.

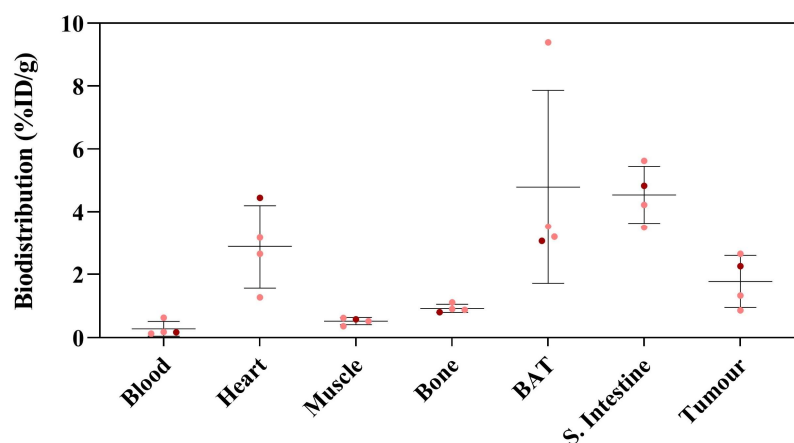


**Figure 4.7** <sup>18</sup>F-mFBG biodistribution 6 h p.i. in SK-N-BE(2)C tumour model following dynamic PET acquisitions. Data are presented as mean %ID/g  $\pm$  SD, n = 4. One mouse did not undergo a dynamic PET scan and is indicated in dark red.

	<sup>18</sup> F-mFBG (%ID/g) 6 h
Blood	$0.28 \pm 0.24$
Heart	$2.88 \pm 1.31$
Muscle	$0.52 \pm 0.11$
Bone	$0.92 \pm 0.13$
Brown adipose	$4.79 \pm 3.07$
Small intestine	$4.54 \pm 0.91$
<b>Tumour</b>	<b><math>1.77 \pm 0.82</math></b>
<b>Tumour: blood</b>	$8.09 \pm 3.73$
<b>Tumour: muscle</b>	$3.36 \pm 1.01$

**Table 4.2** Biodistribution of <sup>18</sup>F-mFBG 6 h p.i. in SK-N-BE(2)C tumour and major organs. Data are presented as mean %ID/g  $\pm$  SD, n = 4. Tumour: blood and tumour: muscle ratios are presented as mean  $\pm$  SD, n = 4.

#### 4.2.5. <sup>18</sup>F-mFBG *in vivo* distribution

Following the dynamic PET scans of <sup>18</sup>F-mFBG distribution *in vivo*, a biodistribution study was assessed using both low (Kelly) and high NET-1 expressing (SK-N-BE(2)C) xenografts. Based on the results of the dynamic scan and previously reported investigations [138], the <sup>18</sup>F-mFBG biodistribution studies were performed at 1 and 4 h p.i.

At 1 h, the uptake was particularly high in the heart (~12.0 %ID/g), BAT (~7.5 %ID/g) and the small intestine (~8.0 %ID/g) (Figure 4.8-A; Table 4.3). A decrease of radioactivity in most of the tissues, but significantly in the heart, spleen, liver and lungs, BAT and intestine, was observed at 4 h p.i. (Figure 4.8-A). The tumour uptake was consistently low in Kelly xenografts from  $0.57 \pm 0.06$  %ID/g measured at 1 h p.i. to  $0.30 \pm 0.14$  at 4 h p.i. The SK-N-BE(2)C tumour uptake was constant with values of  $2.84 \pm 0.80$  at 1 h and  $2.96 \pm 1.38$  %ID/g at 4 h p.i. The difference in tumour uptake between SK-N-BE(2)C and Kelly xenografts was significantly different at 4 h p.i. ( $p = 0.03$ ) (Figure 4.8-B), although not at 1 h p.i.,  $p = 0.06$ . The tumour:blood and tumour:muscle ratios showed no difference between the investigated time points when Kelly xenografts were analysed (Table 4.3). However, in the SK-N-BE(2)C model, the tumour:blood ratios increased from  $7.37 \pm 1.85$  to  $17.69 \pm 10.00$  at 1 and 4 h p.i., respectively, and the tumour:muscle ratios increased from  $2.85 \pm 1.01$  to  $6.24 \pm 3.64$  at the same time points (Table 4.3).

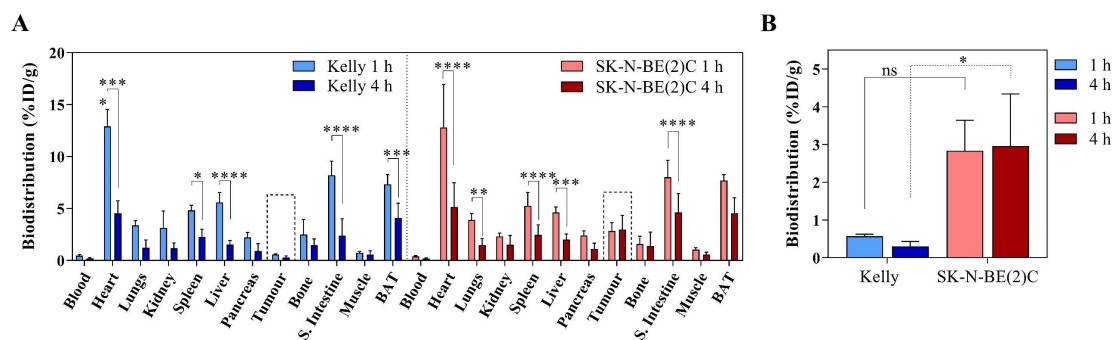


**Figure 4.8** A) Organ and B) tumour biodistribution of <sup>18</sup>F-mFBG 1 and 4 h after injection (~8 MBq) in mice bearing either Kelly or SK-N-BE(2)C xenografts. Data are presented as mean %ID/g ± SD, n ≥ 3, \* p < 0.05, \*\* p < 0.01, \*\*\* p < 0.001, \*\*\*\* p < 0.0001; 2-way ANOVA with Sidak post-hoc test. S. Intestine = Small intestine, BAT = Brown adipose tissue.

	<sup>18</sup> F-mFBG (%ID/g)			
	Kelly		SK-N-BE(2)C	
	1 h	4 h	1 h	4 h
Blood	0.47 ± 0.10	0.18 ± 0.07	0.38 ± 0.07	0.18 ± 0.06
Heart	12.91 ± 1.62	4.55 ± 1.20	12.79 ± 4.15	5.15 ± 2.33
Lungs	3.38 ± 0.44	1.22 ± 0.75	3.90 ± 0.61	1.48 ± 0.62
Kidney	3.14 ± 1.62	1.17 ± 0.50	2.31 ± 0.32	1.51 ± 0.89
Spleen	4.82 ± 0.48	2.26 ± 0.74	5.25 ± 1.28	2.46 ± 0.96
Liver	5.59 ± 0.93	1.53 ± 0.39	4.62 ± 0.52	2.00 ± 0.55
Pancreas	2.20 ± 0.48	0.91 ± 0.72	2.40 ± 0.44	1.10 ± 0.56
<b>Tumour</b>	<b>0.57 ± 0.06</b>	<b>0.30 ± 0.14</b>	<b>2.84 ± 0.80</b>	<b>2.96 ± 1.38</b>
Bone	2.49 ± 1.45	1.47 ± 0.61	1.58 ± 0.74	1.39 ± 1.33
Small intestine	8.20 ± 1.37	2.39 ± 1.62	8.00 ± 1.64	4.63 ± 1.81
Muscle	0.74 ± 0.11	0.56 ± 0.36	1.04 ± 0.19	0.56 ± 0.23
Brown adipose	7.33 ± 0.93	4.08 ± 1.43	7.70 ± 0.56	4.54 ± 1.49
<b>Tumour:blood</b>	<b>1.25 ± 0.26</b>	<b>1.52 ± 0.11</b>	<b>7.37 ± 1.85</b>	<b>17.69 ± 10.00</b>
<b>Tumour:muscle</b>	<b>0.79 ± 0.18</b>	<b>0.56 ± 0.25</b>	<b>2.85 ± 1.01</b>	<b>6.24 ± 3.64</b>

**Table 4.3** Biodistribution of <sup>18</sup>F-mFBG (~8 MBq) 1 and 4 h p.i. in mice bearing Kelly or SK-N-BE(2)C tumour xenografts. Data are presented as mean %ID/g ± SD, n ≥ 3. Tumour:blood and tumour:muscle ratios are presented as mean ± SD, n ≥ 3.

#### 4.2.6. <sup>123</sup>I-mIBG *in vivo* distribution

<sup>123</sup>I-mIBG clinical imaging is usually performed 24 h (and sometimes up to 48 h) p.i. of the tracer. In line with this, and previously reported preclinical studies [138], I assessed

<sup>123</sup>I-mIBG biodistribution in NB xenograft bearing mice 24 h p.i. of the radiotracer (~20 MBq) (Figure 4.9, Table 4.4).

The tumour uptake of <sup>123</sup>I-mIBG in the Kelly xenograft model was low ( $0.07 \pm 0.01$  %ID/g) and similar to background as indicated by the tumour:blood and tumour:muscle ratios of  $1.14 \pm 0.17$  and  $0.91 \pm 0.73$ , respectively. In comparison, with a value of  $1.19 \pm 0.59$  %ID/g, the SK-N-BE(2)C tumour showed greater uptake of <sup>123</sup>I-mIBG ( $p < 0.0001$ ) which ultimately was reflected in high tumour:background ratios (i.e. tumour:blood =  $28.12 \pm 13.60$ , tumour:muscle =  $14.32 \pm 8.13$ ). In both xenograft models, amongst the normal tissues, the heart (~0.9 %ID/g), the small intestine (~1.0 %ID/g) and the BAT (~0.9 %ID/g) showed the highest radiotracer uptake values (Table 4.4).

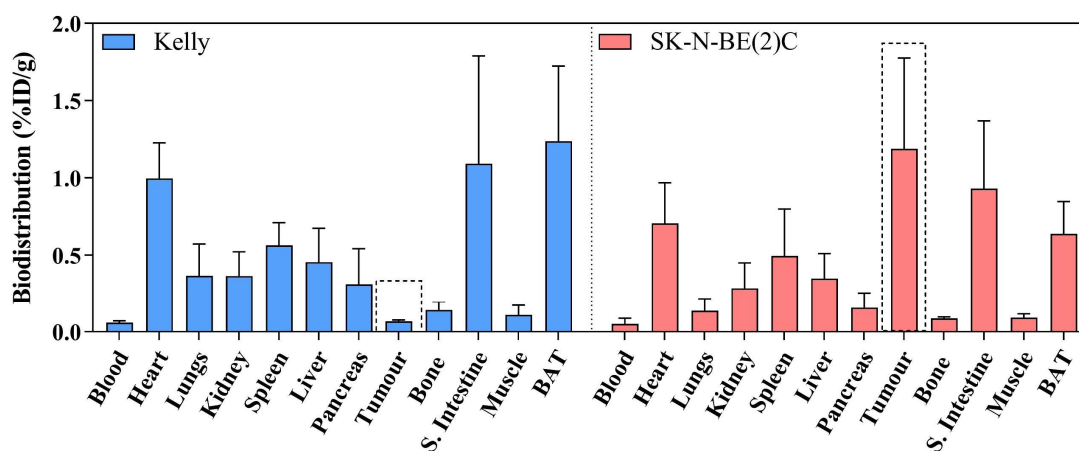


**Figure 4.9** Biodistribution of <sup>123</sup>I-mIBG 24 h after injection (~20 MBq) in mice bearing either Kelly or SK-N-BE(2)C xenografts. Data are presented as mean %ID/g  $\pm$  SD, n = 3. Statistics were calculated by 2-way ANOVA with Sidak post-hoc test. S. Intestine = Small intestine, BAT = Brown adipose tissue.

	<sup>123</sup> I-mIBG (%ID/g)	
	Kelly 24 h	SK-N-BE(2)C 24 h
Blood	0.06 ± 0.01	0.05 ± 0.04
Heart	1.00 ± 0.23	0.71 ± 0.26
Lungs	0.37 ± 0.20	0.14 ± 0.08
Kidney	0.37 ± 0.16	0.29 ± 0.17
Spleen	0.56 ± 0.15	0.50 ± 0.30
Liver	0.46 ± 0.22	0.35 ± 0.16
Pancreas	0.31 ± 0.23	0.16 ± 0.10
<b>Tumour</b>	<b>0.07 ± 0.01</b>	<b>1.19 ± 0.59</b>
Bone	0.14 ± 0.05	0.09 ± 0.01
Small intestine	1.09 ± 0.70	0.93 ± 0.44
Muscle	0.11 ± 0.06	0.09 ± 0.02
Brown adipose	1.24 ± 0.49	0.64 ± 0.21
<b>Tumour: blood</b>	<b>1.14 ± 0.17</b>	<b>28.12 ± 13.60</b>
<b>Tumour: muscle</b>	<b>0.91 ± 0.73</b>	<b>14.32 ± 8.13</b>

**Table 4.4** Organ biodistribution of <sup>123</sup>I-mIBG 24 h after injection (~20 MBq) in mice bearing either Kelly or SK-N-BE(2)C xenografts. Data are presented as mean %ID/g ± SD, n = 3. Tumour: blood and tumour: muscle ratios are presented at mean ± SD.

#### 4.2.7. <sup>18</sup>F-mFBG PET/CT static imaging

Static <sup>18</sup>F-mFBG PET/CT imaging was performed in both Kelly and SK-N-BE(2)C tumour-bearing mice at both 1 and 4 h p.i. to corroborate the biodistribution data. PET/CT image acquisition 1 h p.i. of <sup>18</sup>F-mFBG (~8 MBq, 100 µL) showed a localisation of radioactivity in the abdomen (small / large intestine), cardiac region, the scruff of the neck (BAT) and bladder. Whereas the SK-N-BE(2)C tumours could be delineated via PET alone at 1 h p.i. (Figure 4.10), the co-registration of PET acquisitions with CT scans was necessary to outline Kelly tumours (Figure 4.10). The 4 h p.i. scans showed a lesser signal from non-target tissues (background) allowing for a clear identification of the SK-N-BE(2)C tumours. No demarcation of Kelly tumour was achievable using PET 4 h p.i. of the radiotracer.

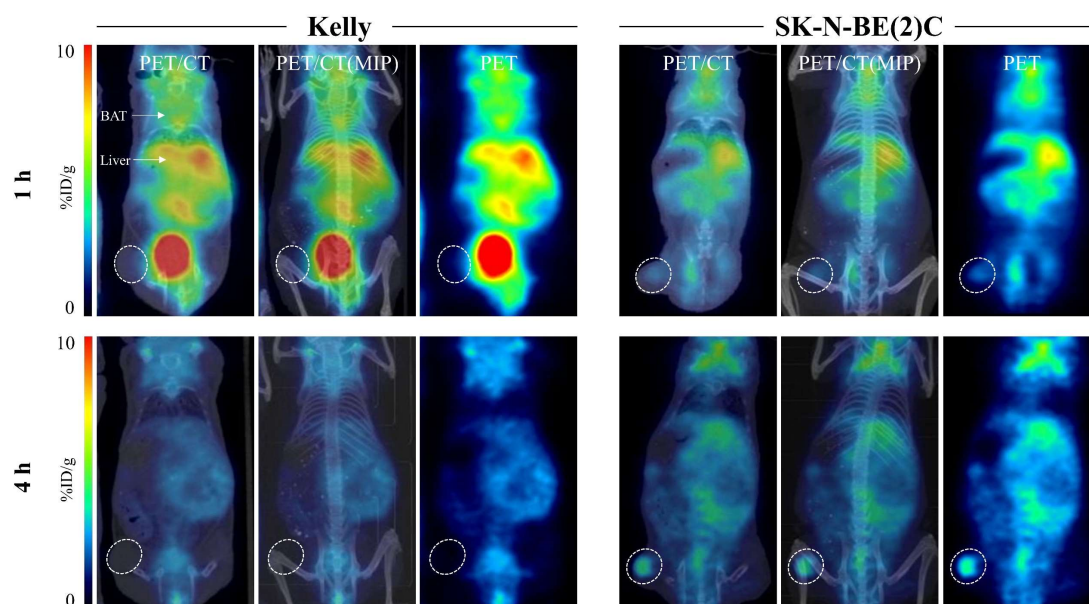


**Figure 4.10** Representative PET and PET/CT images 1 h (top) and 4 h (bottom) p.i. of  $^{18}\text{F}$ -mFBG ( $\sim 8$  MBq) in Kelly (left) and SK-N-BE(2)C (right) tumour models. White dotted line indicates the tumour. PET images are presented as a 2D cross section in the centre of the tumour. MIP = maximum intensity projection of CT.

#### 4.2.8. $^{18}\text{F}$ -mFBG PET quantification

To perform PET quantification, a 3D volume of interest (VOI) was drawn around the tumour-associated PET signal, cross referenced with the CT acquisition, and subsequently automatically contoured to highlight the hottest 50 % of voxels within the VOI. Both the average signal ( $\text{PET}_{50}$ ) of all the voxels, and of the hottest 50 voxels ( $\text{PET}_{\text{HotAv}}$ ), were taken for quantification. These data are presented as a percentage of the injected dose per gram of tissue (%ID/g), whereby the tumour was assumed to have a density of  $1 \text{ g/cm}^3$ .

Owing to the low PET tumour signal in Kelly xenografts, it was not possible to draw a VOI using the PET images alone. Therefore, in this case and generally in the instance of non-avid tumours, co-registered CT scans were necessary to ensure that the drawn VOI appropriately encapsulated the tumour region. As a result, the  $\text{PET}_{50}$  uptakes in Kelly tumours were  $1.12 \pm 0.34$  and  $0.69 \pm 0.26$  %ID/g at 1 and 4 h p.i., respectively. These

values also matched the PET<sub>HotAv</sub> quantification ( $1.12 \pm 0.36$  and  $0.69 \pm 0.28$  %ID/g at 1 and 4 h p.i., respectively). In the SK-N-BE(2)C model, the PET<sub>50</sub> uptakes were  $2.59 \pm 0.57$  and  $3.73 \pm 1.19$  %ID/g at 1 and 4 h, respectively. Again, these values paralleled the PET<sub>HotAv</sub> quantification ( $2.59 \pm 0.60$  and  $3.83 \pm 1.24$  %ID/g at 1 and 4 h p.i., respectively) (Figure 4.11).

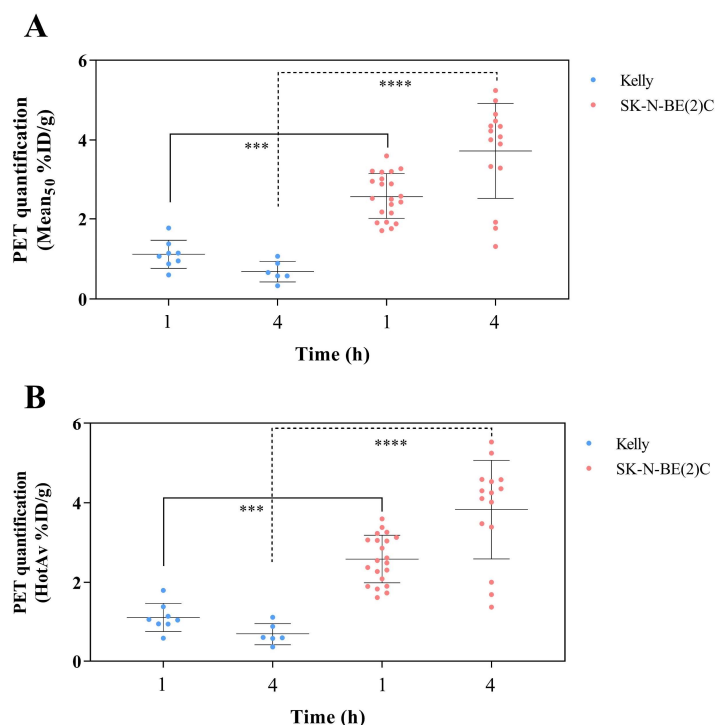


**Figure 4.11** PET quantification of Kelly and SK-N-BE(2)C NB tumours with <sup>18</sup>F-mFBG using **A)** PET<sub>50</sub> and **B)** PET<sub>HotAv</sub> 1 and 4 h p.i. Data are presented as mean %ID/g  $\pm$  SD, each symbol representing a mouse. \*\*\*  $p < 0.001$ , \*\*\*\*  $p < 0.0001$ ; one-way ANOVA with Sidak post-hoc test.

All mice used in this experiment were first imaged and then culled for biodistribution studies. This provided the two sets of tumour uptake quantification data from the same injection to compare and correlate. A linear regression fit between PET quantification and biodistribution data was performed and showed good concordance with an  $r^2$  of 0.73 and 0.72 when using the PET<sub>50</sub> or PET<sub>HotAv</sub> quantification methods, respectively (Figure

4.12). The slope of each line-of-best-fit was 0.72 and 0.71 for the  $\text{PET}_{50}$  and  $\text{PET}_{\text{HotAv}}$ , respectively, and the y-intercept was 0.58 for the  $\text{PET}_{50}$  and 0.62 for the  $\text{PET}_{\text{HotAv}}$ .

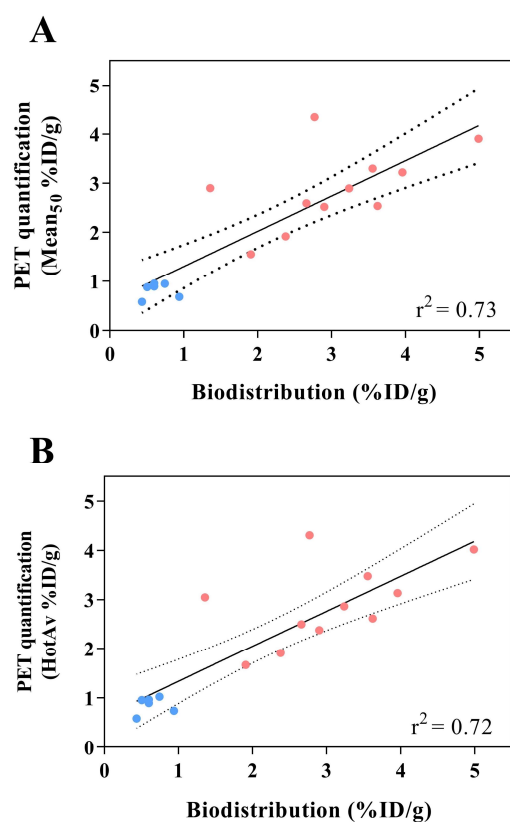


**Figure 4.12** Correlation between PET quantification and biodistribution values for pair-matched tumours. **A)**  $\text{PET}_{50}$  and **B)**  $\text{PET}_{\text{HotAv}}$ . Dotted line represents 95 % CI.

#### 4.2.9. *Ex vivo* tumour analysis

After imaging, autoradiography of tumour slices were performed to assess radiotracer's distribution. Kelly and SK-N-BE(2)C tumour specimens were also processed by WB to assess the total NET-1 expression levels in tumour lysates.

Autoradiography of tumour slices taken after  $^{18}\text{F}$ -mFBG administration (1 h p.i.) showed a generally diffuse, very low radioactivity signal in the Kelly xenograft, whereas a high and uniform radioactivity distribution in the SK-N-BE(2)C tumour sections (Figure 4.13).

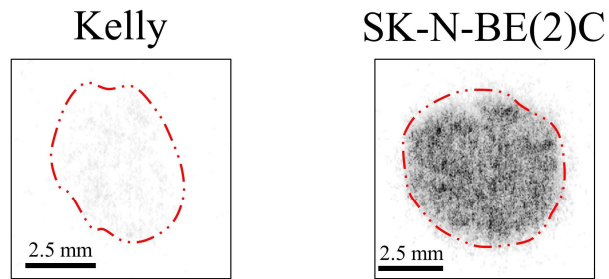


**Figure 4.13** Autoradiography exposition (4 h) of Kelly and SK-N-BE(2)C tumour sections on to X-ray film. Red dotted line indicates the tumour slice outline.

WB performed on three tumour lysates showed a lower expression of NET-1 protein in Kelly tumours compared with SK-N-BE(2)C (Figure 4.14). These results were in concordance to the *in vitro* findings (Figure 4.3).

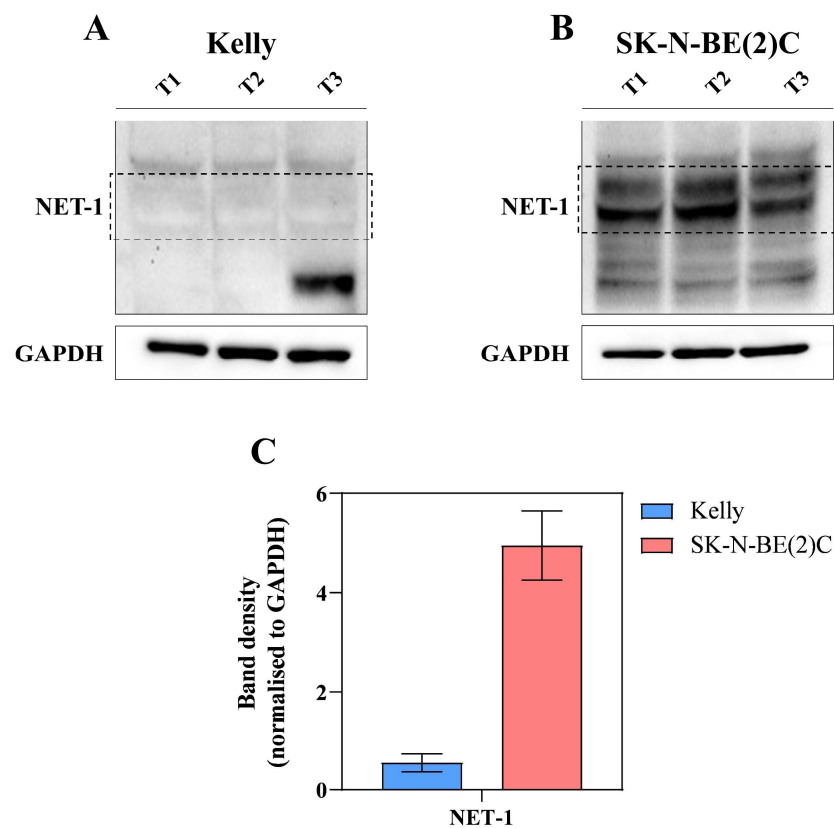


**Figure 4.14** *Ex vivo* WB analysis of A) Kelly and B) SK-N-BE(2)C xenografts of NET-1 protein in three tumour lysates (T1/T2/T3). GAPDH was used as a loading control. Black dotted line indicates purported NET-1 band region. C) Quantification of NET-1 band density normalised to GAPDH. Data are presented as mean  $\pm$  SD (n = 3 per group).

#### **4.2.10. <sup>18</sup>F-mFBG PET/CT imaging of kidney capsule NB model**

In order to confirm the sensitivity of <sup>18</sup>F-mFBG in detecting NB in a clinically relevant location, as a proof of concept, two mice bearing either Kelly or SK-N-BE(2)C tumours within the kidney capsule were generated. Following cell injection in to the left kidney, the tumour growth was monitored using MRI (1 T, Aspect scanner). When tumours reached ~3 mm in diameter, mice were injected with <sup>18</sup>F-mFBG (~8 MBq, 100 µL), and scanned 4 h p.i. H&E staining later confirmed the presence of both Kelly and SK-N-BE(2)C tumours. (Figure 4.15).

In line with the subcutaneous model, the kidney-capsule Kelly tumours could not be delineated on the PET images alone. Conversely, it was possible to demarcate the SK-N-BE(2)C tumours due to the specific uptake of <sup>18</sup>F-mFBG in this case (Figure 4.15). However, it was difficult to distinguish the tumour signal from PET images alone compared to the subcutaneous model, but CT co-registration confirmed the anatomical location of the xenograft. After image acquisition, the kidneys were harvested and measured in a gamma counter. When comparing the radioactivity concentrations in the left (tumour-bearing; 0.79 %ID/g) to the right kidney (non-tumour-bearing; 0.82 %ID/g), no difference was observed in the Kelly model. Conversely, a greater uptake was observed in the SK-N-BE(2)C tumour-bearing kidney (1.74 %ID/g) against the non-tumour-bearing kidney (1.03 %ID/g).

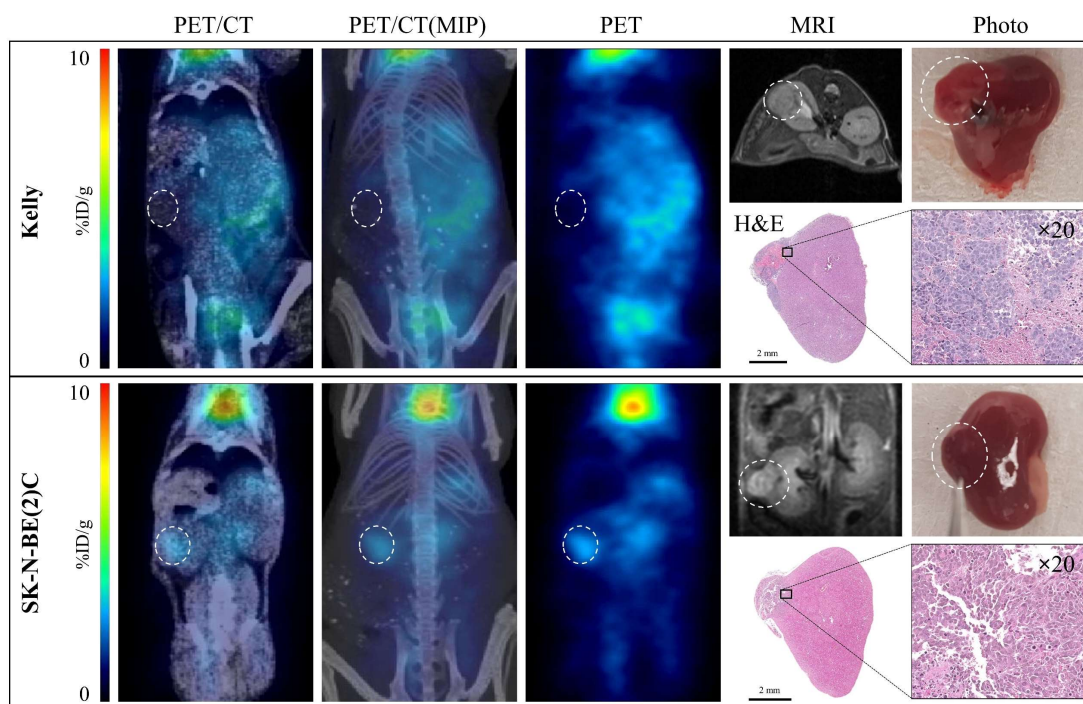


**Figure 4.15** PET and PET/CT images of kidney capsule NB models 4 h post  $^{18}\text{F}$ -mFBG injection. The MR images and H&E staining of tissue sections shows the presence of the tumours and their location in the kidney capsule. Owing to motion blur during image acquisition in both the Kelly and SK-N-BE(2)C tumour bearing mice, an axial and coronal field of view has been presented for each MR image, respectively. White dotted circles indicate the tumour. PET images are presented as a 2D cross section in the centre of the tumour. MIP = maximum intensity projection of CT

#### 4.2.11. $^{123}\text{I}$ -mIBG and $^{131}\text{I}$ -mIBG SPECT/CT imaging

As  $^{123}\text{I}$ -mIBG is an established agent used in clinical imaging of NB, I planned next to perform an *in vivo* imaging study using this radiotracer with the aim to further corroborate the  $^{18}\text{F}$ -mFBG PET imaging data. Kelly and SK-N-BE(2)C tumour-bearing mice were injected with  $^{123}\text{I}$ -mIBG ( $\sim 20$  MBq,  $100\ \mu\text{L}$ ) and imaged by SPECT/CT. Unfortunately, 24 h post-injection visualisation of the tumour or other organs was not possible due to the suboptimal quality of the  $^{123}\text{I}$ -mIBG SPECT/CT images (Figure 4.16-A). To investigate the cause of the low quality images, the SPECT scanner was tested using a syringe phantom of uniform  $^{123}\text{I}$  activity distribution ( $4.7$  MBq). The same parameters from the *in vivo* acquisitions were used. As shown in Figure 4.16-B, the image outlines a

heterogeneous distribution of activity along the syringe. Moreover, the signal intensity profile of the syringe activity identifies differences in peak signal as great as 45 % at the centre of the syringe.

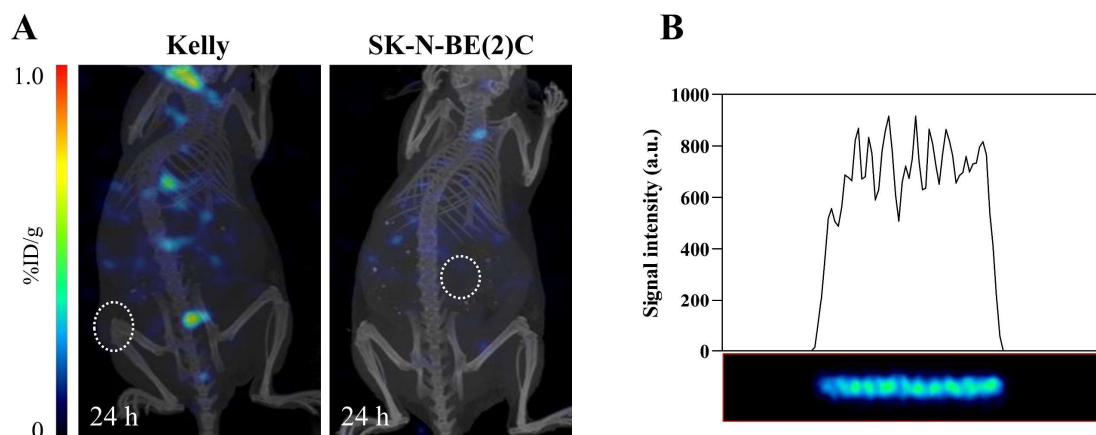


**Figure 4.16 A)** SPECT/CT images of in Kelly (left) and SK-N-BE(2)C (right) tumour-bearing mice 24 h p.i. of  $^{123}\text{I}$ -mIBG (20 MBq). White dotted circles indicate the tumours. **B)** SPECT acquisition of a  $^{123}\text{I}$ -mIBG needle source and line profile of signal intensity.

Beyond its role as a therapeutic agent,  $^{131}\text{I}$ -mIBG also release  $\gamma$  photons which can be imaged by 2D scintigraphy and SPECT. Therefore, I performed a validation study of the imaging of this agent using the Albira SPECT/CT unit. High energy collimators (suitable for collection 364 keV photons) were substituted in for  $^{131}\text{I}$  imaging and an appropriate energy window applied to the acquisition parameters.  $^{131}\text{I}$ -mIBG imaging was performed 24 h, 48 h and 6 d p.i. of the radiotracer in SK-N-BE(2)C tumour-bearing mice (Figure 4.17-A). The signal from the tumour could be clearly visualised after 24 and 48 h p.i. After 6 days, visualisation of  $^{131}\text{I}$ -mIBG distribution was not possible using SPECT.

The decay of  $^{131}\text{I}$  through high energy  $\beta^-$  results in the phenomenon of Cerenkov luminescence. I therefore employed these optical imaging properties to further demonstrate  $^{131}\text{I}$ -mIBG tumour accumulation and substantiate the concordant SPECT

acquisitions. Cerenkov imaging demonstrated  $^{131}\text{I}$ -mIBG accumulation in the tumour comparable to SPECT imaging (Figure 4.17-B).

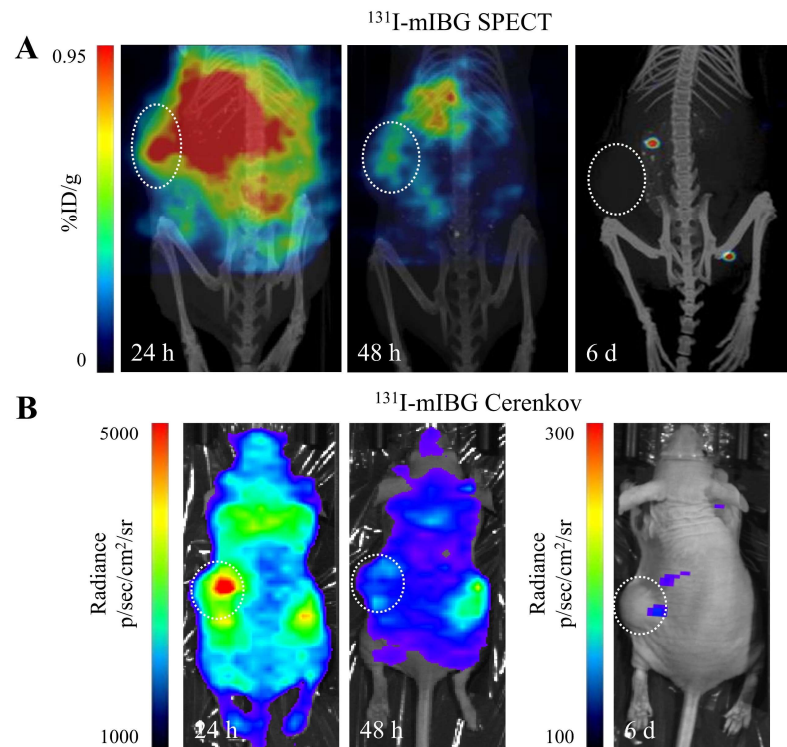


**Figure 4.17** Representative **A)** SPECT/CT and **B)** Cerenkov luminescence images of SK-N-BE(2)C tumour-bearing mice captured 24 h, 48 h and 6 d p.i. of  $^{131}\text{I}$ -mIBG (20 MBq).  $n = 2$ . White dotted circles indicate tumour volume.

### 4.3. Discussion

The radioactive compounds <sup>123</sup>I- and <sup>131</sup>I-mIBG are widely used for the imaging and therapy, respectively, of NB owing to the overexpression of tumour-associated NET-1. Specifically, a <sup>123</sup>I-mIBG baseline scan is a necessary prerequisite for <sup>131</sup>I-mIBG therapy to determine mIBG-avid disease. <sup>123</sup>I-mIBG tumour uptake represents an important measure of disease progression and the increased accumulation of the radiotracer in cancerous lesions is generally associated with an unfavourable outcome [330]. Furthermore, an early response to chemotherapy, monitored by <sup>123</sup>I-mIBG imaging, correlates with good prognosis and improved EFS and OS in high-risk and advanced disease [331]. However, <sup>123</sup>I-mIBG imaging is primarily a descriptive technique, making clinical interpretation and accurate quantitation of a the <sup>131</sup>I-mIBG dose:response relationship challenging. Semi-quantitative scoring systems have been developed (i.e. CURIE or SIOPEN visual scoring system) to provide an objective and uniform way for the evaluation of disease burden and efficacy of therapy [241, 332, 333]. However, PET imaging agents able to measure NET-1 activity would improve both the detection and the quantitation of the disease burden and could provide information of an appropriate and efficacious delivery dose of the therapeutic <sup>131</sup>I-mIBG to the tumour.

For that purpose, <sup>18</sup>F-mFBG, a fluorinated analogue of <sup>123</sup>I-mIBG, has been developed and investigated. Promising data in five NB patients indicates that <sup>18</sup>F-mFBG has similar biodistribution to that of the iodinated correspondent, but faster clearance, higher imaging resolution, and improved assessment of lesion radiotracer uptake [288]. Of note, a new European clinical trial, which began in 2020, is investigating the feasibility of <sup>18</sup>F-mFBG-PET in NET-1 expressing neuroendocrine tumours [NCT04258592].

#### **4.3.1. <sup>18</sup>F-mFBG production**

Firstly, for the use in our preclinical setting, a regular supply of the non-commercially available <sup>18</sup>F-mFBG was necessary. In that respect, the PET Radiochemistry team developed a reliable two-step automated process which consistently produced the tracer in a suitable amount and quality for my experiments, with thanks to Professor Véronique Gouverneur of Oxford University for supplying the necessary precursor. Additionally, the radiosynthesis procedure was developed on disposable cassette based automated system (Trasis AiO) and provided great potential for the GMP-compliant production of <sup>18</sup>F-mFBG for routine clinical use. The design and preparation of the tracer is outside the scope of my research, so no more details in the matter will be discussed.

#### **4.3.2. Correlation of NET-1 expression to <sup>18</sup>F-mFBG and <sup>123</sup>I-mIBG uptake *in vitro***

To begin my investigations in to the use of <sup>18</sup>F-mFBG as an imaging tracer for NET-1 expressing tumours, I first sought to characterise the basal NET-1 protein expression in different NB cell lines *in vitro*. This would allow me to confirm the relationship between NET-1 levels and <sup>18</sup>F-mFBG cell uptake. Further, <sup>18</sup>F-mFBG was compared to the mainstay NET-1 imaging tracer <sup>123</sup>I-mIBG to qualify the fluorinated analogue as a robust surrogate for the iodinated form.

As expected, and in line with previously reported studies [138], uptake of both <sup>18</sup>F-mFBG and <sup>123</sup>I-mIBG correlated with the NET-1 expression levels determined by WB. Clear parallels could be observed between the low and high NET-1 expression in the Kelly and SK-N-BE(2)C cell lines, respectively, (Figure 4.3) and their corresponding low and high radiotracer uptake (Figure 4.4). The relationship between tracer uptake and protein expression in the intermediary NET-1 expressing cell lines, SK-N-SH and NBL5, was not as straightforward. Determination of NET-1 levels by WB band density indicated

similar levels of the protein between the two cell lines, which was in turn around 4 times lower compared to SK-N-BE(2)C. <sup>18</sup>F-mFBG cell uptake showed, however, a greater accumulation of the radiotracer in to the intermediary NET-1 expressing cell lines, with around 53 and 76 % of the SK-N-BE(2)C uptake in SK-N-SH and NBL5 cells, respectively. Moreover, despite WB data suggesting similar levels of the transporter between the two cell lines, the radiotracer uptake in the NBL5 cell line was significantly greater compared to the SK-N-SH cell line. The results seem to indicate that the total transporter expression levels detected by WB may not directly correlate to the radiotracer accumulation in to the cell. Similar findings have been investigated and described by Dubois *et al.* [114], where the researchers evaluated the association of NET-1 protein score (by IHC) in NB tumours against mIBG avidity. Although a significant association between NET-1 and mIBG avidity could be seen, the results demonstrated an imperfect association in some NB tumours (i.e. patients with high NET-1 grading and mIBG non-avid tumours and patients with low NET grading and mIBG avid tumours).

The disparity between the results from the protein levels assessed by WB (Figure 4.3) and the *in vitro* cell uptake of <sup>18</sup>F-mFBG assessments (Figure 4.4) could be an influence of high levels of cytoplasmic NET-1 protein in some of the tested cell lines (i.e. SK-N-BE(2)C and SK-N-SH). Cytoplasmic NET-1 is not involved in the transport of the radiotracers in to the cell, but it could be included in the NET-1 protein band on an immunoblot. As a consequence, the actual membrane associated NET-1 activity in the SK-N-BE(2)C and SK-N-SH cell lines is lower than the protein levels detected by WB resulting in a lower than expected tracer uptake (i.e. lack of correlation between WB assessed NET-1 expression and radiotracer avidity).

The results showed that, like <sup>123</sup>I-mIBG, <sup>18</sup>F-mFBG could clearly quantify the radiotracer avidity as a function of NET-1 transporter function in the *in vitro* setting. Moreover, the

data indicated that WB was useful but not the most suitable method for the assessment of the protein quantities for the purpose of determining the correlation between the NET-1 expression levels and radiotracer uptake. As a proposition of further investigation, greater insight in to the localisation of the NET-1 protein could be obtained by performing live cell flow cytometry with fluorescently-labelled NET-1 antibodies, or performing a pull-down of membrane associated proteins from cell lysates.

#### **4.3.3. <sup>18</sup>F-mFBG dynamic PET imaging and time-activity curves**

The first step in confirming the optimal imaging parameters for <sup>18</sup>F-mFBG in my investigations was to estimate the radiotracer's kinetics in a mouse model bearing a NET-1 positive SK-N-BE(2)C tumour. Owing to restrictions in the Home Office project licence, I designed the experiment over the course of two scans with a gap in the middle to allow the mouse to fully recover from anaesthesia. Although this is not the typical setup to assess the dynamics of a small molecule imaging agent, the imaging still provided a picture of the accumulation of the agent to the tumour and its excretion through the kidney and bladder.

For the tumour, one major observation was in an apparent mismatch in tumour signal between the first and second PET acquisition (Figure 4.5). This phenomenon was attributed to the reconstruction algorithm used and the tumour signal not reaching convergence because of the very radioactive bladder signal in nearby geometry to the relatively colder tumour signal—leading to an underestimation of the tumour signal in the first scan. Following reconstruction with 20, 24 and 30 MLEM iterations, the calculated tumour associated radiotracer activity increased with further iterations in all mice. This was most notable between 12 and 20 iterations from the end of the first scan (when the bladder was at its fullest). In the second scan, after the bladder had been naturally voided by the mouse, the signal quantification increased only slightly between

12 and 20 iterations, suggesting the tumour was already reaching convergence. Increased iterations to 24 and 30 times also increased the noise of the acquisition, when looking at the voxel signal variance in the tumour VOI.

Ultimately, the acquisitions highlighted tumour uptake of the radiotracer plateaued around 100 min p.i. and minimal clearance of the agent was seen. On the other hand, there was continued clearance of the radiotracer from the heart, which suggested that a greater tumour:background could be achieved at later imaging time points.

#### 4.3.4. *In vivo* <sup>18</sup>F-mFBG and <sup>123</sup>I-mIBG biodistribution

Following the dynamic imaging and the clearest distinction between low and high NET-1 expressing cell lines using <sup>18</sup>F-mFBG *in vitro*, I went on to further investigate the radiotracer distribution in mouse models bearing Kelly (NET-1 low) and SK-N-BE(2)C (NET-1 high) subcutaneous xenografts. This would allow me to assess the differences in accumulation of the radiotracer *in vivo*, which I compared to both the distribution of <sup>123</sup>I-mIBG as the clinical standard. The results of this comparison would also corroborate the work performed by Zhang *et al.* using the two radiotracers [138].

The 1 h p.i. biodistribution data showed that <sup>18</sup>F-mFBG accumulates in the heart, small intestine and BAT (Figure 4.8, Table 4.3). This was attributed to the abundance of NE/NET-1 mediated sympathetic innervation of these tissues [99, 101, 334]. Indeed, cardiac imaging is performed using NE analogues (including <sup>123</sup>I-mIBG) for the assessment of abnormalities in sympathetic innervation [335]. Of interest, BAT is more abundant in young children and women [336] and although the quantity of brown fat generally reduces with age, BAT uptake is an important observation when using <sup>18</sup>F-mFBG for disease imaging. This is to avoid false-positive assessments due to BAT uptake in clinical studies with infants and young children, especially as the BAT can be

found in the paravertebral and perirenal areas of the body, nearby to NB origin sites [337, 338].

After 4 h p.i. of <sup>18</sup>F-mFBG, there was a significant clearance from non-target tissues (Figure 4.8, Table 4.3). Uptake in the bone, specifically the knee joint, showed some radioactivity uptake in both xenograft models, but no increase in <sup>18</sup>F signal from 1 to 4 h p.i. was recorded. An enhanced accumulation of signal in the bone is usually indicative of free <sup>18</sup>F, usually a consequence of radiotracer de-fluorination [339]. This suggests that <sup>18</sup>F-mFBG was metabolically stable in the mouse. Reported <sup>18</sup>F-mFBG metabolite analysis has further shown excellent *in vivo* stability in man [288].

Ultimately, accumulation of <sup>18</sup>F-mFBG was specific to SK-N-BE(2)C tumours, which expressed the NET-1 protein and not in non-NET-1 expressing Kelly tumours. Comparing the data from 1 and 4 h p.i., no difference between Kelly or SK-N-BE(2)C tumour uptake was seen. This recapitulated the dynamic PET scans in the SK-N-BE(2)C model, whereby tumour accumulation had plateaued from 100 min to the 6 h time point.

With a longer half-life and imaging at later time points, <sup>123</sup>I-mIBG biodistribution data were collected at 24 h p.i. (Figure 4.9, Table 4.4) and compared with the 4 h p.i. data collected with <sup>18</sup>F-mFBG. The recorded tumour:blood and tumour:muscle ratios were the same for the non-avid Kelly tumour, whereas greater ratios for the iodinated analogue was observed in the avid SK-N-BE(2)C tumour model. This could be attributed to the longer clearance time for the tracer from the non-target tissues. Importantly, both the data for <sup>18</sup>F-mFBG and <sup>123</sup>I-mIBG paralleled tumour and normal organ biodistribution of the previously reported data by Zhang *et al.* in low and high NET-1 expressing NB xenografts [138].

#### 4.3.5. <sup>18</sup>F-mFBG PET/CT imaging and quantification

One of the principal motives for substituting the labelling isotope from <sup>123</sup>I to <sup>18</sup>F was to take advantage of both the radionuclide (i.e. half-life and emission energy) and the PET imaging systems used habitually in the clinic for <sup>18</sup>F-FDG scans. In line with the biodistribution studies, PET/CT images were acquired to qualitatively measure <sup>18</sup>F-mFBG uptake in the low and high NET-1 expressing NB xenograft models. Further, it has yet to be investigated whether robust PET quantification of <sup>18</sup>F-mFBG signals can provide a non-invasive insight in to NB tumour phenotype beyond just the notation of avid versus non-avid disease. Therefore, I set out to implement a method of simple yet robust <sup>18</sup>F-mFBG PET quantification in NB xenograft models.

PET imaging of both Kelly and SK-N-BE(2)C xenografts highlighted an intense signal from the abdominal region (small/large intestine) 1 h p.i. of the radiotracer (Figure 4.10). Also visible were the heart and BAT, which paralleled the biodistribution data. The subcutaneous SK-N-BE(2)C tumour could be clearly delineated at 1 h but this was not possible with the non-avid Kelly xenograft. After 4 h p.i., the signal from the non-target organs reduced, allowing for greater contrast of the NET-1 positive tumour against the background. This confirmed the *in vivo* <sup>18</sup>F-mFBG accumulation based on the NET-1 transporter function and demonstrated that PET imaging is able to discriminate between <sup>18</sup>F-mFBG-avid and non-avid NB lesions.

I went on to visualise <sup>18</sup>F-mFBG tumour uptake in a more clinically relevant model. As NB most commonly arises from the adrenal gland, I used a pseudo-orthotopic kidney-capsule NB mouse model. Importantly, I captured the radiotracer uptake in the SK-N-BE(2)C, NET-1 positive lesions, however owing to a smaller tumour size compared to the subcutaneous model and background signals from the abdominal region, localisation of the tumour was more difficult in this model (Figure 4.15). Co-registering PET with CT

imaging allowed for better delineation of the tumour volume against healthy background tissues. Nevertheless, in the clinical setting, <sup>18</sup>F-mFBG PET have produced robust imaging data for NB lesions located in the lower abdomen and pelvic regions [288], thus negating some of the issues I observed whilst trying to visualise tumours near the abdominal region.

For quantification of the tumour-associated <sup>18</sup>F-mFBG signal on the PET images, a volume of interest (VOI) was drawn around the tumour region. An automatic isocontour to the hottest 50 % of voxels was assigned to encapsulated the majority of the tumour signal for positive lesions and reduce inter-user variability. Both the mean of all voxels in the isocontour (PET<sub>50</sub>) and the mean of the hottest 50 voxels (PET<sub>HotAv</sub>) were acquired. In an ideal situation, the same uptake values are determined from the imaging and the biodistribution data, indicating that the calculated activity from the images is accurately obtained. When a linear regression was used to define the correlation between the two experimental uptake quantities, the biodistribution paralleled the PET<sub>50</sub> and PET<sub>HotAv</sub> quantification from all mice showing a good correlation (based on the  $r^2$  values). However, with a y-intercept of approximately 0.6 and the slope of the line-of-best fit around 0.72, each of the PET<sub>50</sub> and PET<sub>HotAv</sub> overestimated radiotracer uptake at lower values, but was a slight underestimate at higher uptake values in the tumour.

For the non-avid Kelly tumour lesions, quantification of the PET signal was more difficult due to the signal spill-over from adjacent tissues such as the bladder and the intestine. CT co-registration was necessary to ensure that an automatic contour to the hottest PET voxels was located within the tumour region and not a result of spill-over from nearby tissues. Also, in tumours with heterogeneous radiotracer distribution, VOIs drawn using an automatic PET isocontour would on one side reduce the variability in the data output but could also contribute to the over-estimation of the whole tumour uptake. In the studies

performed herein the occurrence of heterogeneous areas of NET-1 expression was limited by the production of xenografts from a single clone cell line. However, in some tumours the above method resulted a higher value attributed to tumour associated <sup>18</sup>F-mFBG by PET compared with the whole tumour uptake data (Figure 4.11). In NB patients, tumours are inherently more heterogeneous than the preclinical models, therefore in this setting, confirmation of the VOI against a co-registered CT would provide a better understanding of the whole tumour radiotracer distribution. For example, VOI could be drawn around each slice of the lesion from the CT image, and the tumour-associated PET signal then calculated. This could provide a good correlation between the PET quantification and actual accumulation, however, this method would be more labour intensive and time consuming. Additionally, this method could be more susceptible to inter-user variability as CT contours may be interpreted differently, resulting in discrepancies in the calculated radiotracer accumulation.

#### **4.3.6. <sup>123</sup>I-mIBG and <sup>131</sup>I-mIBG SPECT/CT imaging**

As a further confirmation of the suitability of <sup>18</sup>F-mFBG PET for NB imaging, I set out to compare SPECT/CT images of the clinically used <sup>123</sup>I-mIBG distribution in both NET-1 low (Kelly) and NET-1 high (SK-N-BE(2)C) tumours. This was performed 24 h p.i of the radiotracer in line with previously reported comparisons between the fluorinated and iodinated NE analogues [138].

Although a series of approaches were assessed (i.e. injection of increasing radiotracer activities, use of single pin-hole collimators of different thickness and application of a variety of algorithms to reconstruct images) it was not possible to visualise *in vivo* <sup>123</sup>I-mIBG distribution using the Albira SPECT/CT system. Initially I investigated whether, due to rapid clearance of <sup>123</sup>I-mIBG, the sensitivity of the SPECT equipment may have been too low to generate a robust image following an injection of 20 MBq of

the radiotracer. However after injecting higher radioactive concentrations of the radiotracer (40 MBq), there was no improvement in the acquisitions. Further, data from scanning a syringe phantom of uniform activity distribution highlighted issues with the acquisition, processing or reconstruction of <sup>123</sup>I images. There was a distinct heterogeneity in the signal across the phantom (Figure 4.16), which confirmed that the <sup>123</sup>I SPECT images were undependable.

Following this, I investigated whether it was possible to visualise <sup>131</sup>I-mIBG *in vivo* distribution using SPECT. Single pin-hole collimators with thicker shielding were used for <sup>131</sup>I imaging compared to <sup>123</sup>I to attenuate the higher energy photons released. Despite only being performed in the high NET-1 expressing tumour model, <sup>131</sup>I SPECT showed a clear uptake in the tumour at both 24 h and 48 h p.i. which was then not visible after 6 days.

Owing to the short field of view possible with the Albira SPECT unit of only 50 mm, I also used Cerenkov imaging to obtain a wider 2D snapshot of <sup>131</sup>I-mIBG distribution in the mouse model (Figure 4.17). Cerenkov luminescence provided a simple and quick image read out that could visualise the tumour associated <sup>131</sup>I-mIBG (Figure 4.17-B). However, being a visible-light based methodology, Cerenkov imaging produced sub-surface images only suitable for the detection of superficial lesions. Although possible to visualise the subcutaneous tumour, it was not possible to see the background distribution that we saw using PET and SPECT imaging, which does not have these same limitations. Ultimately, Cerenkov imaging was a quick and simple technique that could be used in future preclinical investigations in to the relationship between <sup>18</sup>F-mFBG imaging and <sup>131</sup>I-mIBG therapy.

#### 4.4. Conclusions and future considerations

I set out to assess  $^{18}\text{F}$ -mFBG radiotracer kinetics in NB models *in vitro* and *in vivo* and compare this with both  $^{123}\text{I}$ - and  $^{131}\text{I}$ -mIBG. The results described demonstrated that the fluorinated NE analogue was a robust alternative to mIBG radiotracers through similar uptake values in NB cells with various NET-1 expressions. Further, the biodistribution of  $^{18}\text{F}$ -mFBG (4 h p.i.) and  $^{123}\text{I}$ -mIBG (24 h) was comparable in both the low and high NET-1 expressing NB tumour models. Unfortunately, a comparison between  $^{18}\text{F}$ -mFBG PET and  $^{123}\text{I}$ -mIBG SPECT could not be carried out due to suboptimal  $^{123}\text{I}$ -mIBG images, however  $^{131}\text{I}$ -mIBG imaging provided further ballast to the biodistribution results of the two radiotracers. This work, alongside the reported use of the agent in clinical trials, supports the potentiality of  $^{18}\text{F}$ -mFBG as a diagnostic radiotracer for NB.

Beyond the use of  $^{123}\text{I}$ -mIBG to characterise the presence of mIBG-avid disease in patients, data from  $^{123}\text{I}$ -mIBG scans are used to estimate the  $^{131}\text{I}$ -mIBG whole-body and organ absorbed dose that is crucial for determining how much of the therapeutic agent can be safely administered to the patient [340, 341]. Delivery of the  $^{131}\text{I}$ -mIBG is limited by the side-effects associated with higher whole-body absorbed doses, however the relationship between a tumours absorbed dose and whole body dose is not frequently considered. There is a developing consensus that the administration of the radio-therapeutic agent should be personalised to each patient as the pharmacokinetics of the compound is different for each individual, principally as a result of different tissue and whole body clearance and metabolism.  $^{123}\text{I}$ -mIBG dosimetry is considered to be a conservative estimate in different tissues compared to  $^{131}\text{I}$ -mIBG potentially owing to the shorter imaging time-frame allowable. A bi-exponential decay is often assumed for this radiotracer which increases the error involved. Although  $^{18}\text{F}$ -mFBG imaging can only be performed at much shorter time points (1 to 4 h p.i.), it has been noted that  $^{18}\text{F}$ -mFBG has

a much faster clearance than its iodinated counterparts [288]. Therefore, it is not inconceivable that <sup>18</sup>F-mFBG imaging could provide a means to estimate <sup>131</sup>I-mIBG dosimetry and thus an optimal delivery of the agent. However, key studies are required to investigate the potential relationship between the two agents. This would include imaging and whole-body/tumour dosimetry of patients with both <sup>18</sup>F-mFBG and <sup>131</sup>I-mIBG, in sequence, to understand if the clearance and tumour uptakes correlated between the agents. It is unclear as to whether there will exist a linear relationship, or if the two agents will have entirely different pharmacokinetics. The increased hydrophilicity of the fluorinated analogue may effect uptake and residence time in tissues, limiting its prognostic potential.

One recent study using <sup>124</sup>I-mIBG PET for the detection of NET-1 positive NB lesions showed superior lesion detection compared to <sup>123</sup>I-mIBG and the authors suggested the potential for carrying out dosimetry [290]. However a small patient cohort and low numbers of patients/carers consenting to a follow up <sup>124</sup>I-mIBG scan meant that data from these investigations are limited. <sup>18</sup>F-mFBG imaging with shorter total imaging periods and hospital stay time is a key factor for further exploration of the fluorinated analogue.

Additional studies to investigate this preclinically would be to consider the peak accumulation of <sup>18</sup>F-mFBG (measured 1–2 h p.i.) in to a tumour and its measured clearance rate (measured 4 h p.i.) from different tissues and the whole body. Subsequently, a personalised <sup>131</sup>I-mIBG dose can then be quantified using SPECT, and potentially Cerenkov imaging, and the estimates validated. Although tumour lesions may be mIBG-avid, further investigations in to the necessary tumour absorbed dose to induce a therapeutic response to <sup>131</sup>I-mIBG could also help determine if patients are likely to respond to molecular radiotherapy and whether it would be useful alone or in combination with other treatments (e.g. radiosensitisers). Using the Th-*MYCN* model, which has been

shown to take up <sup>131</sup>I-mIBG [342], would be an extremely interesting model to use for further investigation, owing to its sporadic and heterogeneous nature making it physiologically relevant to NB.

## Chapter 5 - <sup>18</sup>F-mFBG PET to monitor changes in NET-1 expression in NB

### 5.1. Introduction

I next assessed the use of <sup>18</sup>F-mFBG to monitor potential changes in the NET-1 expression in NB following therapeutic intervention. From this, one could establish the use of the radiotracer as a tool to optimise combination therapies with <sup>131</sup>I-mIBG in order to enhance targeted tumour cell killing.

As previously mentioned, the response rate to <sup>131</sup>I-mIBG monotherapy in refractory and relapsed NB still remains around 50 %. It has been shown that higher tumour uptake of <sup>131</sup>I-mIBG produces more favourable outcomes in NB [142, 343]. However, by simply increasing the overall dose delivered to the patients, early studies showed a greater incidence of therapy-induced toxicities, such as myelosuppression, from whole body exposure to the radioactivity [129, 130]. Therefore, combination approaches to specifically increase the radioactive payload to the NB tumour can result in augmented cell damage and death. As an example, the histone deacetylase (HDAC) inhibitor vorinostat has been shown to increase NET-1 expression and function in NB cells [344], resulting in greater accumulation of <sup>123</sup>I-mIBG. The drug also sensitises cells to radiation induced cell death through cell cycle arrest and persistence of  $\gamma$ H2AX foci [345-347]. For those reasons, a treatment regimen combining vorinostat and <sup>131</sup>I-mIBG is now under clinical investigation to evaluate tumour response and associated side effects [NCT02035137].

One of the key risk-factors in HR-NB is the amplification of the *MYCN* oncogene which results in high MYCN protein expression. MYCN is associated with cell proliferation, cell growth, and the maintenance of an undifferentiated cell state in NB [41]. Targeting either the transcription of *MYCN* or the stabilisation of the MYCN protein have been substantially investigated preclinically [75, 90, 348] with BET targeting agents such as

molibresib (GSK525762) [NCT01587703] and BMS-986158 [NCT03936465], that are currently investigated in clinical trials. Additionally, several studies are examining the effect of mTOR and Akt inhibition on the depression of MYCN in relapsed or refractory disease [84, 349]. The Akt/mTOR axis is of particular interest due to its central role in several tumorigenic pathways involved in cell growth, proliferation and survival [350]. Opel *et al.* have also highlighted the negative interaction of phosphorylated Akt (at S473 and T308) in the progression of NB. The researchers showed a reduced OS in patients with high p-Akt levels and further positive correlation with *MYCN* amplification [81]. Degradation of MYCN mediated by PI3k/mTOR/Akt inhibitors has been widely demonstrated [84, 351, 352], but clinical trials have been restricted by the dose limiting toxicities of these drugs in children and the mixed clinical responses in both adult and paediatric cancer [353-357]. On that account, using PI3k/mTOR/Akt inhibitors in combination with other therapies may provide more robust clinical responses. Interestingly, Dubois *et al.* reported that patients with *MYCN* amplification have lower NET-1 protein levels than those who are *MYCN* non-amplified [114]. Therefore, targeting *MYCN*/*MYCN* and NET-1 could enhance therapeutic efficacy in NB.

AZD2014 (vistusertib) is a second generation mTOR complex 1 and 2 (mTORC1/2) inhibitor [358] that has shown to control tumour growth in *in vivo* breast and ovarian cancer models, presenting downregulation of mTOR substrates p-S6<sup>S240/244</sup>, p-4EBP1<sup>T37/46</sup> and p-Akt<sup>S473</sup> [359, 360]. Additionally, when used as a single agent in early clinical trials, it has exhibited promising clinical responses in pancreatic and breast cancer patients [361]. However, AZD2014 has failed to produce robust disease management and, in some cases, was less effective compared to first generation mTOR inhibitors such as everolimus [93, 94, 362]. Following exciting preclinical results, AZD2014 was initially proposed in the paediatric ESMART trial [NCT02813135] for solid tumours (including

NB) [90-92], but the drug has subsequently been pulled from this investigation (and by the manufacturer) due to the suboptimal responses seen in adult patients.

Despite these unfavourable findings, ongoing research in to uses of AZD2014 have offered potential future applications of dual mTORC1/2 inhibitors. For example, Yu *et al.* showed that AZD2014 causes cell cycle arrest and can radiosensitise selected oral squamous cell carcinoma (OSCC) cell lines [363]. Further, Mattoo *et al.* demonstrated that AZD2014 can augment the effects of PARP inhibitors through defective homologous recombination (HR) repair, potentiating anti-tumour effects *in vivo* [364]. More recently, AZD2014 has been shown to induce neuroblast differentiation and apoptosis in the Th-MYCN NB genetically engineered mouse model [365].

On this background, I explored the effects of AZD2014 on *MYCN*-amplified NB cell lines. I investigated its ability to enhance NET-1 cell expression for the potential objective of sensitising NB to <sup>131</sup>I-mIBG targeted radiotherapy.

The mechanisms by which NET-1 expression is regulated in NB is still unclear. However, it has been shown that deletion of mTORC2 in mice leads to increased levels of the NET-1 transporter in the sympathetic ganglia [366] and, therefore, treatment with mTORC1/2 inhibitors may also influence NET-1 activity in NB cells. Additionally, Robertson *et al.* demonstrated that the insulin-triggered induction of the RTK signalling pathway decreases NET-1 cell surface expression [367]. The authors also showed that targeted inhibition of the Akt protein restored NET-1 surface expression that was reduced by the insulin treatment [367]. Finally, it has been hypothesised that the increased NET-1 expression following vorinostat-targeted actions on HDAC may proceed through inhibition of non-genomic functions of the drug. For example, it has been shown that disruption of HDAC interactions with protein phosphatase 1 causes subsequent dephosphorylation of Akt at S473 [368]. Hence, aberrant activation of the

PI3k/mTOR/Akt pathway may impair NET-1 expression and function. Downregulation of the pathway through mTORC1/2 inhibition may promote NET-1 expression and function in NB (Figure 5.1).

I therefore used AZD2014 as an mTORC1/2 inhibitor and assessed its effects on NB cell lines and *in vivo* tumour models. Furthermore, I investigated the ability of <sup>18</sup>F-mFBG to monitor *in vitro* and *in vivo* changes in NET-1 transporter expression following AZD2014 intervention.

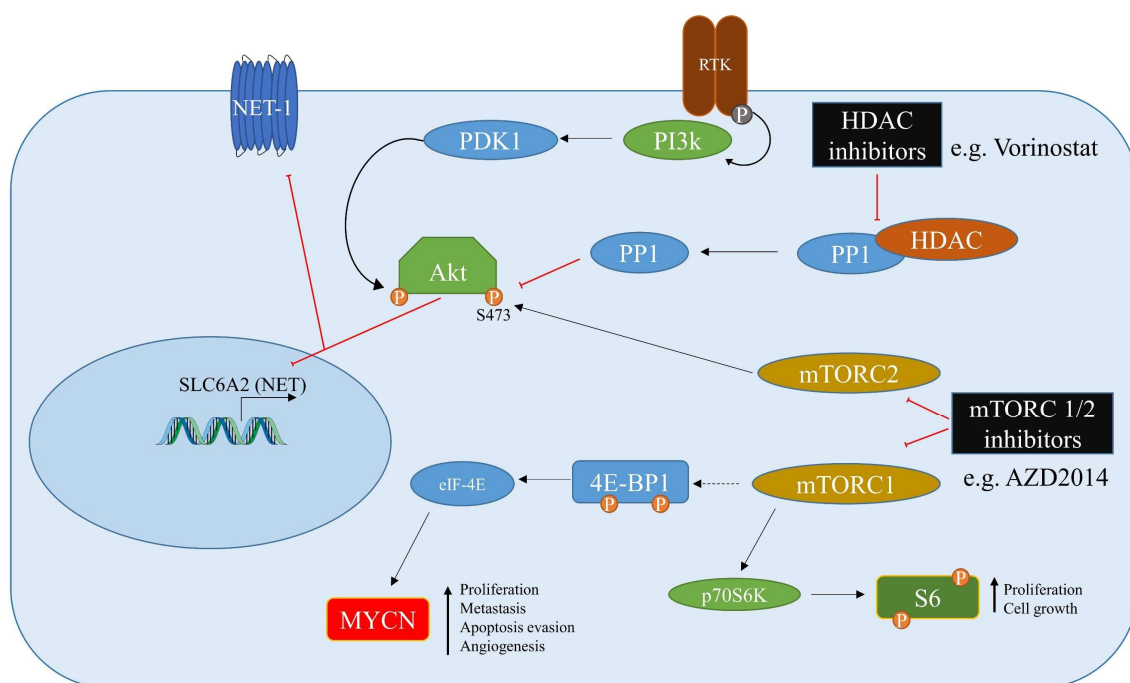


**Figure 5.1** Schematic representation of the role of the PI3k/Akt/mTOR pathway in the repression of NET-1 expression and function in HR-NB. A proposed mechanism of signalling inhibition with vorinostat (HDAC inhibitor) or AZD2014 (mTORC1/2 inhibitor) and signalling on NET-1 synthesis and surface expression in NB.

## 5.2. Results

### 5.2.1. AZD2014 cell viability in MYCN amplified and non-amplified NB cell lines

I first determined the drug concentration that reduces the cell viability by 50 % (GI<sub>50</sub>). For this purpose, a set of NB cell lines was incubated with AZD2014 (0–1 μM) for 72 h. The cell lines with MYCN overexpression, Kelly and SK-N-BE(2)C (Figure 5.2-A), had a GI<sub>50</sub> of 523 nM (95 % confidence interval (CI) = 459–607 nM) and 374 nM (95 % CI = 316–455 nM), respectively (Figure 5.2-B). The SK-N-SH and NBL5 cell lines, which have normal MYCN expression (Figure 5.2-A), had an approximated GI<sub>50</sub> of 1.54 μM (95 % CI = 1.29–2.05 μM) and 1.24 μM (95 % CI = 0.90–2.40 μM), respectively, which were extrapolated from the curves (Figure 5.2-B). From these results, working concentrations of AZD2014 ranging from 0 to 500 nM were chosen for all the following *in vitro* experiments. As MYCN amplification is a hallmark of high-risk disease, the MYCN over-expressing Kelly and SK-N-BE(2)C cell lines were used for the following studies.

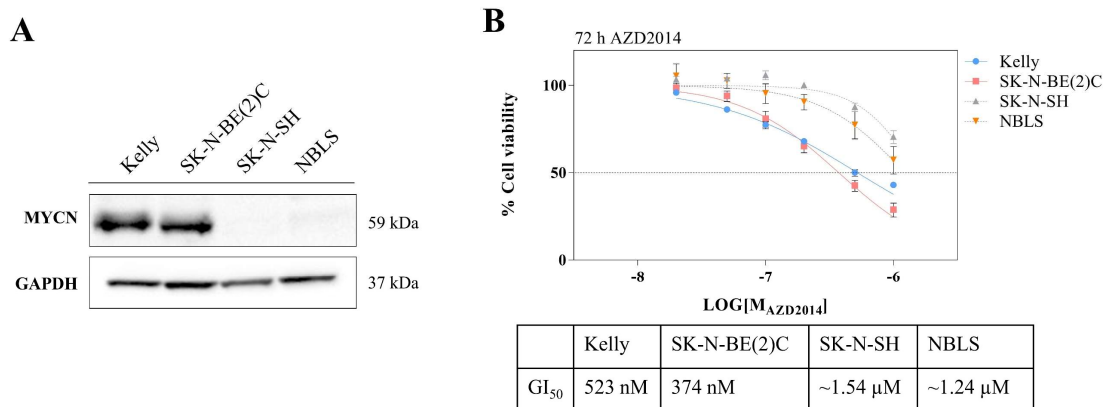


**Figure 5.2** **A)** Representative WB of MYCN expression in a set of NB cells lines. **B)** Cell viability after incubation of the set of NB cells with AZD2014 (0–1 μM) for 72 h and their GI<sub>50</sub> values. Data presented as mean ± SEM, n ≥ 2 performed in triplicate.

When Kelly and SK-N-BE(2)C cells were incubated with up to 500 nM AZD2014 for just 24 h, a cell viability of  $75.36 \pm 3.30$  % and  $71.54 \pm 4.73$  % of the control was recorded, respectively (Figure 5.3-A). Cell cycle analysis (Figure 5.3-B) showed an approximate 1.5-fold increase in the percentage of both cell lines in the G0/G1 phase after incubation with 200 or 500 nM AZD2014 compared with the vehicle control. This coincided with a concentration dependent fall in the percentage of cells in the S phase in both cell lines. A small reduction in the number of Kelly cells in G2/M was observed after treatment with 500 nM AZD2014, although this was not seen in SK-N-BE(2)C cells despite a fall at 200 nM.

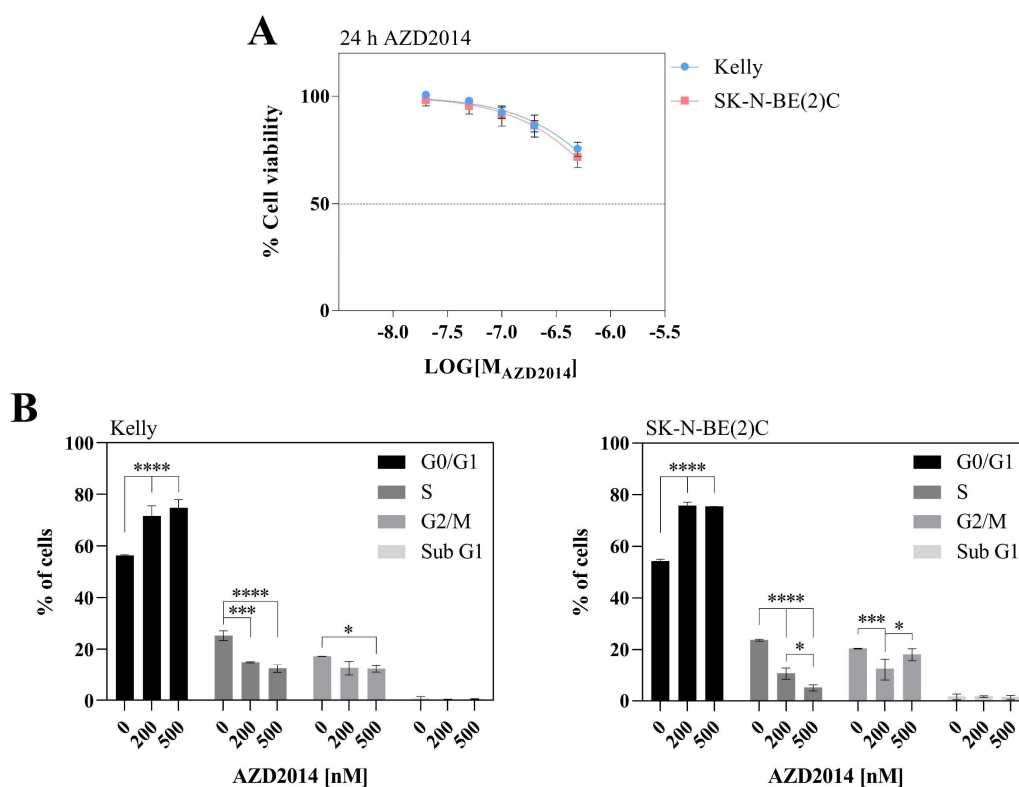


**Figure 5.3** **A**) Cell viability of Kelly and SK-N-BE(2)C cells incubated with AZD2014 (0–500 nM) for 24 h. Data are presented a mean  $\pm$  SEM,  $n = 4$  independent experiments performed in triplicate. **B**) Cell cycle analysis of Kelly (left) and SK-N-BE(2)C (right) cells incubated with AZD2014 (0–500 nM) for 24 h. Data are presented a mean  $\pm$  SD,  $n = 2$  independent experiments. Significance indicated by \*  $p < 0.05$ , \*\*  $p < 0.01$ , \*\*\*  $p < 0.001$ , \*\*\*\*  $p < 0.0001$ ; 2-way ANOVA with Tukey’s post-hoc test.

### **5.2.2. AZD2014-induced mTORC1/2 inhibition and enhanced NET-1 expression in *MYCN* amplified cell lines**

To measure the proposed mTORC1/2 inhibition induced by AZD2014 in Kelly and SK-N-BE(2)C cells, I measured key protein levels involved in the mTOR pathway by WB following incubation with the drug (0–500 nM).

As shown in Figure 5.4, in both cell lines the levels of phosphorylated ribosomal S6 (p-S6<sup>240/244</sup>) and phosphorylated eukaryotic translation initiation factor 4E-binding protein 1 (p-4EBP1<sup>T37/T46</sup>) were reduced in a concentration-dependent manner after 24 and 72 h incubation with AZD2014. Total S6 remained the same, whereas 4EBP1 levels showed some density contraction. However, quantification performed by measuring the WB protein band density indicated that phosphorylated levels of the 4EBP1 were reduced to a greater degree, compared to total protein, at the highest concentration of the drug (500 nM) (Figure 5.5). Inhibition of mTORC2 was evaluated through a decrease in Akt phosphorylation at serine 473 (p-Akt<sup>S473</sup>). In the Kelly cell line, incubation with AZD2014 reduced the levels of total Akt protein and p-Akt<sup>S473</sup> to a similar degree. In the SK-N-BE(2)C cell line, although total Akt levels began to drop after incubation with the drug, p-Akt<sup>S473</sup> levels were the same or even higher compared to the control cells. Of note, the 24 h results are based on the analysis of total Akt expression from only one available blot. A more comprehensive analysis will be described later on.

Since the simultaneous blockade of both mTOR complexes has been shown to lead to *MYCN* degradation in NB cells [84], I also looked at the *MYCN* protein levels after treatment with AZD2014 (Figure 5.4). At the highest concentration of the drug (i.e. 500 nM), *MYCN* expression levels in Kelly cells were reduced mildly, compared to the control, after 24 h, but not after 72 h incubation. *MYCN* levels in the SK-N-BE(2)C cell line were slightly reduced after 72 h. A decrease was detectable already after 24 h

incubation with the drug, although the results could be based on only one blot. Further investigations at this time point are described later on.

I then tested the hypothesis that AZD2014 could affect the total protein expression of NET-1. Assessed by WB, a drug concentration-dependent increase in NET-1 expression was observed in the SK-N-BE(2)C cell lines at 24 and 72 h post drug incubation, although the difference was not significant after quantification of band density (Figure 5.4 and Figure 5.5). A robust analysis of NET-1 levels was not possible in the Kelly cell line because of the overall low expression of the protein.

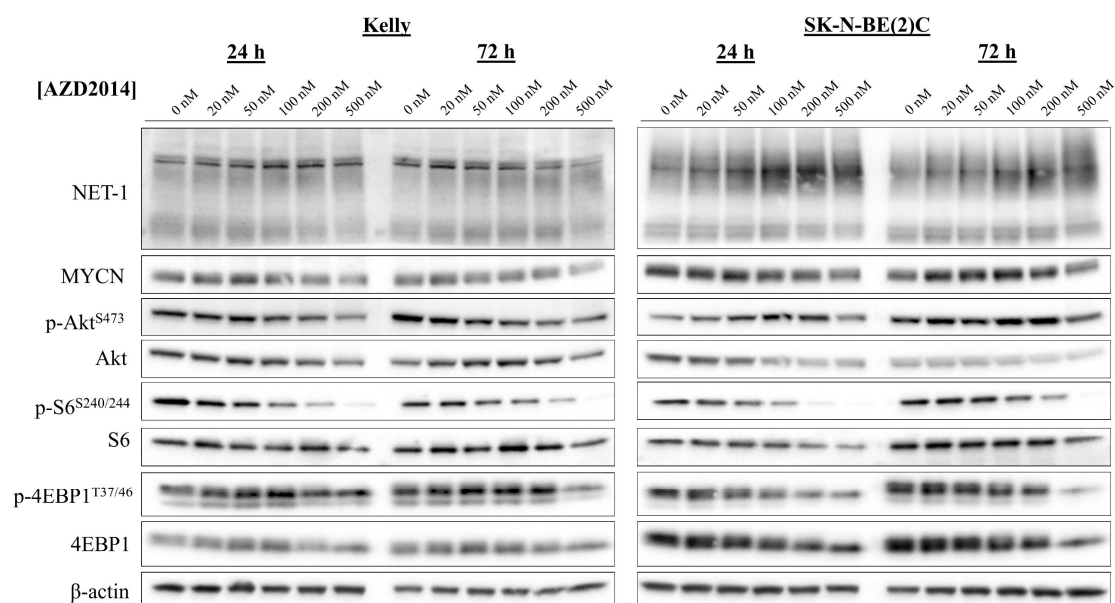


**Figure 5.4** WB of Kelly and SK-N-BE(2)C cell lysates after incubation with increasing quantities of AZD2014 (0–500 nM) for 24 and 72 h.

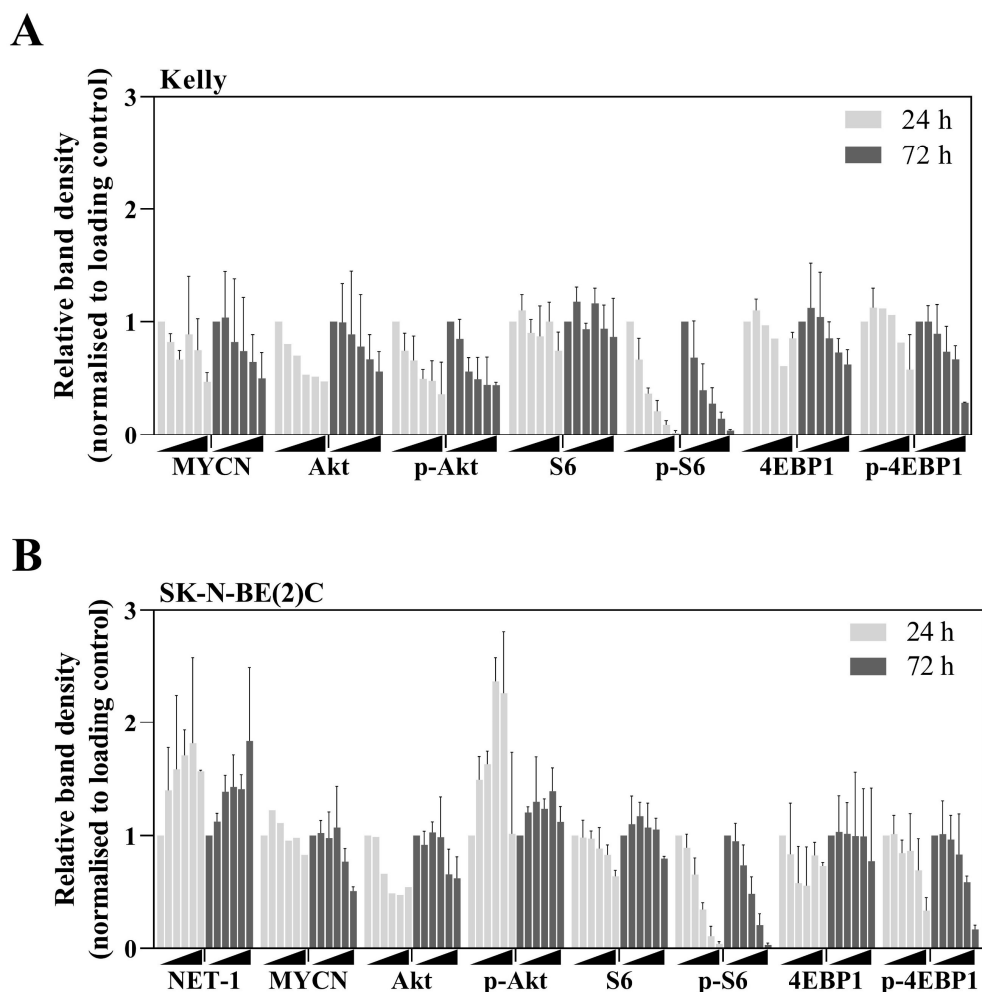


**Figure 5.5** Densitometry of Kelly and SK-N-BE(2)C WB after incubation with increasing concentrations of AZD2014 (▲ indicates the increasing drug concentrations: 0, 20, 50, 100, 200 and 500 nM) for 24 and 72 h.  $n \geq 1$  of independent experiments.

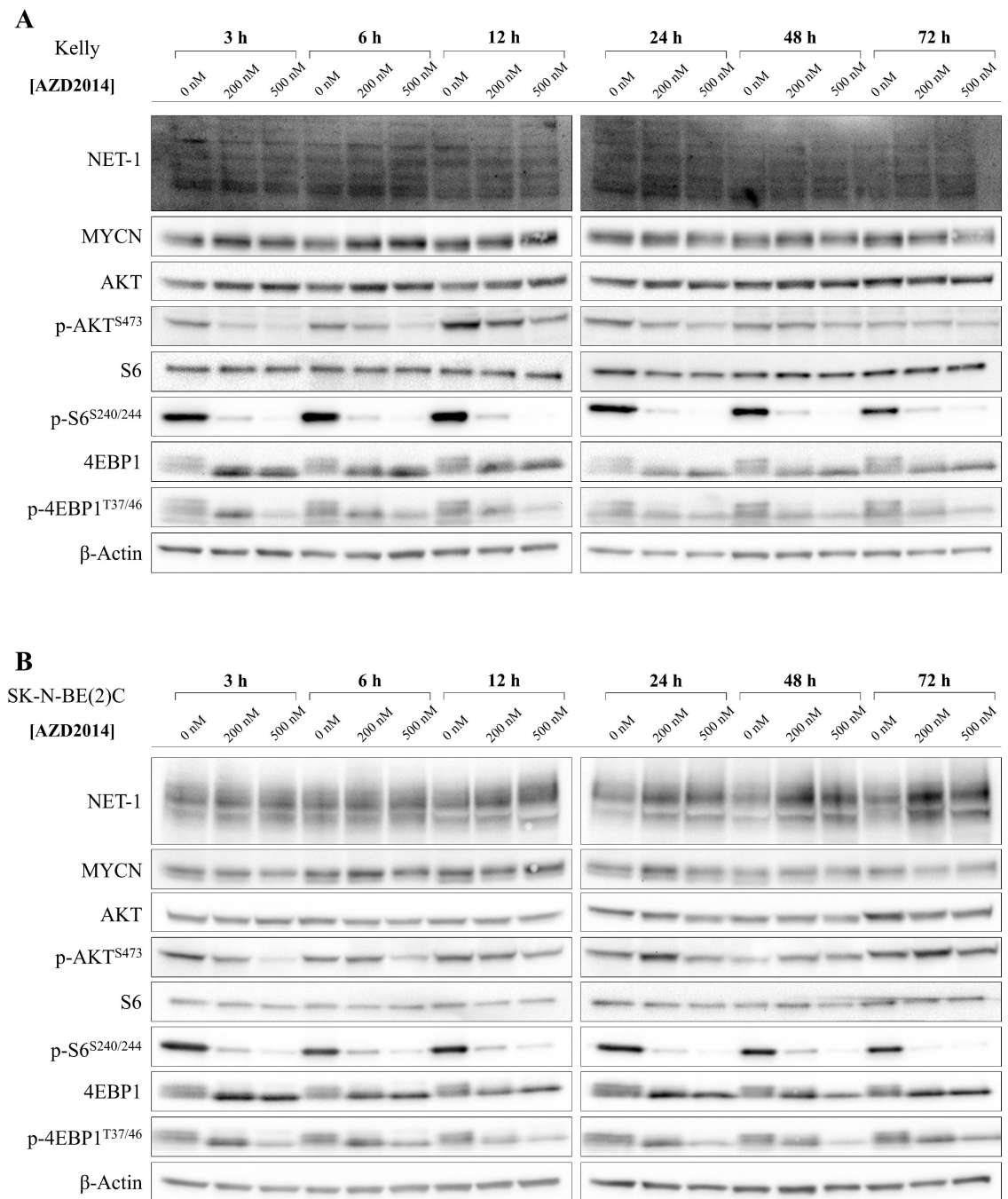
In order to investigate in more detail the dynamics of AZD2014-induced mTORC1/2 inhibition and NET-1 modulation in NB, I performed WB analysis of protein expression after incubating both cell lines with the two highest concentrations of the drug (i.e. 200 and 500 nM) from 3 to 72 h. Band density was also calculated and is presented in Figure 5.7.

As a measure of mTORC1 inhibition, p-S6<sup>S240/244</sup> and p-4EBP1<sup>T37/46</sup> levels decreased as early as 3 h in a concentration-dependent manner and no recovery of the phosphorylated proteins was observed at all points up to 72 h. Examining the mTORC2 activity, p-Akt<sup>S473</sup>

levels showed a concentration-dependent decrease at the earliest time points (3 and 6 h) in both cell lines. However, when the cells were incubated with the drug for longer times, the levels of the phosphorylated protein showed a time-dependent recovery of phosphorylation. Additionally, the expression of Akt in both cell lines was the same between the control and AZD2014 treated cells at all time points (Figure 5.6).

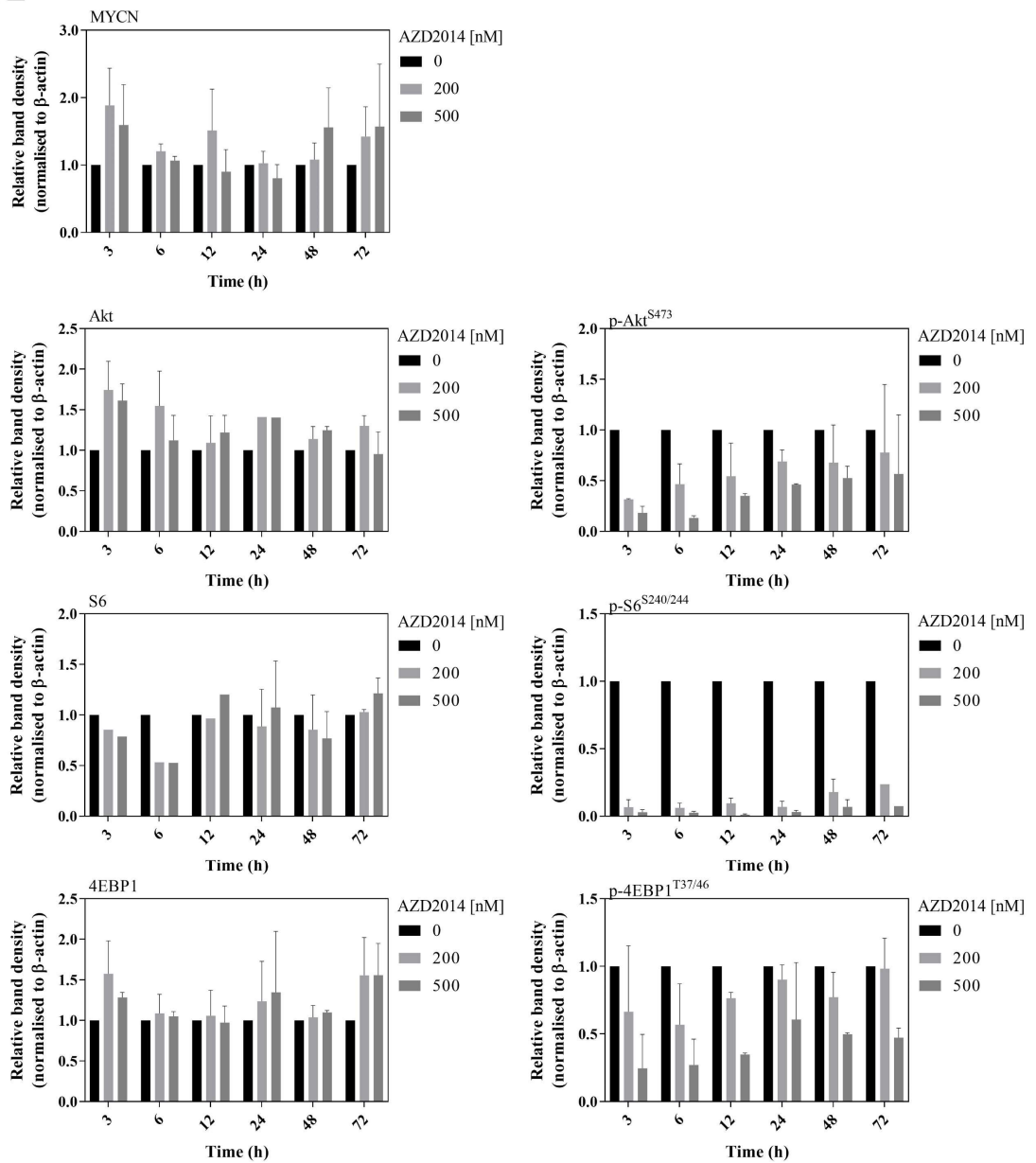
When both 200 and 500 nM of the drug were used on the Kelly cell line, there were no significant changes in the quantity of MYCN protein compared with the untreated controls at any time point (Figure 5.6-A). At 3 h, MYCN levels in SK-N-BE(2)C cells treated with 500 nM drug showed a small drop, however this effect was not sustained (Figure 5.6-B).

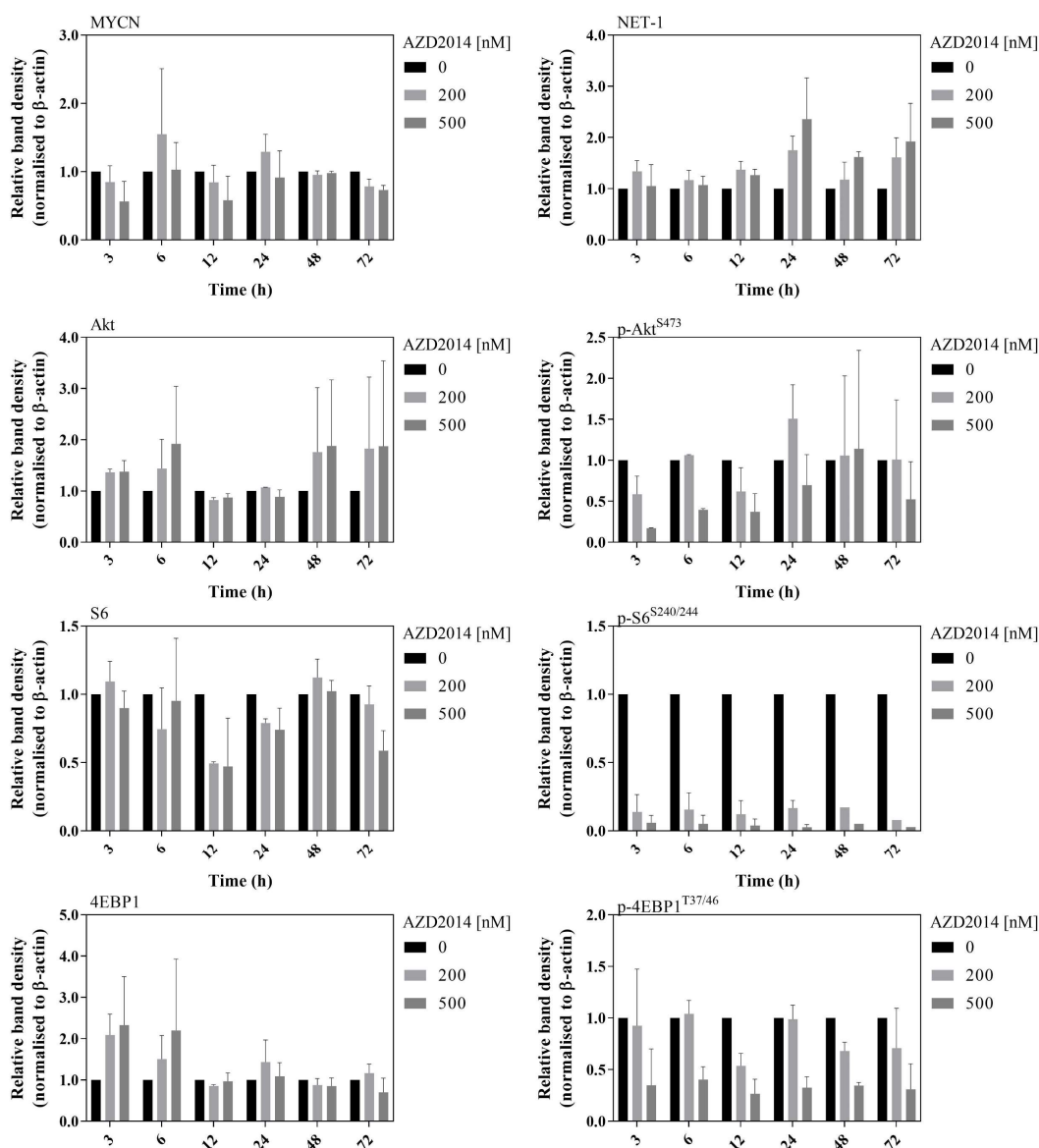
Owing to the low expression of NET-1 in the Kelly cell line, densitometry analysis of the transporter levels was not possible (Figure 5.7-A). In SK-N-BE(2)C, NET-1 immunoblots showed increased protein levels as early as 24 h incubation with 200 and 500 nM of AZD2014, up to 72 h. These variations were not significant as indicated by the band density calculations (Figure 5.7-B).



**Figure 5.6** WB analysis of **A**) Kelly and **B**) SK-N-BE(2)C cell lysates after incubation with AZD2014 (0, 200 and 500 nM) for 3 to 72 h.

**A**



**B**

**Figure 5.7** Densitometry of A) Kelly and B) SK-N-BE(2)C WBs after incubation with increasing concentrations of AZD2014 (0–500 nM) for 3 to 72 h.  $n \geq 1$  of independent experiments.

### 5.2.3. $^{18}\text{F}$ -mFBG and $^{123}\text{I}$ -mIBG uptake in AZD2014 treated cells

To assess whether  $^{18}\text{F}$ -mFBG could detect the changes in NET-1 protein expression following AZD2014 treatment, cell uptake studies were performed. Although it was not possible to properly analyse NET-1 expression by WB in Kelly cells, they were used in the following experiments together with SK-N-BE(2)C cells. The radiotracer was used on both cell lines after incubation with AZD2014 (0–500 nM) for either 24 or 72 h. The

time points were selected based on the NET-1 levels in SK-N-BE(2)C cells according to the WBs. In order to inhibit the active NET-1 transport, desipramine (DMI) was added to some cells prior the radioactive agent. Independent cell viability assays were performed to normalise uptake to differences in cell number following AZD2014 incubation and data were presented as a percentage of the control group in each cell line.

After treatment with the drug for 24 h, the quantity of <sup>18</sup>F-mFBG (150 kBq) in Kelly cell line increased by  $36.63 \pm 25.22$  % in the 500 nM AZD2014 treatment group compared to the control (0 nM). No significant change in the radiotracer uptake was observed in SK-N-BE(2)C cell lines after 24 h drug treatment at any drug concentration (Figure 5.8).

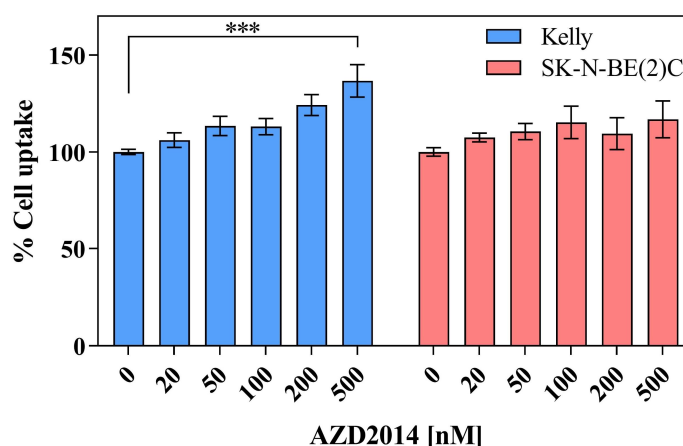


**Figure 5.8** <sup>18</sup>F-mFBG uptake in Kelly and SK-N-BE(2)C cells treated with AZD2014 (0–500 nM) for 24 h. Data are presented as mean  $\pm$  SEM, n = 3 independent experiments, performed in triplicate. Significance indicated by \*\*\* p < 0.001; 2-way ANOVA with Tukey’s post-hoc test.

After the 72 h AZD2014 treatment, a clear concentration-dependent increase in <sup>18</sup>F-mFBG cell uptake was observed in both Kelly and SK-N-BE(2)C cell lines compared to the untreated control. Although a significant increase in uptake was already observed in Kelly cells treated with 100 nM of AZD2014 (p < 0.01), the highest enhancements (by  $122.56 \pm 6.18$  % and  $248.14 \pm 37.48$  %) were recorded after incubation with 200 nM and

500 nM of the drug, respectively (Figure 5.9-A). The SK-N-BE(2)C cell line showed a  $85.44 \pm 20.81$  % and  $141.74 \pm 29.72$  % greater uptake of <sup>18</sup>F-mFBG after the treatment with 200 nM and 500 nM AZD2014, respectively. After pre-incubation with 50  $\mu$ M of DMI, the <sup>18</sup>F-mFBG uptake in untreated Kelly cells decreased by over 50 %, compared to the control, (0 (DMI), Figure 5.9-A) and fell by over 90 % in the 500 nM AZD2014-pretreated Kelly cells (500 (DMI), Figure 5.9-A). Also in SK-N-BE(2)C cells, desipramine inhibited the radiotracer uptake by over 97 % in both the control and treatment groups (Figure 5.9-A).

To confirm these findings, a cell uptake assay was also performed with <sup>123</sup>I-mIBG. Uptake of <sup>123</sup>I-mIBG increased in a concentration-dependent manner in AZD2014 treated Kelly and SK-N-BE(2)C cell lines. The radiotracer uptake increased by nearly four-fold in Kelly cells incubated with 500 nM of the drug. Further, radiotracer levels in SK-N-BE(2)C cells doubled in the 500 nM AZD2014 group. Again, desipramine was able to significantly lower the radiotracer uptake in both cell lines (Figure 5.9-B).

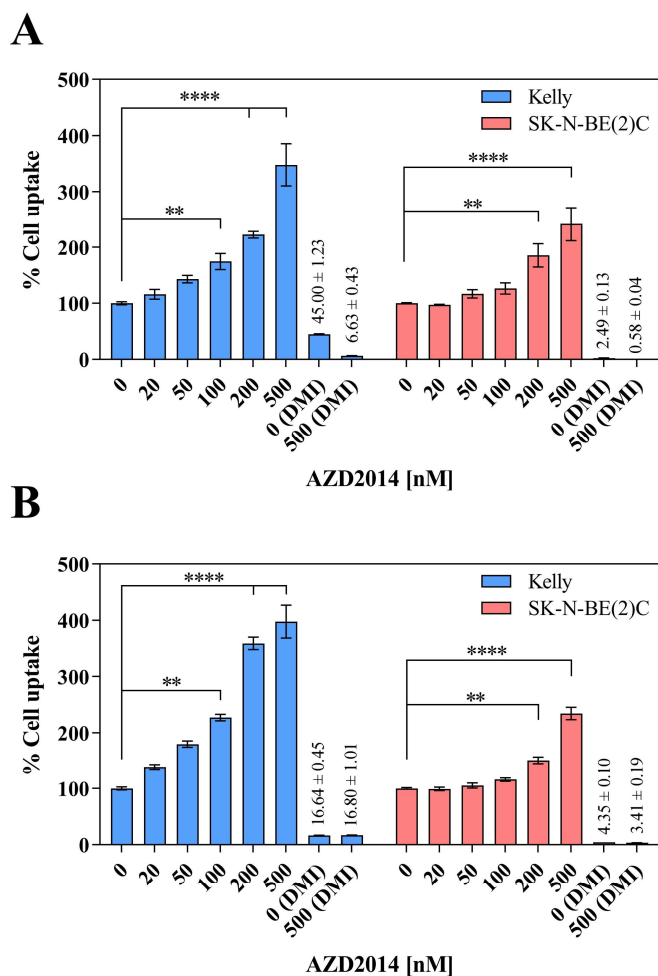


**Figure 5.9** A) <sup>18</sup>F-mFBG and B) <sup>123</sup>I-mIBG uptake in Kelly and SK-N-BE(2)C cells treated with AZD2014 (0–500 nM) for 72 h with and without NET-1 inhibitor desipramine (DMI; 50  $\mu$ M; 15 min pre-incubation). Data are presented as mean  $\pm$  SEM; n = 2 independent experiments, performed in triplicate. DMI (blocking) studies were performed n = 1, and presented as mean  $\pm$  SD. Significance indicated by \*\* = p < 0.01, \*\*\* p < 0.001, \*\*\*\* p < 0.0001; 2-way ANOVA with Tukey’s post-hoc test.

#### 5.2.4. AZD2014 *in vivo* toxicity and NB tumour growth

Following the observations of increased <sup>18</sup>F-mFBG uptake in AZD2014-treated cells *in vitro*, I next planned to investigate the effect of the drug *in vivo* using Kelly and SK-N-BE(2)C xenograft models and <sup>18</sup>F-mFBG PET. Before that, the AZD2014 *in vivo* toxicity and the NB tumour growth during treatment were assessed.

In this regard, SK-N-BE(2)C tumour bearing mice were treated with a bolus oral gavage of 20 mg/kg/day AZD2014 or vehicle control for 1, 3 and 7 days. At this dosing schedule, no toxicities were observed and the body weight remained stable in all mice for the whole duration of the treatment (Figure 5.10). A set of SK-N-BE(2)C and Kelly tumour bearing mice were treated with 25 mg/kg/day AZD2014 (bolus dose) for up to 3 days. Mild toxicities were observed after 3 days in the drug-treatment group, including mild emaciation and lethargy. Collectively, at the higher dose, AZD2014-treated mice lost weight during the treatment schedule. One major toxicity was observed whereby one mouse was sacrificed after losing >20 % body mass over the three day treatment-period and was not used for further *in vivo* investigations (Figure 5.10).

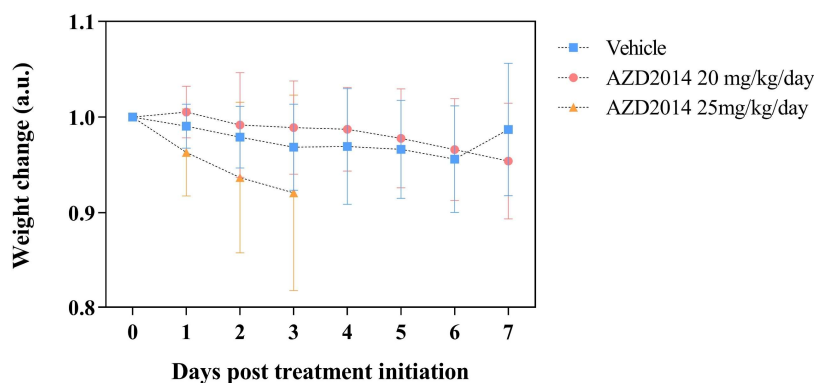


**Figure 5.10** Change in mouse body weight following treatment with either AZD2014 (20 and 25 mg/kg/day) or vehicle (10 % DMSO, 90 % PEG400) for up to 7 d. Data are presented as mean  $\pm$  SD,  $n \geq 4$  per group. Statistical differences were measured for by a two-way ANOVA with Tukey post-hoc analysis.

The tumour size was determined by daily calliper readings during treatment, and is presented in Figure 5.11 as change from the treatment start date (Day 0). At Day 0, tumour sizes were 75–150 mm<sup>3</sup>. Measurements of tumour volume indicated that in the vehicle treated group, Kelly tumours doubled over the 3-day treatment period to ~2.3 times their size compared to day 0. During either the 20 or the 25 mg/kg/day AZD2014 dosing

regimen, Kelly tumours increased size but were significantly smaller than the vehicle control. Their size became a maximum of  $1.75 \pm 0.13$  ( $p = 0.01$ ) and  $1.24 \pm 0.17$  ( $p < 0.0001$ ) times larger, respectively, over the same period (Figure 5.11-A). SK-N-BE(2)C tumours sizes in the vehicle treated group were  $1.94 \pm 0.44$  times greater than baseline after 3 days treatment. Similar results were recorded for both the 20 mg/kg/day AZD2014 ( $1.82 \pm 0.76$  larger compared to day 0) and the 25 mg/kg/day treatment group ( $1.55 \pm 0.38$  times greater than baseline) after 3-days treatment. However, at the highest drug dose, the tumours reached a maximum size increment after the second of the 3 days of treatment ( $2.09 \pm 0.42$  times the day-0 size) (Figure 5.11-B). During the longer study (7 days), the vehicle and 20 mg/kg/day AZD2014 treatment groups mean tumour size increased by  $8.25 \pm 4.75$  ( $n = 4$ ) and  $4.55 \pm 2.61$  ( $n = 5$ ) times, respectively. The difference between groups was not significant ( $p = 0.74$ ) (Figure 5.11-B).

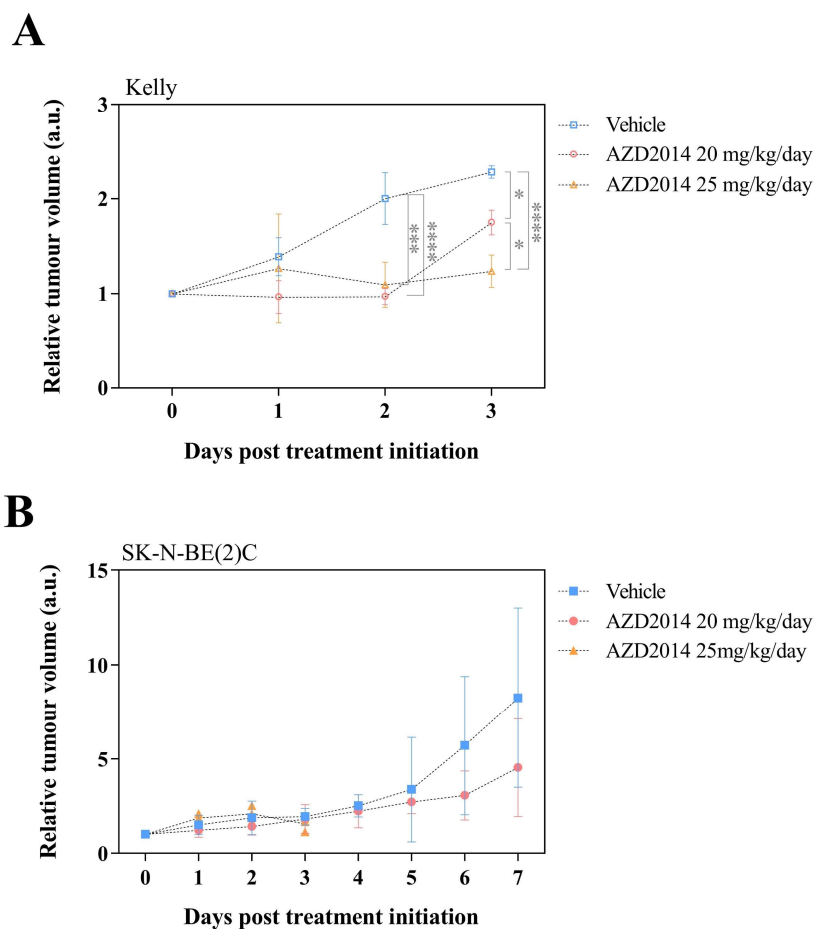


**Figure 5.11** Relative tumour size, normalised to first day of treatment (Day 0), of **A**) Kelly and **B**) SK-N-BE(2)C xenografts during the treatment with either AZD2014 (20 or 25 mg/kg/day) or vehicle (10 % DMSO, 90 % PEG400). Data are presented as mean  $\pm$  SD,  $n \geq 3$  per group. During the 3-day period, comparative statistics were performed using 2-way ANOVA and Tukey post-hoc analysis. When comparing the 7-d protocols, multiple t-tests were performed with Holm-sidak correction.

#### **5.2.5. PET imaging and tumour uptake quantification after AZD2014 treatment**

I next investigated whether the AZD2014 treatment could induce potential differences in tumour NET-1 expression *in vivo*. Based on the toxicity and NB tumour growth results, I used the following treatment regimens:

- 1) SK-N-BE(2)C tumour model (high NET-1 expression) treated with vehicle and 20 mg/kg/day AZD2014 for 1, 3, and 7 days;
- 2) SK-N-BE(2)C tumour model treated with 25 mg/kg/day AZD2014 for 3 days;
- 3) Kelly tumour model (low NET-1 expression) treated with vehicle, 20 and 25 mg/kg/day AZD2014 for 3 days;

To detect the prospective tumour changes, 24 h after the final given dose, I performed an <sup>18</sup>F-mFBG PET/CT (4 h p.i. of the radiotracer) and quantified tumour uptake in each model. PET imaging acquisitions and tumour uptake quantification were performed as described in the previous chapter.

In the case of the SK-N-BE(2)C xenograft model, all tumours could be delineated from the PET imaging in both the vehicle and AZD2014-treated groups. Tumour delineation from PET imaging of the Kelly model was not possible after either vehicle, 20 or 25 mg/kg/day AZD2014 treatment since there was no clear tumour signal in all groups. At the end of each scan, a co-registered CT was acquired for an accurate determination of the tumour volume in all mice. Representative PET/CT and 2D coronal PET slices from acquisitions are shown in Figure 5.12, Figure 5.13 and Figure 5.14.

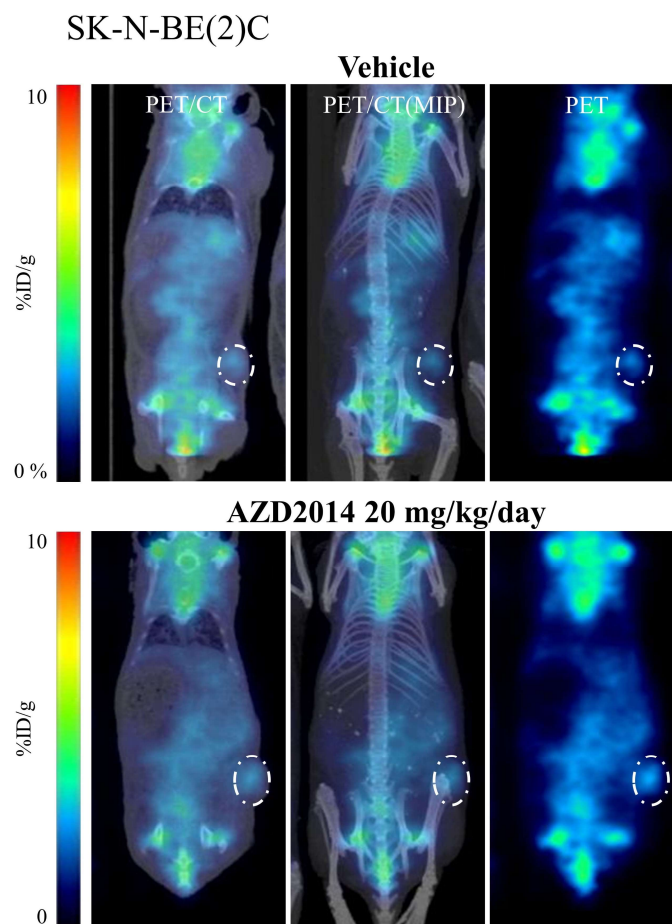


**Figure 5.12** 2D PET/CT, PET/CT(MIP) and PET coronal plane images 4 h p.i. of  $^{18}\text{F}$ -mFBG in SK-N-BE(2)C tumour bearing mice treated for 1 d with vehicle (top) or AZD2014 20 mg/kg/day (bottom). The white dotted line indicates the tumour. PET images are presented as a 2D cross section in the centre of the tumour. MIP = maximum intensity projection.

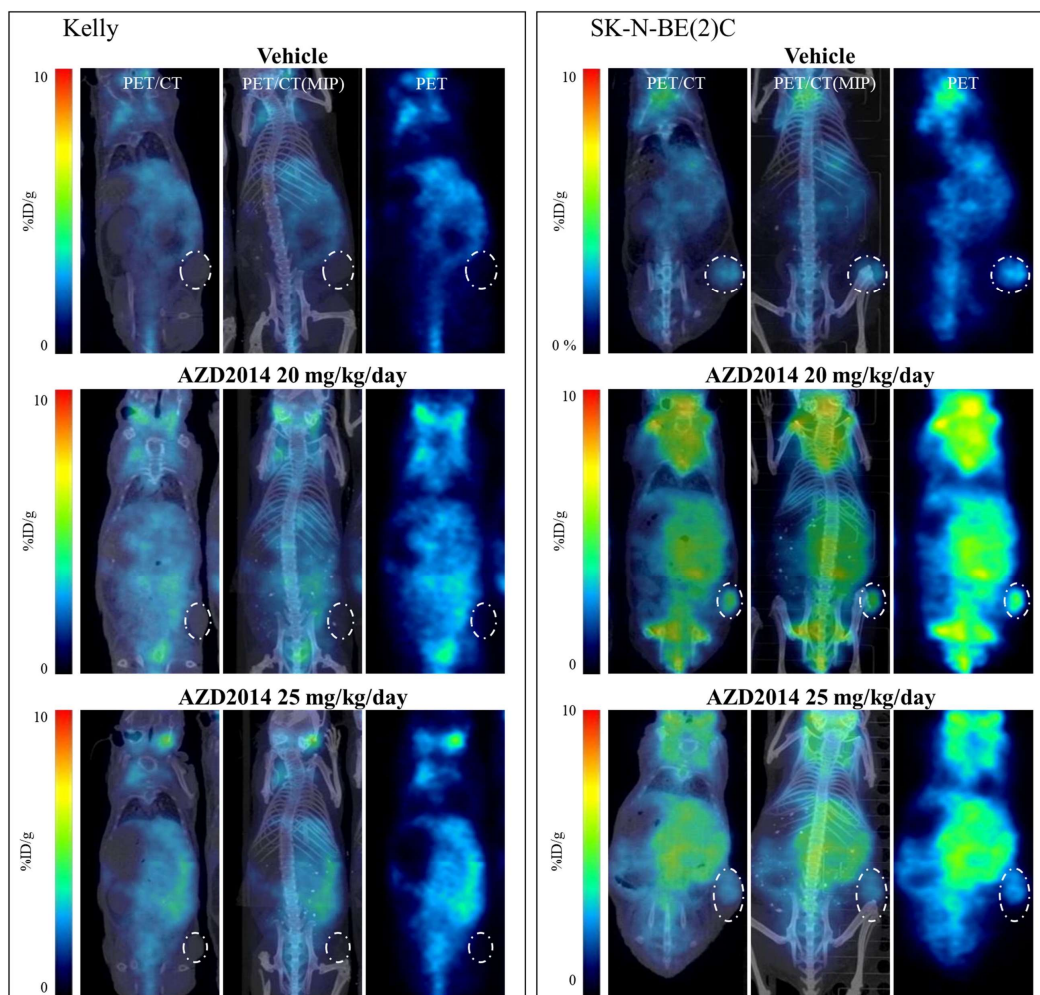


**Figure 5.13** 2D PET/CT, PET/CT(MIP) and PET coronal plane images 4 h p.i. of  $^{18}\text{F}$ -mFBG in Kelly (left) and SK-N-BE(2)C (right) tumour bearing mice treated for 3 d with vehicle (top) or AZD2014 20 mg/kg/day (middle) and 25 mg/kg/day (bottom). The white dotted line indicates the tumour. PET images are presented as a 2D cross section in the centre of the tumour. MIP = maximum intensity projection.

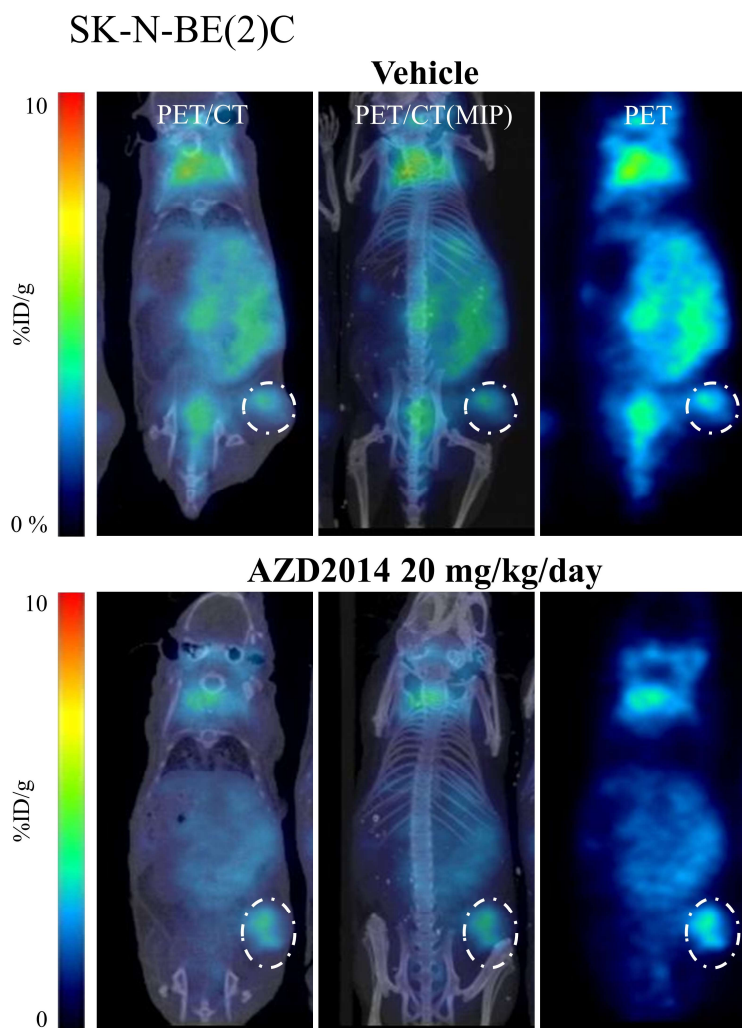


**Figure 5.14** 2D PET/CT, PET/CT(MIP) and PET coronal plane images 4 h p.i. of  $^{18}\text{F}$ -mFBG in SK-N-BE(2)C tumour bearing mice treated for 7 d with vehicle (top) or AZD2014 20 mg/kg/day (bottom). The white dotted line indicates the tumour. PET images are presented as a 2D cross section in the centre of the tumour. MIP = maximum intensity projection.

Quantification of the  $^{18}\text{F}$ -mFBG tumour signal from PET was performed to determine any effects on tumour uptake in response to AZD2014 treatment.

In the SK-N-BE(2)C model, the  $\text{PET}_{50}$  tumour uptakes in the vehicle control group were  $3.09 \pm 1.62$ ,  $2.97 \pm 0.46$ , and  $2.73 \pm 1.02$  %ID/g at 1, 3, and 7 days, respectively. In animals treated with AZD2014 (20 mg/kg/day),  $\text{PET}_{50}$  tumour uptakes were  $3.48 \pm 0.57$ ,  $3.36 \pm 1.12$ , and  $3.93 \pm 1.60$  %ID/g after 1, 3, and 7 days, respectively (Figure 5.15-A).

No statistical difference in tumour radiotracer distribution between the vehicle and the AZD2014 treatment groups was detected after 1 ( $p > 0.99$ ), 3 ( $p > 0.99$ ) or 7 ( $p = 0.78$ ) days. A similar pattern was observed in the quantification using PET<sub>HotAv</sub> (Figure 5.15-B).

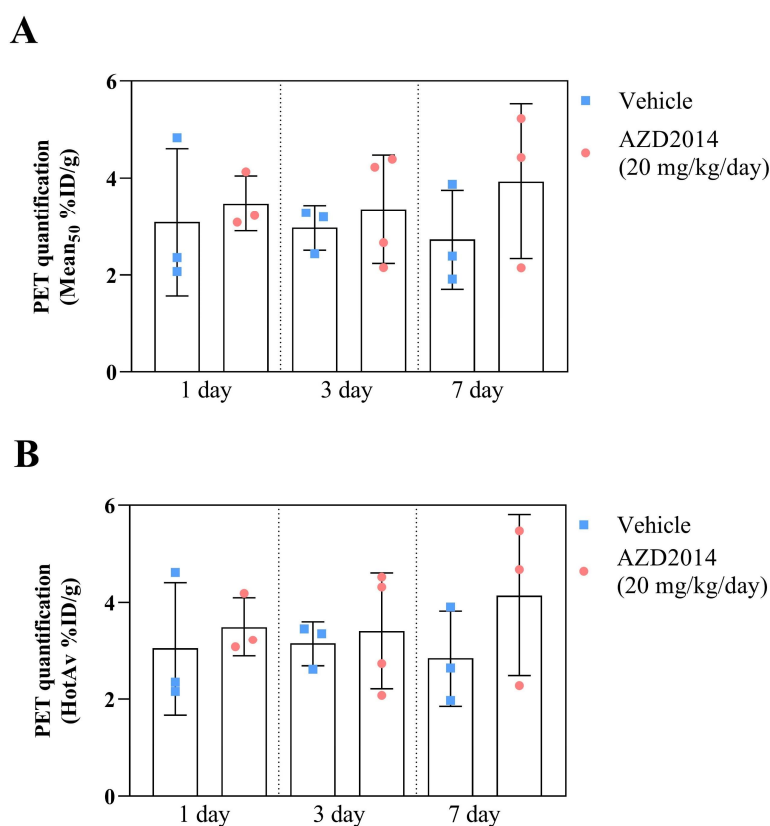


**Figure 5.15 A)** PET<sub>50</sub> and **B)** PET<sub>HotAv</sub> quantification of SK-N-BE(2)C tumour uptake after 1, 3 or 7-d treatment with vehicle (10 % DMSO, 90 % PEG400) or AZD2014 (20 mg/kg/day). Data are presented as mean %ID/g  $\pm$  SD; each dot represents one animal,  $n \geq 3$  per group. Comparative statistics were performed using one-way ANOVA and Sidak post-hoc analysis.

<sup>18</sup>F-mFBG PET quantification was equally performed in SK-N-BE(2)C tumours in mice treated for 3 days with the higher dose of AZD2014 (25 mg/kg/day). Only two mice were assessed after drug treatment due to toxic effects of the compound at this dose. There was a slight decrease in PET<sub>50</sub> radiotracer uptake value after AZD2014 treatment ( $2.31 \pm 0.22$  %ID/g) compared to the vehicle control group ( $2.97 \pm 0.46$  %ID/g) (Figure 5.16-A).

However the PET<sub>HotAv</sub> tumour signals were equivalent at  $3.14 \pm 0.46$  %ID/g for the vehicle group and  $3.38 \pm 0.53$  in the AZD2014 group (Figure 5.16-B).

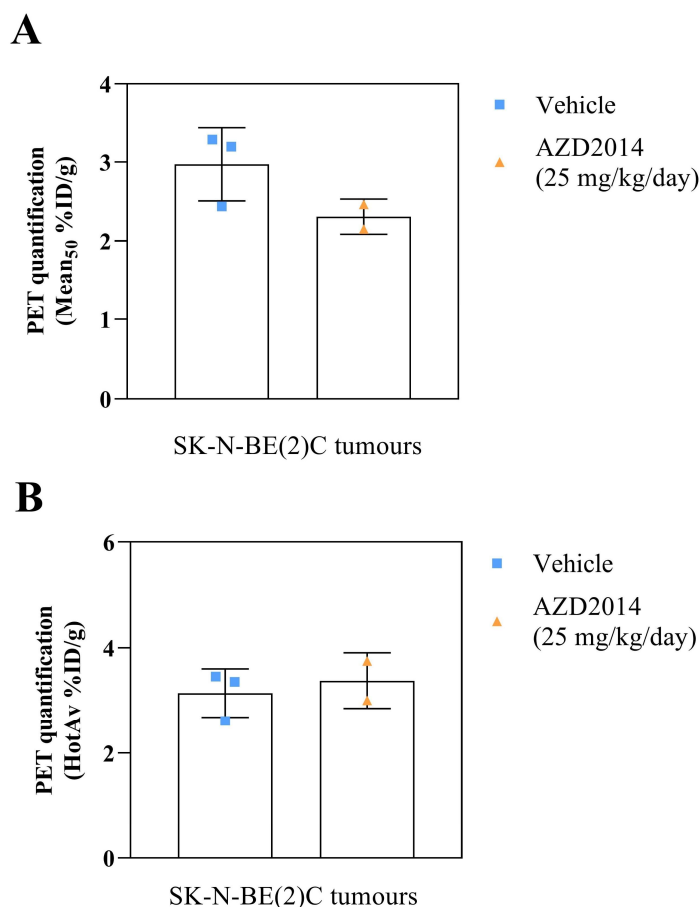


**Figure 5.16** A) PET<sub>50</sub> and B) PET<sub>HotAv</sub> PET quantification of SK-N-BE(2)C tumour uptake after 3 days treatment with vehicle (10 % DMSO, 90 % PEG400) or AZD2014 (25 mg/kg/day). Data are presented as mean %ID/g  $\pm$  SD, each dot represents one animal. Comparative statistics were performed using one-way ANOVA and Sidak post-hoc analysis.

PET<sub>50</sub> quantification in the Kelly tumours showed no difference in radiotracer uptake between the vehicle treated ( $0.87 \pm 0.23$  %ID/g), 20 mg/kg/day ( $0.87 \pm 0.11$  %ID/g) or 25 mg/kg/day ( $0.75 \pm 0.34$  %ID/g) AZD2014 treated animals (Figure 5.17-A). In the lower AZD2014 dose group, although only two mice were examined, there was a lack of any effect in tumour uptake so the study at this dose was not continued. The PET<sub>HotAv</sub> measurements also indicated no difference between the vehicle group ( $1.33 \pm 0.50$

%ID/g) versus the low and high AZD2014-dose groups ( $1.07 \pm 0.38$  and  $1.15 \pm 0.62$  %ID/g, respectively) (Figure 5.17-B).

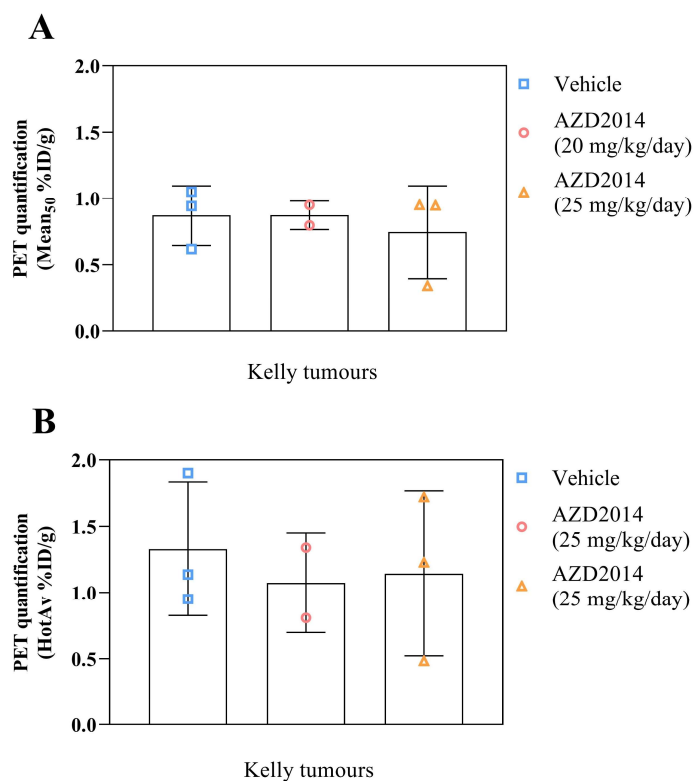


**Figure 5.17** A) PET<sub>50</sub> and B) PET<sub>HotAv</sub> PET quantification of Kelly tumour uptake after 3 days treatment with vehicle (10 % DMSO, 90 % PEG400) or AZD2014 (20 or 25 mg/kg/day). Data are presented as mean %ID/g  $\pm$  SD,  $n \geq 2$ , each dot represents one animal. Statistical differences were measured by an unpaired Student's T-test with Holm-Sidak analysis.

### 5.2.6. <sup>18</sup>F-mFBG biodistribution studies after AZD2014 treatment

Immediately following the PET acquisition (4 h p.i. of <sup>18</sup>F-mFBG), biodistribution studies were performed for each group of mice.

Firstly, <sup>18</sup>F-mFBG uptake in the major non-target organs showed no significant differences between the vehicle control and AZD2014-treated SK-N-BE(2)C tumour-bearing mice (20 mg/kg/day = 1, 3 and 7-day treatment; 25 mg/kg/day = 3-day treatment) (Table 5.1). Again, at the highest dose of AZD2014 (25 mg/kg/day), only 2 animals

bearing SK-N-BE(2)C tumours could be assessed as one animal was sacrificed owing to the toxic effects of the compound. The highest non-tumour uptake was seen in the heart, small intestine and BAT, as described in the previous chapter. Uptake in the BAT after 7 day AZD2014 (20 mg/kg/day) was greater compared to all animals treated for 1 or 3 days, but it was not different to the 7-day vehicle group ( $p = 0.16$ ). A higher bone uptake was observed in the 1 d p.i. animals (both vehicle and drug treatment) compared to the other time-points (Table 5.1). After 3 d treatment with 25 mg/kg/day AZD2014, the difference in uptake in the small intestine compared to the vehicle control was not significant ( $p = 0.10$ ).

	<sup>18</sup> F-mFBG biodistribution 4 h p.i. (%ID/g)						
	1 Day Vehicle	1 Day AZD2014 (20 mg/kg/day)	3 Day Vehicle	3 Day AZD2014 (20 mg/kg/day)	3 Day AZD2014 (25 mg/kg/day)	7 Day Vehicle	7 Day AZD2014 (20 mg/kg/day)
Blood	0.18 ± 0.02	0.18 ± 0.04	0.18 ± 0.08	0.17 ± 0.03	0.13 ± 0.02	0.17 ± 0.06	0.32 ± 0.14
Heart	4.38 ± 1.68	4.34 ± 2.38	3.64 ± 0.89	3.20 ± 0.35	3.45 ± 1.31	5.87 ± 2.80	4.17 ± 1.63
Lungs	1.22 ± 0.37	1.27 ± 0.68	1.15 ± 0.23	1.04 ± 0.10	0.79 ± 0.23	1.86 ± 0.64	1.33 ± 0.36
Kidney	0.79 ± 0.36	0.98 ± 0.04	1.13 ± 0.47	1.06 ± 0.35	0.67 ± 0.04	1.09 ± 0.16	1.02 ± 0.15
Spleen	3.19 ± 0.63	2.93 ± 0.82	2.08 ± 1.29	2.39 ± 0.90	1.97 ± 0.42	1.75 ± 0.67	1.64 ± 0.46
Liver	1.94 ± 0.30	1.63 ± 0.69	1.96 ± 0.02	1.91 ± 0.40	1.33 ± 0.38	2.15 ± 0.30	2.64 ± 0.46
Pancreas	1.01 ± 0.18	1.09 ± 0.42	1.25 ± 0.51	1.30 ± 0.41	0.78 ± 0.29	2.81 ± 1.72	3.08 ± 1.80
<b>Tumour</b>	<b>2.76 ± 1.14</b>	<b>3.29 ± 1.01</b>	<b>2.39 ± 0.10</b>	<b>3.39 ± 1.67</b>	<b>1.37 ± 0.26</b>	<b>2.17 ± 1.01</b>	<b>2.61 ± 1.19</b>
Small intestine	4.50 ± 0.24	4.79 ± 1.21	5.32 ± 0.11	4.80 ± 1.05	2.86 ± 0.75	6.22 ± 0.35	6.87 ± 1.86
Muscle	0.60 ± 0.13	0.59 ± 0.16	0.53 ± 0.19	0.53 ± 0.08	0.47 ± 0.03	0.67 ± 0.07	0.75 ± 0.02
Brown adipose	5.14 ± 0.38	5.47 ± 0.45	5.15 ± 0.78	5.07 ± 1.33	3.84 ± 0.42	6.08 ± 2.45	8.08 ± 0.72
Bone	4.98 ± 2.18	4.55 ± 2.15	1.64 ± 0.45	2.09 ± 2.20	1.31 ± 0.10	1.13 ± 0.20	0.63 ± 0.54
<b>Tumour:blood</b>	<b>15.27 ± 5.32</b>	<b>17.72 ± 2.35</b>	<b>14.47 ± 4.61</b>	<b>19.99 ± 9.09</b>	<b>10.39 ± 0.12</b>	<b>15.55 ± 13.55</b>	<b>8.06 ± 2.57</b>
<b>Tumour:muscle</b>	<b>4.44 ± 0.94</b>	<b>5.74 ± 1.77</b>	<b>4.89 ± 1.48</b>	<b>6.16 ± 2.34</b>	<b>2.91 ± 0.39</b>	<b>3.36 ± 1.90</b>	<b>3.50 ± 1.62</b>

**Table 5.1** Biodistribution of <sup>18</sup>F-mFBG in SK-N-BE(2)C tumour-bearing mice (4 h p.i.) following the treatment with either AZD2014 (20 or 25 mg/kg/day) or vehicle (10 % DMSO, 90 % PEG400). Data are presented as mean %ID/g ± SD. For vehicle and 20 mg/kg/day,  $n \geq 3$  per group. At 25 mg/kg/day AZD2014,  $n = 2$ . Tumour:blood and tumour:muscle ratios are presented as mean ± SD.

Biodistribution of the Kelly xenograft models showed a similar <sup>18</sup>F-mFBG tracer uptake in non-target tissues following 3-day treatment between the vehicle and AZD2014 groups (20 and 25 mg/kg/day) (Table 5.2). As previously mentioned, at the lower dose only 2 mice were examined as no effect of the drug had been seen and therefore, it was deemed unethical to continue the study.

	<sup>18</sup> F-mFBG biodistribution 4 h p.i. (%ID/g)		
	Vehicle	AZD2014 (20 mg/kg/day)	AZD2014 (25 mg/kg/day)
Blood	0.22 ± 0.05	0.19 ± 0.01	0.19 ± 0.03
Heart	6.34 ± 1.41	6.36 ± 1.81	4.22 ± 0.85
Lungs	1.52 ± 0.22	1.53 ± 0.26	1.31 ± 0.39
Kidney	1.11 ± 0.47	1.07 ± 0.04	0.97 ± 0.17
Spleen	3.77 ± 0.82	3.94 ± 0.09	4.58 ± 0.77
Liver	2.37 ± 0.71	1.73 ± 0.08	2.08 ± 0.45
Pancreas	1.26 ± 0.28	1.35 ± 0.24	1.25 ± 0.21
<b>Tumour</b>	0.39 ± 0.13	0.49 ± 0.00	0.74 ± 0.25
Bone	1.43 ± 0.83	1.42 ± 0.48	0.99 ± 0.07
Small intestine	6.57 ± 1.12	6.55 ± 1.84	7.30 ± 1.11
Muscle	0.74 ± 0.23	0.75 ± 0.26	0.64 ± 0.17
Brown adipose	5.84 ± 2.44	8.78 ± 1.53	7.20 ± 0.88
<b>Tumour:blood</b>	1.75 ± 0.29	2.54 ± 0.17	4.16 ± 1.89
<b>Tumour:muscle</b>	0.53 ± 0.01	0.69 ± 0.23	1.23 ± 0.61

**Table 5.2** Biodistribution of <sup>18</sup>F-mFBG in Kelly NB xenografts following treatment either with AZD2014 (20 and 25 mg/kg/day) or vehicle (10 % DMSO, 90 % PEG400) for 3 days. Data presented as mean %ID/g ± SD, n ≥ 2 per group. Tumour:blood and tumour:muscle ratios are presented as mean ± SD.

Regarding the SK-N-BE(2)C tumour uptake, biodistribution values were similar in both the AZD2014 and the vehicle treated animals at all time points (Table 5.1, Figure 5.18). With a value of  $3.40 \pm 1.67$  %ID/g, tumour uptake showed no significant difference between the 3-days 20 mg/kg/day AZD2014 treated tumours compared to the vehicle control ( $2.39 \pm 0.10$  %ID/g) ( $p = 0.82$ ) (Table 5.1). However, a greater tumour:blood and tumour:muscle ratios were observed in the 20 mg/kg/day group ( $19.99 \pm 9.09$  and  $6.16 \pm 2.34$ , respectively) compared to the control group ( $14.47 \pm 4.61$  and  $4.89 \pm 1.48$ , respectively) (Table 5.1). After treatment with the highest dose of AZD2014 (25 mg/kg/day), the tumour uptake was  $1.37 \pm 0.36$  %ID/g ( $p = 0.91$  compared to the vehicle group;  $n = 2$ ). After the 7-days treatment, there was no difference between the AZD2014-treated tumour uptake ( $2.61 \pm 1.19$  %ID/g) compared to the vehicle alone ( $2.25 \pm 0.84$  %ID/g) (Figure 5.18). This resulted in a similar tumour:muscle ratio between the two groups. However, the tumour:blood ratio was lower in the AZD2014-treated group ( $8.06$

$\pm 2.57$ ) compared to the vehicle group ( $15.55 \pm 13.55$ ) owing to a slightly higher, although not significantly so, blood signal ( $p > 0.99$ ) (Table 5.1).

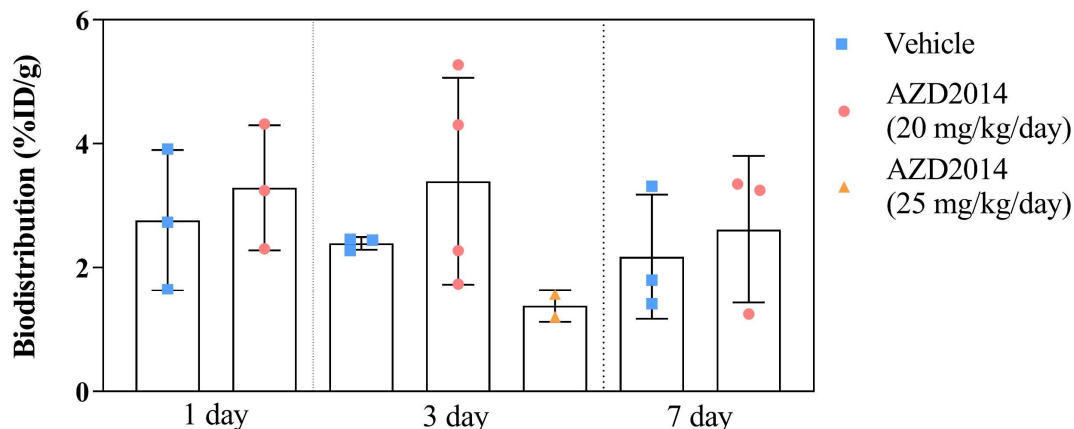


**Figure 5.18** Tumour uptake of <sup>18</sup>F-mFBG in SK-N-BE(2)C tumour-bearing mice following the treatment with either AZD2014 (20 or 25 mg/kg/day) or vehicle (10 % DMSO, 90 % PEG400) for 1, 3 or 7 d. Data are presented as mean %ID/g  $\pm$  SD, each point represents one animal. Statistics were performed using 2-way ANOVA and Tukey post-hoc analysis.

Kelly xenografts showed a small but not significant increase ( $p = 0.68$ ) in <sup>18</sup>F-mFBG uptake between the 25 mg/kg/day AZD2014-treatment group ( $0.74 \pm 0.25$  %ID/g) and the control ( $0.39 \pm 0.13$  %ID/g) (Table 5.2). The resulting tumour:blood and tumour:muscle ratios were slightly higher in the AZD2014-treated animals with values of  $4.16 \pm 1.89$  and  $1.23 \pm 0.61$ , respectively, compared to the vehicle group ( $1.75 \pm 0.29$  and  $0.53 \pm 0.01$ , respectively).

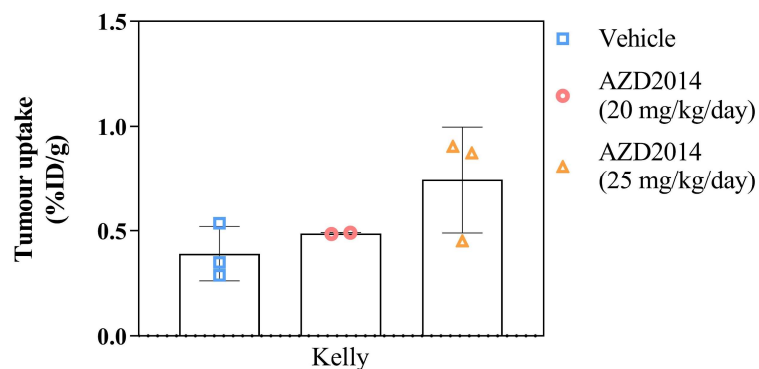


**Figure 5.19** Tumour uptake of  $^{18}\text{F}$ -mFBG in Kelly xenografts following treatment with either AZD2014 (20 or 25 mg/kg/day) or vehicle (10 % DMSO, 90 % PEG400) for 3 days. Data are presented as mean %ID/g  $\pm$  SD, each point represents one animal. Statistical differences were measured by an unpaired Student's T-test with Holm-Sidak analysis.

A comparison between the PET and the biodistribution quantifications showed that the data had a good correlation with a coefficient of determination ( $r^2$ ) of 0.83 using the  $\text{PET}_{50}$  and the slope of the line-of-best-fit was 0.93 (Figure 5.20-A). Correlation between biodistribution and the  $\text{PET}_{\text{HotAv}}$  values was slightly weaker with an  $r^2$  of 0.74 and a slope of 0.84 (Figure 5.20-B). Further, PET quantification slightly overestimated biodistribution data in both settings, with a y-intercept of 0.61 and 1.01 %ID/g by the  $\text{PET}_{50}$  and  $\text{PET}_{\text{HotAv}}$ , respectively.

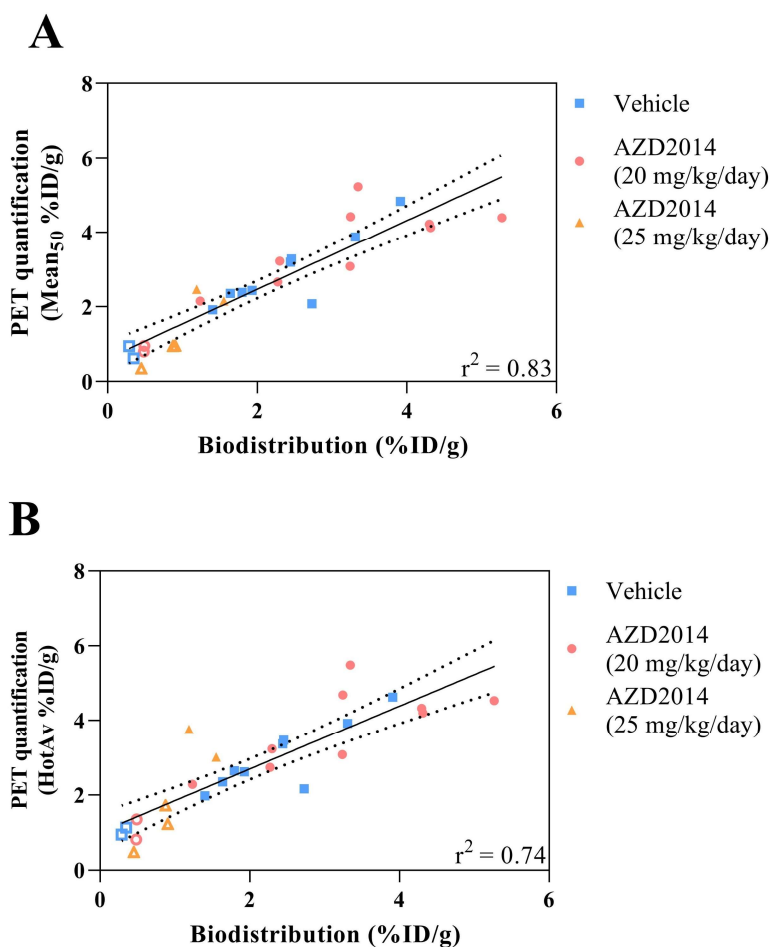


**Figure 5.20** Correlation between **A)** PET<sub>50</sub> and **B)** PET<sub>HotAv</sub> quantification and biodistribution values in Kelly (open shapes) and SK-N-BE(2)C (filled shapes) tumours after 1, 3 or 7-d treatment with AZD2014 (20 or 25 mg/kg/day) or vehicle (10 % DMSO, 90 % PEG400). The dotted line represents the 95 % CI.

### 5.2.7. *Ex vivo* tumour analysis after AZD2014 treatment

Following PET imaging and biodistribution, *ex vivo* analyses (i.e. autoradiography, WB, quantitative-rtPCR and immunohistochemistry) were performed on the excised Kelly and SK-N-BE(2)C tumours, after 3 days treatment with AZD2014 (20 or 25 mg/kg/day) or vehicle control, to determine the effects of the drug on the tumours.

### 5.2.7.1. Autoradiography

Autoradiography was performed on vehicle and AZD2014-treated (3-day only) SK-N-BE(2)C tumours excised 4 h p.i. of <sup>18</sup>F-mFBG. The radioactivity in the vehicle treated tumour was more uniformly distributed than in the AZD2014 treated tumours (Figure 5.21). After 20 mg/kg/day AZD2014 a more heterogeneous distribution could be seen in the tumour slices, with areas showing both greater and similar signal intensities compared to the control group. This was further illustrated at the highest drug dose, with the left hand side of the tumour showing a high uptake of the radiotracer, and the right hand side showing very low signal (Figure 5.21).

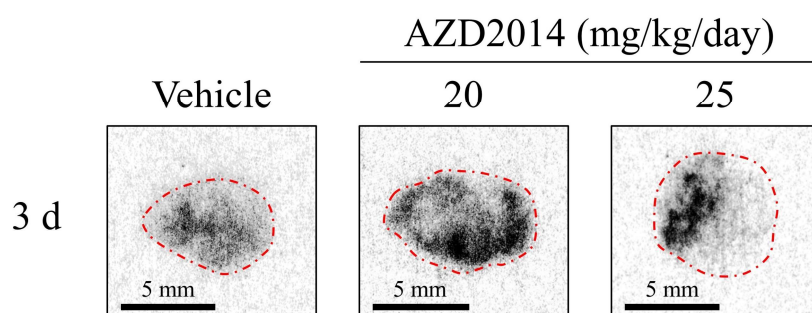


**Figure 5.21** Representative autoradiography expositions (4 h) of SK-N-BE(2)C tumour slices after 3-days treatment with vehicle or AZD2014 (20 and 25 mg/kg/day). Red dotted line indicates the tumour outline.

### 5.2.7.2. Western blot

WB was performed to measure changes in phosphorylation status of mTOR target proteins Akt, S6 and 4EBP1.

In the Kelly model, tumours were analysed after 3-day treatment with vehicle or 25 mg/kg/day AZD2014. I observed no difference in total or phosphorylated levels of Akt or 4EBP1 proteins between the vehicle and AZD2014 treated groups (n = 2) (Figure 5.22). For total and phosphorylated S6 protein there were higher levels in the AZD2014 treated tumour lysates than in the control, although no significance was calculated (n = 2).

However, the ratio between the S6 and p-S6<sup>S240/244</sup> levels was the same for both groups. For NET-1, band density evaluation showed that the total NET-1 expression was low in all tumours regardless of treatment (Figure 5.22-A). No measurable difference was observed in transporter expression between the three days-long vehicle and 25 mg/kg/day AZD2014 treatment groups (n = 2) (Figure 5.22-B).

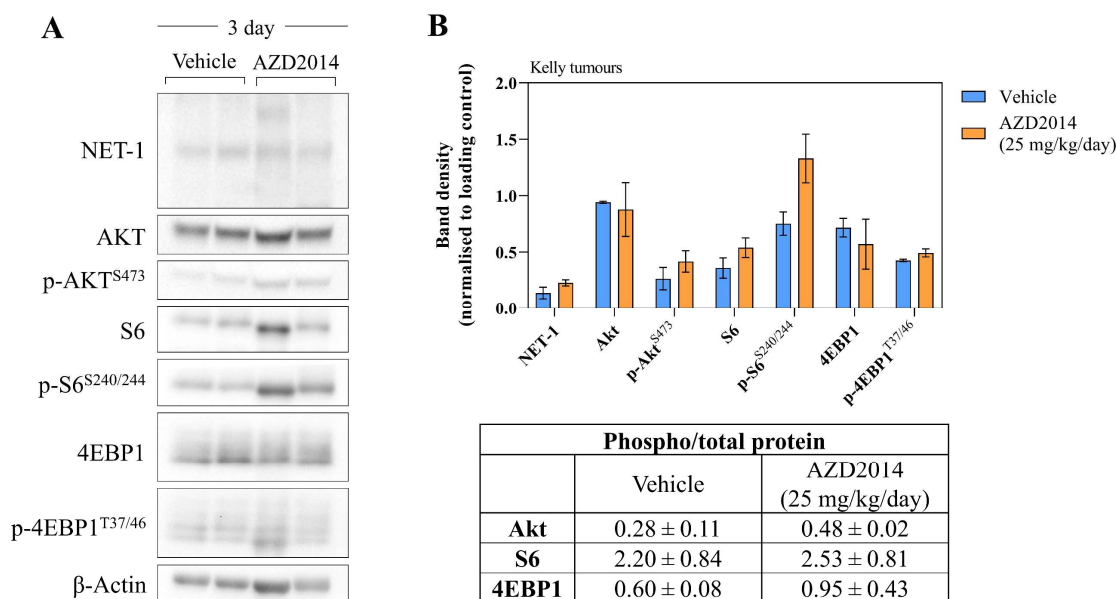


**Figure 5.22** **A)** WB of Kelly tumour lysates after 3 days treatment with vehicle (10 % DMSO, 90 % PEG400) or AZD2014 (25 mg/kg/day). **B)** Protein band density was normalised to the loading control ( $\beta$ -actin) and the ratio between phosphorylated and total protein calculated therein. Data are presented as mean  $\pm$  SD, n = 2 per group. Statistical differences were measured by multiple T-tests with Holm-Sidak analysis.

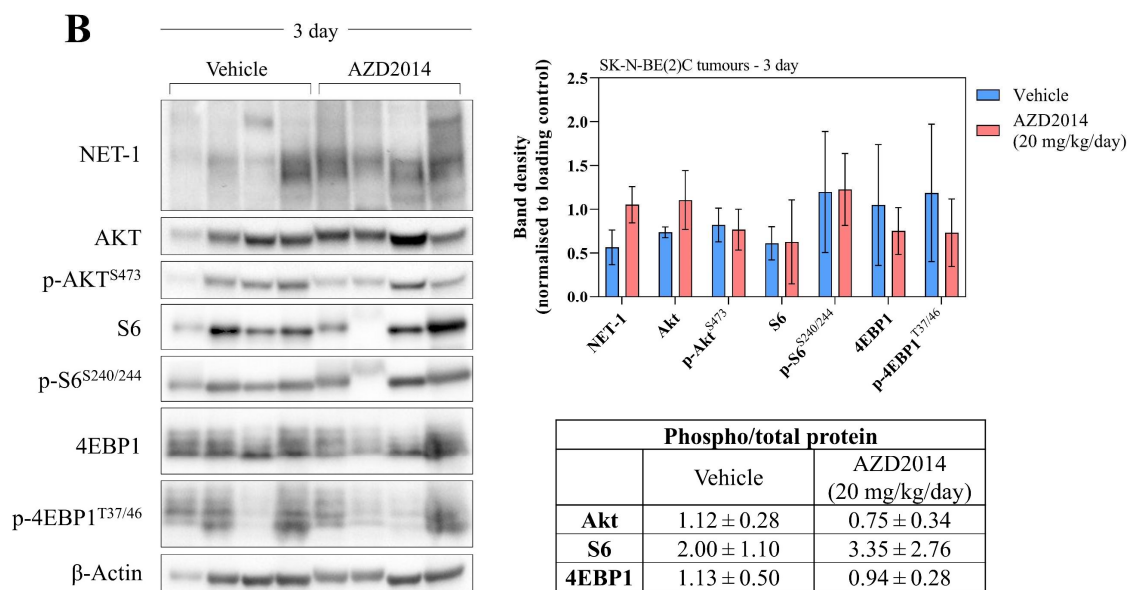
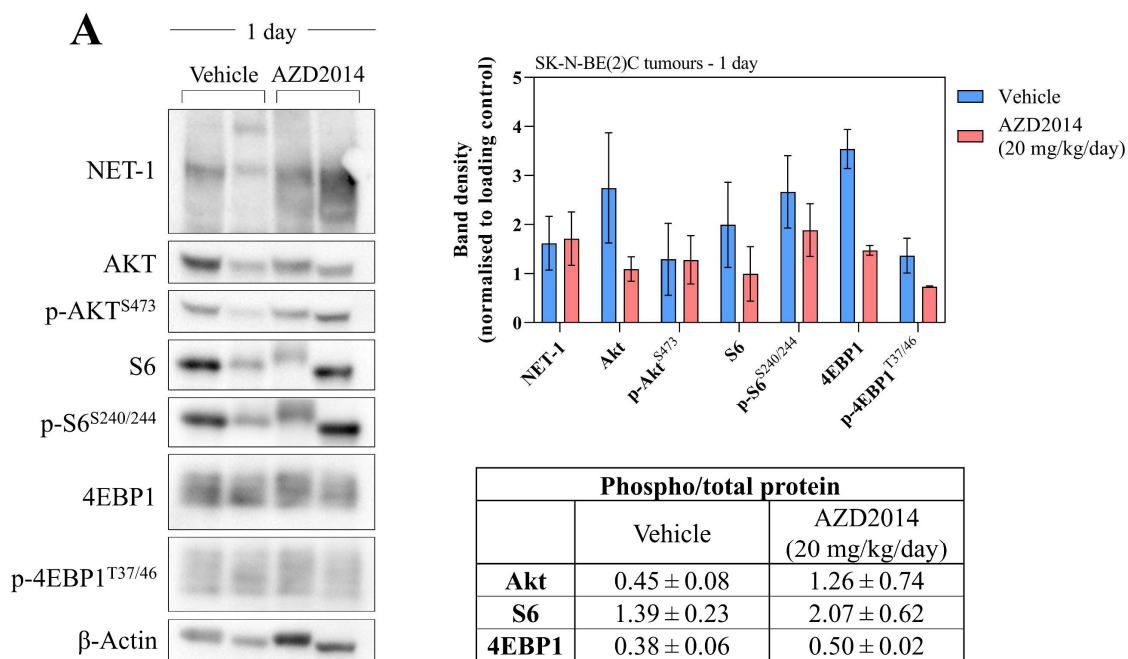
WB was performed on SK-N-BE(2)C tumours treated with vehicle or 20 mg/kg/day AZD2014 for 1, 3 and 7 d.

After 1 day, there was a reduction in the total Akt, S6 and 4EBP1 levels in the AZD2014 treatment tumours compared to the vehicle, although no significance was calculated (n = 2). Further, no change in phosphorylated forms of the proteins were observed (n = 2). Together, this resulted in an apparent increase in the relative levels of the phosphorylated proteins, determined by the phospho/total protein ratio (Figure 5.23-A).

Conversely, after 3 days treatment, total Akt levels were slightly higher in the AZD2014 treatment group than the vehicle group ( $p = 0.37$ ;  $n = 4$ ) but no difference was observed in the phosphorylated levels of the protein ( $p = 0.98$ ;  $n = 4$ ) (Figure 5.23-B). Both total and phosphorylated S6 and 4EBP1 proteins showed no measurable difference between all treatment groups ( $p > 0.88$  for all bands;  $n = 4$ ). Equally, no change was observed in the ratio of phosphorylated protein to total protein after drug treatment (Figure 5.23-B).

In the 7-day-treated tumour lysates, band intensity was less for all proteins compared to the vehicle tumours, although none was significant. Total 4EBP1 and total S6 recorded the greatest difference with a  $p = 0.18$  and  $0.34$ , respectively ( $n = 3$ ). Equally, no change in the ratio of phospho/total of each protein in the tumour samples was seen between the AZD2014 treatment and the vehicle control tumours (Figure 5.23-C).

Regarding NET-1 expression, there was no difference in NET-1 expression after just 1 day (Figure 5.23-A). After 3 days, the AZD2014 treatment caused a slight increase in NET-1 protein in these tumours compared to the vehicle group ( $p = 0.10$ ;  $n = 4$ ) (Figure 5.23-B). After 7 days, the measured NET-1 expression from the tumour lysates was lower in the AZD2014-treatment group compared to the vehicle, although this was not significant ( $p = 0.66$ ;  $n = 3$ ) (Figure 5.23-C).



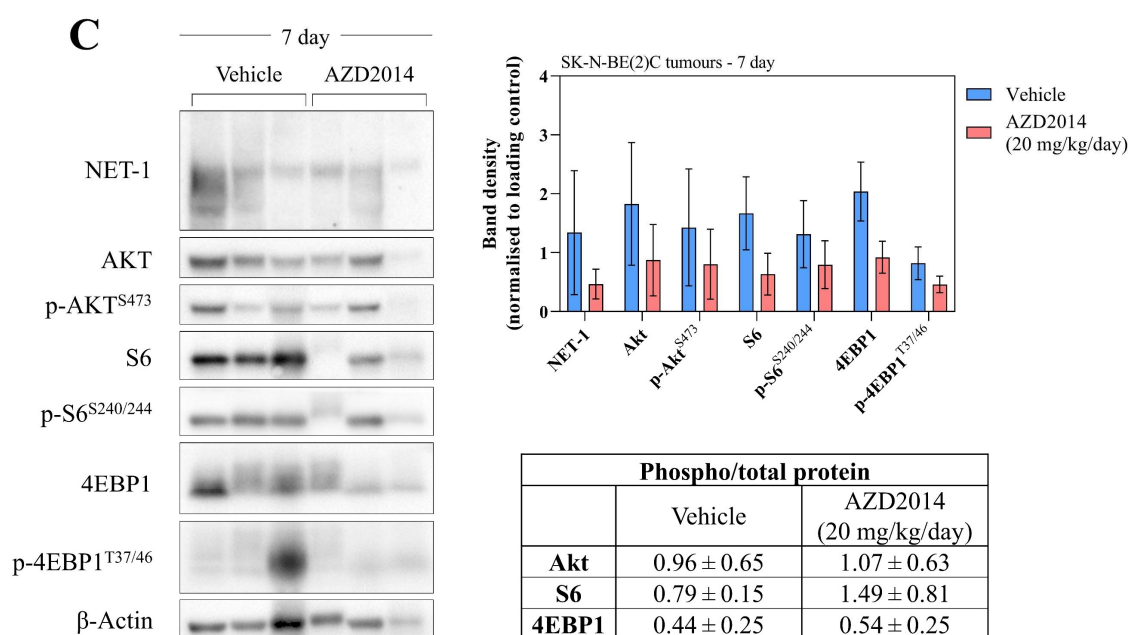


**Figure 5.23** WB of SK-N-BE(2)C tumour lysates after **A)** 1 d **B)** 3 d and **C)** 7 d treatment with vehicle (10 % DMSO, 90 % PEG400) or AZD2014 (20 mg/kg/day). Protein band density was normalised to the loading control ( $\beta$ -actin) and the ratio between phosphorylated and total protein calculated therein. Data are presented as mean  $\pm$  SD,  $n \geq 2$  per group. Statistical differences were measured by multiple T-tests with Holm-Sidak analysis.

### 5.2.7.3. Immunohistochemistry

Two markers of mTORC1 inhibition, p-S6<sup>S240/244</sup> and p-4EBP1<sup>T37/46</sup>, were further investigated by IHC staining of Kelly and SK-N-BE(2)C tumour slices after 3-days treatment with vehicle or AZD2014 (20 and 25 mg/kg/day).

In the vehicle-treated Kelly tumours, p-S6<sup>S240/244</sup> and p-4EBP1<sup>T37/46</sup> staining was seen throughout the tumour slice. Total 4EBP1 was also uniformly expressed. In the slice of the tumour treated with 20 and 25 mg/kg/day AZD2014, total 4EBP1 remained constant, whilst the phosphorylated protein showed some reduced expression at the highest AZD2014 dose (Figure 5.24-A). p-S6<sup>S240/244</sup> staining also was lower at the centre of the tumour, but it remained high at the edges.

In the SK-N-BE(2)C tumours, p-4EBP1<sup>T37/46</sup> levels showed some reduction after 3-days 20 mg/kg/day AZD2014 treatment compared to the vehicle group. This was further enhanced in the 25 mg/kg/day AZD2014-treated tumour. Total 4EBP1 staining showed a reduction in a similar dose-dependent manner but was still present in the treated tumours. Levels of p-S6<sup>S240/244</sup> were heterogeneous in the vehicle control tumour, with some areas showing no staining. There was no observable difference in the 20 mg/kg/day AZD2014 treatment group, but after the 25 mg/kg/day regimen there was a global reduction in p-S6<sup>S240/244</sup> levels (Figure 5.24-B).

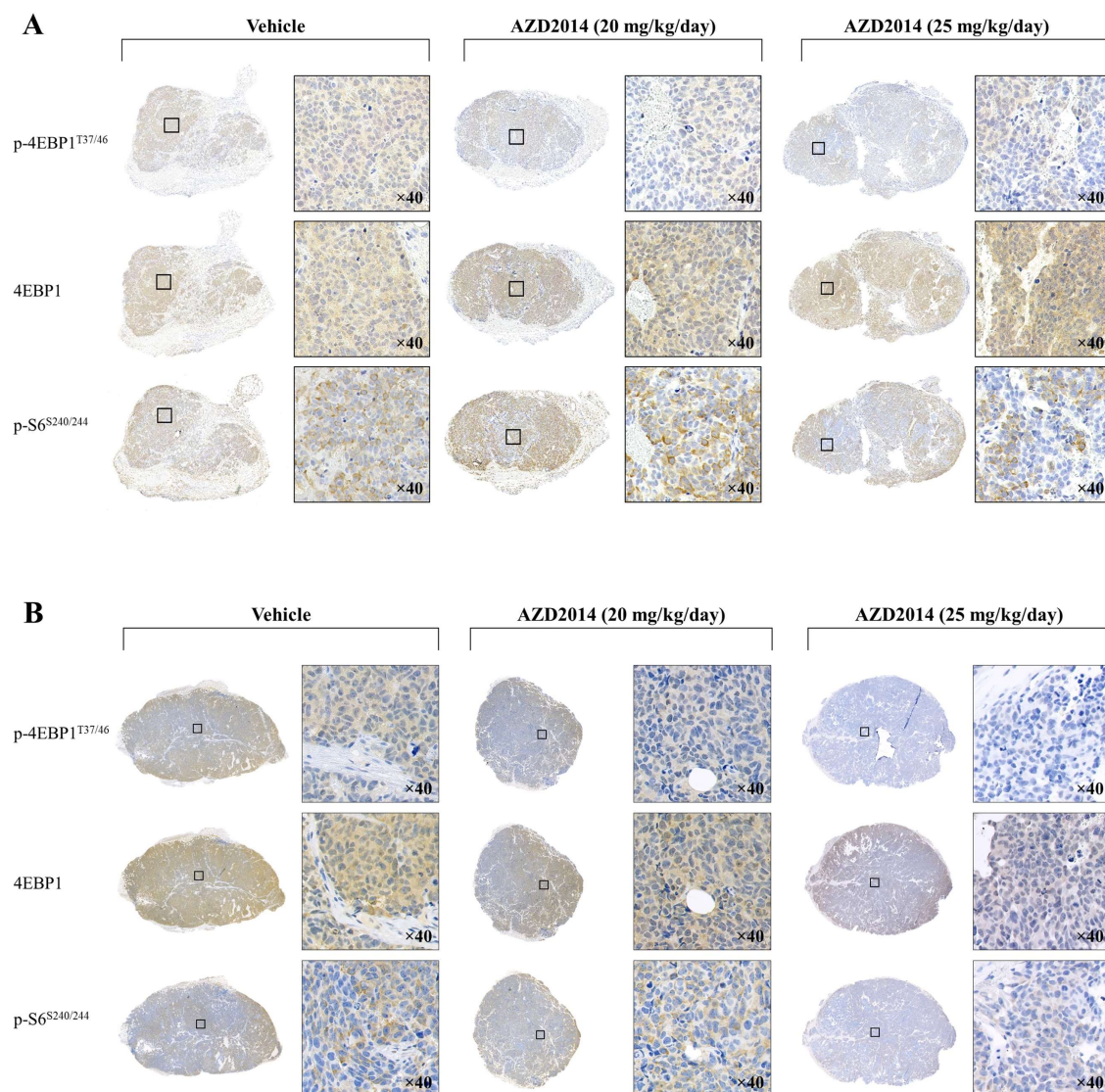


**Figure 5.24** Representative IHC staining of p-4EBP1<sup>T37/46</sup>, 4EBP1 and p-S6<sup>S240/244</sup> in **A**) Kelly and **B**) SK-N-BE(2)C tumour slices after 3 days treatment with vehicle (10 % DMSO, 90 % PEG400) or AZD2014 (20 and 25 mg/kg/day). Area captured for ×40 image is shown in the whole slice with the black box.

#### 5.2.7.4. Quantitative-rtPCR

To assess whether there were any drug-triggered changes in the *SLC6A2* gene expression (which encodes for NET-1 protein), I further investigated *SLC6A2* mRNA expression levels in tumour samples following 3-day treatment with AZD2014 or vehicle control by quantitative reverse-transcriptase polymerase chain reaction (Q-rtPCR). In SK-N-BE(2)C and Kelly models, only the lower dose AZD2014 (20 mg/kg/day) was investigated due to

the limited availability of the tumour material. As seen in Figure 5.25, *SLC6A2* mRNA expression doubled in Kelly xenografts after the drug treatment compared to the control. In the SK-N-BE(2)C tumours, the levels of *SLC6A2* mRNA remained unchanged.

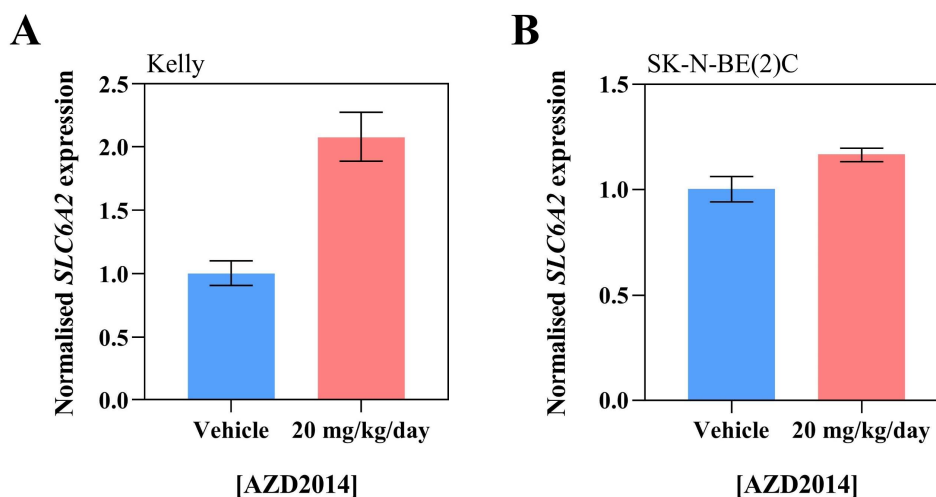


**Figure 5.25** *SLC6A2* mRNA expression measured by Q-rtPCR in **A)** Kelly and **B)** SK-N-BE(2)C tumours after a 3-day treatment with AZD2014 (20 mg/kg/day) or vehicle (10 % DMSO, 90 % PEG400). Data are normalised to the mRNA expression in the vehicle treated control tumours and presented as mean  $\pm$  expression limits, n = 2 per group, performed in triplicate.

### 5.3. Discussion

Therapies for patients with HR-NB which operate by blocking the activity of the *MYCN* oncogene through inhibition of the PI3k/Akt/mTOR axis are of particular interest in the clinic [41, 60, 349]. Although only studied in Phase 1 trials, monotherapy with mTOR/Akt inhibitors have yet to provide robust tumour control in paediatric cancers [356, 357, 369]. Therefore, combining these type of drugs with other chemo- or molecular radiotherapy agents may provide better disease management. Interestingly, Dubois *et al.* reported that NB patients with *MYCN* amplification have comparatively lower NET-1 protein levels than those who are *MYCN* non-amplified [114], suggesting that *MYCN* amplification impedes mature neural cell features such as NET-1 expression [132]. Therefore, a combined strategy, by which *MYCN* is inhibited and NET-1 levels could be primed for <sup>131</sup>I-mIBG targeting, may be of particular benefit.

During the instigation of my work, the dual mTORC1/2 inhibitor AZD2014 was a promising agent for the use in cancer therapy in both mono- and combination therapies [360][NCT02193633]. It was developed to inhibit components of the PI3k/mTOR/Akt pathway known to be hijacked in many cancer types and had shown exciting preclinical efficacy [358, 359, 370]. In 2018, however, the drug was discontinued and pulled from clinical trials because the agent underperformed compared to other mTOR inhibitors already available on the market [93]. Despite this, the AZD2014-induced type of inhibition and its effects on cancer cells (e.g. the enhancement of NET-1 protein levels in NB models) were deemed suitable for verifying the objectives of my project and could also offer some insight in to potential combined therapeutic strategies with similar drugs.

Currently, combination therapies including <sup>131</sup>I-mIBG as a NET-1-dependent molecular radiotherapy agent are under investigation [344-346, 371]. The imaging agent <sup>123</sup>I-mIBG could be used to monitor the therapy effects on the tumour NET-1 expression. However,

although beneficial, it has yet to be incorporated in to the clinical trials [372] [NCT02035137]. This could be due to the need for multiple imaging sessions (pre/post therapy) and the long injection-to-scan time (usually 24 h) requiring longer patient hospitalisation. Further, as quantitative SPECT is not in routine clinical practice, describing <sup>123</sup>I-mIBG tumour uptake is limited to a binary ‘avid’ or ‘non-avid’ measurement. Therefore <sup>18</sup>F-mFBG PET imaging can provide a convenient and important means to quantify tumour radiotracer (and thus the equivalent molecular radiotherapeutic) uptake by SUV calculations and enhance our understanding on appropriate agents to use in combination with <sup>131</sup>I-mIBG therapy.

### **5.3.1. AZD2014-induced mTORC1/2 inhibition in NB cells**

In the MYCN-overexpressing cell lines (Kelly and SK-N-BE(2)C) and cells with a non-amplified MYCN (NBL5 and SK-N-SH), the degree to which AZD2014 influenced cell viability was assessed to determine appropriate concentrations of the drug for the proceeding experiments. The concentration of AZD2014 required to reduce NB cell growth by 50% (GI<sub>50</sub>), after 72 h incubation, were lower in the MYCN-overexpressing cell lines (~374 and ~523 nM for Kelly and SK-N-BE(2)C cells, respectively) suggesting a selected sensitivity of this phenotype to mTORC1/2 inhibition. Indeed, in the MYCN-non-amplified cells, the GI<sub>50</sub> was not reached in the range of drug concentrations used and the values were therefore estimated from the curves (> 1 μM for both SK-N-SH and NBL5 cells) (Figure 5.2).

As MYCN overexpression is a key hallmark of HR-NB, the Kelly and SK-N-BE(2)C cell lines were chosen for further investigations. After just 24 h, AZD2014 caused growth inhibition in both Kelly and SK-N-BE(2)C cell lines. Furthermore, cell cycle analysis showed that this was in part due to G1/G0 cell cycle arrest (Figure 5.3) and cells did not commit to a proliferative phenotype. Similar results have been achieved by other research

groups in hepatocellular carcinoma (HCC) [370] and OSCC [363], with the latter further demonstrating the radiosensitisation ability of AZD2014 on cells treated with 4 Gy X-irradiation.

Six AZD2014 concentrations (0, 20, 50, 100, 200 and 500 nM) were considered for suitable characterisation of the changes in protein expression whilst also minimising the degree of cell death. Inhibition of the mTOR complex 1 is characterised by the downregulation of the phosphorylation of the S6 (S240/244) and 4EBP1 (T37/46) substrates [373]. The mTOR complex 2 is most importantly responsible of the phosphorylation of Akt at the S473 residue [374], thus inhibiting this complex leads to p-Akt<sup>S473</sup> downregulation. AZD2014 has robustly shown to inhibit these markers in various cancer models [359, 370] and Xu *et al.* demonstrated that AZD8055, the predecessor to AZD2014, prominently reduces phosphorylation levels of all three previously mentioned substrates in NB [352]. Further, the mTOR inhibitors Torin-1 and NVPBEZ235 have shown robust downregulation of these phosphor-proteins which ultimately led to the downregulation of MYCN protein [84]. Therefore, I investigated the effect of AZD2014 on my NB cell lines with the aim to confirm a MYCN inhibitory response.

Initially, I performed WB analysis of NB cells (Kelly and SK-N-BE(2)C) treated with AZD2014 for 24 and 72 h. At these time points, in both cell lines, I observed a promising and distinct drug concentration-dependent decrease of both p-4EBP1<sup>T37/46</sup> and p-S6<sup>S240/244</sup>, indicating an inhibition of the mTORC1 kinase activity. However, in this primary investigation the levels of p-Akt<sup>S473</sup> were similar to total Akt at both time points and all drug concentrations (0, 20, 50, 100, 200 and 500 nM) (Figure 5.4 and Figure 5.5).

Given that the dual inhibition of both mTOR complexes is associated with MYCN protein stability [84], I also measured the effect of AZD2014 on MYCN levels. As p-Akt<sup>S473</sup> levels were not robustly reduced in these experiments, I expected to see small to no

change in MYCN protein in both cell lines. Indeed, there was only minimal evidence of a reduced MYCN level after treatment for 24 h and 72 h in the Kelly cell line that was ultimately not significant to the untreated controls. In the SK-N-BE(2)C cell line, MYCN levels were the same at 24 h and only a small reduction in protein expression was seen after 72 h incubation with the drug (Figure 5.4 and Figure 5.5). Although higher drug concentrations may result in greater MYCN depression, they were not investigated because they would result in a greater cell death and consequent impediment of WB analysis.

As originally hypothesised, decreased phosphorylation of Akt at Ser473 may be a common consequence of both HDAC and mTORC2 inhibition that causes perturbed NET-1 levels [344, 366, 368]. Despite no changes in p-Akt<sup>S473</sup> levels in this work, NET-1 expression showed a concentration-dependent increase following AZD2014 incubation (Figure 5.4 and Figure 5.5). Unfortunately, the NET-1 levels in the low expressing Kelly cell line could not be determined properly using the WB technique. Therefore, my observations were based only on the results achieved from the SK-N-BE(2)C cells.

All together, these initial results prompted me to investigate the dynamics of AZD2014 mTORC1/2 inhibition by treating the cells with the highest drug concentrations previously examined (200 and 500 nM) and analysing the proteins' quantity during a 3–72 h time course. In this experiment, p-S6<sup>S240/244</sup> and p-4EBP1<sup>T37/46</sup> levels were potently reduced in both cell lines at each time point (Figure 5.6 and Figure 5.7). Interestingly, p-Akt<sup>S473</sup> levels of both cell lines decreased compared to the controls at the earliest time points (3 and 6 h), however, this was not sustained. A time-dependent recovery of p-Akt<sup>S473</sup> levels was observed in each cell line and they returned to baseline after 72 h incubation with the drug (500 nM) in Kelly cells and after as early as 24 h in

SK-N-BE(2)C cells (Figure 5.6 and Figure 5.7). This could be indicative of the activation of a resistance mechanism [89, 375]. For example, it could be possible that the mTORC1 inhibition leads to an upregulation of RTKs, such as the insulin receptor, at the cell surface with a consequent re-activation of the PI3k/Akt pathway [376]. A more focused investigation is needed to understand the processes of p-Akt<sup>S473</sup> recovery following AZD2014 treatment. Equally, there was a lack of robust reduction of MYCN seen in both the Kelly and SK-N-BE(2)C cells at each time point. This reiterated the findings from my previous study and also those by Vaughan *et al.* detailing that dual mTORC1 and mTORC2 inhibition is necessary for MYCN downregulation [84].

Despite these unpredicted drug effects, a clear increase of NET-1 expression was detected in SK-N-BE(2)C cell line after 24 h treatment with AZD2014 and was sustained until the last time point (72 h) of the test. This result prompted following studies as to whether the drug-induced NET-1 increase was reflected by a rise of <sup>18</sup>F-mFBG cell uptake.

### **5.3.2. <sup>18</sup>F-mFBG as a tool to measure changes in NET-1 function following AZD2014 treatment *in vitro*.**

Following the WB findings showing that AZD2014 increased NET-1 expression, at least in the SK-N-BE(2)C cell line from 24 h onwards, I investigated the use of <sup>18</sup>F-mFBG to quantify NET-1 activity in the cells following 24 and 72 h drug treatment. I also assessed whether radiotracer uptake in Kelly cells could identify changes in NET-1 expression that could not be visualised by WB. Also, the WB methodology I employed detects the total NET-1 levels, which include the cell membrane-associated and the cytoplasmic-located protein, without differentiating them (discussed in previous chapter). As a consequence, the WB-assessed level of NET-1 may not directly correlate to the cell uptake of NE analogues. The use of <sup>18</sup>F-mFBG, that enters the cell exclusively through the transporter

situated on the cell membrane, may give a more accurate representation of changes in NET-1 function following AZD2014 intervention than WB.

The 24 h-long treatment caused no difference in <sup>18</sup>F-mFBG uptake in the SK-N-BE(2)C cell line compared to the control, but in Kelly cells a small but significant increase was observed in the 500 nM treatment group (Figure 5.8). This suggested that, although not detected by WB, NET-1 levels or function was influenced by the AZD2014 treatment in the low expressing cell line and <sup>18</sup>F-mFBG could identify it.

After a longer incubation time (72 h), I saw a greater uptake of <sup>18</sup>F-mFBG following AZD2014 treatment in both cell lines: the uptake more than doubled in SK-N-BE(2)C cells whilst it tripled in the Kelly cells compared to their respective control cells (Figure 5.9-A). To ensure the findings with <sup>18</sup>F-mFBG were well founded, I performed a cell uptake assay using the conventional NET-1 imaging agent <sup>123</sup>I-mIBG and compared the outcomes. The results obtained using <sup>123</sup>I-mIBG predominantly paralleled those I found with the fluorinated analogue, although the increases in radiotracer accumulation in the Kelly cell line were slightly greater for the iodinated agent (Figure 5.9-B). This may simply be due to the different molar activities of each radiotracer used in the investigation. Another option could be the greater influx of <sup>123</sup>I-mBG compared to <sup>18</sup>F-mFBG in NET-1 expressing cells linked to the higher hydrophilicity and lower affinity for NET-1 of the fluorinated radiotracer compared to the iodinated analogue [138]. Nevertheless, <sup>18</sup>F-mFBG was able to quantitatively measure changes in NET-1 function following AZD2014 treatment in both low and high-NET-1-expressing cell lines to a similar degree to the conventional radiotracer.

### 5.3.3. Monitoring *in vivo* effects of AZD2014 treatment with <sup>18</sup>F-mFBG

I next assessed the effects of AZD2014 *in vivo* using mouse models of NB (SK-N-BE(2)C and Kelly xenografts) and investigated whether <sup>18</sup>F-mFBG was able to monitor changes in tumour NET-1 expression post treatment.

The inhibitor doses of 20 and 25 mg/kg/day (bolus administration) used in this investigation were selected based on previous reports and on other studies carried out within the Institute of Cancer Research during these investigations [360, 365]. Toxicity of the agent was determined by daily monitoring the animals' physical appearance and measuring their body weight (Figure 5.10). The 20 mg/kg/day AZD2014 dose was well tolerated in all mouse models throughout the 7-day study. At the higher dose (25 mg/kg/day), however, the schedule was ultimately too toxic to the animals with one incidence of weight loss over the limits detailed in the Home Office project licence. Therefore, the experiments in the following work were performed using the 20 mg/kg/day dosing schedule for 7 days and the 25 mg/kg/day regimen for just 3 days.

Tumours size was also measured daily to determine any anti-tumour effects of the therapy. At the lower dose, there was some minor SK-N-BE(2)C tumour control demonstrated by a slight reduction in tumour size compared to the vehicle control at day 7 (Figure 5.11). After treatment with 25 mg/kg/day, the SK-N-BE(2)C tumours were a similar size compared to both the vehicle and 20 mg/kg/day tumours for the 3-day treatment duration. In the Kelly model, tumour volumes increased in all groups, but AZD2014 treatment caused a dose-dependent reduction in tumour growth compared to the vehicle control after just 3-days treatment.

<sup>18</sup>F-mFBG was used to determine the presence and then the extent of AZD2014-induced changes in tumour NET-1 expression *in vivo*. For that purpose, SK-N-BE(2)C and Kelly tumour-bearing mice were injected with <sup>18</sup>F-mFBG and PET/CT scans were performed

4 h p.i. (Figure 5.13). PET quantification was carried out as described in the previous chapter, in which the PET<sub>50</sub> and PET<sub>HotAv</sub> values both provided a similarly robust surrogate measure to actual biodistribution of <sup>18</sup>F-mFBG.

Initially, PET imaging and biodistribution were performed in SK-N-BE(2)C tumour bearing animals after 1, 3 and 7 days treatment with vehicle or 20 mg/kg/day AZD2014. Although at each time point PET quantification (both PET<sub>50</sub> and PET<sub>HotAv</sub> values) showed no significant enhancement of the tumour signal between the vehicle control and the AZD2014 treated mice (Figure 5.15), when considered singularly, some tumours in the AZD2014 treated groups displayed slightly higher accumulation of the radiotracer than others.

Therefore, following this first study, <sup>18</sup>F-mFBG PET was performed following a 3-day 25 mg/kg/day AZD2014 treatment regimen using SK-N-BE(2)C xenograft models to see whether a higher drug dose was able to induce greater NET-1 changes that could be picked up via PET. The calculated PET<sub>50</sub> values within the tumours indicated a fall in radiotracer uptake (Figure 5.16). Conversely, the PET<sub>HotAv</sub> values showed no difference between the vehicle and AZD2014 treatment groups.

In the Kelly model, with low NET-1 expression, PET quantification was difficult due to the low uptake of the radiotracer. This limited any contrast between the tumour and other tissues. Despite this, no difference in tumour uptake could be observed, after PET<sub>50</sub> quantification, between animals treated with either the vehicle control or both AZD2014 regimens (Figure 5.17-A). Compared to PET<sub>50</sub>, PET<sub>HotAv</sub> values are higher in each of the Kelly treatment groups with also a more pronounced variability of uptakes amongst the single tumours within each group (Figure 5.17-B). This could be attributed to the inclusion of a the spill-over signal from nearby tissue with high radiotracer uptake (i.e.

the small intestine) at the edges of the VOI. This could result in misinterpretation of the data using this  $PET_{HotAv}$  in tumours with low radiotracer uptake.

After each PET scan, organ and tumour biodistribution was performed. Considering the major non-target organs, there was no evidence of difference in radiotracer uptake between the vehicle and both 20 and 25 mg/kg/day AZD2014 treatment groups at any time point for both SK-N-BE(2)C and Kelly-tumour models. Of note, the blood value in the SK-N-BE(2)C-bearing mice in the 7-day AZD2014-treatment group (20 mg/kg/day) was higher than the vehicle group, although not significantly so (Table 5.1). This contributed to a lower tumour:blood ratio in these animals. The higher blood-associated radioactivity levels could be the result of an impaired renal clearance from the toxicity to the kidney caused by the extended exposure to the drug. In fact, a Phase 2 clinical trial revealed that a third of patients receiving AZD2014 showed an increase in creatinine levels (grade 1 and 2 toxicity) [93] which is indicative of impaired kidney function [377].

Biodistribution studies also indicated an isolated high bone uptake in both of the 1-day SK-N-BE(2)C-tumour bearing animal groups (Table 5.1). As this was not observed again during the study and being that different batches of the tracer were used for each time point, I speculated that it could be attributed to the quality of the <sup>18</sup>F-mFBG produced on the day and a possible higher defluorination of the agent in the animals. Importantly, as the high bone uptake was not different between the AZD2014 and vehicle treatment groups, it suggested that the drug was not the contributing factor.

The biodistribution analysis showed no significant change in the tracer uptake in the SK-N-BE(2)C tumours following any treatment schedule. Despite a small increase after 3-days treatment with 20 mg/kg/day AZD2014, the higher dose (25 mg/kg/day) did not further enhance tumour uptake. In fact, the radiotracer distribution to the tumour dropped to half that of the lower dose (Table 5.1 and Figure 5.18). These results were reminiscent

of the PET<sub>50</sub> quantification, suggesting this method was more representative of the actual radiotracer distribution in the whole tumour compared to the PET<sub>HotAv</sub>.

In the Kelly model, the biodistribution study showed a small increase in radiotracer uptake in the tumour only after treatment at the highest drug concentration (Table 5.2 and Figure 5.19). However, as these values remained very low, the after-treatment-tumours would still be considered as non-avid for <sup>18</sup>F-mFBG.

A comparison was drawn between the biodistribution data and the PET values acquired (PET<sub>50</sub> and PET<sub>HotAv</sub>) to validate the robustness of the PET quantification methodology (Figure 5.20). Importantly, both PET<sub>50</sub> and PET<sub>HotAv</sub> data showed a good correlation to the biodistribution values as demonstrated by the  $r^2$  values. Interestingly, the PET<sub>HotAv</sub> showed a slightly weaker correlation to the biodistribution score than PET<sub>50</sub> (Figure 5.20-B). This may be a factor of tumours with a more heterogeneous radiotracer uptake, whereby the PET<sub>HotAv</sub> only measures the very peak of the radiotracer's level in the tumour. Further, there is likely overestimation of the non-avid Kelly tumours as the PET measurements are prone to spill-over signal from adjacent tissues with high radiotracer uptake. By both PET<sub>50</sub> and PET<sub>HotAv</sub> quantification, the %ID/g calculated was an overestimation of the actual biodistribution measure, demonstrated by a positive y-intercept of 0.6 and 1.0 %ID/g, respectively. Further, the slope of the linear regression curves should be close to 1, which was truer for the PET<sub>50</sub> (0.93) compared to the PET<sub>HotAv</sub> (0.84). In general, both image quantifications metrics produced reliable results; however, PET<sub>50</sub> was a better reflection of the whole tumour <sup>18</sup>F-mFBG uptake than PET<sub>HotAv</sub> (Figure 5.20).

Although AZD2014 increased NET-1 expression and <sup>18</sup>F-mFBG cell uptake *in vitro*, no distinct differences in tumour radiotracer uptake was seen *in vivo*. The outcome of the PET imaging and biodistribution experiments could indicate the following possible

scenarios: 1) <sup>18</sup>F-mFBG is not a good imaging tool for monitoring NET-1 levels *in vivo*; 2) <sup>18</sup>F-mFBG is a good radiotracer for the assessment of NET-1 levels but the AZD2014 dose regimen used in the test was suboptimal and had to be modified to have any measurable effects on the tumours' biology; 3) The sample power was too low. A larger cohort in each treatment group could give greater power to the analysis especially when small changes are observed; 4) AZD2014 has additional effects on the tumour which can interfere with the radiotracer accumulation.

The following *ex vivo* studies were performed to help clarify these findings. An additional correlation study between NET-1 expression and <sup>18</sup>F-mFBG tumour uptake was also carried out.

#### **5.3.4. *Ex vivo* NB tumour analysis after AZD2014 treatment**

I performed *ex vivo* analysis on the tumours to assess the effects of AZD2014 in the NB tumour xenografts.

Immediately following tumour excision, I performed autoradiography on the SK-N-BE(2)C 3-day treated tumours to ascertain the distribution of the <sup>18</sup>F-mFBG signal across a tumour slice. In the vehicle treated animal, autoradiography showed a uniform distribution of the radiotracer, however both the 20 mg/kg/day and 25 mg/kg/day treated tumours had a more heterogeneous signal. Most prominently, at the highest drug dose, there was a clear contrasting signal between the left side (high activity distribution) and right side (low activity distribution) of the tumour section. The details behind these observed differences could not be elucidated from autoradiography alone, however, the areas of low signal may correspond to either areas of low NET-1 expression, or to non-viable tumour in response to AZD2014 treatment, or viable tumour but an impaired delivery of the radiotracer to all areas of the lesion. The areas of high uptake in the drug-

treated tumours may also indicate that the AZD2014-triggered augmentation of <sup>18</sup>F-mFBG uptake in these cells through an increased NET-1 activity.

Next, I assesses the classical markers of mTOR inhibition and NET-1 expression by WB to determine whether the treatment regimen induced biological changes in the tumours (Figure 5.22). WB band density was measured to account for varied protein loading densities between tissue samples (as observed in the loading control, GAPDH). Accurate determination of true tissue lysate protein levels were difficult to measure in haemorrhagic tissue samples, where pigments interfered with BCA colorimetric quantification.

After treatment of Kelly tumours with 25 mg/kg/day AZD2014, no differences were observed in total or phosphorylated Akt or 4EBP1, however the ratio of phosphorylated to total protein showed a slight increase in the AZD2014 treated tumours. When the S6 protein was examined, AZD2014 treated tumours showed greater band intensity in both total and phosphorylated protein, but the relative phosphorylation (phospho/total ratio) was equivalent between the treatment groups. NET-1 expression was low in all Kelly tumour samples, which corresponded to the low <sup>18</sup>F-mFBG uptake in these tumours (Figure 5.22). Nevertheless, there was a slight trend towards an increase in NET-1 expression after 25 mg/kg/day AZD2014 treatment compared to the vehicle group (Figure 5.19).

In the SK-N-BE(2)C models, WB highlighted a general reduction in total Akt, S6 and 4EBP1 levels following 1 day of treatment with 20 mg/kg/day AZD2014 (Figure 5.23-A). However, the levels of the phosphorylated proteins were not as greatly reduced resulting in a slightly higher phosphorylation ratio for all the measured proteins in the treated tumours versus the vehicle control. Conversely, in tumour lysates from the 3-day treatment group, both the total and phosphorylated protein levels were the same

between each group and therefore, the phospho/total ratios were no different between AZD2014 (20 mg/kg/day) and vehicle treated tumours (Figure 5.23-B). In the tumours treated for 7 days with the drug (20 mg/kg/day), both the total and the phosphorylated forms of Akt, S6 and 4EBP1 were also lower, resulting in similar phosphorylation ratios between the groups (Figure 5.23).

Regarding the tumour NET-1 status in the SK-N-BE(2)C model, no difference in the protein levels was observed after 1 day of treatment with AZD2014 compared to the vehicle group (Figure 5.23-A). However, after the 3-day AZD2014 (20 mg/kg/day) treatment regime, NET-1 levels were higher than in the vehicle-treated tumours, although this was not significant ( $p = 0.10$ ) (Figure 5.23-B). Interestingly, after 7 d, WB revealed a lower NET-1 expression in the AZD2014 treated tumours. This also coincided with the global reduction in the other proteins examined by WB in these tissue samples (Figure 5.23-C). Overall, no major drug effects could be identified by WB in tumours after any kind of treatment regimen.

WBs were performed by sampling one core (~20 mg) of the whole tumour volume (~100–400 mg) which was amalgamated in to one lysate sample. Therefore the data collected using this method are able only to inform on general protein expression, since they cannot discriminate between areas with different protein expression. Further, this method cannot distinguish whether the lysates were produced from tumour regions deficient or rich in stroma and therefore, tumour lysates are not a direct comparison from protein expression in only the NB cells following a treatment. Further, Caron *et al.* showed that both total and phosphorylated Akt, 4EBP1 and S6 levels can not only differ by ~32 % from the same protein lysates run on different gels, but also vary by as much as 50 % from intra-tissue sampling [378]. Therefore, from my current data, deciphering

the role of relative phosphorylation between these tissue samples could result in misinterpretations and misleading conclusions.

IHC was further performed on some tumour samples with the object to assess the localisation and extent of staining and therefore, the expression of 4EBP1, p-4EBP1<sup>T37/46</sup> and pS6<sup>S240/244</sup> proteins (indicating possible mTORC1/2 inhibition) through the tissue cross section. In the Kelly tumours, the staining for 4EBP1 was alike between all treatment groups suggesting that the total 4EBP1 protein was not affected by the drug. The staining for p-4EBP1<sup>T37/46</sup> and p-S6<sup>S240/244</sup> was reduced in a drug-dose dependent manner, compared to the control (Figure 5.24-A), and the staining was not uniform throughout the tumour slice. This was observed also in the SK-N-BE(2)C tumours samples, however the staining for total 4EBP1 was reduced across the tumour sections at the highest dose of the drug implying a certain effect of AZD2014 on the protein expression (Figure 5.24-B). This was reminiscent of the contraction of the total 4EBP1 WB band observed when SK-N-BE(2)C cells were incubated with AZD2014 for 24 h (Figure 5.4).

The differences in the selected proteins' staining, shown by my IHC studies, suggest that the highest dose of the drug caused detectable changes to the tumour *in vivo*. The degree to which the lower dose (20 mg/kg/day) affected the expression of 4EBP1, p-4EBP1<sup>T37/46</sup>, and p-S6<sup>S240/244</sup> proteins was decidedly less evident in both tumour models than the higher dose (Figure 5.24).

Of note, IHC as a technique to assess protein expression, has some limitations. One of them is linked to the sampling as the analysis of one single 5 µm thick tumour specimen is not enough to have a comprehensive picture of the location and levels of the proteins of interest in the tumour. In my case, multiple slices across the whole tumour would be required to assess properly the effects of AZD2014 in my NB tumours.

As previously mentioned when discussing the *in vitro* data, WB could not provide an accurate measure of NET-1 protein quantity (as well as small levels changes following therapy) in the low-NET-1 expressing Kelly cell line. For this reason, to determine if the AZD2014 treatment influenced the NET-1 production, I assessed *SLC6A2* mRNA (NET-1 transcript) levels by Q-rtPCR in tumour samples after treatment with 20 mg/kg/day AZD2014 over 3 days (Figure 5.25). I observed that, after the treatment, NET-1 transcript levels doubled in the Kelly tumours compared to the vehicle control suggesting that the drug enhanced NET-1 status at a transcriptional level. Interestingly, in the SK-N-BE(2)C tumours, no difference in *SLC6A2* mRNA expression was detected between the treatment group and the vehicle group, despite the small change in NET-1 tumour levels seen by WB. This difference between WB and Q-rtPCR results may have been an artefact caused by using samples collected from different regions of the tumours, which may have been affected by AZD2014 to a greater or lesser degree. However, Dubois *et al.* also showed a lack of correlation between *SLC6A2* levels and NET-1 protein expression in NB tumours, and importantly they demonstrated that the tumour's avidity to <sup>123</sup>I-mIBG is dictated by the protein level rather than mRNA expression [114].

Together, the *ex vivo* analyses on NB tumours after AZD2014 treatment showed a degree of mTORC1/2 inhibition at the highest dose of the drug in both xenograft models. It was difficult to ascertain any effects of AZD2014 at the lower dose (20 mg/kg/day), however, there was some evidence that NET-1 expression was influenced in the SKN-BE(2)C model after 3 days treatment according to the WB data.

### **5.3.5. Correlation between NET-1 protein expression and <sup>18</sup>F-mFBG tumour uptake**

Finally, to understand the discordant <sup>18</sup>F-mFBG tumour uptakes following AZD2014 treatments, the relationship between NET-1 protein expression (analysed by WB) and

<sup>18</sup>F-mFBG tumour uptake (recorded by PET or biodistribution) was examined. To achieve that, I performed a correlation between the measurements using linear regression (Figure 5.26). In the vehicle treated animals group, there was a strong correlation between both the PET and biodistribution values and the tumour NET-1 levels ( $r^2 = 0.92\text{--}0.96$ ) and the slope of the line was approximately  $\sim 7.2$  (range 6.6–7.7). This analysis suggests that the tracer uptake is proportional to the transporter expression in this range. In the AZD2014 treated animals, there was weak correlation between the PET/biodistribution values and the NET-1 expression status, indicated by a goodness-of-fit ( $r^2$ ) of 0.30–0.49. Furthermore, the slope of the curve was less steep (range 2.6–3.4) than the vehicle group. This suggests that the radiotracer uptake in the treated tumours was lower and more unpredictable than expected. This behaviour could be possibly linked to molecular effects of AZD2014 itself. Of note, mTOR inhibition has been shown to promote anti-angiogenic effects [379, 380] through either downregulation of neovasculature or the breakdown of mature vessels already present within the tumour. Both of these events are seen with the mTOR inhibitor everolimus [381]. The reduced tumour vasculature would affect the delivery of the radiotracer and its consequent tumour uptake. Additional studies should be performed to confirm the cause of the irregular radiotracer uptake and the lack of correlation with the NET-1 tumour expression.

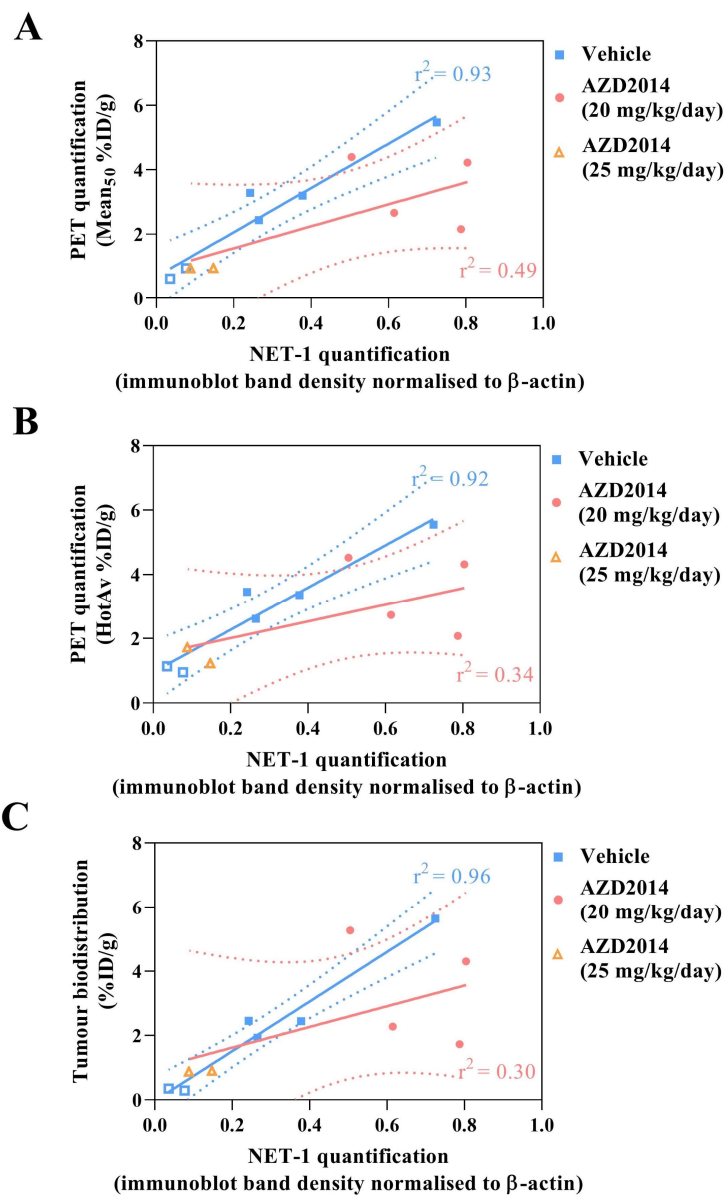


**Figure 5.26** Correlation of NET-1 protein expression (WB band density) and tumour  $^{18}\text{F}$ -mFBG uptake by **A**) PET<sub>50</sub> (%ID/g) **B**) PET<sub>HotAv</sub> (%ID/g) and **C**) Biodistribution (%ID/g) in Kelly (open shapes) and SK-N-BE(2)C (filled shapes) tumours. The dotted line indicates the 95 % CI. Each dot represents a single tumour.

#### 5.4. Conclusions and future directions

The objective of this work was to assess the potential of <sup>18</sup>F-mFBG to quantify changes in NET-1 expression in response to pharmacological intervention using the dual mTORC1/2 inhibitor, AZD2014. The radiotracer could be a likely candidate for PET imaging to predict <sup>131</sup>I-mIBG tumour avidity during combination therapy. Although the drug used in this study has been discontinued, its mTOR inhibition effects offered an insight in to the complications in combination strategies.

From my *in vitro* studies, I found that AZD2014 successfully inhibited its target proteins and caused an increase in <sup>18</sup>F-mFBG uptake in two *MYCN* amplified NB cell lines suggesting an elevation in NET-1 levels. However, the mechanisms behind the rise in NET-1 levels following AZD2014 treatment could not be fully elucidated as p-Akt<sup>S473</sup> levels were not consistently reduced. On that matter, some research groups proposed that either the activation of MAPK pathways or the downregulation of PKC could also influence NET-1 levels [382, 383]. Additional investigations would be needed to confirm whether the AZD2014-induced NET-1 changes were due to activation of alternative pathways.

Despite promising *in vitro* data, when the AZD2014 treatment was carried out on NB xenograft models, no increase of <sup>18</sup>F-mFBG radiotracer uptake in to the tumour was observed in the drug-treated mice compared to the vehicle alone. Indeed, at the highest dose, AZD2014 reduced the radiotracer accumulation in the tumour. IHC analysis of isolated tumours showed some changes caused by the drug on some of the mTOR pathway proteins (i.e p-4EBP1<sup>T37/46</sup> and p-S6<sup>S240/244</sup>) suggesting that AZD2014 treatment targeted the tumours. However, no significant changes in NET-1 levels were observed. Importantly, when a correlation between NET-1 protein expression score assessed by WB and the <sup>18</sup>F-mFBG uptake (PET quantification) was performed, the vehicle treated

tumours correlated well with the radiotracer uptake confirming that <sup>18</sup>F-mFBG is a good marker for tumour NET-1 expression. However, that correlation was lost in the AZD2014 treated tumours. Possibly, the AZD2014 treatment perturbed the delivery and distribution of the radiotracer throughout the tumour.

Further work needs to be implemented to find out the reasons behind this effect. One key experiment should investigate the changes in NB tumour vascularisation following treatment with mTORC1/2 inhibitors. A repressed vasculature would explain the lower-than expected tumour uptake of the radiotracer and ultimately would be detrimental to the development of a combination therapy that includes an mTOR inhibitor and <sup>131</sup>I-mIBG. The effects of the drug would result in a reduced delivery of the molecular radiotherapy agent and therefore, a suboptimal therapeutic benefit despite any increase in NET-1 expression in tumour cells.

Finally, research in to prospective combination agents to use with <sup>131</sup>I-mIBG will continue in hopes of enhancing tumour control whilst minimising off-target toxicities. The work I presented herein demonstrates the necessity of a quantitative measure of mIBG avidity in NB tumours that could hopefully provide the greatest understanding of both positive and negative tumour responses during these treatments.

## Chapter 6 - <sup>89</sup>Zr-labelled Dinutuximab-Beta for imaging GD2 positive NB

### 6.1. Introduction

So far, the focus of my thesis has been investigating PET imaging of NET-1 expression in NB. In this last section, I have explored the imaging of alternative molecular targets in NB. Specifically, my attention was addressed to the membrane associated ganglioside GD2 following the promising, although not fully understood, therapeutic advances in anti-GD2 immunotherapy in the clinic.

In recent years, immunotherapy has revolutionised cancer treatment [384, 385]. Specifically, monoclonal antibodies (mAbs) able to target a particular cancer cell antigen with very high affinity, can produce a therapeutic effect and has been applied to the treatment of different cancer types (passive immunotherapy). Rituximab was the first FDA approved mAb for non-Hodgkin's lymphoma. Since then, around 30 agents have been licensed for clinical use in cancer, and many more are on the horizon [386]. Dinutuximab (ch14.18; approved in 2015 by the FDA), and Dinutuximab-Beta (ch14.18(CHO); EMA approved in 2017), are full-length mAbs targeting the ganglioside GD2. Much alike NET-1, GD2 is expressed near ubiquitously in NB and is relatively restricted in normal healthy tissue [143, 164].

Early clinical trials demonstrated an improved EFS and OS in NB patients receiving GD2 immunotherapy (ch14.18 GD2 antibody) compared to standard of care [171, 387]. Moreover, multiple iterations of the antibody structure and the combination with co-stimulatory cytokines has led to improvements in patient outcome whilst mitigating some of the side effects linked to GD2 immunotherapy [193, 194, 388]. These secondary reactions notably include pain and host immunogenicity, both of which may limit patient wellbeing and therapeutic efficacy. Even so, the long-term OS (>5 years) remains around 40–60 % in HR-NB patients [190, 388, 389].

The high target specificity of full-length mAbs and the simultaneous spatial restriction of the antigen are attractive characteristics suitable for molecular imaging. Numerous research groups have radiolabelled clinically approved therapeutic antibodies and investigated their *in vivo* distribution profiles to provide insight in to variations of the lesion-specific phenotype throughout the therapy. Within NB, early studies used the <sup>131</sup>I-radiolabelled murine anti-GD2 mAb m3F8 to image disease dissemination with high sensitivity and specificity [318, 390]. However, because of the high radiation dose from the β<sup>-</sup> emissions of the radiohalogen, the application of <sup>131</sup>I labelled biomolecules is more preferable for therapeutic compared to diagnostic aims. Both m3F8 and ch14.18 mAbs have been radiolabelled with <sup>131</sup>I and assessed for radioimmunotherapy. However, during the targeted molecular radiotherapy, patients suffered dose-limiting myeloablation from the beta radiation [197, 391, 392].

In imaging, immunoPET is a modality that combines the high targeting specificity of mAbs and the sensitivity of the PET technique. Importantly, the development and increased availability of long-lived PET radionuclides suitable for antibody radiolabelling allowed for a resurgence of tumour antigen specific antibody-based radioconjugates to be used in immunoPET.

Owing to its chemical similarities to the SPECT radionuclide <sup>123</sup>I, and showing potential to predict <sup>131</sup>I dosimetry, <sup>124</sup>I was initially investigated as a promising immunoPET radionuclide. A phase 2 trial for medullablastoma examined the potentiality of GD2-targetting <sup>124</sup>I/<sup>131</sup>I-m3F8 as a theranostic pair [393]. Unfortunately, some characteristics of <sup>124</sup>I, such as its limited availability, prohibitive cost and the high energy positron and photon emissions that interfere with the image acquisition and resolution, limited the use of the radionuclide.

Alternative available PET radionuclides such as <sup>64</sup>Cu and <sup>89</sup>Zr are compatible with immunoPET for a variety of reasons. Both radiometals have half-lives (<sup>64</sup>Cu = 12.7 h, <sup>89</sup>Zr = 78.4 h) well matched to the circulating half-life of full-length antibodies (up to 27 d); both radiolabels are relatively accessible as they can be produced in a medical cyclotron [394, 395]. Additionally, unlike iodine, they are both residualising radioisotopes (labels that produce radioactive catabolites that are retained in the cells), promoting prolonged radioactivity uptake in tumours and sustained contrast between target and non-target tissues. Unfortunately, these residualising radiometals have a tendency to be retained also in the liver, being the major site of catabolism of full-size mAbs [396]. This limits the detection of liver metastases and increases the radiation-induced toxicity to the organ.

To their disadvantage, both radioisotopes have low positron branching fractions (<sup>64</sup>Cu = 17.5%, <sup>89</sup>Zr = 22.7%), and the other emissions need to be taken into account when performing PET image acquisition. Positron emissions from <sup>64</sup>Cu are of a similar energy to <sup>18</sup>F (~278 MeV and 250 MeV, respectively) and so the mean positron range is nearly half that of <sup>89</sup>Zr (0.7 mm versus 1.3 mm), giving <sup>64</sup>Cu greater intrinsic resolution. However, ~38 % of emissions from <sup>64</sup>Cu are β<sup>-</sup>. GD2 antibodies labelled with <sup>64</sup>Cu have highlighted the potential to demarcate NB tumours based on their GD2 expression status [397-399]. But because of the β<sup>-</sup> decay, whilst potentially useful for a combined therapeutic effect, <sup>64</sup>Cu has restricted applications for diagnostic and serial imaging. <sup>89</sup>Zr on the other hand has no β<sup>-</sup> decay, but decays to the stable <sup>89</sup>Y via <sup>89m</sup>Y (half life = 15.84 s) by emitting 909 keV γ rays. The energy of these photons fall outside of energy window of PET detectors (350–650), yet, if the photons undergo scatter and lose some energy, they may interfere with the true PET coincidences.

On this background, I sought to investigate the ability of <sup>89</sup>Zr radiolabelled Dinutuximab-Beta (ch14.18(CHO)) to visualise and quantify GD2 expression in models of NB. Although over 95% of NB tumours are estimated to express GD2 in abundance, there is some evidence of a heterogeneous and dynamic expression of the tumour antigen [400-402]. Importantly, Terzic *et al.* showed that relapse following GD2 immunotherapy correlated with lower GD2 expression in tumour samples measured by IHC [402]. This highlights the importance of investigating tumour GD2 expression to further our understanding of the underlying causes of poor responses following targeted immunotherapy.

## 6.2. Results

### 6.2.1. Characterisation of NB GD2 expression *in vitro*

To first assess the GD2 expression in selected NB cell lines, I performed live cell flow cytometry (FC) using a commercially available GD2 antibody labelled with two different fluorescent dyes (14G2A-PE and 14G2A-FITC) as well as a non-specific FITC-antibody conjugate (IgG2A-FITC) as control. Further, I evaluated the *in vitro* binding of IRDye700DX-ch14.18(CHO) (indicated as IR700-ch14.18(CHO)) that was produced in house. The preparation of the near-infra-red (NIR) conjugate was performed by Dr Chiara Da Pieve (PET Radiochemistry team, The Institute of Cancer Research, UK) by attaching the IRDye700DX-NHS ester to the ch14.18(CHO) mAb (Dinutuximab-Beta).

Firstly, the GD2 status in a panel of six NB cell lines was assessed using the 14G2A-PE antibody (Figure 6.1). There was positive 14G2A-PE staining in NBLS, Kelly and SK-N-AS cell lines, whereas SHEP1, SK-N-BE(2)C and SK-N-SH had no appreciable shift in the histogram peak (Figure 6.1). To estimate the relative GD2 expression between each cell line, the median fluorescence intensity (MFI) was calculated and the mean of at least three independent experiments determined therein. The highest MFI was observed in NBLS cells ( $10321 \pm 4018$ ), whereas an intermediary expression was seen in both Kelly and SK-N-AS cell lines with an MFI of  $2998 \pm 326$  and  $3636 \pm 906$ , respectively. In the SK-N-BE(2)C cell line, corresponding to low GD2 expression, a low MFI ( $73 \pm 42$ ) was observed. GD2 expression in the SHEP1 and SK-N-SH cells was estimated to be negligible with an MFI of  $3 \pm 2$  and  $1 \pm 1$ , respectively (Figure 6.1). As seen by the flow cytometry histogram profile, SK-N-AS cell line showed a broad GD2-positive population distribution, however, in the Kelly cell line two main sub-populations of cells with different GD2 expression levels could be detected (Figure 6.1). The population with

the higher ganglioside levels (Kelly-GD2<sup>High</sup>) was isolated by FACS. Following isolation, these cells showed the highest MFI (69449 ± 7868) (Figure 6.1).

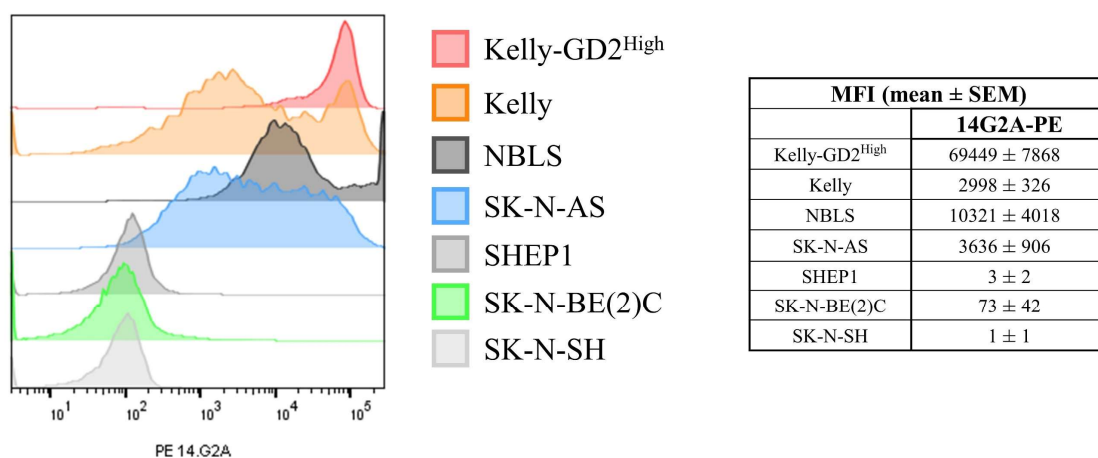


**Figure 6.1** Representative FC histograms of PE-14G2A binding (left) and median fluorescence intensity (MFI) of NB cells with different GD2 expression levels. MFI was measured  $\geq 3$  independent experiments and the data are presented as mean  $\pm$  SEM.

Based on the preliminary assessment, a further study using 14G2A-FITC, an alternative GD2-specific antibody-dye conjugate to 14G2A-PE, was performed on Kelly-GD2<sup>High</sup>, Kelly, SK-N-AS and SK-N-BE(2)C cell lines. The isotopic fluorescent conjugate IgG2A-FITC was used as control to verify the non-specific binding.

Although with a lower fluorescence intensity, a similar binding was seen in all cell lines incubated with 14G2A-FITC compared to 14G2A-PE (Figure 6.2). Moreover, in all cases a low binding of the non-specific IgG control antibody was observed. The MFI of IgG2A ranged from 1  $\pm$  1 to 20  $\pm$  10 in the Kelly and SK-N-BE(2)C cell lines, respectively.

I then characterised the specificity of binding *in vitro* of IR700-ch14.18(CHO) using the same four cell lines. Low binding was observed in the SK-N-BE(2)C cell population (62  $\pm$  10 MFI), whereas SK-N-AS and Kelly cells were GD2 positive with relative MFI of 578  $\pm$  24 and 1018  $\pm$  209, respectively. The isolated Kelly-GD2<sup>High</sup> population had the highest fluorescence intensity in the tested cell lines with 13574  $\pm$  1052.

IR700-ch14.18(CHO) FC histogram highlighted the broad GD2-positive population distribution in SK-N-AS as well as the dual population in the original Kelly cell line (Figure 6.2). Ultimately, as seen by the flow histograms, the binding pattern of IR700-ch14.18(CHO) was similar to the 14G2A-PE and 14G2A-FITC antibodies (Figure 6.2).

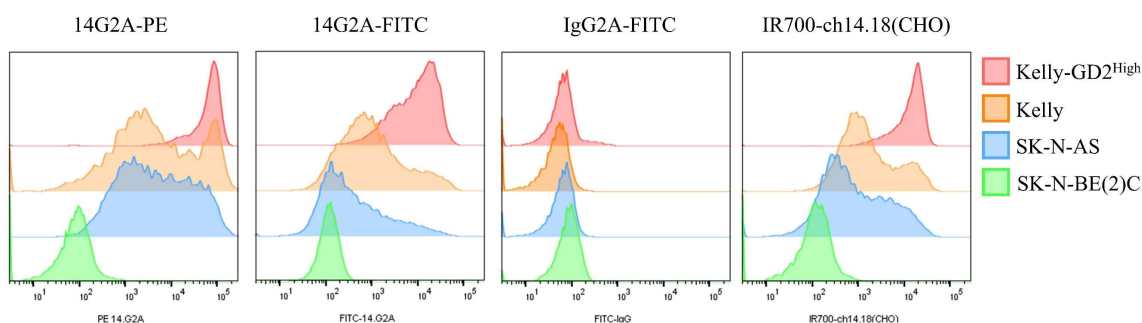


**Figure 6.2** Representative FC histograms of PE, FITC or IRDye700DX labelled anti-GD2 antibodies and IgG2A-FITC non-specific control antibody in a panel NB cell lines.

To further confirm the GD2 expression, I carried out live cell confocal microscopy in the NB cell lines using IR700-ch14.18(CHO) (Figure 6.3). After incubation with the fluorescent conjugate and the nuclear counterstain Hoechst®33342, the Kelly-GD2<sup>High</sup> cell line showed uniform and high GD2 expression on the cell surface. A clear dual population was observed in the Kelly cell line with some cells having a high and others having little to no signal on the cell surface. The SK-N-AS and SK-N-BE(2)C cells showed a moderate to weak and no GD2 expression, respectively.

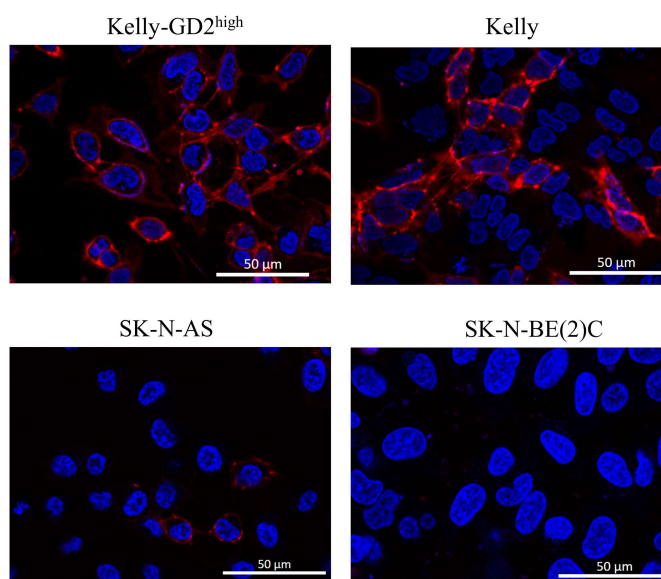


**Figure 6.3** IR700-ch14.18(CHO) confocal microscopy in NB cell lines. Red = IR700-ch14.18(CHO) GD2 staining, Blue = Hoechst@33342 nuclear staining.  $\times 40$  magnification.

### 6.2.2. Immunofluorescence of NB tumour samples

Following these *in vitro* observations, I investigated the GD2 expression in frozen-fixed tumour samples (SK-N-AS, Kelly and SK-N-BE(2)C) using IR700-ch14.18(CHO). SK-N-AS tumours showed a uniform and high expression of the ganglioside, whereas SK-N-BE(2)C cells had very low levels (Figure 6.4). The Kelly tumour sample, generated from the original Kelly cell line, was characterised by intermediary staining that indicated a heterogeneous GD2 expression (Figure 6.4).

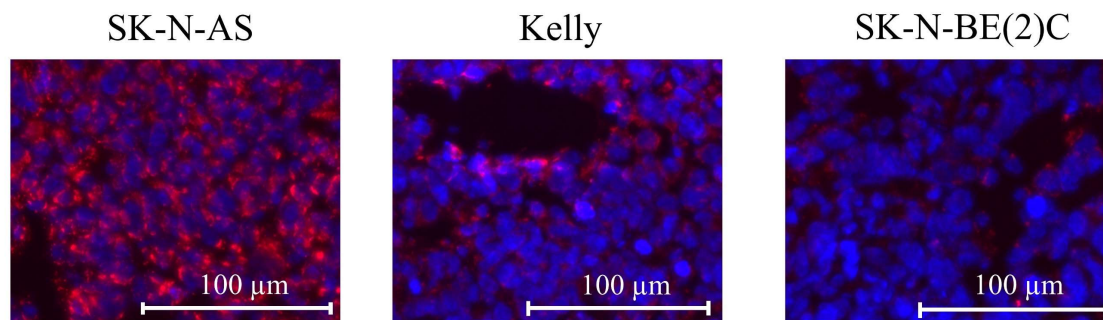


**Figure 6.4** Immunofluorescence of frozen-fixed SK-N-AS, Kelly and SK-N-BE(2)C tumour slices after incubation with GD2-targeting IR700-ch14.18(CHO) (red) and DAPI nuclear counterstain (blue).  $\times 40$  magnification.

### 6.2.3. $^{89}\text{Zr}$ labelling of ch14.18(CHO) and stability of the radioconjugate

The GD2-targeting antibody ch14.18(CHO) was radiolabelled with  $^{89}\text{Zr}$  to assess its ability to visualise and quantify GD2 expression in models of NB. In order to radiolabel proteins, such as mAbs, with radiometals, a suitable chelator must be first attached to the biomolecule. With the aid of Dr Chiara Da Pieve (PET Radiochemistry team, The Institute of Cancer Research, UK), the bifunctional chelator p-NCS-Bz-DFO was attached to lysine residues on ch14.18(CHO) (Figure 6.5). DFO was also conjugated to the IgG1 control antibody following the same procedure. After purification of the DFO-ch14.18(CHO) conjugate, the number of DFO attached to ch14.18(CHO) was determined by mass spectrometry by Mr Meirion Richards (Structural Chemistry Group, Cancer Therapeutics, The Institute of Cancer Research, UK). From the mass spectrometry quantification, the DFO:ch14.18(CHO) ratio was 0.67.

$^{89}\text{Zr}$  labelling was performed by reacting the immunoconjugates with  $^{89}\text{Zr}$ -oxalate at room temperature (Figure 6.5) with the help of Dr Chiara Da Pieve (PET Radiochemistry team, The Institute of Cancer Research, UK). Radiometal incorporations of  $81.0 \pm 6.3\%$  ( $n = 5$ ) and  $61.1 \pm 18.31\%$  ( $n = 2$ ) were obtained for DFO-ch14.18(CHO) and DFO-IgG1, respectively. After purification, both radioimmunoconjugates were obtained with

a RCP of >99 % and a specific activity of 0.19–0.25 MBq/ $\mu\text{g}$  and 0.14–0.14 MBq/ $\mu\text{g}$  for  $^{89}\text{Zr}$ -DFO-ch14.18(CHO) and  $^{89}\text{Zr}$ -DFO-IgG1, respectively.

Further, the stability of  $^{89}\text{Zr}$ -DFO-ch14.18(CHO) in mouse serum was tested up to 7 days. ITLC analysis showed that, after 24 h,  $97.30 \pm 0.87$  % of the radioactivity remained bound to the antibody which fell to  $92.10 \pm 2.08$  % after 3 days and  $83.83 \pm 0.35$  % after 7 days incubation in mouse serum (Figure 6.6).

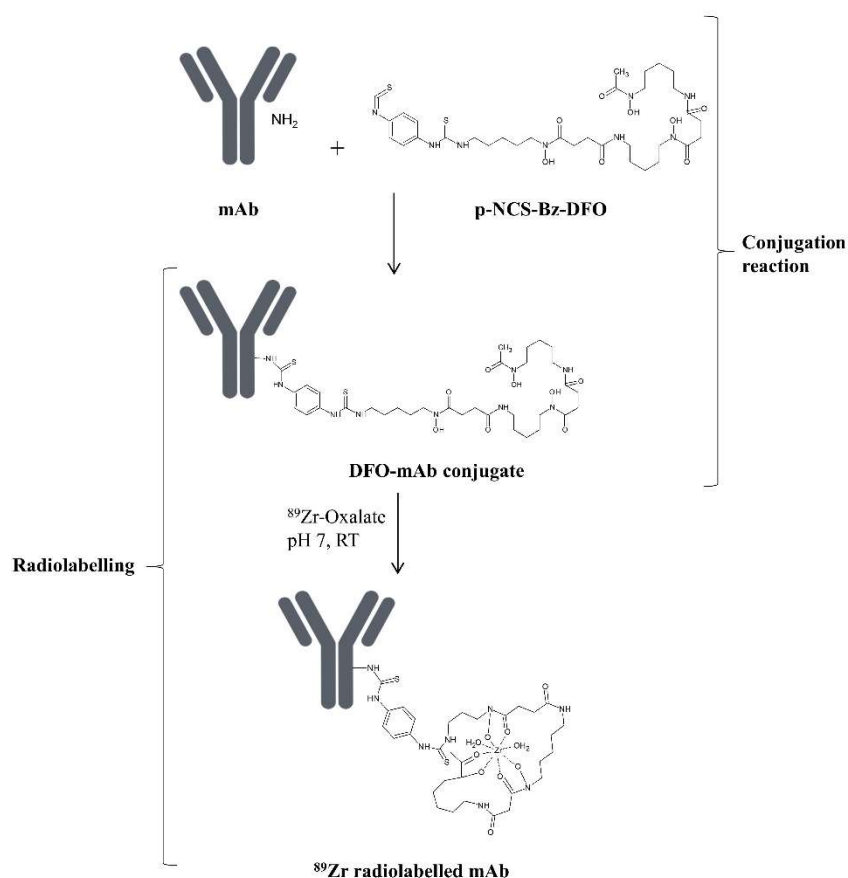


**Figure 6.5** Schematic of the p-NCS-Bz-DFO conjugation to mAb and radiolabelling of DFO-mAb conjugate with  $^{89}\text{Zr}$ .

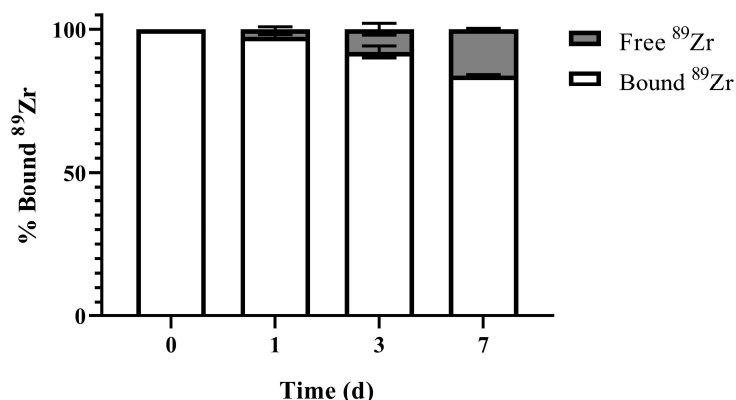


**Figure 6.6** Mouse serum stability of <sup>89</sup>Zr-DFO-ch14.18(CHO) at 37 °C determined by ITLC. N = 1, performed in triplicate. Data are presented as mean ± SD.

#### 6.2.4. <sup>89</sup>Zr-DFO-ch14.18(CHO) cell specificity of binding assay

A specificity of binding assay was performed using <sup>89</sup>Zr-DFO-ch14.18(CHO) (5 nM) on NB cell lines with different GD2 expression status. The results, presented as number of counts/cell/min, showed a negligible cell-associated radioactivity in the low-GD2 expressing SK-N-BE(2)C cell line ( $0.03 \pm 0.01$  CPM/cell), and intermediary activity uptake in the SK-N-AS and Kelly cell lines ( $0.41 \pm 0.03$  and  $0.62 \pm 0.04$  CPM/cell, respectively) (Figure 6.7). The isolated high-GD2 expressing Kelly-GD2<sup>High</sup> showed the greatest <sup>89</sup>Zr-DFO-ch14.18(CHO) cell binding ( $1.91 \pm 0.17$  CPM/cell). When the non-specific <sup>89</sup>Zr-radiolabelled human IgG1  $\kappa$  antibody (indicated as <sup>89</sup>Zr-DFO-IgG1) was incubated with the same set of cell lines a significantly lower cell associated activity, compared to <sup>89</sup>Zr-DFO-ch14.18(CHO), was observed in the Kelly-GD2<sup>High</sup> ( $p < 0.0001$ ), Kelly ( $p < 0.0001$ ) and SK-N-AS ( $p < 0.01$ ) cells and an equivalent very low binding was detected in the SK-N-BE(2)C cell line (0.01–0.02 CPM/cell in each cell line). Further, binding of <sup>89</sup>Zr-DFO-ch14.18(CHO) was significantly reduced in Kelly-GD2<sup>High</sup> ( $p < 0.0001$ ) and Kelly ( $p < 0.001$ ) cells by pre-incubating the cells with a 50-fold excess of non-radiolabelled ch14.18(CHO) (Figure 6.7). In the SK-N-AS cells, pre-incubated with non-radioactive mAb, the radioconjugate binding was decreased but not

significantly ( $p = 0.12$ ). SK-N-BE(2)C cells showed the same very low associated radioactivity independently from the experimental conditions (Figure 6.7).

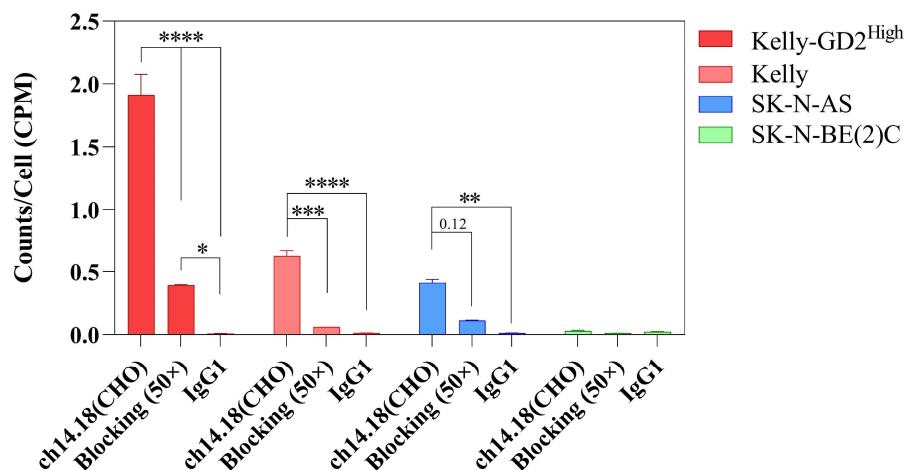


**Figure 6.7** <sup>89</sup>Zr-DFO-Antibody specificity of binding in NB cells. A 50-fold excess of non-radiolabelled antibody was used in the blocking study. Data are presented as mean  $\pm$  SEM. For ch14.18(CHO)  $n = 3$  independent experiments were performed in triplicate. For IgG,  $n = 2$  independent experiments were performed in triplicate. For the blocking study,  $n = 1$  experiment was performed in triplicate with data presented as mean  $\pm$  SD. \*  $p < 0.05$ , \*\*  $p < 0.01$ , \*\*\*  $p < 0.001$ , \*\*\*\*  $p < 0.0001$ ; 2-way ANOVA with Tukey post-hoc test.

A significant ( $p < 0.0001$ ) reduction in <sup>89</sup>Zr-DFO-ch14.18 binding in cells was observed after serial passaging of the Kelly cell lines. Both Kelly-GD2<sup>High</sup> and the original Kelly cell line showed a reduced cell associated radioactivity in cells with multiple passages (p10 or p14) compared with early passage cells (p2) (Figure 6.8).

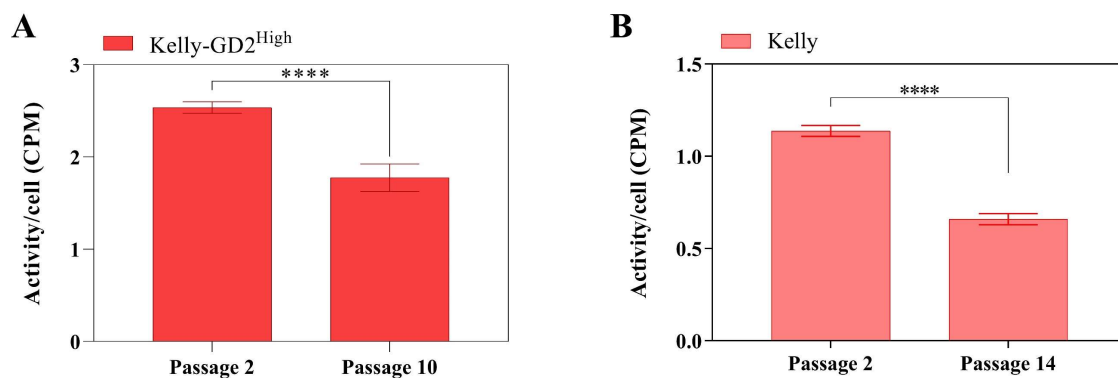


**Figure 6.8**  $^{89}\text{Zr}$ -DFO-ch14.18(CHO) binding in A) Kelly-GD2<sup>High</sup> and B) Kelly cells after few and multiple passages *in vitro*. Data are presented as mean  $\pm$  SD, n = 1 experiment performed in triplicate. \*\*\*\* p < 0.0001; unpaired t-test.

### 6.2.5. PET imaging of $^{89}\text{Zr}$ -DFO-ch14.18(CHO)/IgG1

Given the higher and uniform expression of GD2 in the SK-N-AS tumour sections and low expression in SK-N-BE(2)C tumours (Figure 6.4), the *in vivo* distribution characteristics of  $^{89}\text{Zr}$ -DFO-ch14.18(CHO) were first assessed in these two xenograft models. PET imaging was performed every 24 h up to 96 h p.i. of the radioconjugate. The non-specific  $^{89}\text{Zr}$ -DFO-IgG1 was also used as control in the GD2-expressing SK-N-AS model to assess the specificity of antibody uptake in the tumour and non-target tissues up to 48 h p.i.

Initially, in the low-GD2 expressing SK-N-BE(2)C model, after 24 h p.i. of  $^{89}\text{Zr}$ -DFO-ch14.18(CHO), a clear delineation of the tumours was possible (Figure 6.9). Moreover, there was clear visualisation of the liver and some radioactivity was localised in the joints of the knee. A time-dependent decrease in the signal from the liver could be seen in these mice up to 96 h p.i. The tumour signal also showed a reduction at 96 h compared to 24 and 48 h in all mice (Figure 6.9). The signal from the bone remained similar throughout the entire imaging period.

$^{89}\text{Zr}$ -DFO-ch14.18(CHO)

SK-N-BE(2)C

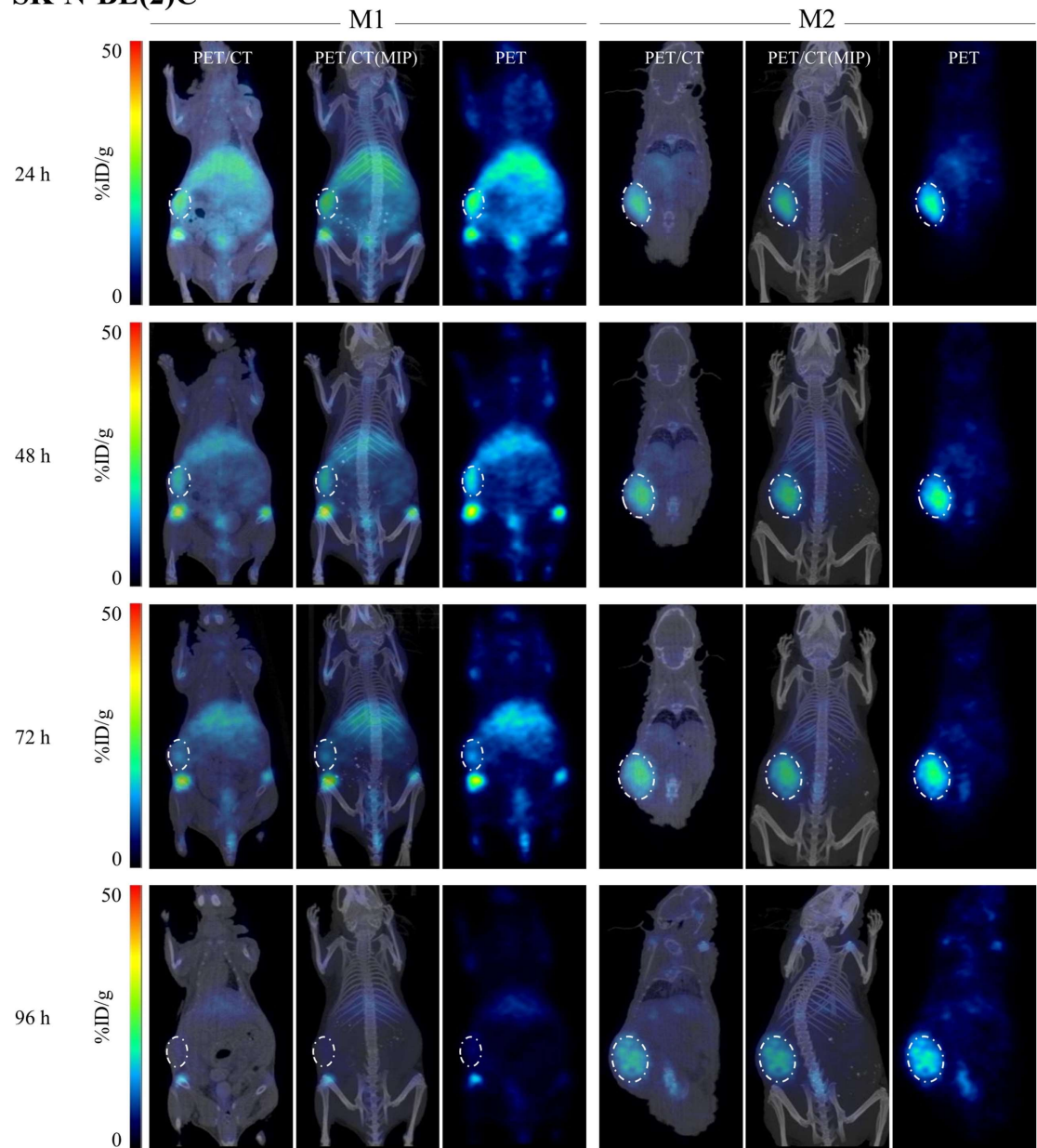


**Figure 6.9**  $^{89}\text{Zr}$ -DFO-ch14.18(CHO) PET/CT, PET/CT(MIP) and 2D coronal plane PET images, 24, 48, 72 and 96 h p.i. in two SK-N-BE(2)C tumour bearing mice. White dotted circle indicates the tumour. PET images are presented as a 2D cross section in the centre of the tumour. MIP = maximum intensity projection of CT.

In the GD2-positive SK-N-AS model, a similarly high signal could be seen from the liver at 24 h, but again this decreased in a time-dependent manner (Figure 6.10). Although not easily defined in the coronal PET slices owing to the location of the tumour and the cross section selection, there was an appreciable <sup>89</sup>Zr signal from the knee joint in each mouse. Already at 24 h there was an observable uptake in the tumour that was maintained up to 96 h p.i. of the radioconjugate. Between the two SK-N-AS tumours shown in Figure 6.10, the uptake in M1 was greater than that of M2. This was representative of the whole mouse cohort, with some mice showing a greater accumulation to the tumours than others of the same model.

$^{89}\text{Zr}$ -DFO-ch14.18(CHO)

SK-N-AS

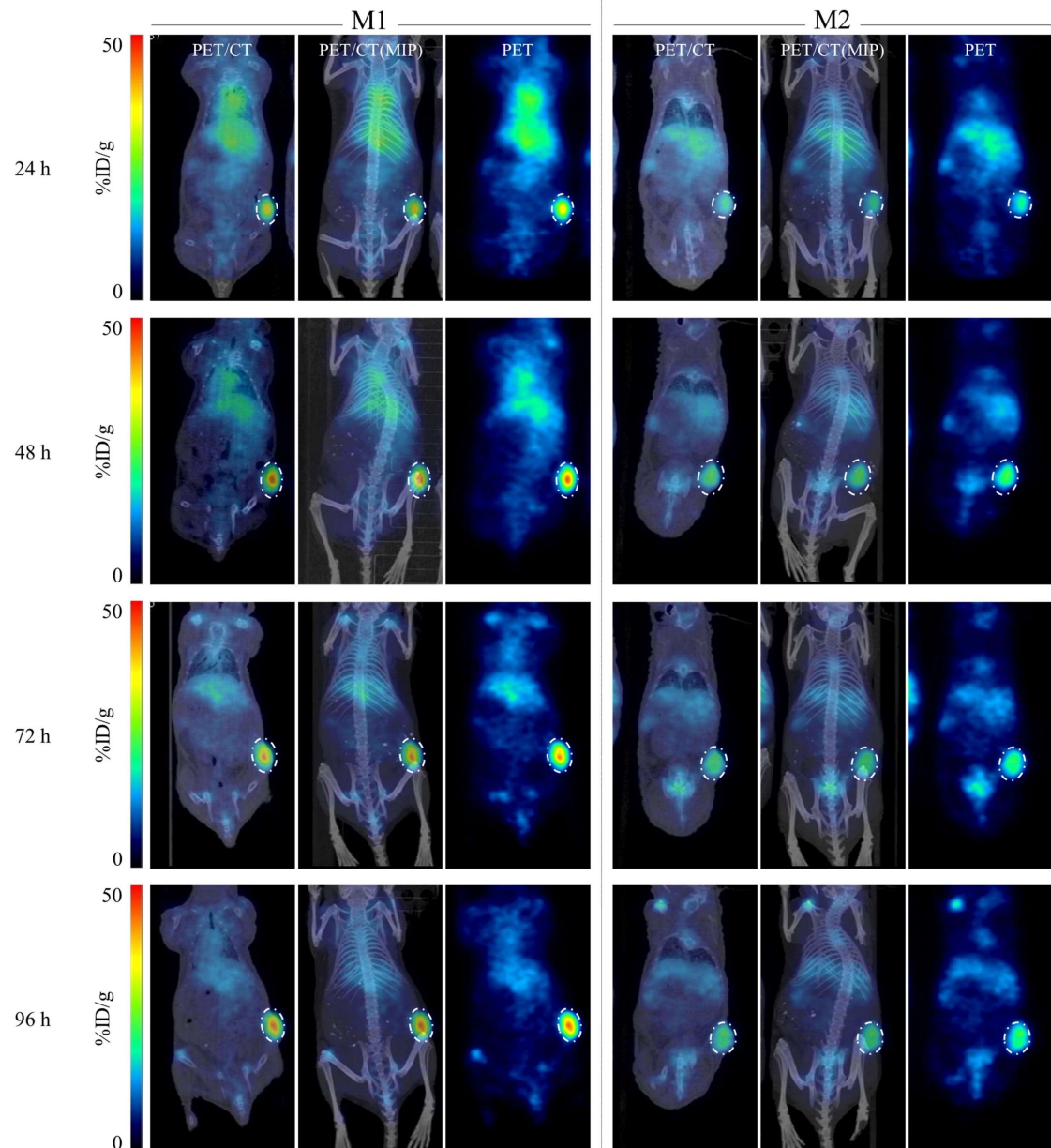


**Figure 6.10**  $^{89}\text{Zr}$ -DFO-ch14.18(CHO) PET/CT, PET/CT(MIP) and 2D coronal plane PET images, 24, 48, 72 and 96 h p.i. in two SK-N-AS tumour bearing mice. White dotted circle indicates the tumour. PET images are presented as a 2D cross section in the centre of the tumour. MIP = maximum intensity projection of CT.

Following injection of <sup>89</sup>Zr-DFO-IgG1 in SK-N-AS tumour bearing mice, a similar distribution between the non-targeted and the GD2-targeted antibody could be seen in the liver, as well as a clear signal in the bone. Tumour retention of the non-specific radioconjugate could be seen at both 24 and 48 h p.i. (Figure 6.1).

**<sup>89</sup>Zr-DFO-IgG1  
SK-N-AS**

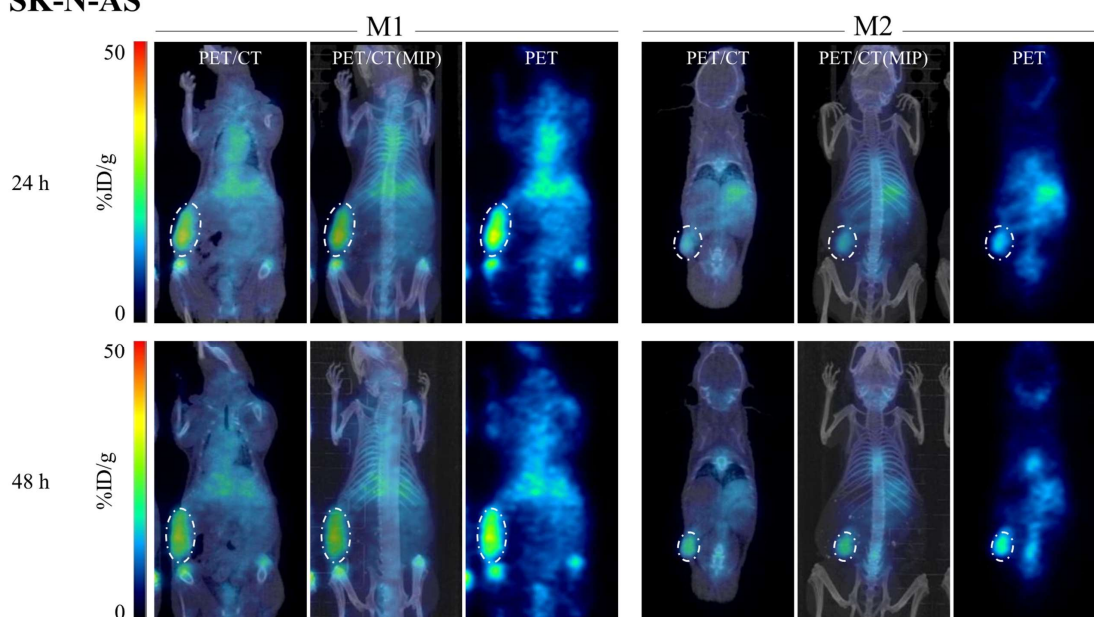


**Figure 6.11** <sup>89</sup>Zr-DFO-IgG1 PET/CT, PET/CT(MIP) and 2D coronal plane PET images, 24 and 48 h p.i. in two SK-N-AS tumour bearing mice. White dotted circle indicates the tumour. PET images are presented as a 2D cross section in the centre of the tumour. MIP = maximum intensity projection of CT.

Quantification of the tumour signal was performed to compare the distribution of each radioconjugate in the xenograft models. For this purpose, the mean signal was calculated from a VOI drawn on the PET/CT images and an automatic isocontour of the hottest 50 % of the pixels was applied (PET<sub>50</sub>).

In the SK-N-BE(2)C tumour, a lower signal from the radioconjugate could be seen after 96 h p.i. ( $12.53 \pm 6.64$  %ID/g) compared to the 48 h time point ( $20.93 \pm 4.60$  %ID/g), although the decrease was not significant ( $p = 0.94$ ) (Figure 6.12). Following injection of

<sup>89</sup>Zr-DFO-ch14.18(CHO) into the SK-N-AS tumour bearing mice, values from PET<sub>50</sub> quantification indicated a radioconjugate uptake in the tumour of  $31.46 \pm 6.64$  %ID/g at just 24 h p.i., which remained consistent after 48 h at  $32.66 \pm 14.50$  %ID/g. After 96 h, there was a slight fall in the signal from the tumours with a mean uptake of  $24.59 \pm 13.51$  %ID/g ( $p = 0.95$ ) compared to the 24 h time point. However, at both 48 and 96 h there was a greater degree of variability between the tumours, with some tumours having nearly 3-times higher uptake of the radioconjugate compared to the lowest (Figure 6.12). In the IgG1 radioconjugate injected mice, the signal quantification in the tumour showed a radioconjugate uptake of  $26.43 \pm 6.62$  %ID/g 48 h p.i. (Figure 6.12).

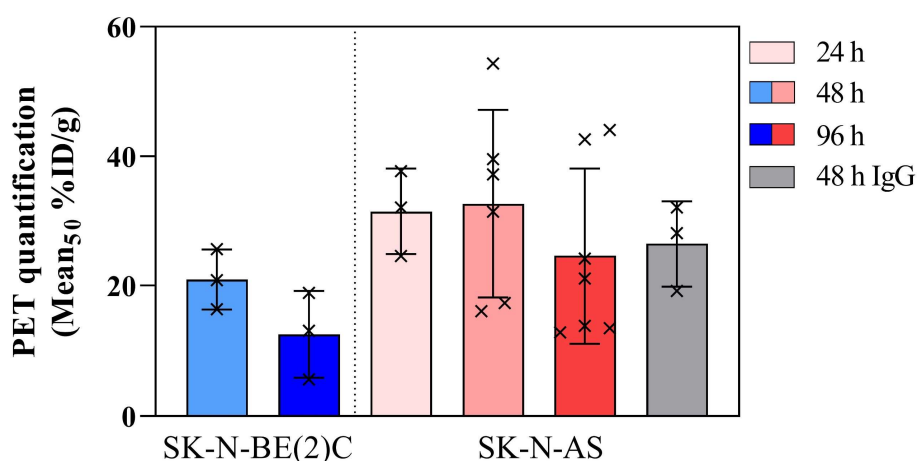


**Figure 6.12** PET<sub>50</sub> quantification of uptake in NB tumours 24, 48 and 96 h p.i. of <sup>89</sup>Zr-DFO-ch14.18(CHO) and 48 p.i. of <sup>89</sup>Zr-DFO-IgG1. Data are presented as mean %ID/g  $\pm$  SD,  $n \geq 3$  per group, each cross represents a single mouse. Significance was determined by one-way ANOVA with Tukey's post hoc analysis.

To assess the signal dynamics from the tumour VOI, PET/CT images were acquired daily up to 96 hr p.i. of the radioconjugate. The variation observed between the SK-N-AS tumours seen at 48 and 96 h (Figure 6.12) could be observed from the first recorded acquisition, 24 h p.i. of <sup>89</sup>Zr-DFO-ch14.18(CHO) (Figure 6.13). The uptake in each

tumour remained stable across the imaging period for most mice, with some increases seen in the tumours with the highest signal (Figure 6.13).

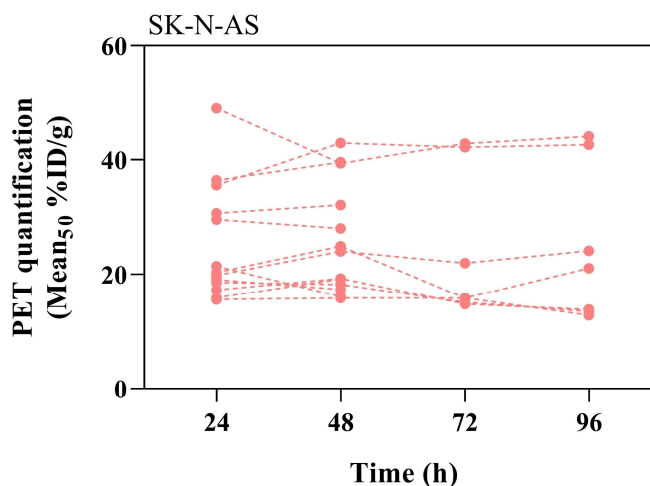


**Figure 6.13** Daily PET<sub>50</sub> quantification of uptake in NB tumours 24, 48, 72 and 96 h p.i. of <sup>89</sup>Zr-DFO-ch14.18(CHO) in SK-N-AS tumour-bearing mice. Dotted lines connect the same mouse scanned on each day of the study. Data are presented as mean %ID/g.

#### 6.2.6. <sup>89</sup>Zr-DFO-ch14.18(CHO)/IgG1 biodistribution

In the SK-N-BE(2)C tumour bearing mice, biodistribution was performed at 48 and 96 h p.i. of the anti-GD2 radioconjugate. After injection of the <sup>89</sup>Zr-DFO-ch14.18(CHO) in the SK-N-AS model, mice were sacrificed at 24, 48 and 96 h p.i., whereas biodistribution of <sup>89</sup>Zr-DFO-IgG1 in this model was performed at 48 h p.i. only.

Firstly, in the SK-N-BE(2)C, low GD2 expressing NB tumour model, the uptake in normal tissue was similar at both 48 h and 96 h p.i. (Figure 6.14, Table 6.1). The spleen (~9 %ID/g), liver (~6.5 %ID/g) and bone (~12.5 %ID/g) showed the greatest radioactivity uptake. All other analysed organs had low retention of the radioconjugate (< ~5 %ID/g). A small but insignificant decrease in blood radioactivity levels could be seen at 96 h (2.09 ± 1.42 %ID/g) compared to 48 h p.i. (4.83 ± 3.89 %ID/g). There was also a slight but insignificant increase in bone uptake from 10.87 ± 3.38 %ID/g at 48 h to 14.24 ± 8.23

%ID/g at 96 h p.i. The radioconjugate uptake in the tumour was found to be  $11.49 \pm 2.68$  %ID/g at 48 h and not significantly different compared to the uptake at 96 h p.i. ( $8.45 \pm 2.87$  %ID/g;  $p = 0.93$ ) (Figure 6.14; Table 6.1).

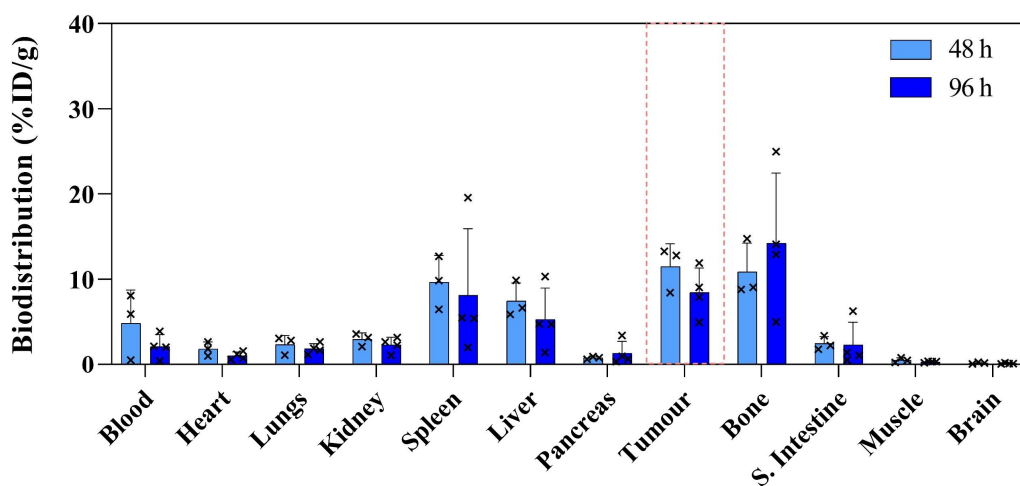


**Figure 6.14** Biodistribution of <sup>89</sup>Zr-DFO-ch14.18(CHO) 48 and 96 h p.i. in mice bearing SK-N-BE(2)C xenografts. Data are presented as mean %ID/g ± SD, n ≥ 3 per group. Each cross represents a single mouse. S. Intestine = Small intestine.

<sup>89</sup> Zr-DFO-ch14.18(CHO) biodistribution (%ID/g)		
	48 h	96 h
Blood	4.83 ± 3.89	2.09 ± 1.42
Heart	1.81 ± 0.82	1.03 ± 0.45
Lungs	2.31 ± 1.08	1.83 ± 0.61
Kidney	2.94 ± 0.77	2.28 ± 0.89
Spleen	9.65 ± 3.13	8.10 ± 7.82
Liver	7.46 ± 2.11	5.28 ± 3.70
Pancreas	0.76 ± 0.14	1.32 ± 1.39
<b>Tumour</b>	<b>11.49 ± 2.68</b>	<b>8.45 ± 2.87</b>
Bone	10.87 ± 3.38	14.24 ± 8.23
Small intestine	2.45 ± 0.81	2.30 ± 2.65
Muscle	0.49 ± 0.27	0.29 ± 0.08
Brain	0.16 ± 0.11	0.11 ± 0.06
<b>Tumour:blood</b>	<b>6.74 ± 8.38</b>	<b>7.48 ± 8.45</b>
<b>Tumour:muscle</b>	<b>27.33 ± 10.31</b>	<b>29.00 ± 3.69</b>

**Table 6.1** Biodistribution of <sup>89</sup>Zr-DFO-ch14.18(CHO) 48 and 96 h p.i. in mice bearing SK-N-BE(2)C xenografts. Data are presented as mean %ID/g ± SD, n ≥ 3 per group.

Secondly, after <sup>89</sup>Zr-DFO-ch14.18(CHO) injection in the SK-N-AS xenografts, biodistribution data showed that the blood activity was the highest at 24 h p.i. ( $11.89 \pm 5.18$  %ID/g) and significantly decreased over the 96 h period ( $2.48 \pm 2.45$  %ID/g;  $p = 0.01$ ) (Figure 6.15, Table 6.2). There was no difference in the uptake of the radioconjugate in the majority of non-target organs (i.e. heart, lungs, kidney, pancreas, small intestine, muscle and brain) between each time point (Figure 6.15) and the 48 and 96 h p.i. figures paralleled that of the SK-N-BE(2)C xenograft model (Figure 6.14). The liver, a key organ in antibody clearance, showed high and constant retention of radioactivity throughout the study with values of  $7.60 \pm 3.20$  %ID/g,  $8.44 \pm 1.28$  %ID/g and  $9.02 \pm 1.75$  %ID/g after 24, 48 and 96 h p.i. of <sup>89</sup>Zr-DFO-ch14.18(CHO), respectively. The measured radioactivity in the spleen was also high from as early as 24 h p.i. ( $10.32 \pm 7.34$  %ID/g) and it increased at each time point up to  $20.01 \pm 10.33$  %ID/g at 96 h p.i. ( $p < 0.01$  compared to the 24 h value). The bone-associated radioactivity increased from  $6.54 \pm 3.34$  %ID/g at 24 h to  $21.31 \pm 6.39$  %ID/g at 96 h p.i. ( $p < 0.0001$ ) (Figure 6.15; Table 6.2). Both the uptake in the spleen ( $p < 0.001$ ) and in the bone ( $p = 0.06$ ) was higher compared to the SK-N-BE(2)C model at 96 h p.i. The mean tumour uptake after 24 h p.i. of <sup>89</sup>Zr-DFO-ch14.18(CHO) was  $26.27 \pm 5.75$  %ID/g, which was similar to the 48 h ( $24.31 \pm 13.59$  %ID/g) and the 96 h time points ( $22.52 \pm 11.18$  %ID/g) (Figure 6.15).

To determine the <sup>89</sup>Zr-DFO-IgG1 organ uptake in the SK-N-AS tumour bearing mice, biodistribution was performed at 48 h p.i. <sup>89</sup>Zr-DFO-IgG1 retention was high in normal tissues such as spleen ( $13.99 \pm 7.85$  %ID/g), liver ( $8.53 \pm 1.99$  %ID/g), and bone ( $16.87 \pm 1.87$  %ID/g) and low in other non-target organs ( $<6$  %ID/g). SK-N-AS tumour uptake of the non-specific <sup>89</sup>Zr-DFO-IgG1 was  $19.90 \pm 7.67$  %ID/g (Figure 6.16; Table 6.2).

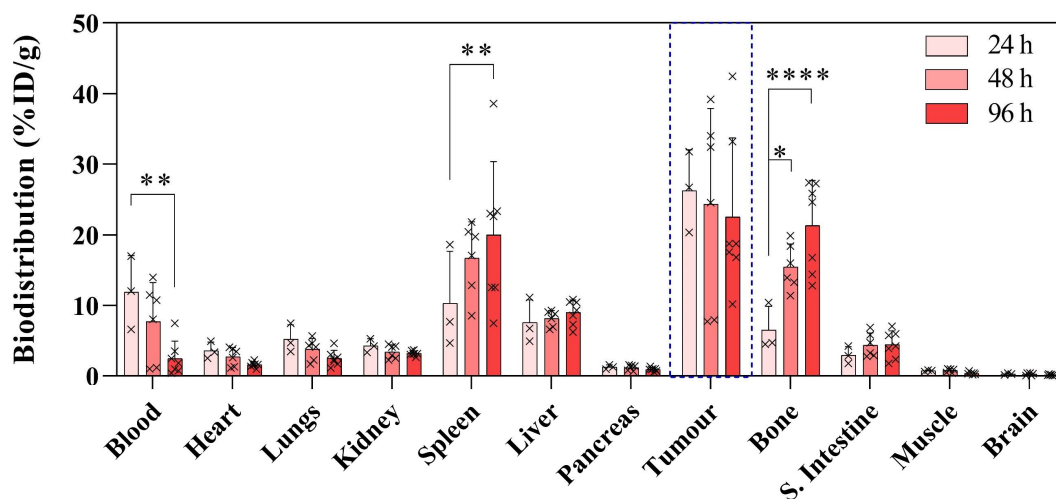


**Figure 6.15** Biodistribution results 24, 48 and 96 h p.i. of  $^{89}\text{Zr}$ -DFO-ch14.18(CHO) in mice bearing SK-N-AS tumour xenografts. Data are presented as mean %ID/g  $\pm$  SD,  $n \geq 3$  per group. Each cross represents a single mouse. \*  $p < 0.05$ , \*\*  $p < 0.01$ , \*\*\*  $p < 0.001$ , \*\*\*\*  $p < 0.0001$ ; 2-way ANOVA with Tukey post-hoc test. S. Intestine = Small intestine.

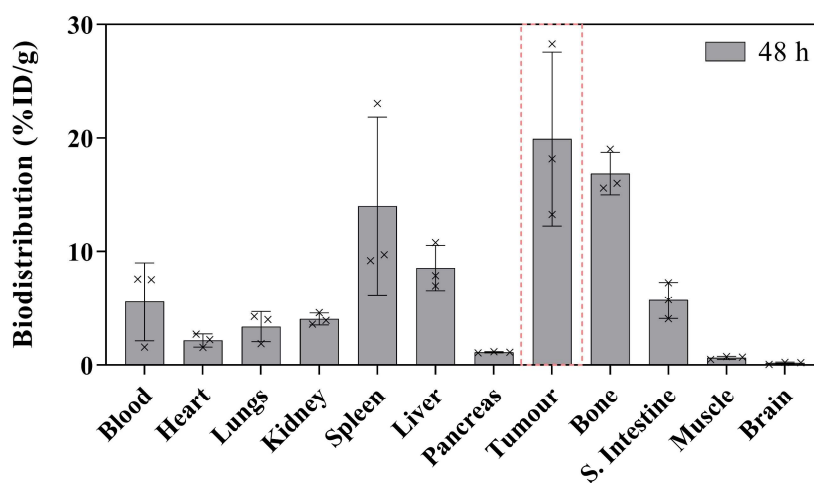


**Figure 6.16** Biodistribution results 48 h p.i. of  $^{89}\text{Zr}$ -DFO-IgG1 in mice bearing SK-N-AS tumour xenografts. Data are presented as mean %ID/g  $\pm$  SD,  $n = 3$ . Each cross represents a single mouse. S. Intestine = Small intestine.

<sup>89</sup> Zr-DFO-ch14.18(CHO) (%ID/g)				<sup>89</sup> Zr-DFO-IgG1 (%ID/g)	
	24 h	48 h	96 h	48 h	
Blood	11.89 ± 5.18	7.73 ± 5.48	2.48 ± 2.45	Blood	5.55 ± 3.45
Heart	3.60 ± 1.22	2.73 ± 1.28	1.61 ± 0.41	Heart	2.15 ± 0.57
Lungs	5.21 ± 2.05	3.79 ± 1.51	2.52 ± 1.12	Lungs	3.35 ± 1.30
Kidney	4.29 ± 0.96	3.42 ± 0.98	3.20 ± 0.35	Kidney	4.01 ± 0.52
Spleen	10.32 ± 7.34	16.73 ± 5.11	20.01 ± 10.33	Spleen	13.99 ± 7.85
Liver	7.60 ± 3.20	8.14 ± 1.13	9.02 ± 1.75	Liver	8.53 ± 1.99
Pancreas	1.27 ± 0.30	1.19 ± 0.38	0.93 ± 0.25	Pancreas	1.11 ± 0.05
<b>Tumour</b>	<b>26.27 ± 5.75</b>	<b>24.31 ± 13.59</b>	<b>22.52 ± 11.18</b>	<b>Tumour</b>	<b>19.90 ± 7.67</b>
Bone	6.54 ± 3.34	15.47 ± 3.22	21.31 ± 6.39	Bone	16.87 ± 1.87
Small intestine	2.96 ± 1.21	4.39 ± 1.70	4.44 ± 1.93	Small intestine	5.66 ± 1.60
Muscle	0.74 ± 0.09	0.78 ± 0.26	0.37 ± 0.18	Muscle	0.63 ± 0.14
Brain	0.28 ± 0.11	0.26 ± 0.16	0.15 ± 0.08	Brain	0.18 ± 0.09
<b>Tumour:blood</b>	<b>2.38 ± 0.61</b>	<b>4.46 ± 2.31</b>	<b>16.45 ± 14.12</b>	<b>Tumour:blood</b>	<b>5.70 ± 5.20</b>
<b>Tumour:muscle</b>	<b>35.31 ± 3.37</b>	<b>28.83 ± 9.13</b>	<b>61.63 ± 13.99</b>	<b>Tumour:muscle</b>	<b>31.88 ± 10.94</b>

**Table 6.2** Biodistribution results 24, 48 and 96 h p.i. of <sup>89</sup>Zr-DFO-ch14.18(CHO) (left) and 48 h p.i. of <sup>89</sup>Zr-DFO-IgG1 (right) in mice bearing SK-N-AS tumour xenografts. Data are presented as mean %ID/g ± SD, n ≥ 3 per group.

A more detailed tumour uptake analysis showed that there was much greater variation in <sup>89</sup>Zr-DFO-ch14.18(CHO) uptake in the high GD2-expressing SK-N-AS than the low GD2-expressing SK-N-BE(2) tumour, with some SK-N-AS tumours showing as low uptake as that of the SK-N-BE(2)C xenograft (Figure 6.17).

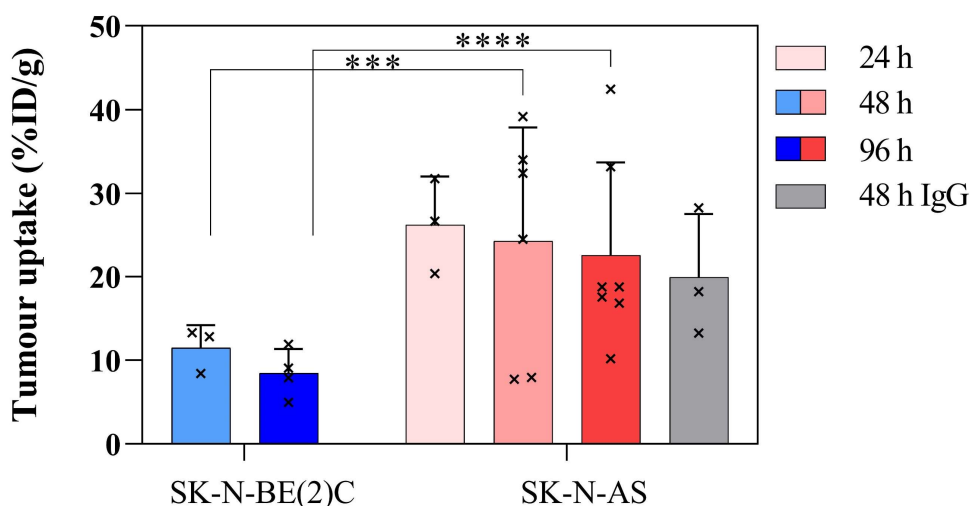


**Figure 6.17** Tumour uptake of <sup>89</sup>Zr-DFO-ch14.18(CHO) at 24, 48 and 96 h p.i. in mice bearing SK-N-BE(2)C and SK-N-AS xenografts and <sup>89</sup>Zr-DFO-IgG1 uptake in SK-N-AS tumour bearing mice at 48 h p.i. Data are presented as mean %ID/g ± SD, n ≥ 3 per group. Each cross represents a single mouse. \*\*\* p < 0.001, \*\*\*\* p < 0.0001 2-way ANOVA with Tukey post-hoc test.

A comparison between the PET<sub>50</sub> quantification and the biodistribution data of the uptake of <sup>89</sup>Zr-DFO-ch14.18(CHO) and <sup>89</sup>Zr-DFO-IgG1 in SK-N-AS xenografts showed a good correlation with a coefficient of determination ( $r^2$ ) of 0.76 (Figure 6.18). PET quantification overestimated the tumour uptake of the radioconjugate, as the slope of the line of best fit was 0.99, but the y-intercept was 5.5.

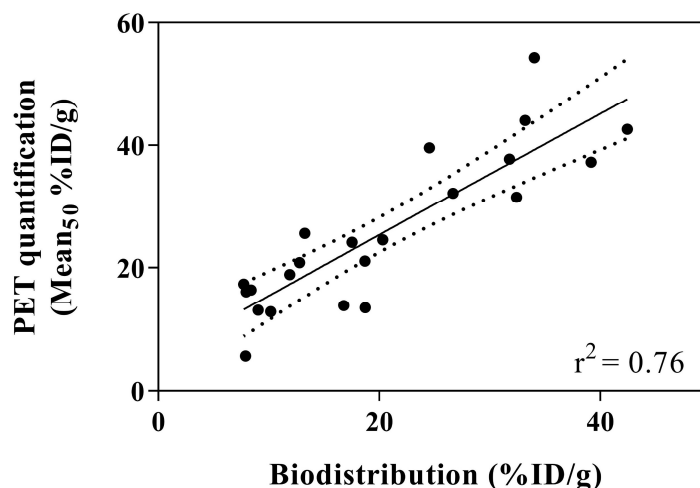


**Figure 6.18** Correlation between PET<sub>50</sub> and biodistribution values in SK-N-BE(2)C and SK-N-AS tumours 24, 48 and 96 h p.i. of <sup>89</sup>Zr-DFO-ch14.18(CHO) or 48 h p.i. of <sup>89</sup>Zr-DFO-IgG1. The dotted line represents the 95 % CI.

### 6.2.7. *Ex vivo* analysis

Following biodistribution, tumour and spleen samples were taken for *ex vivo* analysis. Autoradiography was performed on samples collected 48 h p.i. of <sup>89</sup>Zr-DFO-ch14.18(CHO) or <sup>89</sup>Zr-DFO-IgG1.

As shown in Figure 6.19, the signal from the GD2 targeted radioconjugate in the SK-N-BE(2)C tumour xenograft was low whereas a higher signal could be seen in segments of the SK-N-AS tumours. However, the two analysed SK-N-AS tumours show an evident difference in radioactivity levels with one having a greater uptake (M1) compared to the other (M2). This was marked by a certain degree of heterogeneity across the tissues, with areas of a greater and lower intensity seen in both tumours (Figure 6.19).

The distribution of <sup>89</sup>Zr-DFO-IgG1 in the SK-N-AS tumour was mostly localised to the borders of the tissue slice (Figure 6.19).

Autoradiography of the spleens of the two SK-N-AS tumour bearing mice showed a divergent radioactivity content and distribution with low and high uptake in mouse M1 and M2, respectively, after injection of <sup>89</sup>Zr-DFO-ch14.18(CHO). The <sup>89</sup>Zr signal was primarily seen on the outer section of the spleen (the red pulp), with only a weak signal in the centre of organ (the white pulp) (Figure 6.19).

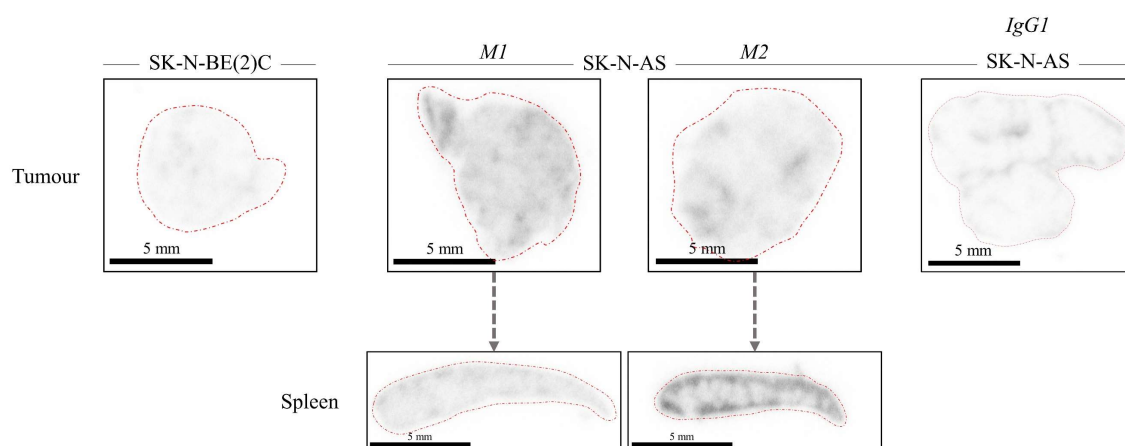


**Figure 6.19** Autoradiography of NB xenograft (top) and mouse spleen (bottom) 48 h p.i. of <sup>89</sup>Zr-DFO-ch14.18(CHO) or <sup>89</sup>Zr-DFO-IgG1 (right). Red dotted line indicates the tissue/organ boundary.

To further investigate whether the signal in the spleen was due to possible GD2 expression in the organ and the consequent specific binding of <sup>89</sup>Zr-DFO-ch14.18 to the ganglioside, I performed multicolour FC on isolated SK-N-AS and SK-N-BE(2)C tumour and spleen cells from mice not injected with the radioconjugate. FC was performed with IR700-ch14.18(CHO) and tumour cells were gated as CD9<sup>+</sup> CD45<sup>-</sup> based on previous reports [403]. In the stained samples, with a value of  $37 \pm 2$ , the spleen MFI was very low and not significantly different from SK-N-BE(2)C tumour ( $1080 \pm 1017$ ;  $p = 0.43$ ). IR700-ch14.18(CHO) binding in the SK-N-AS tumour was significantly greater than both

the spleen ( $p < 0.001$ ) and the SK-N-BE(2)C tumour ( $p < 0.001$ ) with a MFI of  $8093 \pm 1306$  (Figure 6.20).

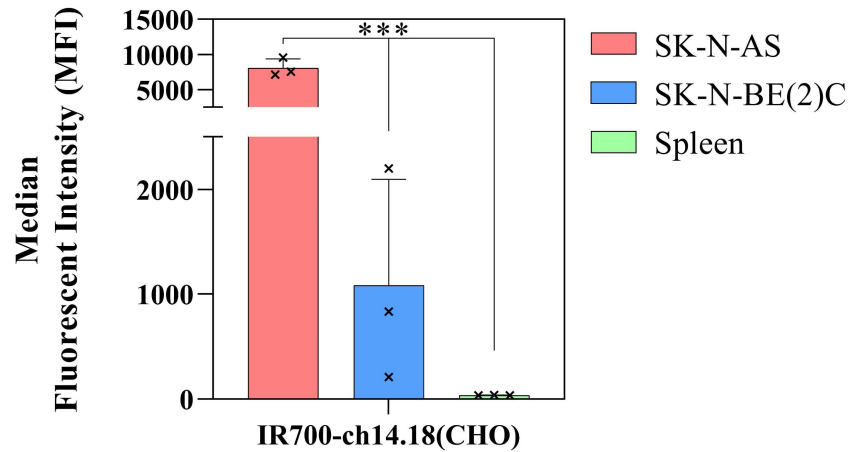


**Figure 6.20** Flow cytometry of *ex vivo* spleen and NB tumour samples presented as MFI of IR700-ch14.18(CHO). Tumour cells were selected to be CD9 positive and CD45 negative. Data are presented as mean MFI  $\pm$  SD. Each sample is represented by a cross. Significance was determined between SK-N-AS tumour and both SK-N-BE(2)C tumour and spleen. \*\*\*  $P < 0.001$  one-way ANOVA with Tukey's post-hoc test analysis.

### 6.3. Discussion

GD2-targeted immunotherapy has improved EFS and OS rates in HR-NB, but 40–60 % of patients still eventually relapse with the disease [190, 388]. Therefore, greater insight into the mechanisms behind the treatment outcome is needed to support better clinical therapy decisions. One key requirement for the success of anti-GD2 immunotherapy is the cell surface expression of the ganglioside. Although it is thought to be expressed ubiquitously in NB, some tumours do not express GD2 and its expression status can also change during treatment [401, 404].

As a surrogate marker for ganglioside expression, analysis of GD2 synthase mRNA levels have shown good correlation to the response to immunotherapy in NB [405]. However, whether a linear relationship exists between GD2 synthase mRNA amounts and actual GD2 expression has not been assessed.

Terzic *et al.* has shown that IHC analysis of GD2 status in NB could provide a useful prognostic marker for immunotherapy effects, with patients with low GD2 expressing tumours more likely to relapse following treatment compared to those with high GD2 expression [402]. In patients with multiple lesions, however, multiple invasive tumour biopsies should be performed to collect useful information of the ganglioside's expression due to its possible heterogeneous presence. Therefore, molecular imaging shows great potential for a non-invasive measurement of NB GD2 expression across the whole body.

Historically, the anti-GD2 antibody m3F8 has been used to visualise NB disease dissemination with both planar scintigraphy (as <sup>131</sup>I-m3F8) and PET (as <sup>124</sup>I-m3F8) imaging [317, 318], with the former highlighting increased lesion detection sensitivity compared to <sup>131</sup>I-mIBG scintigraphy [318]. However, the widespread use of GD2 targeted molecular imaging has been limited because of the low quality of <sup>131</sup>I imaging and the high costs and low availability of the PET radioisotope <sup>124</sup>I. More recently, alternative

radiolabels have been investigated for anti-GD2 immunoPET, most notably <sup>64</sup>Cu and <sup>89</sup>Zr [320, 397, 399].

Multiple GD2 mAbs have been developed for immunotherapy including: the murine mAbs m3F8 and 14G2A, the chimeric mAbs ch14.18 (Dinutuximab) and ch14.18(CHO) (Dinutuximab-Beta), and the humanised mAbs hu3F8 and hu14.18K322A [406, 407]. The humanised antibodies have been established to reduce the potential side effects associated with GD2 immunotherapy, such as HAMA and HACA host immunogenicity and pain [193, 194]. However, only Dinutuximab and Dinutuximab-Beta have so far been approved for clinical use by the FDA and EMA, respectively.

Therefore, for the purpose of my investigations, I chose to work with the European approved Dinutuximab-Beta which was radiolabelled with <sup>89</sup>Zr and used to assess the GD2 expression in NB cell lines (*in vitro*) and NB xenografts (*in vivo*).

### **6.3.1. Characterisation of GD2 expression in NB cell lines**

I first assessed GD2 levels in a panel of NB cell lines *in vitro* using FC. Binding of the commercially available anti-GD2 antibody, PE-14G2A, indicated high GD2 expression in the NBL5, SK-N-AS and Kelly cell lines and low expression in the SK-N-BE(2)C, SK-N-SH and SHEP1 cells (Figure 6.1). From the FC histograms, which amalgamates the fluorescence intensity of each cell within the chosen fluorescent channel, I observed a broader peak in the SK-N-AS cell line compared to NBL5. Further, two distinct populations of Kelly cells with medium and high binding of the antibody could be seen (Figure 6.1). I used FACS to isolate the high GD2 expressing cells (Kelly-GD2<sup>High</sup>), with the aim to employ them to assess the affinity (i.e. dissociation constant or  $K_D$ ) of ch14.18(CHO) by saturation assay and to determine the immunoreactive fraction of the radiolabelled antibody. Although NBL5 cells showed high GD2 expression from this

initial study, I did not continue with this cell line due to the relative difficulty to grow it *in vitro*.

Following the findings from the PE-14G2A FC experiment, I performed a similar test on the isolated Kelly-GD2<sup>High</sup>, the original Kelly, SK-N-AS, and SK-N-BE(2)C cell lines using the FITC-labelled 14G2A antibody and its colour matched isotype FITC-IgG2A conjugate as control. As expected, the binding of the GD2-specific FITC-14G2A conjugate on the various cells was similar to the previously evaluated PE-14G2A. Importantly, the IgG2A isotype control showed lack of binding for GD2 target and therefore a minimal non-specific binding across each cell line (Figure 6.2).

Although the labelled 14G2A antibodies were successfully used to estimate GD2 expression in these studies, I wanted to confirm the binding specificity of ch14.18(CHO), as this would be the antibody I subsequently used for *in vivo* imaging. I therefore assessed the in-house produced IRDye700DX-labeled Dinutuximab-Beta (IR700-ch14.18(CHO)) antibody in the same cell lines to confirm its GD2 binding specificity. IRDye700DX was chosen for both FC and confocal microscopy as it has a high fluorescence intensity and is more photostable following excitation compared to the PE fluorophore. The dye is also commercially available with the NHS-ester reactive group allowing for straightforward conjugation to the ch14.18(CHO) antibody (<https://www.licor.com/bio/reagents/irdye-700dx-nhs-ester>).

As expected, the FC histograms of IR700-ch14.18(CHO) in each of the four cell lines matched those of the labelled 14G2A antibodies, showing low GD2 expression in the SK-N-BE(2)C cells, medium expression in SK-N-AS and Kelly cells, and a high expression in the isolated Kelly-GD2<sup>High</sup> cells (Figure 6.2). Next, my plan was to perform a saturation assay to determine the  $K_D$  as indication of the ch14.18(CHO) target affinity using IR700-ch14.18(CHO) and the Kelly-GD2<sup>High</sup> cell population. However, as the assay required an

amount of material (i.e. unconjugated ch14.18(CHO)) that was not yet available in the lab, I was unable to carry out the necessary experiments. However, previous reports have shown that Dinutuximab-Beta (ch14.18(CHO)) has an approximate  $K_D$  of ~11.2 nM [408], indicating a good GD2 affinity [409].

I also performed live cell confocal microscopy with IR700-ch14.18(CHO), to visualise GD2 expression in individual NB cells (Figure 6.3). The results paralleled the findings from FC in all cell lines. Notably, the low and high GD2 populations in the unsorted Kelly cell line were easily identified. Using the same labelled antibody, I performed immunofluorescence staining of archived frozen-fixed NB xenografts, to confirm their GD2 expression status (Figure 6.4). In line with the *in vitro* data, the SK-N-BE(2)C tumour had low expression of the ganglioside, however, the tumour did not completely lack GD2 expression. In the Kelly xenograft, which was generated using the unsorted Kelly cells, there was a medium expression of GD2, with regions of higher and lower intensity staining similar to the two populations seen by FC and confocal microscopy. In the SK-N-AS tumour, a high and uniform GD2 expression was seen, which contrasted the relatively weak staining observed in the confocal images acquired from live cells. An early study by Tsuchida *et al.* showed that tumour derived melanoma cells cultured *in vitro* alter their ganglioside expression compared to the original tumour phenotype [410]. Further, the authors demonstrated that the ganglioside expression pattern was revived in these cells when xenograft tumours were generated in mouse models. This may account for the inverse results I observed in the SK-N-AS tumour cell phenotype. The immunofluorescence staining experiment was crucial for choosing the more suitable xenograft models for the following *in vivo* studies.

### 6.3.2. <sup>89</sup>Zr-DFO-ch14.18(CHO) *in vitro* characterisation

In order to radiolabel ch14.18(CHO) with <sup>89</sup>Zr, I first needed to attach an appropriate chelator to the antibody. The hexadentate chelator p-NCS-Bz-DFO was used (Figure 6.5). Iron-chelator deferoxamine (DFO) has been used for many years for the treatment of iron overload disease [411]. Importantly, this type of iron-binding ligand showed to be valuable in <sup>89</sup>Zr radiochemistry [412] and Meijs *et al.* and other research groups demonstrated the good *in vitro* stability of the DFO-<sup>89</sup>Zr complex [413, 414]. To achieve the DFO-mAb conjugate, the bifunctional chelator p-NCS-Bz-DFO was attached to the mAb by reacting with lysine residues on the protein (Figure 6.5). Dinutuximab and Dinutuximab-Beta have a large number of lysine residues (48 of which 34 are on the heavy chain, 14 are within the light chain including 3 lysines situated in the purported complementarity determining region of the antibody) [415]. Therefore, reaction of the antibody with p-SCN-Bn-DFO are likely to produce randomly generated conjugates (i.e. not site specific conjugation). In my case, after incubation of ch14.18(CHO) with an excess of p-SCN-Bn-DFO and after purification of the final product (DFO-ch1.418(CHO)), a number of chelates per antibody of 0.67 was confirmed by mass spectrometry. The determination of the immunoreactive fraction using the radiolabelled conjugate would be required to fully assess the antigen recognition of the modified antibody [416]. Unfortunately, the available amount of antibody (i.e. unconjugated ch14.18(CHO)) was not sufficient for all studies I planned to perform. However, the low number of antibody-associated DFO molecules was most probably not affecting the antigen recognition of radiolabelled ch14.18(CHO) antibody to a great degree.

The DFO-IgG1 conjugate was prepared following the same protocol used for DFO-ch14.18(CHO). In this case, the number of chelates per antibody was not determined

because, as the antibody is designed to be non-specific, the attachment of the chelator molecule would not affect the protein affinity or specificity to any antigen.

Following conjugation, <sup>89</sup>Zr radiolabelling was performed by Dr Chiara Da Pieve (PET radiochemistry team, The Institute of Cancer Research, UK). The radiolabelled antibodies were isolated with high RCP (>99 %) and a specific activity similar to that of previously reported data [417]. <sup>89</sup>Zr-DFO-ch14.18(CHO) showed good stability after 1 and 3 days in mouse serum with under 10 % loss of the radiometal from the radioconjugate. After 7 days, nearly 20 % demetallation was observed indicating a certain long-term instability of the radioconjugate (Figure 6.6).

Next, I assessed the binding specificity of <sup>89</sup>Zr-DFO-ch14.18(CHO) in selected NB cell lines with different GD2 expression (i.e. Kelly-GD2<sup>High</sup>, Kelly, SK-N-AS and SK-N-BE(2)C). The cell binding assay reflected the previously reported FC data, whereby Kelly-GD2<sup>High</sup> had the greatest recorded cell associated radioactivity, Kelly and SK-N-AS cells had intermediary binding, and SK-N-BE(2)C cells showed minimal binding (Figure 6.7). However it was not possible to determine the cell heterogeneity observed by FC in the Kelly cell line using this method. In the Kelly-GD2<sup>High</sup> population, even after incubation with a 50-fold molar excess of non-radiolabelled antibody, the relative counts were still high which suggested an insufficient blocking in this high GD2 expressing cell line. Across all cell lines, cell associated radioactivity was negligible after incubation with <sup>89</sup>Zr-DFO-IgG1, further confirming the specificity of the anti-GD2 antibody. As could not have access to large quantities of the antibody, further characterisation of the binding affinity of <sup>89</sup>Zr-DFO-ch14.18(CHO) could not be performed and will have to be implemented in the future, together with the already mentioned assessment of the radioconjugate's immunoreactive fraction.

Interestingly, during the same experiment, I performed a cell binding assay on Kelly and Kelly-GD2<sup>High</sup> cell lines from early and late cell passages and showed a decreased cell associated radioactivity in the latter cell population (Figure 6.8). This could be a result of antigen shedding in these cells. NB cells have been shown to shed their gangliosides both *in vitro* and *in vivo* and may be a mechanism of immune evasion to enhance tumour growth [159, 164, 418-420]. It was therefore deemed essential to use early passage cell lines for experiments assessing GD2 expression in NB cells.

### 6.3.3. <sup>89</sup>Zr-DFO-ch14.18(CHO)/IgG1 PET imaging

Following the *in vitro* observations, I went on to characterise the PET imaging capabilities of <sup>89</sup>Zr-DFO-ch14.18(CHO) in NB mouse models. This work was carried out in the low GD2 expressing xenograft, SK-N-BE(2)C, and the high GD2 expressing xenograft, SK-N-AS, following the results from the *ex vivo* staining of frozen-fixed tumour samples. Although the isolated Kelly-GD2<sup>High</sup> cell line showed the greatest MFI from the FC data, this cell line was not chosen due to the relative difficulty to grow the tumour *in vivo* compared to SK-N-AS. Additionally, I assessed the distribution of the non-specific <sup>89</sup>Zr-DFO-IgG1 in the SK-N-AS xenograft as control.

After injection of either <sup>89</sup>Zr-DFO-ch14.18(CHO) or <sup>89</sup>Zr-DFO-IgG1, there was a clear liver uptake in all mice at 24 h p.i. (Figure 6.9, Figure 6.10, and Figure 6.11). This is likely due to the organ's role as a major site of antibody processing and metabolism even at the earliest time point analysed [396, 421]. Further, as <sup>89</sup>Zr is a residualising isotope, catabolism of the radioconjugate in the liver would result in retention of radioactivity in the tissue throughout the whole study [422]. From the PET images, at all time points, there was a clear signal in the bone. As observed during the serum stability test, <sup>89</sup>Zr-DFO-ch14.18(CHO) showed a certain degree of demetallation (Figure 6.6). It is likely that the radioconjugate released free <sup>89</sup>Zr ions also *in vivo*, that preferentially

accumulate in the bone. Abou *et al.* highlighted the preferential accumulation of <sup>89</sup>Zr ions specifically in the mineralized constituents of the bone (i.e. phosphates of the epiphysis) [423]. The authors also demonstrated injecting <sup>89</sup>Zr-DFO directly in the mice did not accumulate in bone due to its rapid excretion [423], therefore, suggesting that cleavage of the <sup>89</sup>Zr-DFO complex from the antibody was not responsible for the release of the radiolabel into circulation. The demetallation of the <sup>89</sup>Zr-DFO complex may be due to the fact that DFO has only 6 of the 8 donor atoms required by the metal to create a very stable chelate (of note, two molecule of water complete the complex structure by occupying the two remaining coordination sites) (Figure 6.5). The incapacity of DFO to fulfil the coordination demand of the radiometal could lead to some instability of <sup>89</sup>Zr-DFO. Different research groups have assessed the potential of alternative chelators for improved <sup>89</sup>Zr radiolabelling properties. Octadentate chelators, which would occupy all 8 coordination sites of the radiometal, may provide better *in vitro* and *in vivo* stability of radioconjugates. However, none have yet to be approved for clinical use [412, 424, 425].

*In vivo* stability of the radioconjugate is an important aspect for the translation in to man. High accumulation of <sup>89</sup>Zr ions in the bone could increase the radioactive dose to this tissue and result in increased bone marrow toxicity [426]. In paediatric patients, circulating free <sup>89</sup>Zr ions may accumulate at the epiphyseal plate (growth plate) as bone growth has not reached developmental maturity in this stage of life. One clinical trial in paediatric patients highlighted a relatively high bone uptake following <sup>89</sup>Zr-DFO-bevacizumab imaging [427], however the authors concluded that further work needs to be carried out to elucidate the extent of <sup>89</sup>Zr-induced bone toxicity.

PET quantification was performed on the radioconjugate uptake in the tumour of each mouse. In the SK-N-BE(2)C model, an appreciable uptake of the <sup>89</sup>Zr-DFO-ch14.18(CHO) was seen at 48 h p.i. A small decrease in the signal from the tumour was

observed after 96 h, which could be attributed to clearance of the radioconjugate from the system (Figure 6.12).

PET quantification of the non-specific <sup>89</sup>Zr-DFO-IgG1 uptake in the SK-N-AS xenograft was also high at 48 h (Figure 6.12). This indicated that the radioconjugate showed non-specific accumulation in the tumour. Injecting the radioconjugate with a lower specific activity could help reduce the tumour signal of these low GD2 expressing tumours.

Regarding specific accumulation of <sup>89</sup>Zr-DFO-ch14.18(CHO) in the SK-N-AS xenograft model, no measurable difference was seen in the PET quantification of each tumour between 24 and 48 h p.i. and there was a small fall in the mean signal observed after 96 h p.i. (Figure 6.12). However, of particular note was the variation in the tumour quantification values, with some tumours showing much lower uptake than others. The low-uptake tumours values were also comparable to the data measured from the low GD2 expressing SK-N-BE(2)C model as well as the <sup>89</sup>Zr-DFO-IgG1 control mice.

As I had performed PET imaging every 24 h up to 96 h p.i. of <sup>89</sup>Zr-DFO-ch14.18(CHO), I was able to assess the dynamic changes in the radioconjugate accumulation in the tumour in the SK-N-AS model during the whole study (Figure 6.13). I observed that a tumour uptake variability, similar to the one detected in the 48 and 96 h p.i. static time scans, started at the earliest time point (24 h) and the tumour signal remained stable throughout the whole imaging study. From the PET imaging alone, this could suggest that either some SK-N-AS tumours did not express the ganglioside or the delivery of the radioconjugate to the tumour was inhibited in some of the mice.

#### **6.3.4. <sup>89</sup>Zr-DFO-ch14.18(CHO)/IgG1 biodistribution**

Immediately following the final PET imaging session of each cohort, tumours and major organs were taken for biodistribution analysis. For <sup>89</sup>Zr-DFO-ch14.18(CHO) this

corresponded to 48 and 96 h in the SK-N-BE(2)C model, and 24, 48 and 96 h in the SK-N-AS model. Biodistribution of the <sup>89</sup>Zr-DFO-IgG1 in SK-N-AS tumour bearing mice was performed at 48 h only.

In the SK-N-BE(2)C, low GD2 expressing tumour model, biodistribution data showed low accumulation in most of non-target organs (heart, lung, kidney, pancreas, small intestine, muscle and brain) (Figure 6.14). In the blood, a relatively low signal was observed at 48 h, which slightly dropped after 96 h p.i. This suggested some clearance of the circulating radioconjugate from the mouse over this time period. The highest radioactive signal from the normal tissue was observed in the spleen, liver and bone (Figure 6.14 and Table 6.1). A number of factors could contribute to the accumulation of the antibody conjugate in the spleen and liver. Firstly, GD2 could be expressed in these organs, however, previous reports have shown that the ganglioside was undetectable in the liver [428], and very low to undetectable expression has been observed in the spleen [428, 429]. Secondly, the capillaries of the liver and spleen are ‘leaky’, meaning the vascular endothelium is fenestrated to facilitate the passage of large molecules and cells between the tissue and the blood [430, 431]. This would allow for the processing and subsequent catabolism of the antibody conjugates in these organs [396, 432]. In the bone, the radioactive signal was high at 48 h and slightly increased after 96 h p.i. (Figure 6.14). This was likely due to demetallation of the radioconjugate *in vivo* and accumulation of free <sup>89</sup>Zr ions in this tissue.

The biodistribution data of the non-targeted <sup>89</sup>Zr-DFO-IgG1 in the SK-N-AS tumour model show radioactivity uptake in all non-target organs very similar to the SK-N-BE(2)C model. The highest activity retention in normal tissue was seen in the liver and spleen (Figure 6.16 and Table 6.2), which suggested that the uptake of <sup>89</sup>Zr-DFO-ch14.18(CHO) was not specific in these organs. Further, a high bone radioactivity showed

a similar degree of *in vivo* instability between the GD2-specific and the non-specific radioconjugates.

In the targeted delivery of <sup>89</sup>Zr-DFO-ch14.18(CHO) in the SK-N-AS xenograft model, I observed similar values in those tissues with low retention of the radioconjugate (heart, lung, kidney, pancreas, small intestine, muscle and brain) between 24, 48 and 96 h p.i. (Figure 6.15 and Table 6.2). Further, the signal observed in the liver was high and it did not change between each time point. The radioactivity in the blood was greatest at 24 h and was significantly reduced after 96 h p.i. Notably, the activity concentrations from these organs at 48 and 96 h was no different to the data from the SK-N-BE(2)C tumour bearing mice or the IgG1 control group.

Conversely, in both the spleen and the bone of the SK-N-AS xenograft model, a time-dependent increase in uptake was detected (Figure 6.15), and the values were also significantly greater than the SK-N-BE(2)C model at the 96 h p.i time point. A comparison between the splenic radioactivity retention and the signal from the bone showed a possible correlation (Figure 6.21,  $r^2 = 0.67$ ). Once in the spleen, <sup>89</sup>Zr-DFO-ch14.18(CHO) could be processed and catabolised, resulting in the release of <sup>89</sup>Zr ions in the blood and subsequently accumulation in the bone.

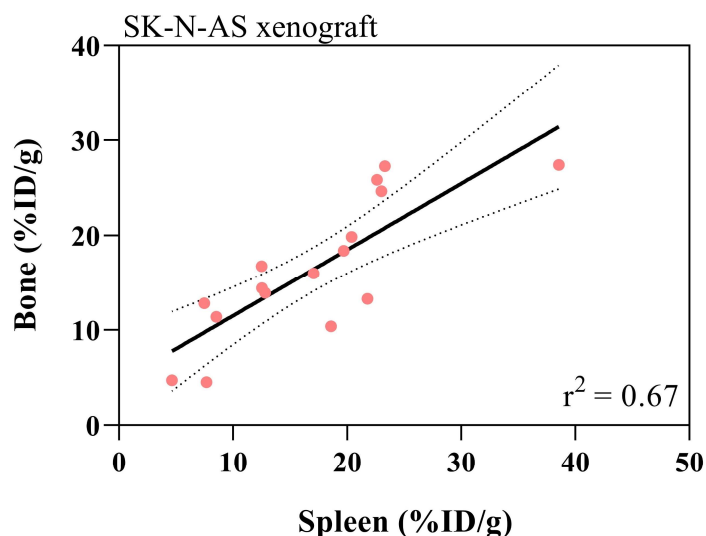


**Figure 6.21** Correlation between uptake values in the spleen and bone of SK-N-AS tumour bearing mice 24, 48 and 96 h p.i. of <sup>89</sup>Zr-DFO-ch14.18(CHO). The dotted line represents the 95 % CI.

Regarding the tumour uptake of <sup>89</sup>Zr-DFO-ch14.18(CHO), the data showed a general time-dependent fall in radioconjugate retention, which was over two-times lower in the SK-N-BE(2)C tumour compared to the SK-N-AS tumour at both 48 and 96 h p.i. However, there was a considerable variability in the uptake values between the SK-N-AS tumours at the later time points (48 and 96 h p.i.) (Figure 6.17) with some tumours having a comparable radioactivity retention to the non-specific <sup>89</sup>Zr-DFO-IgG1 control.

The possible explanation of the low <sup>89</sup>Zr-DFO-ch14.18(CHO) uptake in some of the SK-N-AS tumours (allegedly high GD2-expressing) could be the presence of low levels of GD2 already on the cells that have been inoculated or in the tumour as a consequence of antigen shedding. Increased circulating levels of GD2 have been shown in the blood of NB patients [161, 433] and the ganglioside has therefore also been investigated as a possible circulating tumour biomarker [434]. Antigen shedding may explain the low tumour uptake since <sup>89</sup>Zr-DFO-ch14.18(CHO) would bind mostly to the antigen in the blood pool and subsequently be cleared through the spleen and liver [435]. In a study

performed by Lee *et al.*, <sup>89</sup>Zr-amatuximab, targeting the actively shed mesothelin antigen, was sequestered in to the liver and spleen of the mouse when injected in low concentrations (i.e. 2 µg) causing a low tumour retention. By increasing the injected amounts of <sup>89</sup>Zr-amatuximab (10 and 60 µg), so that the antibody was in molar excess of the circulating antigen, the authors achieved an increase in blood radioactivity and ultimately tumour uptake. Further, the radioactivity levels in the spleen and liver were decreased. Finally, the authors demonstrated that, by using the <sup>89</sup>Zr-B3 radioconjugate against the non-shed Lewis-Y antigen, the tumour uptake was similar at both low and high injected doses [436]. Together this could offer a potential reason of the low tumour uptake in some of the SK-N-AS-tumour bearing mice. Injecting higher quantities than 10 µg of <sup>89</sup>Zr-DFO-ch14.18(CHO) could increase the tumour uptake whilst minimising non-target uptake.

### **6.3.5. *Ex vivo* analysis in the NB tumour and mouse spleen**

Following the biodistribution studies, I performed autoradiography of spleen and tumours slices (48 h p.i.) to confirm the localisation and distribution of <sup>89</sup>Zr-DFO-ch14.18(CHO) and <sup>89</sup>Zr-DFO-IgG1. I also performed FC from tissues excised from naïve tumour (not injected with the radioconjugate) and spleens from SK-N-BE(2)C and SK-N-AS bearing mice to assess the GD2 expression.

Autoradiography showed that the distribution of the anti-GD2 <sup>89</sup>Zr-DFO-ch14.18(CHO) was low across the SK-N-BE(2)C tumour slices and lower compared to the GD2-positive SK-N-AS tumours. However, there was a clear difference between the SK-N-AS tumour samples taken from two separate mice, with the specimen from one animal (M1) showing a much higher radioactive signal compared to the other (M2). However, the radioactivity signal was heterogeneous across both M1 and M2 tumour slices. The spleens from the same mice were excised and autoradiographed. An inverse signal was observed in the

spleen segments compared to the corresponding tumour specimens, with low spleen signal observed in M1 and high in M2 (Figure 6.19). Of note, the signal was mostly limited to the red pulp (outer regions) of the spleen. The principal role of the spleen's red pulp is to filter the blood of dying erythrocytes and other macromolecules (including antibodies) [437]. The Fc region of antibodies is recognised by Fc $\gamma$  receptor expressing cells such as splenic macrophages in the red pulp. Phagocytosis of the radioconjugate by splenic macrophages would contribute to the baseline accumulation of the activity in this tissue [432]. Additionally, as already mentioned previously, possible <sup>89</sup>Zr-DFO-ch14.18(CHO) bound to blood circulating GD2 is rapidly directed to and catabolised in the splenic red pulp. It has been shown that, upon antibodies binding to their antigen, there is an increase in clearance rate of the complex [438, 439].

To investigate the GD2 expression in SK-N-AS and SK-N-BE(2)C tumours and spleen, I excised and macerated the tissues and performed FC analysis using IR700-ch14.18(CHO). In the tumour samples, I used a multicolour FC setup and sorted NB tumour cells for PE-CD9 positivity and BV510-CD45 negativity according to previous publications [403]. This would allow me to estimate the GD2 targeting of IR700-ch14.18(CHO) specifically to the tumour cell population. Within the spleen, I was interested in the GD2 status regardless of the cellular lineage, therefore, cells were only gated on the IR700 channel. The FC data showed that the SK-N-AS tumours expressed a high level of GD2, whereas the SK-N-BE(2)C had low expression of the ganglioside. GD2 levels in the spleen were undetectable, suggesting that the <sup>89</sup>Zr-DFO-ch14.18(CHO) spleen uptake was not target specific (Figure 6.20).

Owing to time-constraints it was not possible to perform immunofluorescence on the excised tumours in the <sup>89</sup>Zr-DFO-ch14.18(CHO) injected animals. This test would be required to confirm the GD2 expression status of each tumour and would determine

whether the low radioactivity uptake in some of the SK-N-AS tumours was the result of low GD2 expression or of the inability of the radioconjugate to reach the tissue.

#### **6.4. Conclusions and future work**

The objective of this chapter was to assess the potential of the <sup>89</sup>Zr radiolabelled ch14.18(CHO) (Dinutuximab-Beta) antibody to visualise and delineate GD2 positive NB tumour xenografts by PET. The preliminary experiments described in this chapter show that <sup>89</sup>Zr-DFO-ch14.18(CHO) was able to measure GD2 expression in a panel of NB cells having different expression levels of the ganglioside. However, the *in vivo* data revealed a non-reproducible uptake of <sup>89</sup>Zr-DFO-ch14.18(CHO) in high GD2-expressing tumours that could be caused by antigen shedding from the NB tumours.

*In vitro* validation studies of the <sup>89</sup>Zr-DFO-ch14.18(CHO), such as its binding affinity and immunoreactive fraction, will be needed to complete the characterisation of the radioconjugate. Further, an *in vivo* dose-escalation study of the radioconjugate should be carried out to optimise the tumour uptake and PET detection of GD2 positive NB tumours.

Although Dinutuximab-Beta immunotherapy has improved patient outcomes in NB, a proportion of patients eventually have disease relapse. Like <sup>123</sup>I-mIBG imaging is a necessary prerequisite for <sup>131</sup>I-mIBG therapy, imaging the ganglioside may appropriately stratify patients likely to respond to the targeting immunotherapy based on tumour GD2 expression.

### Chapter 7 - General Conclusions

The aim of this project was to develop and investigate PET agents to assess the expression of molecular markers of NB. Nowadays, molecular imaging of NB use  $^{123}\text{I}$ -mIBG SPECT for the planning of individualised  $^{131}\text{I}$ -mIBG treatment of norepinephrine transporter (NET-1) expressing tumours. However, because of the advantages of PET over SPECT imaging, the use of the fluorinated NE analogue,  $^{18}\text{F}$ -mFBG, can provide greater detail of the tumour NET-1 expression, whilst being beneficial for patient wellbeing. Additionally, alternative molecular targets, such as GD2, are investigated for potential targeted therapeutic intervention of NB. Therefore, molecular imaging can non-invasively gather information on the tumour expression status of these alternative targets. This would improve patient's stratification for the delivery of the most appropriate treatment regimens.

#### 7.1. $^{18}\text{F}$ -mFBG PET as a tool to measure NET-1 status in NB

Within the first part of this thesis, I set out to assess whether  $^{18}\text{F}$ -mFBG PET would be a suitable alternative to  $^{123}\text{I}$ -mIBG imaging in NB models. The results demonstrated that the fluorinated NE analogue was a robust alternative to the mIBG radiotracer through similar *in vitro* cell uptake and *in vivo* pharmacokinetics. Unfortunately, a comparison between  $^{18}\text{F}$ -mFBG PET and  $^{123}\text{I}$ -mIBG SPECT could not be carried out due to suboptimal  $^{123}\text{I}$ -mIBG images.

However,  $^{18}\text{F}$ -mFBG PET quantification was an accurate measure of radiotracer uptake in NB tumours. Further research examining the prognostic potential of the radiotracer would help determine the optimal dosing strategies for  $^{131}\text{I}$ -mIBG therapy.

#### 7.2. $^{18}\text{F}$ -mFBG PET to monitor changes in NET-1 expression in NB

Next, I used the  $^{18}\text{F}$ -mFBG radiotracer to quantify changes in NET-1 expression in response to pharmacological intervention using a dual mTORC1/2 inhibitor, AZD2014.

Strategies that increase NET-1 expression in NB tumours could improve the uptake of the molecular radiotherapy agent,  $^{131}\text{I}$ -mIBG, and lead to enhanced tumour control. During my investigations, I demonstrated that AZD2014 treatment leads to an increase of  $^{18}\text{F}$ -mFBG uptake *in vitro*. Conversely, the *in vivo* changes in tumour radiotracer retention were negligible. This could be due to AZD2014 secondary effects that reduced the delivery of the radiotracer to the tumour. Therefore, my work has highlighted the necessity of a quantitative measure of mIBG avidity in NB tumours during combination therapy.

All these findings clearly indicate that research in to the development of novel combination therapy protocols with  $^{131}\text{I}$ -mIBG should continue. Moreover, elucidating the mechanisms by which NET-1 protein levels are regulated could offer an insight in to other candidate drugs that may enhance mIBG uptake in NB. Last but not least, performing quantitative PET studies alongside combination therapy strategies would be essential to optimise current and future treatment schedules. This would endorse the use of the radiotracer for routine clinical NB tumour phenotyping during the treatment.

### **7.3. $^{89}\text{Zr}$ -labelled Dinutuximab-Beta to measure GD2 expression in NB**

In the final part of the thesis, I focused on the development and characterisation of  $^{89}\text{Zr}$  radiolabelled Dinutuximab-Beta ( $^{89}\text{Zr}$ -DFO-ch14.18(CHO)) to visualise and delineate GD2 positive NB tumours *in vivo*. The preliminary data suggested that  $^{89}\text{Zr}$ -DFO-ch14.18(CHO) could successfully differentiate between low and high GD2 expressing cells *in vitro*. However, further characterisation of the radioconjugate is still required to define its binding affinity and the immunoreactive fraction.

*In vivo* assessment of  $^{89}\text{Zr}$ -DFO-ch14.18(CHO) demonstrated the need for further optimisation of the amount of the radioconjugate injected. Potentially owing to GD2 shedding from the tumour to the blood, the delivery of the radioconjugate was hindered

## Conclusions

---

in some of the mice bearing high GD2 expressing tumour xenografts. Therefore,  $^{89}\text{Zr}$ -DFO-ch14.18(CHO) dose-escalation studies would have to be performed to confirm it and find the more suitable imaging dose. Nevertheless, the proof of concept studies I presented clearly indicate that imaging tumour GD2 expression could be an invaluable tool for the stratification of patients for GD2 targeted immunotherapy.

---

**Chapter 8 - References**

- [1] F. Berthold, C. Spix, P. Kaatsch, and F. Lampert, "Incidence, Survival, and Treatment of Localized and Metastatic Neuroblastoma in Germany 1979–2015," in *Paediatr Drugs*, vol. 19no. 6), 2017, pp. 577-93.
- [2] M. L. Bernstein *et al.*, "A population-based study of neuroblastoma incidence, survival, and mortality in North America," *Journal of Clinical Oncology*, vol. 10, no. 2, pp. 323-329, 1992/02/01 1992.
- [3] T. Sawada, T. Kidowaki, T. Sugimoto, and T. Kusunoki, "Incidence of neuroblastoma in infancy in Japan," *Medical and Pediatric Oncology*, vol. 12, no. 2, pp. 101-103, 1984/01/01 1984.
- [4] "Childhood Cancer Statistics, England Annual report 2018," *National Cancer Registration and Analysis Service*, Document 2018.
- [5] J. M. Maris, M. D. Hogarty, R. Bagatell, and S. L. Cohn, "Neuroblastoma," *The Lancet*, vol. 369, no. 9579, pp. 2106-2120, 2007.
- [6] J. I. Johnsen, C. Dyberg, and M. Wickström, "Neuroblastoma—A Neural Crest Derived Embryonal Malignancy," (in English), *Frontiers in Molecular Neuroscience*, Review vol. 12, no. 9, 2019-January-29 2019.
- [7] S. Gilbert, *Developmental Biology*, 6th ed. Sunderland (MA): Sinauer Associates, 2000.
- [8] J. A. Tomolonis, S. Agarwal, and J. M. Shohet, "Neuroblastoma pathogenesis: deregulation of embryonic neural crest development," (in eng), *Cell and tissue research*, vol. 372, no. 2, pp. 245-262, 2018.
- [9] G. Papaioannou and K. McHugh, "Neuroblastoma in childhood: review and radiological findings," (in eng), *Cancer Imaging*, vol. 5, pp. 116-27, Sep 30 2005.
- [10] C. U. Louis and J. M. Shohet, "Neuroblastoma: molecular pathogenesis and therapy," (in eng), *Annual review of medicine*, vol. 66, pp. 49-63, 2015.
- [11] H. Werner, P. Daltro, T. Davaus, and E. Araujo Júnior, "Fetal neuroblastoma: ultrasonography and magnetic resonance imaging findings in the prenatal and postnatal IV-S stage," (in eng), *Obstetrics & gynecology science*, vol. 59, no. 5, pp. 407-410, 2016.
- [12] L. M. Franks, A. Bollen, R. C. Seeger, D. O. Stram, and K. K. Matthay, "Neuroblastoma in adults and adolescents: an indolent course with poor survival," (in eng), *Cancer*, vol. 79, no. 10, pp. 2028-35, May 15 1997.
- [13] N. Gaspar *et al.*, "Neuroblastoma in adolescents," (in eng), *Cancer*, vol. 98, no. 2, pp. 349-55, Jul 15 2003.
- [14] N. C. Colon and D. H. Chung, "Neuroblastoma," (in eng), *Advances in pediatrics*, vol. 58, no. 1, pp. 297-311, 2011.
- [15] K. K. Matthay *et al.*, "Neuroblastoma," *Nat Rev Dis Primers*, vol. 2, p. 16078, Nov 10 2016.
- [16] G. M. Brodeur *et al.*, "International criteria for diagnosis, staging, and response to treatment in patients with neuroblastoma," *Journal of Clinical Oncology*, vol. 6, no. 12, pp. 1874-1881, 1988/12/01 1988.
- [17] V. Castel *et al.*, "Prospective evaluation of the International Neuroblastoma Staging System (INSS) and the International Neuroblastoma Response Criteria (INRC) in a multicentre setting," *European Journal of Cancer*, vol. 35, no. 4, pp. 606-611, 1999/04/01/ 1999.
- [18] T. Monclair *et al.*, "The International Neuroblastoma Risk Group (INRG) staging system: an INRG Task Force report," (in eng), *J Clin Oncol*, vol. 27, no. 2, pp. 298-303, Jan 10 2009.

## References

---

- [19] W. B. London *et al.*, "Evidence for an age cutoff greater than 365 days for neuroblastoma risk group stratification in the Children's Oncology Group," (in eng), *J Clin Oncol*, vol. 23, no. 27, pp. 6459-65, Sep 20 2005.
- [20] S. L. Cohn *et al.*, "The International Neuroblastoma Risk Group (INRG) classification system: an INRG Task Force report," (in eng), *Journal of clinical oncology : official journal of the American Society of Clinical Oncology*, vol. 27, no. 2, pp. 289-297, 2009.
- [21] W. B. London *et al.*, "Clinical and biologic features predictive of survival after relapse of neuroblastoma: a report from the International Neuroblastoma Risk Group project," (in eng), *Journal of clinical oncology : official journal of the American Society of Clinical Oncology*, vol. 29, no. 24, pp. 3286-3292, 2011.
- [22] K. S. Mylonas, D. Schizas, and K. P. Economopoulos, "Adrenal ganglioneuroma: What you need to know," (in eng), *World journal of clinical cases*, vol. 5, no. 10, pp. 373-377, 2017.
- [23] B. Decarolis *et al.*, "Treatment and outcome of Ganglioneuroma and Ganglioneuroblastoma intermixed," *BMC Cancer*, vol. 16, no. 1, p. 542, 2016/07/27 2016.
- [24] T. Kamijo and A. Nakagawara, "Molecular and genetic bases of neuroblastoma," *Int J Clin Oncol*, vol. 17, no. 3, pp. 190-5, Jun 2012.
- [25] J. A. Ross and S. M. Davies, "Screening for Neuroblastoma: Progress and Pitfalls," *Cancer Epidemiology Biomarkers & Prevention*, vol. 8, no. 2, p. 189, 1999.
- [26] J. M. Maris, "The biologic basis for neuroblastoma heterogeneity and risk stratification," (in eng), *Curr Opin Pediatr*, vol. 17, no. 1, pp. 7-13, Feb 2005.
- [27] G. M. Brodeur, "Neuroblastoma: biological insights into a clinical enigma," *Nature Reviews Cancer*, vol. 3, no. 3, pp. 203-216, 2003/03/01 2003.
- [28] H. Shimada *et al.*, "The International Neuroblastoma Pathology Classification (the Shimada system)," *Cancer*, vol. 86, no. 2, pp. 364-372, 1999/07/15 1999.
- [29] D. L. Casey, B. H. Kushner, N.-K. V. Cheung, S. Modak, M. P. LaQuaglia, and S. L. Wolden, "Local Control With 21-Gy Radiation Therapy for High-Risk Neuroblastoma," (in eng), *International journal of radiation oncology, biology, physics*, vol. 96, no. 2, pp. 393-400, 2016.
- [30] W. B. Seaman and M. D. Eagleton, "Radiation Therapy of Neuroblastoma," *Radiology*, vol. 68, no. 1, pp. 1-8, 1957/01/01 1957.
- [31] G. M. Brodeur, "Spontaneous regression of neuroblastoma," (in eng), *Cell Tissue Res*, vol. 372, no. 2, pp. 277-286, May 2018.
- [32] F. Peinemann, E. C. van Dalen, and F. Berthold, "Rapid COJEC Induction Therapy for High-risk Neuroblastoma Patients - Cochrane Review," (in eng), *Klin Padiatr*, vol. 228, no. 3, pp. 130-4, Apr 2016. Rapid COJEC Induktionstherapie bei Hochrisiko-Patienten mit Neuroblastom - Cochrane Review.
- [33] D. Valteau-Couanet, G. Schleiermacher, S. Sarnacki, and C. Pasqualini, "[High-risk neuroblastoma treatment strategy: The experience of the SIOPEN group]," (in fre), *Bull Cancer*, vol. 105, no. 10, pp. 918-924, Oct 2018. Prise en charge des neuroblastomes de haut risque : l'experience du groupe europeen SIOPEN.
- [34] K. K. Matthay *et al.*, "Treatment of High-Risk Neuroblastoma with Intensive Chemotherapy, Radiotherapy, Autologous Bone Marrow Transplantation, and 13-cis-Retinoic Acid," *New England Journal of Medicine*, vol. 341, no. 16, pp. 1165-1173, 1999/10/14 1999.
- [35] R. Ladenstein *et al.*, "Busulfan and melphalan versus carboplatin, etoposide, and melphalan as high-dose chemotherapy for high-risk neuroblastoma (HR-

- NBL1/SIOPEN): an international, randomised, multi-arm, open-label, phase 3 trial," (in eng), *Lancet Oncol*, vol. 18, no. 4, pp. 500-514, Apr 2017.
- [36] K. K. Matthay *et al.*, "Long-term results for children with high-risk neuroblastoma treated on a randomized trial of myeloablative therapy followed by 13-cis-retinoic acid: a children's oncology group study," (in eng), *J Clin Oncol*, vol. 27, no. 7, pp. 1007-13, Mar 1 2009.
- [37] M. Qayed *et al.*, "Tandem stem cell rescue as consolidation therapy for high-risk neuroblastoma," *Pediatric Blood & Cancer*, vol. 58, no. 3, pp. 448-452, 2012.
- [38] M. M. Elzembely *et al.*, "Late effects in high-risk neuroblastoma survivors treated with high-dose chemotherapy and stem cell rescue," *Pediatric Blood & Cancer*, vol. 66, no. 1, p. e27421, 2019.
- [39] N. R. Pinto *et al.*, "Advances in Risk Classification and Treatment Strategies for Neuroblastoma," (in eng), *Journal of clinical oncology : official journal of the American Society of Clinical Oncology*, vol. 33, no. 27, pp. 3008-3017, 2015.
- [40] M. Schwab *et al.*, "Amplified DNA with limited homology to myc cellular oncogene is shared by human neuroblastoma cell lines and a neuroblastoma tumour," (in eng), *Nature*, vol. 305, no. 5931, pp. 245-8, Sep 15-21 1983.
- [41] M. Huang and W. A. Weiss, "Neuroblastoma and MYCN," *Cold Spring Harb Perspect Med*, vol. 3, no. 10, p. a014415, Oct 01 2013.
- [42] K. Campbell *et al.*, "Association of MYCN copy number with clinical features, tumor biology, and outcomes in neuroblastoma: A report from the Children's Oncology Group," (in eng), *Cancer*, vol. 123, no. 21, pp. 4224-4235, 2017.
- [43] C. V. Dang, "MYC on the path to cancer," (in eng), *Cell*, vol. 149, no. 1, pp. 22-35, 2012.
- [44] D. M. Miller, S. D. Thomas, A. Islam, D. Muench, and K. Sedoris, "c-Myc and cancer metabolism," (in eng), *Clinical cancer research : an official journal of the American Association for Cancer Research*, vol. 18, no. 20, pp. 5546-5553, 2012.
- [45] G. J. Yoshida, "Emerging roles of Myc in stem cell biology and novel tumor therapies," (in eng), *Journal of experimental & clinical cancer research : CR*, vol. 37, no. 1, pp. 173-173, 2018.
- [46] B. A. Malynn *et al.*, "N-myc can functionally replace c-myc in murine development, cellular growth, and differentiation," (in eng), *Genes & development*, vol. 14, no. 11, pp. 1390-1399, 2000.
- [47] H. Hirvonen, T. P. Mäkelä, M. Sandberg, H. Kalimo, E. Vuorio, and K. Alitalo, "Expression of the myc proto-oncogenes in developing human fetal brain," (in eng), *Oncogene*, vol. 5, no. 12, pp. 1787-97, Dec 1990.
- [48] K. A. Zimmerman *et al.*, "Differential expression of myc family genes during murine development," (in eng), *Nature*, vol. 319, no. 6056, pp. 780-3, Feb 27-Mar 5 1986.
- [49] M. V. Ruiz-Pérez, A. B. Henley, and M. Arsenian-Henriksson, "The MYCN Protein in Health and Disease," *Genes*, vol. 8, no. 4, p. 113, 03/30 2017.
- [50] A. C. Davis, M. Wims, G. D. Spotts, S. R. Hann, and A. Bradley, "A null c-myc mutation causes lethality before 10.5 days of gestation in homozygotes and reduced fertility in heterozygous female mice," (in eng), *Genes Dev*, vol. 7, no. 4, pp. 671-82, Apr 1993.
- [51] J. Charron *et al.*, "Embryonic lethality in mice homozygous for a targeted disruption of the N-myc gene," (in eng), *Genes Dev*, vol. 6, no. 12a, pp. 2248-57, Dec 1992.
- [52] T. Teitz *et al.*, "Preclinical Models for Neuroblastoma: Establishing a Baseline for Treatment," *PLOS ONE*, vol. 6, no. 4, p. e19133, 2011.

## References

---

- [53] W. A. Weiss, K. Aldape, G. Mohapatra, B. G. Feuerstein, and J. M. Bishop, "Targeted expression of MYCN causes neuroblastoma in transgenic mice," (in eng), *EMBO J*, vol. 16, no. 11, pp. 2985-95, Jun 2 1997.
- [54] N. Bown *et al.*, "Gain of Chromosome Arm 17q and Adverse Outcome in Patients with Neuroblastoma," *New England Journal of Medicine*, vol. 340, no. 25, pp. 1954-1961, 1999/06/24 1999.
- [55] O. Altungoz, N. Aygun, S. Tumer, E. Ozer, N. Olgun, and M. Sakizli, "Correlation of modified Shimada classification with MYCN and 1p36 status detected by fluorescence in situ hybridization in neuroblastoma," *Cancer Genetics and Cytogenetics*, vol. 172, no. 2, pp. 113-119, 2007/01/15/ 2007.
- [56] S. De Brouwer *et al.*, "Meta-analysis of neuroblastomas reveals a skewed ALK mutation spectrum in tumors with MYCN amplification," *Clinical cancer research*, vol. 16, no. 17, pp. 4353-4362, 2010.
- [57] A. Ma, T. Moroy, R. Collum, H. Weintraub, F. W. Alt, and T. K. Blackwell, "DNA binding by N- and L-Myc proteins," (in eng), *Oncogene*, vol. 8, no. 4, pp. 1093-1098, 1993/04// 1993.
- [58] L. Cheung, J. E. M. Haber, and M. D., "The MYCN Oncogene," 2013.
- [59] D. Levens, "You Don't Muck with MYC," (in eng), *Genes Cancer*, vol. 1, no. 6, pp. 547-554, Jun 1 2010.
- [60] H. Beltran, "The N-myc Oncogene: Maximizing its Targets, Regulation, and Therapeutic Potential," *Molecular Cancer Research*, vol. 12, no. 6, p. 815, 2014.
- [61] S. K. Sjöstrom, G. Finn, W. C. Hahn, D. H. Rowitch, and A. M. Kenney, "The Cdk1 complex plays a prime role in regulating N-myc phosphorylation and turnover in neural precursors," (in eng), *Dev Cell*, vol. 9, no. 3, pp. 327-38, Sep 2005.
- [62] T. Otto, "MYCN and Its Posttranslational Regulation in Neuroblastoma," *Pediatric and Adolescent Medicine*, vol. 20, pp. 47-58, 11/09 2015.
- [63] G. M. Brodeur, R. C. Seeger, M. Schwab, H. E. Varmus, and J. M. Bishop, "Amplification of N-myc in untreated human neuroblastomas correlates with advanced disease stage," (in eng), *Science*, vol. 224, no. 4653, pp. 1121-4, Jun 8 1984.
- [64] R. C. Seeger *et al.*, "Association of multiple copies of the N-myc oncogene with rapid progression of neuroblastomas," (in eng), *N Engl J Med*, vol. 313, no. 18, pp. 1111-6, Oct 31 1985.
- [65] G. Raschella *et al.*, "Lack of correlation between N-myc and MAX expression in neuroblastoma tumors and in cell lines: implication for N-myc-MAX complex formation," (in eng), *Cancer Res*, vol. 54, no. 8, pp. 2251-5, Apr 15 1994.
- [66] R. Zeid *et al.*, "Enhancer invasion shapes MYCN-dependent transcriptional amplification in neuroblastoma," (in eng), *Nature genetics*, vol. 50, no. 4, pp. 515-523, 2018.
- [67] C. J. Thiele, C. P. Reynolds, and M. A. Israel, "Decreased expression of N-myc precedes retinoic acid-induced morphological differentiation of human neuroblastoma," (in eng), *Nature*, vol. 313, no. 6001, pp. 404-6, Jan 31-Feb 6 1985.
- [68] R. K. Wada *et al.*, "Cell type-specific expression and negative regulation by retinoic acid of the human N-myc promoter in neuroblastoma cells," (in eng), *Oncogene*, vol. 7, no. 4, pp. 711-7, Apr 1992.
- [69] P. Sonawane *et al.*, "Metabolic characteristics of 13-cis-retinoic acid (isotretinoin) and anti-tumour activity of the 13-cis-retinoic acid metabolite 4-oxo-13-cis-retinoic acid in neuroblastoma," (in eng), *Br J Pharmacol*, vol. 171, no. 23, pp. 5330-44, Dec 2014.

## References

---

- [70] L. Guglielmi *et al.*, "MYCN gene expression is required for the onset of the differentiation programme in neuroblastoma cells," *Cell Death Dis*, vol. 5, p. e1081, Feb 20 2014.
- [71] C. Cetinkaya *et al.*, "Combined IFN-gamma and retinoic acid treatment targets the N-Myc/Max/Mad1 network resulting in repression of N-Myc target genes in MYCN-amplified neuroblastoma cells," (in eng), *Mol Cancer Ther*, vol. 6, no. 10, pp. 2634-41, Oct 2007.
- [72] A. Sabò and B. Amati, "Genome Recognition by MYC," *Cold Spring Harbor Perspectives in Medicine*, vol. 4, no. 2, 2014.
- [73] I. Müller *et al.*, "Targeting of the MYCN protein with small molecule c-MYC inhibitors," (in eng), *PLoS one*, vol. 9, no. 5, pp. e97285-e97285, 2014.
- [74] H. Zirath *et al.*, "MYC inhibition induces metabolic changes leading to accumulation of lipid droplets in tumor cells," *Proceedings of the National Academy of Sciences*, vol. 110, no. 25, p. 10258, 2013.
- [75] A. Puissant *et al.*, "Targeting MYCN in neuroblastoma by BET bromodomain inhibition," *Cancer Discov*, vol. 3, no. 3, pp. 308-23, Mar 2013.
- [76] S. A. Piha-Paul *et al.*, "Phase 1 Study of Molibresib (GSK525762), a Bromodomain and Extra-Terminal Domain Protein Inhibitor, in NUT Carcinoma and Other Solid Tumors," *JNCI Cancer Spectrum*, vol. 4, no. 2, 2019.
- [77] J. Lewin *et al.*, "Phase Ib Trial With Birabresib, a Small-Molecule Inhibitor of Bromodomain and Extraterminal Proteins, in Patients With Selected Advanced Solid Tumors," (in eng), *J Clin Oncol*, vol. 36, no. 30, pp. 3007-3014, Oct 20 2018.
- [78] S. A. Piha-Paul *et al.*, "First-in-Human Study of Mivebresib (ABBV-075), an Oral Pan-Inhibitor of Bromodomain and Extra Terminal Proteins, in Patients with Relapsed/Refractory Solid Tumors," *Clinical Cancer Research*, vol. 25, no. 21, p. 6309, 2019.
- [79] E. Watts *et al.*, "Designing Dual Inhibitors of Anaplastic Lymphoma Kinase (ALK) and Bromodomain-4 (BRD4) by Tuning Kinase Selectivity," (in eng), *Journal of medicinal chemistry*, vol. 62, no. 5, pp. 2618-2637, 2019.
- [80] A. Efeyan and D. M. Sabatini, "mTOR and cancer: many loops in one pathway," (in eng), *Current opinion in cell biology*, vol. 22, no. 2, pp. 169-176, 2010.
- [81] D. Opel, C. Poremba, T. Simon, K.-M. Debatin, and S. Fulda, "Activation of Akt Predicts Poor Outcome in Neuroblastoma," *Cancer Research*, vol. 67, no. 2, p. 735, 2007.
- [82] L. Chesler *et al.*, "Inhibition of phosphatidylinositol 3-kinase destabilizes Mycn protein and blocks malignant progression in neuroblastoma," (in eng), *Cancer Res*, vol. 66, no. 16, pp. 8139-46, Aug 15 2006.
- [83] J. I. J. Kogner *et al.*, "Inhibitors of mammalian target of rapamycin downregulate MYCN protein expression and inhibit neuroblastoma growth," (in En), *Oncogene*, Research vol. 27, no. 20, p. 2910, 2007-11-19 2007.
- [84] L. Vaughan *et al.*, "Inhibition of mTOR-kinase destabilizes MYCN and is a potential therapy for MYCN-dependent tumors," *Oncotarget*, vol. 7, no. 36, pp. 57525-57544, 2016 2016.
- [85] B. Georger *et al.*, "Phase II trial of temsirolimus in children with high-grade glioma, neuroblastoma and rhabdomyosarcoma," *European Journal of Cancer*, vol. 48, no. 2, pp. 253-262, 2012/01/01/ 2012.
- [86] O. J. Becher *et al.*, "A phase I study of single-agent perifosine for recurrent or refractory pediatric CNS and solid tumors," *PLOS ONE*, vol. 12, no. 6, p. e0178593, 2017.

## References

---

- [87] L. Graham *et al.*, "A phase II study of the dual mTOR inhibitor MLN0128 in patients with metastatic castration resistant prostate cancer," *Investigational New Drugs*, vol. 36, no. 3, pp. 458-467, 2018/06/01 2018.
- [88] T. Doi *et al.*, "A Phase I study of intravenous PI3K inhibitor copanlisib in Japanese patients with advanced or refractory solid tumors," (in eng), *Cancer chemotherapy and pharmacology*, vol. 79, no. 1, pp. 89-98, 2017.
- [89] D.-q. Xu *et al.*, "Induction of MEK/ERK activity by AZD8055 confers acquired resistance in neuroblastoma," *Biochemical and Biophysical Research Communications*, vol. 499, no. 3, pp. 425-432, 2018/05/15/ 2018.
- [90] E. R. Tucker, E. Poon, and L. Chesler, "Targeting MYCN and ALK in resistant and relapsing neuroblastoma," 2019.
- [91] S. J. Forrest, B. Georger, and K. A. Janeway, "Precision medicine in pediatric oncology," (in eng), *Current opinion in pediatrics*, vol. 30, no. 1, pp. 17-24, 2018.
- [92] P. E. Zage, "Novel therapies for relapsed and refractory neuroblastoma," *Children*, vol. 5, no. 11, p. 148, 2018.
- [93] T. Powles *et al.*, "A Randomised Phase 2 Study of AZD2014 Versus Everolimus in Patients with VEGF-Refractory Metastatic Clear Cell Renal Cancer," (in eng), *Eur Urol*, vol. 69, no. 3, pp. 450-6, Mar 2016.
- [94] T. A. Eyre *et al.*, "A phase II study to assess the safety and efficacy of the dual mTORC1/2 inhibitor vistusertib in relapsed, refractory DLBCL," *Hematological Oncology*, vol. 37, no. 4, pp. 352-359, 2019/10/01 2019.
- [95] S. Mohlin *et al.*, "Anti-tumor effects of PIM/PI3K/mTOR triple kinase inhibitor IBL-302 in neuroblastoma," (in eng), *EMBO Mol Med*, vol. 11, no. 8, p. e10058, Aug 2019.
- [96] M. Moreno-Smith *et al.*, "p53 Nongenotoxic Activation and mTORC1 Inhibition Lead to Effective Combination for Neuroblastoma Therapy," (in eng), *Clin Cancer Res*, vol. 23, no. 21, pp. 6629-6639, Nov 1 2017.
- [97] N. H. Chen, M. E. Reith, and M. W. Quick, "Synaptic uptake and beyond: the sodium- and chloride-dependent neurotransmitter transporter family SLC6," (in eng), *Pflugers Arch*, vol. 447, no. 5, pp. 519-31, Feb 2004.
- [98] J. Zhou, "Norepinephrine transporter inhibitors and their therapeutic potential," (in eng), *Drugs of the future*, vol. 29, no. 12, pp. 1235-1244, 2004.
- [99] R. J. Phillips and T. L. Powley, "Innervation of the gastrointestinal tract: patterns of aging," (in eng), *Autonomic neuroscience : basic & clinical*, vol. 136, no. 1-2, pp. 1-19, 2007.
- [100] W. Hasan, "Autonomic cardiac innervation: development and adult plasticity," (in eng), *Organogenesis*, vol. 9, no. 3, pp. 176-193, Jul-Sep 2013.
- [101] T. J. Bartness, C. H. Vaughan, and C. K. Song, "Sympathetic and sensory innervation of brown adipose tissue," (in eng), *Int J Obes (Lond)*, vol. 34 Suppl 1, pp. S36-42, Oct 2010.
- [102] M. J. Gelfand, "123I-MIBG uptake in the neck and shoulders of a neuroblastoma patient: damage to sympathetic innervation blocks uptake in brown adipose tissue," *Pediatric Radiology*, vol. 34, no. 7, pp. 577-579, 2004/07/01 2004.
- [103] I. Góral, K. Łątka, and M. Bajda, "Structure Modeling of the Norepinephrine Transporter," (in eng), *Biomolecules*, vol. 10, no. 1, Jan 7 2020.
- [104] N. H. Fraeyman, F. H. De Smet, E. J. Van de Velde, E. J. Moerman, and A. F. De Schaepdryver, "Release of dopamine, noradrenaline and dopamine B-hydroxylase from mouse neuroblastoma," (in eng), *Life Sci*, vol. 35, no. 6, pp. 619-29, Aug 6 1984.
- [105] S. E. Gitlow, L. M. Bertani, A. Rausen, D. Gribetz, and S. W. Dziedzic, "Diagnosis of neuroblastoma by qualitative and quantitative determination of

- catecholamine metabolites in urine," (in eng), *Cancer*, vol. 25, no. 6, pp. 1377-83, Jun 1970.
- [106] N. Marchese, S. Canini, L. Fabi, and L. Famularo, "Paediatric reference values for urinary catecholamine metabolites evaluated by high performance liquid chromatography and electrochemical detection," (in eng), *Eur J Clin Chem Clin Biochem*, vol. 35, no. 7, pp. 533-7, Jul 1997.
- [107] V. Strenger *et al.*, "Diagnostic and prognostic impact of urinary catecholamines in neuroblastoma patients," *Pediatric Blood & Cancer*, vol. 48, no. 5, pp. 504-509, 2007/05/01 2007.
- [108] I. R. N. Verly *et al.*, "Catecholamines profiles at diagnosis: Increased diagnostic sensitivity and correlation with biological and clinical features in neuroblastoma patients," *European Journal of Cancer*, vol. 72, pp. 235-243, 2017/02/01/ 2017.
- [109] C. H. Kim, P. Ardayfio, and K. S. Kim, "An E-box motif residing in the exon/intron 1 junction regulates both transcriptional activation and splicing of the human norepinephrine transporter gene," (in eng), *J Biol Chem*, vol. 276, no. 27, pp. 24797-805, Jul 6 2001.
- [110] K. A. Streby, N. Shah, M. A. Ranalli, A. Kunkler, and T. P. Cripe, "Nothing but NET: A review of norepinephrine transporter expression and efficacy of 131I-mIBG therapy," (in en), *Pediatric Blood & Cancer*, vol. 62, no. 1, pp. 5-11, 2017.
- [111] A. G. Kippenberger, D. J. Palmer, A. M. Comer, J. Lipski, L. D. Burton, and D. L. Christie, "Localization of the Noradrenaline Transporter in Rat Adrenal Medulla and PC12 Cells," *Journal of Neurochemistry*, vol. 73, no. 3, pp. 1024-1032, 1999/09/01 1999.
- [112] R. J. Mairs, A. Livingstone, M. N. Gaze, T. E. Wheldon, and A. Barrett, "Prediction of accumulation of 131I-labelled meta-iodobenzylguanidine in neuroblastoma cell lines by means of reverse transcription and polymerase chain reaction," (in eng), *Br J Cancer*, vol. 70, no. 1, pp. 97-101, Jul 1994.
- [113] A. Armour, S. H. Cunningham, M. N. Gaze, T. E. Wheldon, and R. J. Mairs, "The effect of cisplatin pretreatment on the accumulation of MIBG by neuroblastoma cells in vitro," *British Journal of Cancer*, vol. 75, no. 4, pp. 470-476, 1997.
- [114] S. G. Dubois *et al.*, "Evaluation of Norepinephrine Transporter Expression and Metaiodobenzylguanidine Avidity in Neuroblastoma: A Report from the Children's Oncology Group," *Int J Mol Imaging*, vol. 2012, p. 250834, 2012.
- [115] A. Iavarone, A. Lasorella, T. Servidei, R. Riccardi, and R. Mastrangelo, "Uptake and storage of m-iodobenzylguanidine are frequent neuronal functions of human neuroblastoma cell lines," (in eng), *Cancer Res*, vol. 53, no. 2, pp. 304-9, Jan 15 1993.
- [116] J. V. Glowniak, J. E. Kilty, S. G. Amara, B. J. Hoffman, and F. E. Turner, "Evaluation of metaiodobenzylguanidine uptake by the norepinephrine, dopamine and serotonin transporters," (in eng), *J Nucl Med*, vol. 34, no. 7, pp. 1140-6, Jul 1993.
- [117] P. G. Montaldo, M. Lanciotti, A. Casalaro, P. Cornaglia-Ferraris, and M. Ponzoni, "Accumulation of m-iodobenzylguanidine by neuroblastoma cells results from independent uptake and storage mechanisms," (in eng), *Cancer Res*, vol. 51, no. 16, pp. 4342-6, Aug 15 1991.
- [118] J. Buck, G. Bruchelt, R. Giergert, J. Treuner, and D. Niethammer, "Specific uptake of m-[125I]iodobenzylguanidine in the human neuroblastoma cell line SK-N-SH," (in eng), *Cancer Res*, vol. 45, no. 12 Pt 1, pp. 6366-70, Dec 1985.
- [119] L. A. Smets, M. Janssen, E. Metwally, and C. Loesberg, "Extracellular storage of the neuron blocking agent meta-iodobenzylguanidine (MIBG) in human

- neuroblastoma cells," (in eng), *Biochem Pharmacol*, vol. 39, no. 12, pp. 1959-64, Jun 15 1990.
- [120] L. Bodei, A. I. Kassis, S. J. Adelstein, and G. Mariani, "Radionuclide therapy with iodine-125 and other auger-electron-emitting radionuclides: experimental models and clinical applications," (in eng), *Cancer Biother Radiopharm*, vol. 18, no. 6, pp. 861-77, Dec 2003.
- [121] A. Ku, V. J. Facca, Z. Cai, and R. M. Reilly, "Auger electrons for cancer therapy – a review," *EJNMMI Radiopharmacy and Chemistry*, vol. 4, no. 1, p. 27, 2019/10/11 2019.
- [122] C. D. Martins, G. Kramer-Marek, and W. J. G. Oyen, "Radioimmunotherapy for delivery of cytotoxic radioisotopes: current status and challenges," *Expert Opinion on Drug Delivery*, vol. 15, no. 2, pp. 185-196, 2018/02/01 2018.
- [123] B. Cornelissen and K. A. Vallis, "Targeting the nucleus: an overview of Auger-electron radionuclide therapy," *Current drug discovery technologies*, vol. 7, no. 4, pp. 263-279, 2010.
- [124] A. I. Kassis, "Therapeutic radionuclides: biophysical and radiobiologic principles," (in eng), *Seminars in nuclear medicine*, vol. 38, no. 5, pp. 358-366, 2008.
- [125] M. Rutgers, C. K. M. Buitenhuis, M. A. van der Valk, C. A. Hoefnagel, P. A. Voûte, and L. A. Smets, "[131I]- and [125I]metaiodobenzylguanidine therapy in macroscopic and microscopic tumors: A comparative study in SK-N-SH human neuroblastoma and PC12 rat pheochromocytoma xenografts," *International Journal of Cancer*, vol. 90, no. 6, pp. 312-325, 2000/12/20 2000.
- [126] S. H. Cunningham, R. J. Mairs, T. E. Wheldon, P. C. Welsh, G. Vaidyanathan, and M. R. Zalutsky, "Toxicity to neuroblastoma cells and spheroids of benzylguanidine conjugated to radionuclides with short-range emissions," *British Journal of Cancer*, vol. 77, no. 12, pp. 2061-2068, 1998/06/01 1998.
- [127] J. C. Sisson *et al.*, "Iodine-125-MIBG to treat neuroblastoma: preliminary report," (in eng), *J Nucl Med*, vol. 31, no. 9, pp. 1479-85, Sep 1990.
- [128] J. C. Sisson, B. Shapiro, R. J. Hutchinson, B. L. Shulkin, and S. Zempel, "Survival of Patients with Neuroblastoma Treated with 125-I MIBG," *American Journal of Clinical Oncology*, vol. 19, no. 2, 1996.
- [129] J. P. Howard *et al.*, "Tumor response and toxicity with multiple infusions of high dose 131I-MIBG for refractory neuroblastoma," *Pediatric Blood & Cancer*, vol. 44, no. 3, pp. 232-239, 2005/03/01 2005.
- [130] J. C. Sisson *et al.*, "Toxicity from treatment of neuroblastoma with 131I-metaiodobenzylguanidine," *European Journal of Nuclear Medicine*, vol. 14, no. 7, pp. 337-340, 1988/09/01 1988.
- [131] K. K. Matthay *et al.*, "Dose escalation study of no-carrier-added 131I-metaiodobenzylguanidine for relapsed or refractory neuroblastoma: new approaches to neuroblastoma therapy consortium trial," (in eng), *J Nucl Med*, vol. 53, no. 7, pp. 1155-63, Jul 2012.
- [132] S. G. DuBois *et al.*, "MIBG avidity correlates with clinical features, tumor biology, and outcomes in neuroblastoma: A report from the Children's Oncology Group," (in eng), *Pediatr Blood Cancer*, vol. 64, no. 11, Nov 2017.
- [133] S. E. Buckley, S. J. Chittenden, F. H. Saran, S. T. Meller, and G. D. Flux, "Whole-body dosimetry for individualized treatment planning of 131I-MIBG radionuclide therapy for neuroblastoma," (in eng), *J Nucl Med*, vol. 50, no. 9, pp. 1518-24, Sep 2009.

- [134] R. J. Mairs *et al.*, "No-carrier-added iodine-131-MIBG: evaluation of a therapeutic preparation," (in eng), *J Nucl Med*, vol. 36, no. 6, pp. 1088-95, Jun 1995.
- [135] S. G. DuBois *et al.*, "Phase I/II study of (131)I-MIBG with vincristine and 5 days of irinotecan for advanced neuroblastoma," (in eng), *Br J Cancer*, vol. 112, no. 4, pp. 644-9, Feb 17 2015.
- [136] P. J. Houghton and V. M. Santana, "Clinical Trials Using Irinotecan," *Journal of Pediatric Hematology/Oncology*, vol. 24, no. 2, pp. 84-85, 2002.
- [137] M. N. Gaze, Y. C. Chang, G. D. Flux, R. J. Mairs, F. H. Saran, and S. T. Meller, "Feasibility of dosimetry-based high-dose 131I-meta-iodobenzylguanidine with topotecan as a radiosensitizer in children with metastatic neuroblastoma," (in eng), *Cancer Biother Radiopharm*, vol. 20, no. 2, pp. 195-9, Apr 2005.
- [138] H. Zhang *et al.*, "Imaging the norepinephrine transporter in neuroblastoma: a comparison of [18F]-MFBG and 123I-MIBG," *Clin Cancer Res*, vol. 20, no. 8, pp. 2182-91, Apr 15 2014.
- [139] G. M. Brodeur and R. Bagatell, "Mechanisms of neuroblastoma regression," (in eng), *Nature reviews. Clinical oncology*, vol. 11, no. 12, pp. 704-713, 2014.
- [140] J. de Kraker, K. A. Hoefnagel, A. C. Verschuur, B. van Eck, H. M. van Santen, and H. N. Caron, "Iodine-131-metaiodobenzylguanidine as initial induction therapy in stage 4 neuroblastoma patients over 1 year of age," *European Journal of Cancer*, vol. 44, no. 4, pp. 551-556, 2008/03/01/ 2008.
- [141] K. C. Kraal, G. A. Tytgat, B. L. van Eck-Smit, B. Kam, H. N. Caron, and M. van Noesel, "Upfront treatment of high-risk neuroblastoma with a combination of 131I-MIBG and topotecan," (in eng), *Pediatr Blood Cancer*, vol. 62, no. 11, pp. 1886-91, Nov 2015.
- [142] J. W. Lee *et al.*, "Incorporation of high-dose (131)I-metaiodobenzylguanidine treatment into tandem high-dose chemotherapy and autologous stem cell transplantation for high-risk neuroblastoma: results of the SMC NB-2009 study," (in eng), *J Hematol Oncol*, vol. 10, no. 1, p. 108, May 16 2017.
- [143] G. Lammie, N. Cheung, W. Gerald, M. Rosenblum, and C. Cordoncardo, "Ganglioside gd(2) expression in the human nervous-system and in neuroblastomas - an immunohistochemical study," (in eng), *Int J Oncol*, vol. 3, no. 5, pp. 909-15, Nov 1993.
- [144] M. Yanagisawa, S. Yoshimura, and R. K. Yu, "Expression of GD2 and GD3 gangliosides in human embryonic neural stem cells," (in eng), *ASN Neuro*, vol. 3, no. 2, Apr 7 2011.
- [145] G. Schulz, D. A. Cheresch, N. M. Varki, A. Yu, L. K. Staffileno, and R. A. Reisfeld, "Detection of Ganglioside GD2 in Tumor Tissues and Sera of Neuroblastoma Patients," *Cancer Research*, vol. 44, no. 12 Part 1, p. 5914, 1984.
- [146] K. Furukawa, K. Takamiya, and K. Furukawa, " $\beta$ 1,4-N-acetylgalactosaminyltransferase—GM2/GD2 synthase: a key enzyme to control the synthesis of brain-enriched complex gangliosides," *Biochimica et Biophysica Acta (BBA) - General Subjects*, vol. 1573, no. 3, pp. 356-362, 2002/12/19/ 2002.
- [147] T. Kolter, "Ganglioside Biochemistry," *ISRN Biochemistry*, vol. 2012, p. 506160, 2012/12/19 2012.
- [148] S. Ngamukote, M. Yanagisawa, T. Ariga, S. Ando, and R. K. Yu, "Developmental changes of glycosphingolipids and expression of glycoconjugates in mouse brains," *Journal of Neurochemistry*, vol. 103, no. 6, pp. 2327-2341, 2007/12/01 2007.
- [149] R. K. Yu, Y. Nakatani, and M. Yanagisawa, "The role of glycosphingolipid metabolism in the developing brain," (in eng), *Journal of lipid research*, vol. 50 Suppl, no. Suppl, pp. S440-S445, 2009.

## References

---

- [150] R. K. Yu, Y.-T. Tsai, T. Ariga, and M. Yanagisawa, "Structures, biosynthesis, and functions of gangliosides--an overview," (in eng), *Journal of oleo science*, vol. 60, no. 10, pp. 537-544, 2011.
- [151] W. H. Xiao, A. L. Yu, and L. S. Sorkin, "Electrophysiological characteristics of primary afferent fibers after systemic administration of anti-GD2 ganglioside antibody," (in eng), *Pain*, vol. 69, no. 1-2, pp. 145-51, Jan 1997.
- [152] Y. J. Liang, Y. Ding, S. B. Levery, M. Lobaton, K. Handa, and S. I. Hakomori, "Differential expression profiles of glycosphingolipids in human breast cancer stem cells vs. cancer non-stem cells," (in eng), *Proc Natl Acad Sci U S A*, vol. 110, no. 13, pp. 4968-73, Mar 26 2013.
- [153] C. Martinez, T. J. Hofmann, R. Marino, M. Dominici, and E. M. Horwitz, "Human bone marrow mesenchymal stromal cells express the neural ganglioside GD2: a novel surface marker for the identification of MSCs," (in eng), *Blood*, vol. 109, no. 10, pp. 4245-8, May 15 2007.
- [154] S. Hettmer, C. Malott, W. Woods, S. Ladisch, and K. Kaucic, "Biological stratification of human neuroblastoma by complex "B" pathway ganglioside expression," (in eng), *Cancer Res*, vol. 63, no. 21, pp. 7270-6, Nov 1 2003.
- [155] K. Kaucic, N. Etue, B. LaFleur, W. Woods, and S. Ladisch, "Neuroblastomas of infancy exhibit a characteristic ganglioside pattern," *Cancer*, vol. 91, no. 4, pp. 785-793, 2001/02/15 2001.
- [156] Z.-L. Wu, E. Schwartz, R. Seeger, and S. Ladisch, "Expression of GD2 Ganglioside by Untreated Primary Human Neuroblastomas," *Cancer Research*, vol. 46, no. 1, p. 440, 1986.
- [157] S. A. Burchill *et al.*, "Recommendations for the standardization of bone marrow disease assessment and reporting in children with neuroblastoma on behalf of the International Neuroblastoma Response Criteria Bone Marrow Working Group," *Cancer*, vol. 123, no. 7, pp. 1095-1105, 2017/04/01 2017.
- [158] M. R. Ifversen, B. Kagedal, L. D. Christensen, C. Rechnitzer, B. L. Petersen, and C. Heilmann, "Comparison of immunocytochemistry, real-time quantitative RT-PCR and flow cytometry for detection of minimal residual disease in neuroblastoma," (in eng), *Int J Oncol*, vol. 27, no. 1, pp. 121-9, Jul 2005.
- [159] R. X. Li and S. Ladisch, "Shedding of human neuroblastoma gangliosides," (in eng), *Biochim Biophys Acta*, vol. 1083, no. 1, pp. 57-64, Apr 24 1991.
- [160] S. Ladisch and Z. L. Wu, "Detection of a tumour-associated ganglioside in plasma of patients with neuroblastoma," (in eng), *Lancet (London, England)*, vol. 1, no. 8421, pp. 136-138, 1985.
- [161] L. Valentino, T. Moss, E. Olson, H.-J. Wang, R. Elashoff, and S. Ladisch, "Shed tumor gangliosides and progression of human neuroblastoma," 1990.
- [162] D. A. Cheresch, M. D. Pierschbacher, M. A. Herzig, and K. Mujoo, "Disialogangliosides GD2 and GD3 are involved in the attachment of human melanoma and neuroblastoma cells to extracellular matrix proteins," *Journal of Cell Biology*, vol. 102, no. 3, pp. 688-696, 1986.
- [163] G. V. Shurin, M. R. Shurin, S. Bykovskaia, J. Shogan, M. T. Lotze, and E. M. Barksdale, "Neuroblastoma-derived Gangliosides Inhibit Dendritic Cell Generation and Function," *Cancer Research*, vol. 61, no. 1, p. 363, 2001.
- [164] Z.-L. W. Ladisch, S. Eileen, S. Robert, and Stephan, "Expression of GD2 Ganglioside by Untreated Primary Human Neuroblastomas," (in en), 1986-01-01 1986.
- [165] S. Julien, M. Bobowski, A. Steenackers, X. Le Bourhis, and P. Delannoy, "How Do Gangliosides Regulate RTKs Signaling?," (in eng), *Cells*, vol. 2, no. 4, pp. 751-67, Dec 6 2013.

## References

---

- [166] A. Cazet *et al.*, "The ganglioside G(D2) induces the constitutive activation of c-Met in MDA-MB-231 breast cancer cells expressing the G(D3) synthase," (in eng), *Glycobiology*, vol. 22, no. 6, pp. 806-16, Jun 2012.
- [167] I. I. Doronin *et al.*, "Ganglioside GD2 in reception and transduction of cell death signal in tumor cells," *BMC Cancer*, vol. 14, no. 1, p. 295, 2014/04/28 2014.
- [168] N. Berois and E. Osinaga, "Glycobiology of neuroblastoma: impact on tumor behavior, prognosis, and therapeutic strategies," (in eng), *Frontiers in oncology*, vol. 4, pp. 114-114, 2014.
- [169] P. Chames, M. Van Regenmortel, E. Weiss, and D. Baty, "Therapeutic antibodies: successes, limitations and hopes for the future," (in eng), *British journal of pharmacology*, vol. 157, no. 2, pp. 220-233, 2009.
- [170] E. Sterner, M. L. Peach, M. C. Nicklaus, and J. C. Gildersleeve, "Therapeutic Antibodies to Ganglioside GD2 Evolved from Highly Selective Germline Antibodies," (in eng), *Cell reports*, vol. 20, no. 7, pp. 1681-1691, 2017.
- [171] A. L. Yu *et al.*, "Anti-GD2 antibody with GM-CSF, interleukin-2, and isotretinoin for neuroblastoma," (in eng), *The New England journal of medicine*, vol. 363, no. 14, pp. 1324-1334, 2010.
- [172] N. K. Cheung *et al.*, "Ganglioside GD2 specific monoclonal antibody 3F8: a phase I study in patients with neuroblastoma and malignant melanoma," (in eng), *J Clin Oncol*, vol. 5, no. 9, pp. 1430-40, Sep 1987.
- [173] K. Mujoo *et al.*, "Functional properties and effect on growth suppression of human neuroblastoma tumors by isotype switch variants of monoclonal antiganglioside GD2 antibody 14.18," (in eng), *Cancer Res*, vol. 49, no. 11, pp. 2857-61, Jun 1 1989.
- [174] "Monoclonal antibody targets and mechanisms of action," in *Therapeutic Antibody Engineering*, W. R. Strohl and L. M. Strohl, Eds.: Woodhead Publishing, 2012, pp. 163-595.
- [175] J. U. Igietseme, X. Zhu, and C. M. Black, "Chapter 15 - Fc Receptor-Dependent Immunity," in *Antibody Fc*, M. E. Ackerman and F. Nimmerjahn, Eds. Boston: Academic Press, 2014, pp. 269-281.
- [176] L. M. Weiner, R. Surana, and S. Wang, "Monoclonal antibodies: versatile platforms for cancer immunotherapy," (in eng), *Nature reviews. Immunology*, vol. 10, no. 5, pp. 317-327, 2010.
- [177] A. Ben-Shmuel, G. Biber, and M. Barda-Saad, "Unleashing Natural Killer Cells in the Tumor Microenvironment-The Next Generation of Immunotherapy?," (in eng), *Frontiers in immunology*, vol. 11, pp. 275-275, 2020.
- [178] U. Seidel, P. Schlegel, and P. Lang, "Natural Killer Cell Mediated Antibody-Dependent Cellular Cytotoxicity in Tumor Immunotherapy with Therapeutic Antibodies," (in English), *Frontiers in Immunology*, Review vol. 4, no. 76, 2013-March-27 2013.
- [179] L. M. Rogers, S. Veeramani, and G. J. Weiner, "Complement in monoclonal antibody therapy of cancer," (in eng), *Immunologic research*, vol. 59, no. 1-3, pp. 203-210, 2014.
- [180] R. Handgretinger *et al.*, "A phase I study of neuroblastoma with the anti-ganglioside GD2 antibody 14.G2a," (in eng), *Cancer Immunol Immunother*, vol. 35, no. 3, pp. 199-204, 1992.
- [181] A. L. Yu *et al.*, "Phase I trial of a human-mouse chimeric anti-disialoganglioside monoclonal antibody ch14.18 in patients with refractory neuroblastoma and osteosarcoma," (in eng), *J Clin Oncol*, vol. 16, no. 6, pp. 2169-80, Jun 1998.
- [182] J. D. Frost *et al.*, "A phase I/IB trial of murine monoclonal anti-GD2 antibody 14.G2a plus interleukin-2 in children with refractory neuroblastoma: a report of

- the Children's Cancer Group," (in eng), *Cancer*, vol. 80, no. 2, pp. 317-33, Jul 15 1997.
- [183] R. Handgretinger *et al.*, "A phase I study of human/mouse chimeric antiganglioside GD2 antibody ch14.18 in patients with neuroblastoma," (in eng), *Eur J Cancer*, vol. 31a, no. 2, pp. 261-7, 1995.
- [184] B. M. Mueller, C. A. Romerdahl, S. D. Gillies, and R. A. Reisfeld, "Enhancement of antibody-dependent cytotoxicity with a chimeric anti-GD2 antibody," (in eng), *J Immunol*, vol. 144, no. 4, pp. 1382-6, Feb 15 1990.
- [185] R. Jefferis, "Glycosylation as a strategy to improve antibody-based therapeutics," (in eng), *Nat Rev Drug Discov*, vol. 8, no. 3, pp. 226-34, Mar 2009.
- [186] N. Siebert *et al.*, "Pharmacokinetics and pharmacodynamics of ch14.18/CHO in relapsed/refractory high-risk neuroblastoma patients treated by long-term infusion in combination with IL-2," (in eng), *mAbs*, vol. 8, no. 3, pp. 604-616, 2016.
- [187] N. Siebert, C. Eger, D. Seidel, M. Juttner, and H. N. Lode, "Validated detection of human anti-chimeric immune responses in serum of neuroblastoma patients treated with ch14.18/CHO," (in eng), *J Immunol Methods*, vol. 407, pp. 108-15, May 2014.
- [188] E. Barker, B. M. Mueller, R. Handgretinger, M. Herter, A. L. Yu, and R. A. Reisfeld, "Effect of a chimeric anti-ganglioside GD2 antibody on cell-mediated lysis of human neuroblastoma cells," (in eng), *Cancer Res*, vol. 51, no. 1, pp. 144-9, Jan 1 1991.
- [189] J. A. Hank *et al.*, "Augmentation of antibody dependent cell mediated cytotoxicity following in vivo therapy with recombinant interleukin 2," (in eng), *Cancer Res*, vol. 50, no. 17, pp. 5234-9, Sep 1 1990.
- [190] R. Ladenstein *et al.*, "Interleukin 2 with anti-GD2 antibody ch14.18/CHO (dinutuximab beta) in patients with high-risk neuroblastoma (HR-NBL1/SIOPEN): a multicentre, randomised, phase 3 trial," (in eng), *Lancet Oncol*, vol. 19, no. 12, pp. 1617-1629, Dec 2018.
- [191] K. L. Osenga *et al.*, "A phase I clinical trial of the hu14.18-IL2 (EMD 273063) as a treatment for children with refractory or recurrent neuroblastoma and melanoma: a study of the Children's Oncology Group," (in eng), *Clin Cancer Res*, vol. 12, no. 6, pp. 1750-9, Mar 15 2006.
- [192] B. H. Kushner, I. Y. Cheung, S. Modak, E. M. Basu, S. S. Roberts, and N. K. Cheung, "Humanized 3F8 Anti-GD2 Monoclonal Antibody Dosing With Granulocyte-Macrophage Colony-Stimulating Factor in Patients With Resistant Neuroblastoma: A Phase 1 Clinical Trial," (in eng), *JAMA Oncol*, vol. 4, no. 12, pp. 1729-1735, Dec 1 2018.
- [193] I. Y. Cheung, B. H. Kushner, S. Modak, E. M. Basu, S. S. Roberts, and N. V. Cheung, "Phase I trial of anti-GD2 monoclonal antibody hu3F8 plus GM-CSF: Impact of body weight, immunogenicity and anti-GD2 response on pharmacokinetics and survival," (in eng), *Oncoimmunology*, vol. 6, no. 11, p. e1358331, 2017.
- [194] D. L. Anghelescu *et al.*, "Comparison of pain outcomes between two anti-GD2 antibodies in patients with neuroblastoma," (in eng), *Pediatr Blood Cancer*, vol. 62, no. 2, pp. 224-228, Feb 2015.
- [195] L. S. Sorkin *et al.*, "Anti-GD(2) with an FC point mutation reduces complement fixation and decreases antibody-induced allodynia," (in eng), *Pain*, vol. 149, no. 1, pp. 135-42, Apr 2010.
- [196] R. K. Yang and P. M. Sondel, "Anti-GD2 Strategy in the Treatment of Neuroblastoma," (in eng), *Drugs of the future*, vol. 35, no. 8, pp. 665-665, 2010.

## References

---

- [197] N.-K. V. Cheung *et al.*, "N7: A novel multi-modality therapy of high risk neuroblastoma (NB) in children diagnosed over 1 year of age," *Medical and Pediatric Oncology*, vol. 36, no. 1, pp. 227-230, 2001.
- [198] S. Modak *et al.*, "Adoptive immunotherapy with haploidentical natural killer cells and Anti-GD2 monoclonal antibody m3F8 for resistant neuroblastoma: Results of a phase I study," (in eng), *Oncoimmunology*, vol. 7, no. 8, p. e1461305, 2018.
- [199] R. M. Richards, E. Sotillo, and R. G. Majzner, "CAR T Cell Therapy for Neuroblastoma," (in eng), *Front Immunol*, vol. 9, p. 2380, 2018.
- [200] C. U. Louis *et al.*, "Antitumor activity and long-term fate of chimeric antigen receptor-positive T cells in patients with neuroblastoma," (in eng), *Blood*, vol. 118, no. 23, pp. 6050-6, Dec 1 2011.
- [201] C. Rossig, S. Kailayangiri, S. Jamitzky, and B. Altvater, "Carbohydrate Targets for CAR T Cells in Solid Childhood Cancers," (in eng), *Front Oncol*, vol. 8, p. 513, 2018.
- [202] A. Heczey *et al.*, "CAR T cells administered in combination with lymphodepletion and PD-1 inhibition to patients with neuroblastoma," *Molecular Therapy*, vol. 25, no. 9, pp. 2214-2224, 2017.
- [203] J. Cheng *et al.*, "Understanding the Mechanisms of Resistance to CAR T-Cell Therapy in Malignancies," (in English), *Frontiers in Oncology*, Review vol. 9, no. 1237, 2019-November-21 2019.
- [204] M. Ahmadzadeh and S. A. Rosenberg, "IL-2 administration increases CD4+CD25hi Foxp3+ regulatory T cells in cancer patients," *Blood*, vol. 107, no. 6, pp. 2409-2414, 2006.
- [205] K. Newick, S. O'Brien, E. Moon, and S. M. Albelda, "CAR T Cell Therapy for Solid Tumors," *Annual Review of Medicine*, vol. 68, no. 1, pp. 139-152, 2017/01/14 2017.
- [206] L. W. Goldman, "Principles of CT and CT technology," *Journal of nuclear medicine technology*, vol. 35, no. 3, pp. 115-128, 2007.
- [207] K. S. Caldemeyer and K. A. Buckwalter, "The basic principles of computed tomography and magnetic resonance imaging," *Journal of the American Academy of Dermatology*, vol. 41, no. 5, pp. 768-771, 1999.
- [208] V. P. B. Grover, J. M. Tognarelli, M. M. E. Crossey, I. J. Cox, S. D. Taylor-Robinson, and M. J. W. McPhail, "Magnetic Resonance Imaging: Principles and Techniques: Lessons for Clinicians," (in eng), *Journal of clinical and experimental hepatology*, vol. 5, no. 3, pp. 246-255, 2015.
- [209] B. M. Dale, M. A. Brown, and R. C. Semelka, *MRI: basic principles and applications*. John Wiley & Sons, 2015.
- [210] G. C. Pereira, M. Traughber, and R. F. Muzic, "The Role of Imaging in Radiation Therapy Planning: Past, Present, and Future," *BioMed Research International*, vol. 2014, p. 231090, 2014/04/10 2014.
- [211] C. Constantinou, J. C. Harrington, and L. A. DeWerd, "An electron density calibration phantom for CT-based treatment planning computers," (in eng), *Med Phys*, vol. 19, no. 2, pp. 325-7, Mar-Apr 1992.
- [212] A. M. Owrangi, P. B. Greer, and C. K. Glide-Hurst, "MRI-only treatment planning: benefits and challenges," (in eng), *Phys Med Biol*, vol. 63, no. 5, p. 05tr01, Feb 26 2018.
- [213] M. A. Schmidt and G. S. Payne, "Radiotherapy planning using MRI," (in eng), *Phys Med Biol*, vol. 60, no. 22, pp. R323-61, Nov 21 2015.
- [214] D. J. Margolis, J. M. Hoffman, R. J. Herfkens, R. B. Jeffrey, A. Quon, and S. S. Gambhir, "Molecular imaging techniques in body imaging," (in eng), *Radiology*, vol. 245, no. 2, pp. 333-56, Nov 2007.

- [215] D. A. Mankoff, "A definition of molecular imaging," (in eng), *J Nucl Med*, vol. 48, no. 6, pp. 18n, 21n, Jun 2007.
- [216] M. A. Pysz, S. S. Gambhir, and J. K. Willmann, "Molecular imaging: current status and emerging strategies," (in eng), *Clinical radiology*, vol. 65, no. 7, pp. 500-516, 2010.
- [217] M. F. Kircher and J. K. Willmann, "Molecular body imaging: MR imaging, CT, and US. Part II. Applications," *Radiology*, vol. 264, no. 2, pp. 349-368, 2012.
- [218] M. A. Ibrahim, B. Hazhirkarzar, and A. B. Dublin, "Magnetic resonance imaging (MRI) gadolinium," in *StatPearls [Internet]*: StatPearls Publishing, 2020.
- [219] R. Steiner, "History and progress on accurate measurements of the Planck constant," (in eng), *Rep Prog Phys*, vol. 76, no. 1, p. 016101, Jan 2013.
- [220] T. Bäck and L. Jacobsson, "The alpha-camera: a quantitative digital autoradiography technique using a charge-coupled device for ex vivo high-resolution bioimaging of alpha-particles," (in eng), *J Nucl Med*, vol. 51, no. 10, pp. 1616-23, Oct 2010.
- [221] M. Makvandi *et al.*, "Alpha-Emitters and Targeted Alpha Therapy in Oncology: from Basic Science to Clinical Investigations," (in eng), *Target Oncol*, vol. 13, no. 2, pp. 189-203, Apr 2018.
- [222] C. Parker *et al.*, "Targeted Alpha Therapy, an Emerging Class of Cancer Agents: A Review," (in eng), *JAMA Oncol*, vol. 4, no. 12, pp. 1765-1772, Dec 1 2018.
- [223] S. Nilsson *et al.*, "Bone-targeted radium-223 in symptomatic, hormone-refractory prostate cancer: a randomised, multicentre, placebo-controlled phase II study," (in eng), *Lancet Oncol*, vol. 8, no. 7, pp. 587-94, Jul 2007.
- [224] C. C. Parker *et al.*, "A randomized, double-blind, dose-finding, multicenter, phase 2 study of radium chloride (Ra 223) in patients with bone metastases and castration-resistant prostate cancer," (in eng), *Eur Urol*, vol. 63, no. 2, pp. 189-97, Feb 2013.
- [225] D. K. Strickland, G. Vaidyanathan, and M. R. Zalutsky, "Cytotoxicity of alpha-particle-emitting m-[211At]astatobenzylguanidine on human neuroblastoma cells," (in eng), *Cancer Res*, vol. 54, no. 20, pp. 5414-9, Oct 15 1994.
- [226] L. Emmett, K. Willowson, J. Violet, J. Shin, A. Blanksby, and J. Lee, "Lutetium (177) PSMA radionuclide therapy for men with prostate cancer: a review of the current literature and discussion of practical aspects of therapy," (in eng), *J Med Radiat Sci*, vol. 64, no. 1, pp. 52-60, Mar 2017.
- [227] J. W. Van Isselt, J. M. de Klerk, H. P. Koppeschaar, and P. P. Van Rijk, "Iodine-131 uptake and turnover rate vary over short intervals in Graves' disease," (in eng), *Nucl Med Commun*, vol. 21, no. 7, pp. 609-16, Jul 2000.
- [228] S. G. DuBois and K. K. Matthay, "Radiolabeled Metaiodobenzylguanidine for the Treatment of Neuroblastoma," (in eng), *Nucl Med Biol*, vol. 35, no. Suppl 1, pp. S35-48, Aug 2008.
- [229] F. D. Guerra Liberal, A. A. Tavares, and J. M. Tavares, "Comparative analysis of 11 different radioisotopes for palliative treatment of bone metastases by computational methods," (in eng), *Med Phys*, vol. 41, no. 11, p. 114101, Nov 2014.
- [230] A. Romer *et al.*, "Somatostatin-based radiopeptide therapy with [177Lu-DOTA]-TOC versus [90Y-DOTA]-TOC in neuroendocrine tumours," (in eng), *Eur J Nucl Med Mol Imaging*, vol. 41, no. 2, pp. 214-22, Feb 2014.
- [231] F. Forrer, H. Uusijärvi, D. Storch, H. R. Maecke, and J. Mueller-Brand, "Treatment with 177Lu-DOTATOC of patients with relapse of neuroendocrine tumors after treatment with 90Y-DOTATOC," (in eng), *J Nucl Med*, vol. 46, no. 8, pp. 1310-6, Aug 2005.

- [232] N. Marincek *et al.*, "Somatostatin-based radiotherapy with [90Y-DOTA]-TOC in neuroendocrine tumors: long-term outcome of a phase I dose escalation study," (in eng), *J Transl Med*, vol. 11, p. 17, Jan 15 2013.
- [233] A. Zemczak *et al.*, "Effect of Peptide Receptor Radionuclide Therapy (PRRT) with tandem isotopes - [90Y]Y/[177Lu]Lu-DOTATATE in patients with disseminated neuroendocrine tumours depending on qualification [18F]FDG PET/CT in Polish multicenter experience - do we need [18F]FDG," (in eng), *Endokrynol Pol*, Apr 20 2020.
- [234] R. Boellaard *et al.*, "FDG PET and PET/CT: EANM procedure guidelines for tumour PET imaging: version 1.0," (in eng), *European journal of nuclear medicine and molecular imaging*, vol. 37, no. 1, pp. 181-200, 2010.
- [235] J. Czernin, M. Allen-Auerbach, D. Nathanson, and K. Herrmann, "PET/CT in Oncology: Current Status and Perspectives," (in eng), *Curr Radiol Rep*, vol. 1, no. 3, pp. 177-190, 2013.
- [236] W. Sihver, J. Pietzsch, M. Krause, M. Baumann, J. Steinbach, and H.-J. Pietzsch, "Radiolabeled Cetuximab Conjugates for EGFR Targeted Cancer Diagnostics and Therapy (†)," *Pharmaceuticals*, vol. 7, no. 3, pp. 311-338, 03/05
- [237] C. B. Johnbeck *et al.*, "Head-to-Head Comparison of 64Cu-DOTATATE and 68Ga-DOTATOC PET/CT: A Prospective Study of 59 Patients with Neuroendocrine Tumors," *J Nucl Med*, vol. 58, no. 3, pp. 451-457, Mar 2017.
- [238] M. Mahesh and M. Madsen, "Addressing Technetium-99m Shortage," *Journal of the American College of Radiology*, vol. 14, no. 5, pp. 681-683, 2017/05/01/ 2017.
- [239] E. National Academies of Sciences and Medicine, *Molybdenum-99 for medical imaging*. National Academies Press, 2016.
- [240] V. Rufini *et al.*, "[123I]MIBG scintigraphy in neuroblastoma: a comparison between planar and SPECT imaging," (in eng), *Q J Nucl Med*, vol. 39, no. 4 Suppl 1, pp. 25-8, Dec 1995.
- [241] K. K. Matthay *et al.*, "Criteria for evaluation of disease extent by 123I-metaiodobenzylguanidine scans in neuroblastoma: a report for the International Neuroblastoma Risk Group (INRG) Task Force," *British Journal of Cancer*, vol. 102, no. 9, pp. 1319-1326, 2010/04/01 2010.
- [242] S. Sharp and M. Gelfand, "Utility of SPECT/CT imaging in neuroblastoma," *Journal of Nuclear Medicine*, vol. 50, no. supplement 2, pp. 200-200, 2009.
- [243] S. E. Sharp, A. T. Trout, B. D. Weiss, and M. J. Gelfand, "MIBG in Neuroblastoma Diagnostic Imaging and Therapy," (in eng), *Radiographics*, vol. 36, no. 1, pp. 258-78, Jan-Feb 2016.
- [244] E. C. Ehman *et al.*, "PET/MRI: Where might it replace PET/CT?," (in eng), *Journal of magnetic resonance imaging : JMRI*, vol. 46, no. 5, pp. 1247-1262, 2017.
- [245] I. Akkurt, K. Gunoglu, and S. S. Arda, "Detection Efficiency of NaI(Tl) Detector in 511–1332 keV Energy Range," *Science and Technology of Nuclear Installations*, vol. 2014, p. 186798, 2014/03/12 2014.
- [246] P. Lecoq, "Development of new scintillators for medical applications," *Nuclear Instruments and Methods in Physics Research Section A: Accelerators, Spectrometers, Detectors and Associated Equipment*, vol. 809, pp. 130-139, 2016/02/11/ 2016.
- [247] P. Zanzonico, "Principles of nuclear medicine imaging: planar, SPECT, PET, multi-modality, and autoradiography systems," (in eng), *Radiat Res*, vol. 177, no. 4, pp. 349-64, Apr 2012.

- [248] A. Rahmim and H. Zaidi, "PET versus SPECT: strengths, limitations and challenges," *Nucl Med Commun*, vol. 29, no. 3, pp. 193-207, Mar 2008.
- [249] "Nuclear medicine: Planar scintigraphy, SPECT and PET/CT," in *Introduction to Medical Imaging: Physics, Engineering and Clinical Applications*, A. Webb and N. B. Smith, Eds. (Cambridge Texts in Biomedical Engineering, Cambridge: Cambridge University Press, 2010, pp. 89-144.
- [250] P. J. Slomka, R. J. H. Miller, L. H. Hu, G. Germano, and D. S. Berman, "Solid-State Detector SPECT Myocardial Perfusion Imaging," (in eng), *J Nucl Med*, vol. 60, no. 9, pp. 1194-1204, Sep 2019.
- [251] R. Massari, A. D'Elia, and A. Soluri, "A new High-Resolution Imaging System (HiRIS2) detector for preclinical SPECT imaging," *Nuclear Instruments and Methods in Physics Research Section A: Accelerators, Spectrometers, Detectors and Associated Equipment*, vol. 917, pp. 25-30, 2019/02/11/ 2019.
- [252] M. Ljungberg, "Absolute Quantitation of SPECT Studies," *Seminars in Nuclear Medicine*, vol. 48, no. 4, pp. 348-358, 2018/07/01/ 2018.
- [253] P. J. Blower, "A nuclear chocolate box: the periodic table of nuclear medicine," (in eng), *Dalton transactions (Cambridge, England : 2003)*, vol. 44, no. 11, pp. 4819-4844, 2015.
- [254] V. Tolmachev, "Choice of Radionuclides and Radiolabelling Techniques," in *Targeted Radionuclide Tumor Therapy: Biological Aspects*, T. Stigbrand, J. Carlsson, and G. P. Adams, Eds. Dordrecht: Springer Netherlands, 2008, pp. 145-174.
- [255] M. Conti and L. Eriksson, "Physics of pure and non-pure positron emitters for PET: a review and a discussion," in *EJNMMI Phys*, vol. 3, 2016.
- [256] J. N. Bryan *et al.*, "Monoclonal antibodies for copper-64 PET dosimetry and radioimmunotherapy," (in eng), *Cancer Biol Ther*, vol. 11, no. 12, pp. 1001-7, Jun 15 2011.
- [257] G. J. Kemerink *et al.*, "Effect of the positron range of 18F, 68Ga and 124I on PET/CT in lung-equivalent materials," *European Journal of Nuclear Medicine and Molecular Imaging*, vol. 38, no. 5, pp. 940-948, 2011/05/01 2011.
- [258] J. van Dalen *et al.*, "Effect of the positron range on the spatial resolution of a new generation pre-clinical PET-scanner using F-18, Ga-68, Zr-89 and I-124," *Journal of Nuclear Medicine*, vol. 49, no. supplement 1, pp. 404P-404P, 2008.
- [259] B. Bai, J. Bading, and P. S. Conti, "Tumor Quantification in Clinical Positron Emission Tomography," *Theranostics*, Review vol. 3, no. 10, pp. 787-801, 2013.
- [260] P. E. Kinahan and J. W. Fletcher, "Positron emission tomography-computed tomography standardized uptake values in clinical practice and assessing response to therapy," (in eng), *Seminars in ultrasound, CT, and MR*, vol. 31, no. 6, pp. 496-505, 2010.
- [261] I. A. Burger, D. M. Huser, C. Burger, G. K. von Schulthess, and A. Buck, "Repeatability of FDG quantification in tumor imaging: averaged SUVs are superior to SUVmax," *Nuclear Medicine and Biology*, vol. 39, no. 5, pp. 666-670, 2012/07/01/ 2012.
- [262] N. C. Krak, R. Boellaard, O. S. Hoekstra, J. W. R. Twisk, C. J. Hoekstra, and A. A. Lammertsma, "Effects of ROI definition and reconstruction method on quantitative outcome and applicability in a response monitoring trial," *European Journal of Nuclear Medicine and Molecular Imaging*, vol. 32, no. 3, pp. 294-301, 2005/03/01 2005.
- [263] G. J. Treuner *et al.*, "Scintigraphic Imaging of Neuroblastoma with [131I]Iodobenzylguanidine," (in English), *The Lancet*, vol. 323, no. 8372, pp. 333-334, 1984/02/11 1984.

- [264] A. Naranjo *et al.*, "Comparison of  $^{123}\text{I}$ -metaiodobenzylguanidine (MIBG) and  $^{131}\text{I}$ -MIBG semi-quantitative scores in predicting survival in patients with stage 4 neuroblastoma: a report from the Children's Oncology Group," (in eng), *Pediatric blood & cancer*, vol. 56, no. 7, pp. 1041-1045, 2011.
- [265] B. Liu, H. Zhuang, and S. Servaes, "Comparison of  $^{123}\text{I}$ MIBG and  $^{131}\text{I}$ MIBG for imaging of neuroblastoma and other neural crest tumors," (in eng), *Q J Nucl Med Mol Imaging*, vol. 57, no. 1, pp. 21-8, Mar 2013.
- [266] P. O. Kiratli, M. Tuncel, and Z. Bar-Sever, "Nuclear Medicine in Pediatric and Adolescent Tumors," *Semin Nucl Med*, vol. 46, no. 4, pp. 308-23, Jul 2016.
- [267] G. A. Yanik *et al.*, "Semiquantitative mIBG scoring as a prognostic indicator in patients with stage 4 neuroblastoma: a report from the Children's oncology group," (in eng), *Journal of nuclear medicine : official publication, Society of Nuclear Medicine*, vol. 54, no. 4, pp. 541-548, 2013.
- [268] V. Lewington *et al.*, " $^{123}\text{I}$ -mIBG scintigraphy in neuroblastoma: development of a SIOOPEN semi-quantitative reporting method by an international panel," (in eng), *Eur J Nucl Med Mol Imaging*, vol. 44, no. 2, pp. 234-241, Feb 2017.
- [269] R. Ladenstein *et al.*, "Validation of the mIBG skeletal SIOOPEN scoring method in two independent high-risk neuroblastoma populations: the SIOOPEN/HR-NBL1 and COG-A3973 trials," (in eng), *Eur J Nucl Med Mol Imaging*, vol. 45, no. 2, pp. 292-305, Feb 2018.
- [270] S. Riaz, H. Bashir, S. J. Khan, and A. Qazi, " $^{131}\text{I}$  mIBG Scintigraphy Curie Versus SIOOPEN Scoring: Prognostic Value in Stage 4 Neuroblastoma," (in eng), *Mol Imaging Radionucl Ther*, vol. 27, no. 3, pp. 121-125, Oct 9 2018.
- [271] Z. Bar-Sever, A. Steinmetz, H. Bernstine, and S. Ash, "Significance of MIBG liver uptake in children with neuroblastoma," *Journal of Nuclear Medicine*, vol. 52, no. supplement 1, pp. 1400-1400, 2011.
- [272] A. Chopra, "(99m)Tc-Methyl diphosphonate," in *Molecular Imaging and Contrast Agent Database (MICAD)* Bethesda (MD): National Center for Biotechnology Information (US), 2004.
- [273] W. McCartney, M. Nusynowitz, B. Reimann, J. Prather, and B. Mazat, " $^{99\text{m}}\text{Tc}$ -diphosphonate uptake in neuroblastoma," *American Journal of Roentgenology*, vol. 126, no. 5, pp. 1077-1081, 1976.
- [274] S. Liu *et al.*, "(99m)Tc-Methylene Diphosphonate Uptake in Soft Tissue Tumors on Bone Scintigraphy Differs Between Pediatric and Adult Patients and Is Correlated with Tumor Differentiation," (in eng), *Cancer management and research*, vol. 12, pp. 2449-2457, 2020.
- [275] E. Turba, G. Fagioli, A. F. Mancini, P. Rosito, A. Galli, and P. Alvisi, "Evaluation of stage 4 neuroblastoma patients by means of MIBG and  $^{99\text{m}}\text{Tc}$ -MDP scintigraphy," (in eng), *J Nucl Biol Med*, vol. 37, no. 3, pp. 107-14, Sep 1993.
- [276] J. M. Gauguier *et al.*, "Evaluation of the utility of (99m) Tc-MDP bone scintigraphy versus MIBG scintigraphy and cross-sectional imaging for staging patients with neuroblastoma," (in eng), *Pediatr Blood Cancer*, vol. 64, no. 11, Nov 2017.
- [277] A. Almuhaideb, N. Papathanasiou, and J. Bomanji, " $^{18}\text{F}$ -FDG PET/CT imaging in oncology," *Annals of Saudi medicine*, vol. 31, no. 1, pp. 3-13, 2011.
- [278] E. K. J. Pauwels, M. J. Ribeiro, J. H. M. B. Stoot, V. R. McCready, M. Bourguignon, and B. Mazière, "FDG Accumulation and Tumor Biology," *Nuclear Medicine and Biology*, vol. 25, no. 4, pp. 317-322, 1998/05/01/ 1998.
- [279] K. Izuishi *et al.*, "Molecular mechanisms of  $^{18}\text{F}$ fluorodeoxyglucose accumulation in liver cancer," *Oncol Rep*, vol. 31, no. 2, pp. 701-706, 2014/02/01 2014.

## References

---

- [280] O. Warburg, "On the Origin of Cancer Cells," *Science*, vol. 123, no. 3191, p. 309, 1956.
- [281] P. P. Hsu and D. M. Sabatini, "Cancer Cell Metabolism: Warburg and Beyond," *Cell*, vol. 134, no. 5, pp. 703-707, 2008/09/05/ 2008.
- [282] C. Love, M. B. Tomas, G. G. Tronco, and C. J. Palestro, "FDG PET of Infection and Inflammation," *RadioGraphics*, vol. 25, no. 5, pp. 1357-1368, 2005/09/01 2005.
- [283] W. Chen, "Clinical applications of PET in brain tumors," *Journal of nuclear medicine*, vol. 48, no. 9, pp. 1468-1481, 2007.
- [284] S. E. Sharp, B. L. Shulkin, M. J. Gelfand, S. Salisbury, and W. L. Furman, "123I-MIBG scintigraphy and 18F-FDG PET in neuroblastoma," (in eng), *J Nucl Med*, vol. 50, no. 8, pp. 1237-43, Aug 2009.
- [285] D. R. Taggart *et al.*, "Comparison of iodine-123 metaiodobenzylguanidine (MIBG) scan and [18F]fluorodeoxyglucose positron emission tomography to evaluate response after iodine-131 MIBG therapy for relapsed neuroblastoma," (in eng), *J Clin Oncol*, vol. 27, no. 32, pp. 5343-9, Nov 10 2009.
- [286] N. D. Papatasiou *et al.*, "18F-FDG PET/CT and 123I-Metaiodobenzylguanidine Imaging in High-Risk Neuroblastoma: Diagnostic Comparison and Survival Analysis," *Journal of Nuclear Medicine*, vol. 52, no. 4, pp. 519-525, April 1, 2011 2011.
- [287] A. Cistaro *et al.*, "124I-MIBG: a new promising positron-emitting radiopharmaceutical for the evaluation of neuroblastoma," *Nucl Med Rev Cent East Eur*, vol. 18, no. 2, pp. 102-6, 2015.
- [288] N. Pandit-Taskar *et al.*, "Biodistribution and Dosimetry of (18)F-Meta-Fluorobenzylguanidine: A First-in-Human PET/CT Imaging Study of Patients with Neuroendocrine Malignancies," (in eng), *J Nucl Med*, vol. 59, no. 1, pp. 147-153, Jan 2018.
- [289] S.-y. Huang *et al.*, "Patient-specific dosimetry using pretherapy [<sup>124</sup>I]miodobenzylguanidine ([<sup>124</sup>I]mIBG) dynamic PET/CT imaging before [<sup>131</sup>I]mIBG targeted radionuclide therapy for neuroblastoma," (in eng), *Molecular imaging and biology*, vol. 17, no. 2, pp. 284-294, 2015.
- [290] M. Aboian *et al.*, "124I-MIBG PET-CT to monitor metastatic disease in children with relapsed neuroblastoma," *Journal of Nuclear Medicine*, May 15, 2020 2020.
- [291] E. Pauwels *et al.*, "Improved resolution and sensitivity of [(18)F]MFBG PET compared with [(123)I]MIBG SPECT in a patient with a norepinephrine transporter-expressing tumour," (in eng), *Eur J Nucl Med Mol Imaging*, May 8 2020.
- [292] M. M. Alauddin, "Positron emission tomography (PET) imaging with (18)F-based radiotracers," (in eng), *Am J Nucl Med Mol Imaging*, vol. 2, no. 1, pp. 55-76, 2012.
- [293] H. Zhang *et al.*, "Synthesis and Evaluation of [(18)F]Fluorine-labeled Benzylguanidine Analogs for Targeting the Human Norepinephrine Transporter," *European journal of nuclear medicine and molecular imaging*, vol. 41, no. 2, pp. 322-332, 10/31 2014.
- [294] F. C. Cook and J. R. G., "Quantitative techniques in 18FDG PET scanning in oncology," (in En), *British Journal of Cancer*, Reviews vol. 98, no. 10, p. 1597, 2008-05-13 2008.
- [295] P. Ziai *et al.*, "Role of Optimal Quantification of FDG PET Imaging in the Clinical Practice of Radiology," *RadioGraphics*, vol. 36, no. 2, pp. 481-496, 2016.
- [296] M. Conti and L. Eriksson, "Physics of pure and non-pure positron emitters for PET: a review and a discussion," *EJNMMI Phys*, vol. 3, no. 1, p. 8, Dec 2016.

- [297] P. K. Garg, S. Garg, and M. R. Zalutsky, "Synthesis and preliminary evaluation of para- and meta-[18F]fluorobenzylguanidine," (in eng), *Nucl Med Biol*, vol. 21, no. 1, pp. 97-103, Jan 1994.
- [298] B. H. Rotstein *et al.*, "Mechanistic studies and radiofluorination of structurally diverse pharmaceuticals with spirocyclic iodonium(iii) ylides," *Chemical Science*, 10.1039/C6SC00197A vol. 7, no. 7, pp. 4407-4417, 2016.
- [299] S. Preshlock *et al.*, "Enhanced copper-mediated 18F-fluorination of aryl boronic esters provides eight radiotracers for PET applications," *Chemical Communications*, 10.1039/C6CC03295H vol. 52, no. 54, pp. 8361-8364, 2016.
- [300] C. Nanni, S. Fanti, and D. Rubello, "18F-DOPA PET and PET/CT," *Journal of Nuclear Medicine*, vol. 48, no. 10, pp. 1577-1579, October 1, 2007 2007.
- [301] A. Piccardo and E. Lopci, "Potential role of 18F-DOPA PET in neuroblastoma," *Clinical and Translational Imaging*, vol. 4, no. 2, pp. 79-86, 2016/04/01 2016.
- [302] A. Piccardo *et al.*, "Comparison of 18F-dopa PET/CT and 123I-MIBG scintigraphy in stage 3 and 4 neuroblastoma: a pilot study," *European Journal of Nuclear Medicine and Molecular Imaging*, vol. 39, no. 1, pp. 57-71, 2012/01/01 2012.
- [303] A. Piccardo *et al.*, "Prognostic value of 18F-DOPA PET/CT at the time of recurrence in patients affected by neuroblastoma," *European Journal of Nuclear Medicine and Molecular Imaging*, vol. 41, no. 6, pp. 1046-1056, 2014/06/01 2014.
- [304] A. V. Mossine *et al.*, "Synthesis of high-molar-activity [18F]6-fluoro-1-DOPA suitable for human use via Cu-mediated fluorination of a BPin precursor," *Nature Protocols*, vol. 15, no. 5, pp. 1742-1759, 2020/05/01 2020.
- [305] H. R. Maecke and J. C. Reubi, "Somatostatin Receptors as Targets for Nuclear Medicine Imaging and Radionuclide Treatment," *Journal of Nuclear Medicine*, vol. 52, no. 6, pp. 841-844, June 1, 2011 2011.
- [306] N. Alexander *et al.*, "Prevalence and Clinical Correlations of Somatostatin Receptor-2 (SSTR2) Expression in Neuroblastoma," (in eng), *J Pediatr Hematol Oncol*, vol. 41, no. 3, pp. 222-227, Apr 2019.
- [307] L. Bodei, V. Ambrosini, K. Herrmann, and I. Modlin, "Current Concepts in (68)Ga-DOTATATE Imaging of Neuroendocrine Neoplasms: Interpretation, Biodistribution, Dosimetry, and Molecular Strategies," (in eng), *J Nucl Med*, vol. 58, no. 11, pp. 1718-1726, Nov 2017.
- [308] J. E. Gains *et al.*, "68Ga-DOTATATE and 123I-mIBG as imaging biomarkers of disease localisation in metastatic neuroblastoma: implications for molecular radiotherapy," (in eng), *Nucl Med Commun*, Aug 10 2020.
- [309] G. Kong *et al.*, "Initial Experience With Gallium-68 DOTA-Octreotate PET/CT and Peptide Receptor Radionuclide Therapy for Pediatric Patients With Refractory Metastatic Neuroblastoma," (in eng), *J Pediatr Hematol Oncol*, vol. 38, no. 2, pp. 87-96, Mar 2016.
- [310] J. E. Gains, N. J. Sebire, V. Moroz, K. Wheatley, and M. N. Gaze, "Immunohistochemical evaluation of molecular radiotherapy target expression in neuroblastoma tissue," (in eng), *Eur J Nucl Med Mol Imaging*, vol. 45, no. 3, pp. 402-411, Mar 2018.
- [311] M. Naji *et al.*, "68Ga-DOTA-TATE PET vs. 123I-MIBG in identifying malignant neural crest tumours," (in eng), *Mol Imaging Biol*, vol. 13, no. 4, pp. 769-775, Aug 2011.
- [312] J. B. Maurice *et al.*, "A comparison of the performance of 68Ga-DOTATATE PET/CT and 123I-MIBG SPECT in the diagnosis and follow-up of

- phaeochromocytoma and paraganglioma," (in eng), *Eur J Nucl Med Mol Imaging*, vol. 39, no. 8, pp. 1266-70, Aug 2012.
- [313] P. Shahrokhi *et al.*, "(68)Ga-DOTATATE PET/CT Compared with (131)I-MIBG SPECT/CT in the Evaluation of Neural Crest Tumors," (in eng), *Asia Ocean J Nucl Med Biol*, vol. 8, no. 1, pp. 8-17, Winter 2020.
- [314] W. Wei, Z. T. Rosenkrans, J. Liu, G. Huang, Q.-Y. Luo, and W. Cai, "ImmunoPET: Concept, Design, and Applications," *Chemical Reviews*, vol. 120, no. 8, pp. 3787-3851, 2020.
- [315] S. Reddy and M. K. Robinson, "Immuno-positron emission tomography in cancer models," (in eng), *Seminars in nuclear medicine*, vol. 40, no. 3, pp. 182-189, 2010.
- [316] B. N. McKnight and N. T. Viola-Villegas, "(89) Zr-ImmunoPET companion diagnostics and their impact in clinical drug development," (in eng), *Journal of labelled compounds & radiopharmaceuticals*, vol. 61, no. 9, pp. 727-738, 2018.
- [317] S. M. Larson *et al.*, "PET scanning of iodine-124-3F9 as an approach to tumor dosimetry during treatment planning for radioimmunotherapy in a child with neuroblastoma," (in eng), *J Nucl Med*, vol. 33, no. 11, pp. 2020-3, Nov 1992.
- [318] S. D. Yeh *et al.*, "Radioimmunodetection of neuroblastoma with iodine-131-3F8: correlation with biopsy, iodine-131-metaiodobenzylguanidine and standard diagnostic modalities," (in eng), *J Nucl Med*, vol. 32, no. 5, pp. 769-76, May 1991.
- [319] A. L. Vāvere *et al.*, "<sup>64</sup>Cu-p-NH<sub>2</sub>-Bn-DOTA-hu14.18K322A, a PET Radiotracer Targeting Neuroblastoma and Melanoma," *Journal of Nuclear Medicine*, vol. 53, no. 11, pp. 1772-1778, November 1, 2012 2012.
- [320] E. R. Butch *et al.*, "Positron Emission Tomography Detects In Vivo Expression of Disialoganglioside GD2 in Mouse Models of Primary and Metastatic Osteosarcoma," *Cancer Research*, p. canres.3340.2018, 2019.
- [321] C. J. Anderson and R. Ferdani, "Copper-64 radiopharmaceuticals for PET imaging of cancer: advances in preclinical and clinical research," (in eng), *Cancer biotherapy & radiopharmaceuticals*, vol. 24, no. 4, pp. 379-393, 2009.
- [322] B. Gutfilen, S. A. Souza, and G. Valentini, "Copper-64: a real theranostic agent," (in eng), *Drug design, development and therapy*, vol. 12, pp. 3235-3245, 2018.
- [323] Robinson *et al.*, "Guidelines for the welfare and use of animals in cancer research," (in En), *British Journal of Cancer*, Research vol. 102, no. 11, p. 1555, 2010-05-25 2010.
- [324] Y. Anongpornjossakul *et al.*, "Iodine-131 metaiodobenzylguanidine (131I-mIBG) treatment in relapsed/refractory neuroblastoma," (in eng), *Nucl Med Commun*, vol. 41, no. 4, pp. 336-343, Apr 2020.
- [325] B. Hu, A. L. Vavere, K. D. Neumann, B. L. Shulkin, S. G. DiMagno, and S. E. Snyder, "A practical, automated synthesis of meta-[(18)F]fluorobenzylguanidine for clinical use," *ACS Chem Neurosci*, vol. 6, no. 11, pp. 1870-9, Nov 18 2015.
- [326] K. J. Makaravage, A. F. Brooks, A. V. Mossine, M. S. Sanford, and P. J. H. Scott, "Copper-Mediated Radiofluorination of Arylstannanes with [18F]KF," *Organic Letters*, vol. 18, no. 20, pp. 5440-5443, 2016/10/21 2016.
- [327] D. Thorek *et al.*, "Cerenkov imaging - a new modality for molecular imaging," (in eng), *Am J Nucl Med Mol Imaging*, vol. 2, no. 2, pp. 163-73, 2012.
- [328] S. Das, D. L. J. Thorek, and J. Grimm, "Cerenkov imaging," (in eng), *Advances in cancer research*, vol. 124, pp. 213-234, 2014.
- [329] A. E. Spinelli *et al.*, "First human Cerenkography," (in eng), *J Biomed Opt*, vol. 18, no. 2, p. 20502, Feb 2013.
- [330] M. Schmidt, T. Simon, B. Hero, H. Schicha, and F. Berthold, "The prognostic impact of functional imaging with (123)I-mIBG in patients with stage 4 neuroblastoma >1 year of age on a high-risk treatment protocol: results of the

- German Neuroblastoma Trial NB97," *Eur J Cancer*, vol. 44, no. 11, pp. 1552-8, Jul 2008.
- [331] K. K. Matthay *et al.*, "Correlation of early metastatic response by 123I-metaiodobenzylguanidine scintigraphy with overall response and event-free survival in stage IV neuroblastoma," *J Clin Oncol*, vol. 21, no. 13, pp. 2486-91, Jul 1 2003.
- [332] N. Ady *et al.*, "A new 123I-MIBG whole body scan scoring method--application to the prediction of the response of metastases to induction chemotherapy in stage IV neuroblastoma," *Eur J Cancer*, vol. 31A, no. 2, pp. 256-61, 1995.
- [333] J. A. Messina *et al.*, "Evaluation of semi-quantitative scoring system for metaiodobenzylguanidine (mIBG) scans in patients with relapsed neuroblastoma," *Pediatr Blood Cancer*, vol. 47, no. 7, pp. 865-74, Dec 2006.
- [334] H. Li, S. K. Ma, X. P. Hu, G. Y. Zhang, and J. Fei, "Norepinephrine transporter (NET) is expressed in cardiac sympathetic ganglia of adult rat," (in eng), *Cell Res*, vol. 11, no. 4, pp. 317-20, Dec 2001.
- [335] A. Chirumamilla and M. I. Travin, "Cardiac applications of 123I-mIBG imaging," (in eng), *Semin Nucl Med*, vol. 41, no. 5, pp. 374-87, Sep 2011.
- [336] J. Nedergaard and B. Cannon, "35 - Brown Adipose Tissue: Development and Function," in *Fetal and Neonatal Physiology (Fifth Edition)*, R. A. Polin, S. H. Abman, D. H. Rowitch, W. E. Benitz, and W. W. Fox, Eds.: Elsevier, 2017, pp. 354-363.e4.
- [337] K. D. Evans, T. A. Tulloss, and N. Hall, "18FDG uptake in brown fat: potential for false positives," (in eng), *Radiol Technol*, vol. 78, no. 5, pp. 361-6, May-Jun 2007.
- [338] J. Sidlo, P. Kvasnicka, and H. Sidlova, "Occurrence of periadrenal brown adipose tissue in adult Slovak population," (in eng), *Neuro Endocrinol Lett*, vol. 40, no. Suppl1, pp. 49-55, Oct 8 2019.
- [339] M. Blau, R. Ganatra, and M. A. Bender, "18F-fluoride for bone imaging," *Seminars in Nuclear Medicine*, vol. 2, no. 1, pp. 31-37, 1972/01/01/ 1972.
- [340] C. Chiesa, R. Castellani, M. Mira, A. Lorenzoni, and G. D. Flux, "Dosimetry in 131I-mIBG therapy: moving toward personalized medicine," (in eng), *Q J Nucl Med Mol Imaging*, vol. 57, no. 2, pp. 161-70, Jun 2013.
- [341] N. Pandit-Taskar, P. Zanzonico, P. Hilden, I. Ostrovnaya, J. A. Carrasquillo, and S. Modak, "Assessment of Organ Dosimetry for Planning Repeat Treatments of High-Dose (131)I-MIBG Therapy: (123)I-MIBG vs. Post-Therapy (131)I-MIBG Imaging," *Clinical nuclear medicine*, vol. 42, no. 10, pp. 741-748, 06/24/nihms-submitted
- [342] R. Accorsi, M. J. Morowitz, M. Charron, and J. M. Maris, "Pinhole imaging of 131I-metaiodobenzylguanidine (131I-MIBG) in an animal model of neuroblastoma," (in eng), *Pediatr Radiol*, vol. 33, no. 10, pp. 688-92, Oct 2003.
- [343] D. Kayano and S. Kinuya, "Current Consensus on I-131 MIBG Therapy," (in eng), *Nuclear medicine and molecular imaging*, vol. 52, no. 4, pp. 254-265, 2018.
- [344] S. S. More *et al.*, "Vorinostat increases expression of functional norepinephrine transporter in neuroblastoma in vitro and in vivo model systems," (in eng), *Clin Cancer Res*, vol. 17, no. 8, pp. 2339-49, Apr 15 2011.
- [345] S. Mueller *et al.*, "Cooperation of the HDAC inhibitor vorinostat and radiation in metastatic neuroblastoma: efficacy and underlying mechanisms," (in eng), *Cancer letters*, vol. 306, no. 2, pp. 223-229, 2011.

- [346] A. Gerelchuluun *et al.*, "Histone Deacetylase Inhibitor Induced Radiation Sensitization Effects on Human Cancer Cells after Photon and Hadron Radiation Exposure," (in eng), *Int J Mol Sci*, vol. 19, no. 2, Feb 7 2018.
- [347] L. Zhu, K. Wu, S. Ma, and S. Zhang, "HDAC inhibitors: a new radiosensitizer for non-small-cell lung cancer," (in eng), *Tumori*, vol. 101, no. 3, pp. 257-62, May-Jun 2015.
- [348] S. G. DuBois *et al.*, "Phase II Trial of Alisertib in Combination with Irinotecan and Temozolomide for Patients with Relapsed or Refractory Neuroblastoma," (in eng), *Clin Cancer Res*, vol. 24, no. 24, pp. 6142-6149, Dec 15 2018.
- [349] G. Barone, J. Anderson, A. D. Pearson, K. Petrie, and L. Chesler, "New strategies in neuroblastoma: Therapeutic targeting of MYCN and ALK," *Clin Cancer Res*, vol. 19, no. 21, pp. 5814-21, Nov 01 2013.
- [350] H. Mei, Y. Wang, Z. Lin, and Q. Tong, "The mTOR signaling pathway in pediatric neuroblastoma," (in eng), *Pediatr Hematol Oncol*, vol. 30, no. 7, pp. 605-15, Oct 2013.
- [351] H. Zhang *et al.*, "mTOR ATP-competitive inhibitor INK128 inhibits neuroblastoma growth via blocking mTORC signaling," (in eng), *Apoptosis : an international journal on programmed cell death*, vol. 20, no. 1, pp. 50-62, 2015.
- [352] D.-Q. Xu *et al.*, "Anti-tumor effect of AZD8055 against neuroblastoma cells in vitro and in vivo," *Experimental Cell Research*, vol. 365, no. 2, pp. 177-184, 2018/04/15/ 2018.
- [353] A. Naing *et al.*, "Safety, tolerability, pharmacokinetics and pharmacodynamics of AZD8055 in advanced solid tumours and lymphoma," (in eng), *Br J Cancer*, vol. 107, no. 7, pp. 1093-9, Sep 25 2012.
- [354] A. Ohtsu *et al.*, "Everolimus for previously treated advanced gastric cancer: results of the randomized, double-blind, phase III GRANITE-1 study," (in eng), *Journal of clinical oncology : official journal of the American Society of Clinical Oncology*, vol. 31, no. 31, pp. 3935-3943, 2013.
- [355] C. Magaway, E. Kim, and E. Jacinto, "Targeting mTOR and Metabolism in Cancer: Lessons and Innovations," (in eng), *Cells*, vol. 8, no. 12, p. 1584, 2019.
- [356] O. J. Becher *et al.*, "A phase I study of perifosine with temsirolimus for recurrent pediatric solid tumors," (in eng), *Pediatr Blood Cancer*, vol. 64, no. 7, Jul 2017.
- [357] A. D. J. Pearson *et al.*, "A phase 1 study of oral ridaforolimus in pediatric patients with advanced solid tumors," (in eng), *Oncotarget*, vol. 7, no. 51, pp. 84736-84747, 2016.
- [358] K. G. Pike *et al.*, "Optimization of potent and selective dual mTORC1 and mTORC2 inhibitors: The discovery of AZD8055 and AZD2014," *Bioorganic & Medicinal Chemistry Letters*, vol. 23, no. 5, pp. 1212-1216, 2013/03/01/ 2013.
- [359] Pike *et al.*, "AZD2014, an Inhibitor of mTORC1 and mTORC2, Is Highly Effective in ER+ Breast Cancer When Administered Using Intermittent or Continuous Schedules," (in en), 2015-11-01 2015.
- [360] A. C. Wong Te Fong *et al.*, "Evaluation of the combination of the dual mTORC1/2 inhibitor vistusertib (AZD2014) and paclitaxel in ovarian cancer models," (in eng), *Oncotarget*, vol. 8, no. 69, pp. 113874-113884, Dec 26 2017.
- [361] B. Basu *et al.*, "First-in-human pharmacokinetic and pharmacodynamic study of the dual m-TORC 1/2 inhibitor, AZD2014," (in eng), *Clin Cancer Res*, vol. 21, no. 15, pp. 3412-9, Aug 1 2015.
- [362] P. Schmid *et al.*, "Fulvestrant Plus Vistusertib vs Fulvestrant Plus Everolimus vs Fulvestrant Alone for Women With Hormone Receptor-Positive Metastatic Breast Cancer: The MANTA Phase 2 Randomized Clinical Trial," (in eng), *JAMA Oncol*, vol. 5, no. 11, pp. 1556-63, Aug 29 2019.

- [363] C. C. Yu *et al.*, "AZD2014 Radiosensitizes Oral Squamous Cell Carcinoma by Inhibiting AKT/mTOR Axis and Inducing G1/G2/M Cell Cycle Arrest," (in eng), *PLoS One*, vol. 11, no. 3, p. e0151942, 2016.
- [364] A. R. Mattoo, A. Joun, and J. M. Jessup, "Repurposing of mTOR Complex Inhibitors Attenuates MCL-1 and Sensitizes to PARP Inhibition," *Molecular Cancer Research*, vol. 17, no. 1, p. 42, 2019.
- [365] K. Zormpas-Petridis *et al.*, "Noninvasive MRI native T1 mapping detects response to MYCN-targeted therapies in the Th-MYCN model of neuroblastoma," *Cancer Research*, p. canres.0133.2020, 2020.
- [366] M. A. Siuta *et al.*, "Dysregulation of the norepinephrine transporter sustains cortical hypodopaminergia and schizophrenia-like behaviors in neuronal rictor null mice," *PLoS Biol*, vol. 8, no. 6, p. e1000393, 2010.
- [367] S. D. Robertson *et al.*, "Insulin reveals Akt signaling as a novel regulator of norepinephrine transporter trafficking and norepinephrine homeostasis," (in eng), *The Journal of neuroscience : the official journal of the Society for Neuroscience*, vol. 30, no. 34, pp. 11305-11316, 2010.
- [368] C.-S. Chen, S.-C. Weng, P.-H. Tseng, H.-P. Lin, and C.-S. Chen, "Histone acetylation-independent effect of histone deacetylase inhibitors on Akt through the reshuffling of protein phosphatase 1 complexes," *Journal of Biological Chemistry*, vol. 280, no. 46, pp. 38879-38887, 2005.
- [369] M. Fouladi *et al.*, "A phase I trial of MK-2206 in children with refractory malignancies: a Children's Oncology Group study," (in eng), *Pediatric blood & cancer*, vol. 61, no. 7, pp. 1246-1251, 2014.
- [370] H. Liao *et al.*, "Dramatic antitumor effects of the dual mTORC1 and mTORC2 inhibitor AZD2014 in hepatocellular carcinoma," (in eng), *American journal of cancer research*, vol. 5, no. 1, pp. 125-139, 2014.
- [371] J. Genolla, T. Rodriguez, P. Minguez, R. Lopez-Almaraz, V. Llorens, and A. Echebarria, "Dosimetry-based high-activity therapy with (131)I-metaiodobenzylguanidine ((131)I-mIBG) and topotecan for the treatment of high-risk refractory neuroblastoma," (in eng), *Eur J Nucl Med Mol Imaging*, vol. 46, no. 7, pp. 1567-1575, Jul 2019.
- [372] S. G. DuBois *et al.*, "Phase 1 Study of Vorinostat as a Radiation Sensitizer with 131I-Metaiodobenzylguanidine (131I-MIBG) for Patients with Relapsed or Refractory Neuroblastoma," (in eng), *Clin Cancer Res*, vol. 21, no. 12, pp. 2715-21, Jun 15 2015.
- [373] R. A. Saxton and D. M. Sabatini, "mTOR Signaling in Growth, Metabolism, and Disease," (in eng), *Cell*, vol. 168, no. 6, pp. 960-976, 2017.
- [374] D. D. Sarbassov, D. A. Guertin, S. M. Ali, and D. M. Sabatini, "Phosphorylation and regulation of Akt/PKB by the rictor-mTOR complex," (in eng), *Science*, vol. 307, no. 5712, pp. 1098-101, Feb 18 2005.
- [375] J. S. Carew, K. R. Kelly, and S. T. Nawrocki, "Mechanisms of mTOR inhibitor resistance in cancer therapy," *Targeted Oncology*, vol. 6, no. 1, pp. 17-27, 2011/03/01 2011.
- [376] J. Tan and Q. Yu, "Molecular mechanisms of tumor resistance to PI3K-mTOR-targeted therapy," (in eng), *Chinese journal of cancer*, vol. 32, no. 7, pp. 376-379, 2013.
- [377] J. Traynor, R. Mactier, C. C. Geddes, and J. G. Fox, "How to measure renal function in clinical practice," (in eng), *BMJ (Clinical research ed.)*, vol. 333, no. 7571, pp. 733-737, 2006.
- [378] M.-A. Caron, S. J. Charette, F. Maltais, and R. Debigaré, "Variability of protein level and phosphorylation status caused by biopsy protocol design in human

- skeletal muscle analyses," *BMC Research Notes*, vol. 4, no. 1, p. 488, 2011/11/10 2011.
- [379] L. C. Kim, R. S. Cook, and J. Chen, "mTORC1 and mTORC2 in cancer and the tumor microenvironment," (in eng), *Oncogene*, vol. 36, no. 16, pp. 2191-2201, Apr 20 2017.
- [380] S. Faes, T. Santoro, N. Demartines, and O. Dormond, "Evolving Significance and Future Relevance of Anti-Angiogenic Activity of mTOR Inhibitors in Cancer Therapy," (in eng), *Cancers*, vol. 9, no. 11, p. 152, 2017.
- [381] H. A. Lane *et al.*, "mTOR inhibitor RAD001 (everolimus) has antiangiogenic/vascular properties distinct from a VEGFR tyrosine kinase inhibitor," (in eng), *Clin Cancer Res*, vol. 15, no. 5, pp. 1612-22, Mar 1 2009.
- [382] P. Mannangatti, O. Arapulisamy, T. S. Shippenberg, S. Ramamoorthy, and L. D. Jayanthi, "Cocaine up-regulation of the norepinephrine transporter requires threonine 30 phosphorylation by p38 mitogen-activated protein kinase," *J Biol Chem*, vol. 286, no. 23, pp. 20239-50, Jun 10 2011.
- [383] O. Arapulisamy, P. Mannangatti, and L. D. Jayanthi, "Regulated norepinephrine transporter interaction with the neurokinin-1 receptor establishes transporter subcellular localization," (in eng), *J Biol Chem*, vol. 288, no. 40, pp. 28599-610, Oct 4 2013.
- [384] L. Galluzzi *et al.*, "Classification of current anticancer immunotherapies," *Oncotarget*, vol. 5, no. 24, p. 12472, 2014.
- [385] H. Zhang and J. Chen, "Current status and future directions of cancer immunotherapy," *Journal of Cancer*, vol. 9, no. 10, p. 1773, 2018.
- [386] R.-M. Lu *et al.*, "Development of therapeutic antibodies for the treatment of diseases," *Journal of Biomedical Science*, vol. 27, no. 1, p. 1, 2020/01/02 2020.
- [387] T. Simon *et al.*, "Long term outcome of high-risk neuroblastoma patients after immunotherapy with antibody ch14.18 or oral metronomic chemotherapy," (in eng), *BMC Cancer*, vol. 11, p. 21, Jan 18 2011.
- [388] M. F. Ozkaynak *et al.*, "A Comprehensive Safety Trial of Chimeric Antibody 14.18 With GM-CSF, IL-2, and Isotretinoin in High-Risk Neuroblastoma Patients Following Myeloablative Therapy: Children's Oncology Group Study ANBL0931," (in eng), *Frontiers in immunology*, vol. 9, pp. 1355-1355, 2018.
- [389] N.-K. V. Cheung, I. Ostrovnaya, D. Kuk, and I. Y. Cheung, "Bone marrow minimal residual disease was an early response marker and a consistent independent predictor of survival after anti-GD2 immunotherapy," (in eng), *Journal of clinical oncology : official journal of the American Society of Clinical Oncology*, vol. 33, no. 7, pp. 755-763, 2015.
- [390] N. K. Cheung *et al.*, "Anti-G(D2) antibody treatment of minimal residual stage 4 neuroblastoma diagnosed at more than 1 year of age," (in eng), *J Clin Oncol*, vol. 16, no. 9, pp. 3053-60, Sep 1998.
- [391] K. Kramer *et al.*, "Compartmental intrathecal radioimmunotherapy: results for treatment for metastatic CNS neuroblastoma," (in eng), *J Neurooncol*, vol. 97, no. 3, pp. 409-18, May 2010.
- [392] S. Modak, K. Kramer, and N. Pandit-Taskar, "Radioimmunotherapy of Neuroblastoma," in *Therapeutic Nuclear Medicine*, R. P. Baum, Ed. Berlin, Heidelberg: Springer Berlin Heidelberg, 2014, pp. 629-638.
- [393] K. Kramer *et al.*, "A phase II study of radioimmunotherapy with intraventricular (131) I-3F8 for medulloblastoma," (in eng), *Pediatric blood & cancer*, vol. 65, no. 1, p. 10.1002/pbc.26754, 2018.

- [394] A. Kasbollah, P. Eu, S. Cowell, and P. Deb, "Review on production of  $^{89}\text{Zr}$  in a medical cyclotron for PET radiopharmaceuticals," (in eng), *J Nucl Med Technol*, vol. 41, no. 1, pp. 35-41, Mar 2013.
- [395] A. Obata *et al.*, "Production of therapeutic quantities of  $(^{64}\text{Cu})$  using a 12 MeV cyclotron," (in eng), *Nucl Med Biol*, vol. 30, no. 5, pp. 535-9, Jul 2003.
- [396] S. J. Hosseinimehr, V. Tolmachev, and A. Orlova, "Liver uptake of radiolabeled targeting proteins and peptides: considerations for targeting peptide conjugate design," *Drug Discovery Today*, vol. 17, no. 21, pp. 1224-1232, 2012/11/01/2012.
- [397] S. D. Voss *et al.*, "Positron emission tomography (PET) imaging of neuroblastoma and melanoma with  $^{64}\text{Cu}$ -SarAr immunoconjugates," (in eng), *Proceedings of the National Academy of Sciences of the United States of America*, vol. 104, no. 44, pp. 17489-17493, 2007.
- [398] J. L. J. Dearling *et al.*, "Imaging cancer using PET--the effect of the bifunctional chelator on the biodistribution of a  $(^{64}\text{Cu})$ -labeled antibody," (in eng), *Nuclear medicine and biology*, vol. 38, no. 1, pp. 29-38, 2011.
- [399] A. L. Vavere *et al.*, " $^{64}\text{Cu}$ -p-NH<sub>2</sub>-Bn-DOTA-hu14.18K322A, a PET radiotracer targeting neuroblastoma and melanoma," (in eng), *J Nucl Med*, vol. 53, no. 11, pp. 1772-8, Nov 2012.
- [400] S. Acosta *et al.*, "Comprehensive characterization of neuroblastoma cell line subtypes reveals bilineage potential similar to neural crest stem cells," *BMC developmental biology*, vol. 9, pp. 12-12, 2009.
- [401] R. S. K. R. V. A. G. B. H. T. S. F. Berthold, "Lack of immunocytological GD2 expression on neuroblastoma cells in bone marrow at diagnosis, during treatment, and at recurrence\* - Schumacher-Kuckelkorn - 2017 - Pediatric Blood & Cancer - Wiley Online Library," *Paediatric Blood and Cancer*, 2016.
- [402] T. Terzic *et al.*, "Expression of Disialoganglioside (GD2) in Neuroblastic Tumors: A Prognostic Value for Patients Treated With Anti-GD2 Immunotherapy," *Pediatric and Developmental Pathology*, vol. 21, no. 4, pp. 355-362, 2018/07/01 2017.
- [403] Y. Komada *et al.*, "Flow cytometric analysis of peripheral blood and bone marrow for tumor cells in patients with neuroblastoma," *Cancer*, vol. 82, no. 3, pp. 591-599, 1998/02/01 1998.
- [404] K. Kramer, W. L. Gerald, B. H. Kushner, S. M. Larson, M. Hameed, and N. K. Cheung, "Disialoganglioside GD2 loss following monoclonal antibody therapy is rare in neuroblastoma," (in eng), *Med Pediatr Oncol*, vol. 36, no. 1, pp. 194-6, Jan 2001.
- [405] I. Y. Cheung, M. S. Lo Piccolo, B. H. Kushner, K. Kramer, and N. K. Cheung, "Quantitation of GD2 synthase mRNA by real-time reverse transcriptase polymerase chain reaction: clinical utility in evaluating adjuvant therapy in neuroblastoma," (in eng), *J Clin Oncol*, vol. 21, no. 6, pp. 1087-93, Mar 15 2003.
- [406] S. Sait and S. Modak, "Anti-GD2 immunotherapy for neuroblastoma," (in eng), *Expert review of anticancer therapy*, vol. 17, no. 10, pp. 889-904, 2017.
- [407] J. Voeller and P. M. Sondel, "Advances in Anti-GD2 Immunotherapy for Treatment of High-risk Neuroblastoma," (in eng), *Journal of pediatric hematology/oncology*, vol. 41, no. 3, pp. 163-169, 2019.
- [408] N.-K. V. Cheung, H. Guo, J. Hu, D. V. Tassev, and I. Y. Cheung, "Humanizing murine IgG3 anti-GD2 antibody m3F8 substantially improves antibody-dependent cell-mediated cytotoxicity while retaining targeting in vivo," *OncImmunity*, vol. 1, no. 4, pp. 477-486, 2012/07/01 2012.

- [409] European Medicines Agency. (2017). *EMA/H/C/003918/0000, Assessment report: Dinutuximab beta Apeiron. International non-proprietary name: dinutuximab beta.*
- [410] T. Tsuchida, M. H. Ravindranath, R. E. Saxton, and R. F. Irie, "Gangliosides of Human Melanoma: Altered Expression &em&gt;in Vivo&lt;/em&gt; and &lt;em&gt;in Vitro&lt;/em&gt;," *Cancer Research*, vol. 47, no. 5, p. 1278, 1987.
- [411] T. B. Chaston and D. R. Richardson, "Iron chelators for the treatment of iron overload disease: relationship between structure, redox activity, and toxicity," (in eng), *Am J Hematol*, vol. 73, no. 3, pp. 200-10, Jul 2003.
- [412] N. B. Bhatt, D. N. Pandya, and T. J. Wadas, "Recent Advances in Zirconium-89 Chelator Development," (in eng), *Molecules*, vol. 23, no. 3, Mar 12 2018.
- [413] W. E. Meijs, J. D. Herscheid, H. J. Haisma, and H. M. Pinedo, "Evaluation of desferal as a bifunctional chelating agent for labeling antibodies with Zr-89," (in eng), *Int J Rad Appl Instrum A*, vol. 43, no. 12, pp. 1443-7, Dec 1992.
- [414] I. Verel, G. W. Visser, R. Boellaard, M. Stigter-van Walsum, G. B. Snow, and G. A. van Dongen, "<sup>89</sup>Zr immuno-PET: comprehensive procedures for the production of <sup>89</sup>Zr-labeled monoclonal antibodies," (in eng), *J Nucl Med*, vol. 44, no. 8, pp. 1271-81, Aug 2003.
- [415] J. C. Almagro, T. R. Daniels-Wells, S. M. Perez-Tapia, and M. L. Penichet, "Progress and Challenges in the Design and Clinical Development of Antibodies for Cancer Therapy," (in English), *Frontiers in Immunology*, Review vol. 8, no. 1751, 2018-January-04 2018.
- [416] T. Lindmo, E. Boven, F. Cuttitta, J. Fedorko, and P. A. Bunn, Jr., "Determination of the immunoreactive fraction of radiolabeled monoclonal antibodies by linear extrapolation to binding at infinite antigen excess," (in eng), *J Immunol Methods*, vol. 72, no. 1, pp. 77-89, Aug 3 1984.
- [417] E. Butch, J. Mishra, V. Amador-Diaz, A. Vavere, and S. Snyder, "Selective detection of GD2-positive pediatric solid tumors using <sup>89</sup>Zr-Dinutuximab PET to facilitate anti-GD2 immunotherapy," *Journal of Nuclear Medicine*, vol. 59, no. supplement 1, p. 170, May 1, 2018 2018.
- [418] R. Li and S. Ladisch, "Abrogation of shedding of immunosuppressive neuroblastoma gangliosides," *Cancer research*, vol. 56, no. 20, pp. 4602-4605, 1996.
- [419] G. Lauc and M. Heffer-Lauc, "Shedding and uptake of gangliosides and glycosylphosphatidylinositol-anchored proteins," *Biochimica et Biophysica Acta (BBA) - General Subjects*, vol. 1760, no. 4, pp. 584-602, 2006/04/01/ 2006.
- [420] L. Valentino, T. Moss, E. Olson, H. Wang, R. Elashoff, and S. Ladisch, "Shed tumor gangliosides and progression of human neuroblastoma," *Blood*, vol. 75, pp. 1564-7, 05/01 1990.
- [421] M. Ovacik and K. Lin, "Tutorial on Monoclonal Antibody Pharmacokinetics and Its Considerations in Early Development," (in eng), *Clinical and translational science*, vol. 11, no. 6, pp. 540-552, 2018.
- [422] R. M. Sharkey *et al.*, "Advantage of residualizing radiolabels for an internalizing antibody against the B-cell lymphoma antigen, CD22," *Cancer Immunology, Immunotherapy*, vol. 44, no. 3, pp. 179-188, 1997/06/01 1997.
- [423] D. S. Abou, T. Ku, and P. M. Smith-Jones, "In vivo biodistribution and accumulation of <sup>89</sup>Zr in mice," (in eng), *Nuclear medicine and biology*, vol. 38, no. 5, pp. 675-681, 2011.
- [424] T. W. Price, J. Greenman, and G. J. Stasiuk, "Current advances in ligand design for inorganic positron emission tomography tracers <sup>68</sup>Ga, <sup>64</sup>Cu, <sup>89</sup>Zr and <sup>44</sup>Sc,"

- Dalton Transactions*, 10.1039/C5DT04706D vol. 45, no. 40, pp. 15702-15724, 2016.
- [425] S. Heskamp, R. Raavé, O. Boerman, M. Rijpkema, V. Goncalves, and F. Denat, "89Zr-immuno-positron emission tomography in oncology: state-of-the-art 89Zr radiochemistry," *Bioconjugate Chemistry*, vol. 28, no. 9, pp. 2211-2223, 2017.
- [426] J. K. Yoon, B. N. Park, E. K. Ryu, Y. S. An, and S. J. Lee, "Current Perspectives on (89)Zr-PET Imaging," (in eng), *Int J Mol Sci*, vol. 21, no. 12, Jun 17 2020.
- [427] M. H. Jansen *et al.*, "Molecular Drug Imaging: 89Zr-Bevacizumab PET in Children with Diffuse Intrinsic Pontine Glioma," *Journal of Nuclear Medicine*, vol. 58, no. 5, pp. 711-716, May 1, 2017 2017.
- [428] W. B. Hamilton, F. Helling, K. O. Lloyd, and P. O. Livingston, "Ganglioside expression on human malignant melanoma assessed by quantitative immune thin-layer chromatography," *International Journal of Cancer*, vol. 53, no. 4, pp. 566-573, 1993/02/20 1993.
- [429] J. Zhao *et al.*, "Attenuation of interleukin 2 signal in the spleen cells of complex ganglioside-lacking mice," (in eng), *J Biol Chem*, vol. 274, no. 20, pp. 13744-7, May 14 1999.
- [430] Y. Cao, J. P. Balthasar, and W. J. Jusko, "Second-generation minimal physiologically-based pharmacokinetic model for monoclonal antibodies," (in eng), *J Pharmacokinet Pharmacodyn*, vol. 40, no. 5, pp. 597-607, Oct 2013.
- [431] J. T. Ryman and B. Meibohm, "Pharmacokinetics of Monoclonal Antibodies," (in eng), *CPT: pharmacometrics & systems pharmacology*, vol. 6, no. 9, pp. 576-588, 2017.
- [432] M. Cataldi, C. Vigliotti, T. Mosca, M. Cammarota, and D. Capone, "Emerging Role of the Spleen in the Pharmacokinetics of Monoclonal Antibodies, Nanoparticles and Exosomes," (in eng), *Int J Mol Sci*, vol. 18, no. 6, Jun 10 2017.
- [433] Z.-L. Wu *et al.*, "Shedding of GD2 ganglioside by human neuroblastoma," *International Journal of Cancer*, vol. 39, no. 1, pp. 73-76, 1987/01/15 1987.
- [434] F. M. Balis *et al.*, "The ganglioside G(D2) as a circulating tumor biomarker for neuroblastoma," (in eng), *Pediatr Blood Cancer*, vol. 67, no. 1, p. e28031, Jan 2020.
- [435] S. A. Shah, "Correlation of Catabolism and Antigen Shedding with Monoclonal Antibody Uptake by Human Colon and Lung Tumor Xenografts," *Tumor Biology*, vol. 12, no. 5, pp. 287-297, 1991.
- [436] J.-H. Lee *et al.*, "Tumor-Shed Antigen Affects Antibody Tumor Targeting: Comparison of Two <sup>89</sup>Zr-Labeled Antibodies Directed against Shed or Nonshed Antigens," *Contrast Media & Molecular Imaging*, vol. 2018, p. 2461257, 2018/03/12 2018.
- [437] S. M. Lewis, A. Williams, and S. C. Eisenbarth, "Structure and function of the immune system in the spleen," (in eng), *Science immunology*, vol. 4, no. 33, p. eaau6085, 2019.
- [438] M. Tabrizi, G. G. Bornstein, and H. Suria, "Biodistribution mechanisms of therapeutic monoclonal antibodies in health and disease," (in eng), *The AAPS journal*, vol. 12, no. 1, pp. 33-43, 2010.
- [439] K. Osato, "Antigen-antibody complexes in the immune response. I. Analysis of the effectiveness of complexes on the primary antibody response," (in eng), *Immunology*, vol. 23, no. 4, pp. 545-557, 1972.